UNIVERSITY COLLEGE LONDON

CO_2 Absorption in Microstructured Membrane Reactors

Achilleas Constantinou

Department of Chemical Engineering

September 2011

Thesis submitted to University College London for the degree of Doctor of Philosophy

ABSTRACT

The objective of this work is to study experimentally and theoretically novel multiphase microreactors and characterize them in relation to hydrodynamics and mass transfer, in order to evaluate, understand and improve their performance. In order to achieve this CO_2 absorption in sodium hydroxide and amine solutions an example of a fast gas-liquid reaction has been investigated in a single microstructured metallic mesh reactor, CRL reactor, PTFE single channel membrane reactor and the silicon nitride mesh reactor.

CO_2 absorption in sodium hydroxide solution was initially studied experimentally and theoretically in a metal microstructured mesh reactor. The differential mass balances to describe the concentration profiles of components in the three domains (gas/membrane/liquid), were solved with Comsol Multiphysics (modeling software for finite element analysis of partial differential equations). The model indicated that the carbon dioxide is consumed within few microns from the gas – liquid interface, and the dominant resistance for mass transfer is located in the mesh because it is wetted by the liquid reactant. In order to overcome the limitation of the extra resistance to the mass transfer in the metallic mesh, PTFE membranes were used in the single channel reactor, which are considered as hydrophobic to aqueous solutions of NaOH and amines. Monoethanolamine solution (MEA) absorbed more CO_2 than diethanolamine (DEA) since the reaction rate constant for MEA is higher than DEA. 8 channel (PTFE) microreactor showed much higher CO_2 removal efficiency than the metallic mesh microreactor. Furthermore the model indicated partial-wetting of the PTFE membrane when NaOH solution was used as an absorbent.

In order to enhance mass transfer staggered herringbones were used on the floor of the liquid side of the single channel PTFE microreactor. No enhancement of mass transfer was observed with the use of staggered herringbones. A possible reason for that is that a limit for the fast

second-order reaction is reached for enhancement and that the apparent reaction rate is independent from mass transfer for our case, or that the herringbones are far away from the reaction zone and cannot create the appropriate stirring for enhancement.

In order to increase throughput, carbon dioxide absorption in sodium hydroxide solution was performed in the metallic mesh ‘scale-out’ reactor (with 4 meshes). CO_2 removal efficiency for the ‘scale-out’ reactor was significantly lower than the single mesh reactor, which is probably due to breakthrough of liquid in the gas phase (stagnant liquid) or uneven flow distribution in each plate of the ‘scale-out’ reactor.

Finally a silicon nitride mesh reactor developed by Bayer Technology Services and FluXXion was used for CO_2 absorption in aqueous solutions of NaOH and DEA. The silicon nitride mesh reactor showed better performance than the PTFE single channel reactor, the metallic 8 channel reactor and the CRL mesh reactor when NaOH was used, due to the very thin membrane of 1 μm thickness, which makes the resistance to mass transfer very small.

Dedicated to my parents

“Τας μεν πόλεις αναθήμασι τας δε ψυχάς μαθήμασι δει κοσμείν.” Σωκράτης

“Η πατρίδα δεν μετριέται με το στρέμμα αλλά μονάχα με της καρδιάς το πύρωμα και το αίμα.” Κωστής Παλαμας

ACKNOWLEDGEMENTS

First, I would like to thank my parents Stelios and Melani, my sister Natasa and her husband Hercules, whose continuous love and support, encouraged me to remain still and fulfil my ambition to do a PhD. In addition to them, I would like to express and send my maximum gratitude to the one and only Helenita Pallarouditsa mou, who definitely played the significant role and helped me the most to finish my PhD (I wish she becomes the best Healthcare Manager ever). Also, I would like to express my gratitude to my best friend Andreas Andreou (he knows better!).

I would like to express my gratitude to my supervisor Prof. Asterio Gavriilidis for his continuous guidance and support during my PhD. Definitely I became a better chemical engineer and particularly a researcher, under his supervision.

I would like to thank my friends from UCL. Mr Alberto Cantu Perez (Pinche) for all his help and all the good time we had together (gossiping in the lab and office for two years). My gratitude to Dr. Enhong Chao, Dr Louis Lam, my friends from crystallization lab Miguel and Olga, which I was stealing things sometimes (but I was always returning them). Especially, I would like to thank my Biochem friends for their help and friendship; Leo and Homam and especially for the nice football matches we had every Wednesday at Regents Park.

Finally, I would like to thank all the people I might have forgotten but they helped me with the one or the other way, during my stay at UCL. Especially, I would like to thank, the technical staff the two best technicians ever Dr. Simon Barass and Mr Mike Gorecky and the technicians from mechanical workshop John, Martin and Eric. Of course, many thanks for his friendship all these years, to Dr. George Manos (I am going to miss the talks about Arsenal, Aek and Panathinaikos).

TABLE OF CONTENTS

TABLE OF FIGURES

LIST OF TABLES

NOTATION

C = concentration (mol/m^3)

D= diffusion coefficient (m^2/s)

$D_h = 4S/P_w$ (m)

E= Enhancement factor (-)

F = molar flowrate (mol/s)

HTU = height of transfer unit (m)

H= Henry's constant (mol/m^3atm)

k = reaction rate constant (m^3/mols)

K= mass transfer coefficient (m/s)

L_e = entrance length (m)

M_H = Hatta number (-)

M_i= molecular weight (g/mol)

m = physical solubility (-)

Pe = Peclet number (-)

p = pressure (Pa)

P = pressure (Pa)

P_w = microchannel wetted perimeter (m)

$Re= \rho u D_h/\mu$

R = overall reaction rate (mol/m^3s)

r_p= pore radius (m)

Sh= Sherwood number (-)

S = microchannel cross-section (m^2)

T = temperature (K)

u = velocity (m/s)

$\vec{u}$ = fluid velocity vector (m/s)

u_{mean} = mean fluid velocity among all microchannels

u(i) = average fluid velocity in the i-th channel

x = transverse coordinate (m)

X_{CO_2} = CO_2 removal eficiency (%)

Y = volumetric flowrate (m^3/s)

z = axial coordinate (m)

Greek Symbols

δ = thickness (m)

ε = mesh open area (-)

ε_m= membrane porosity

θ = contact angle (^{o})

λ= mean free path (M^2L^2/t^2mol)

μ = viscosity (Pa.s)

ρ= density (Kg/m^3)

τ= residence time (s)

τ_m= tortuosity of pores (-)

Subscripts

A_{mi} = Monoethanolamine, Diethanolamine

A_c = acetone

B,W= breakthrough of the wetting phase

B,NW= breakthrough of the non-wetting phase

b= bulk

CO_2 = carbon dioxide

C,W= wetting phase critical filling pressure

C,NW= non-wetting phase critical filling pressure

DEA = diethanolamine

G = gas phase

gas = carbon dioxide

g=gas phase

i = carbon dioxide, sodium hydroxide

i= interface (see chapter 2)

I= species diffuse (see chapter 2)

L = liquid phase

l=liquid phase

liquid = sodium hydroxide

MEA= monoethanolamine

M = mesh

m= membrane

NaOH = sodium hydroxide

NW= non-wetting phase

W= wetting phase

out = outlet

in = inlet

Superscripts

G = gas phase

L = liquid phase

M = mesh

CHAPTER 1

INTRODUCTION

CO_2 is one of the major greenhouse gases. Capture of CO_2 by various techniques has been a research focus in recent years. Conventional techniques such as column absorption for CO_2 capture are energy-consuming [1] and not easy to operate because of flooding and foaming problems. Hollow fiber membrane contactor (HFMC) is a promising alternative technique under rapid development. In a membrane contactor, the gas stream flows on one side and the absorbent liquid flows on the other side of the membrane without dispersion of one phase in to the other, thus avoiding the problems often encountered in the conventional apparatus such as flooding and foaming. Contact is achieved either with a thin membrane film as a intermediate or by using a microporous membrane. Furthermore, with a membrane, it is possible to create substantially more interfacial area per volume than is common in conventional methods. By using the microporous membrane to separate the two phases an interface is formed in the pores and mass transfer occurs by diffusion across the interface just as in conventional methods. Membrane systems that are designed to form an interface between two components (liquid/liquid, liquid/gas, gas/gas) are commonly referred to as membrane contactors. Microfabricated meshes are the microengineered analogue of membranes. Recent developments in the area of microengineered structures for chemical processing [2] have made it possible to manufacture micromeshes from various materials by techniques such as standard mask lithography or laser interference lithography [3]. Thin meshes with straight pores, micrometer-range pore size, and a regular arrangement can be obtained [4]. Such micromeshes combine the advantages of minimising mass transfer resistance with high porosity and regular patterned pore structured having at the same time good mechanical strength. They can be easily incorporated in the design of microdevices for

processing at microscale [5]. In microengineered systems, mass and heat transfer are intensified. Microreactors can be used for many chemical reaction processes to achieve high yields of production. This is a result of the isothermal conditions which can be achieved in the microchannels and generate greater conversions and selectivities. However, since this approach is at a micro scale, although it has been successfully used for analytical purposes [6], staggering microreactors, a process known as scale-out or numbering-up, can increase the production volume. This capability of staggering many microreactors has attracted many pharmaceutical and chemical production industries [7].

The objective of this work is to study experimentally and theoretically novel multiphase microreactors and characterize them in relation to hydrodynamics and mass transfer, in order to understand and improve their performance. Furthermore, there is no research work on CO_2 absorption using mesh microstructured reactors so far, hence the significance of this work is the use of the advantages of mesh microreactors mentioned before (e.g. enhancement of heat and mass transfer) in order to intensify CO_2 absorption. The performance of membrane microstructured reactors will be compared (chapter 6) with hollow fiber membrane reactors which have been used for CO_2 absorption (see chapter 2). Carbon dioxide capture followed by sequestration, is one of the solutions being explored at international level, to achieve the necessary deep reductions in greenhouse gas emissions. In order to achieve these objectives comprehensive parametric studies were performed in a microstructured metallic mesh reactor, CRL mesh reactor, PTFE single channel membrane reactor and the silicon nitride mesh reactor for CO_2 absorption in aqueous solutions of NAOH and amines.

Chapter 2 summarizes the literature about membrane contactors and micro gas-liquid, liquid-liquid contactors. In addition the current status of the development of CO_2 capture technology is reviewed.

Chapter 3 investigates the fluid flow distribution in the geometry of a single microreactor by varying geometrical parameters such as: width of inlet and outlet flow distribution regions, different shapes of inlet and outlet flow distribution regions, shifting the channels in parallel, effect of the channels, in order to approach a design which allows for flow uniformity over the microplate.

Chapter 4 studies theoretically and experimentally carbon dioxide absorption in sodium hydroxide solution in a metal mesh microreactor. In order to evaluate, understand and

improve its performance parameters such as: gas and liquid flowrates, membranes with different porosities, different gas film thicknesses, type of the flow and gas residence time were investigated.

Chapter 5 describes CO_2 absorption in solutions of monoethanolamine (MEA) and diethanolamine (DEA) in a single channel membrane PTFE microstructured reactor. The use of the PTFE membrane is to overcome the limitation of the extra resistance to the mass transfer in the metallic mesh, since the pores of the metallic mesh are liquid-filled. Further investigation of the PTFE single channel reactor was focused on parameters such as: gas flowrates, membrane contact area between the gas and the liquid, different amine solutions, and liquid concentrations.

Chapter 6 studies theoretically and experimentally CO_2 absorption in sodium hydroxide solution in a single channel membrane PTFE microstructured reactor. In the case of chemical absorption, a higher CO_2 flux is achieved using aqueous NaOH solution than aqueous amine solutions. Higher CO_2 removal efficiency was observed when PTFE membrane in the 8 channel reactor (contact area between gas and liquid is approximately 11.3 times larger than the contact area of the single channel PTFE membrane reactor) was used compared to the metallic mesh reactor due to less restriction in mass transfer in the membrane. The effect of partial wetting and the influence of the distances between pore to pore is studied theoretically. Further investigations were focused on parameters such as: gas flowrates, membrane contact area between the gas and the liquid, liquid concentrations and different liquid absorbents.

Chapter 7 studies the effect of staggered herringbones (grooves engraved on the floor of the liquid channel in order to enhance mass transfer) on CO_2 absorption when the PTFE single channel reactor was used, and NaOH was used as an absorbent liquid. For this reason two different structures of staggered herringbones (AB and ABCD) were used. In one case the staggered herringbones were engraved in the acrylic plate and in the other the staggered herringbones were engraved in silicon inserts which they were placed in the liquid side of the reactor. Furthermore, three dimensional simulations were executed with and without the staggered herringbones in order to examine the effect of staggered herringbones on CO_2 absorption. In addition, analytical model which describes acetone mass transfer from water solution to the nitrogen stream flowing co-currently was formulated in order to examine the effect of staggered herringbones on stripping of acetone from water.

Chapter 8 investigates experimentally the effect of ultrasound on carbon dioxide absorption in sodium hydroxide when the PTFE membrane microstructured reactor was used. Different orientations of the reactor were examined as well in the ultrasound bath in order to achieve streaming in the liquid side of the membrane reactor.

Chapter 9 studies carbon dioxide absorption in sodium hydroxide solution when the metallic mesh scale-out reactor (with 4 meshes) was used, in order to compare its performance with the metallic mesh reactor (1-mesh). In order to ensure equal flow distribution in each plate of the scale out reactor, CFD simulations were carried out. In addition, to improve the performance of the 'scale-out' reactor, experiments were performed when inserts with different channels width (0.2, 0.5, 0.75, 1 mm) were installed in every inlet of the scale out reactor.

Chapter 10 describes experimentally and theoretically CO_2 absorption in sodium hydroxide and amine solutions when a silicon nitride mesh reactor developed by Fluxxion (Netherlands) and Bayer technology services was used. Various conditions such as gas and liquid flowrates, different types of solutions (NaOH, amines), type of the flow, liquid film thicknesses were investigated. The silicon nitride mesh reactor was found to have the best performance on CO_2 removal efficiency compared to the single PTFE membrane reactor, the metallic mesh rector and the CRL mesh reactor due to the very thin membrane of 1μm thicknes.

Chapter 11 summarizes the results from the different reactors studied in this thesis along with the major contributions of this work and future areas of research.

CHAPTER 2

LITERATURE SURVEY

2.1 Introduction

Multiphase liquid-liquid or gas-liquid systems, either catalytic or non-catalytic, account for a large number of unit operations in chemical processes. Multiple mass transfer operations (distillation, extraction, absorption, etc.), heat transfer operations (condensation, evaporation, heating, etc.) and reaction processes often use multiphase systems. One of the problems related to conventional methods is the interaction between the two phases such that problems occur due to foaming, formation of emulsions and so forth due to the interdependence of the two phases. Membrane technology offers an alternative method where a non-dispersive interface is created between the two phases. In order to separate the two phases (gas/liquid) a microporous membrane is used and an interface is formed in the pores and mass transfer occurs by diffusion across the interface. Systems that are designed to form an interface between two components (liquid/liquid, gas/liquid, gas/gas) are commonly refered as membrane contactors. Membrane contactors can be used for several applications such as gas absorption, stripping, distillation, pervaporation and extraction. Various topics relevant to membrane contactors such as continuous phase systems, phase separation in microchannels, membrane gas/liquid contactors are reviewed in this chapter.

2.2 Continuous Phase Microsystems

In continuous – phase microcontactors the gas and the liquid phases form two streams which are fed separately in the liquid and gas chamber of the contactor and are also taken away separately at the outlet of the contactor without dispersing the one phase into the other [8]. The advantages of such contactors are that the phases are not intermixed, and the gas/liquid interfaces are well-defined. The breakthrough of one phase into the other phase may cause unwanted froth, foam or emulsion and makes difficult the separation of the two phases. The critical issue in operating the microcontactors is the maintenance of the gas/liquid interface.

In the falling film microreactor [9] see Figure 2.1 (developed by Institute fur Mikrotechnik Mainz (IMM)), the main characteristic is that it generates a thin falling film of several 10 μm thickness flowing by the means of gravity forces.

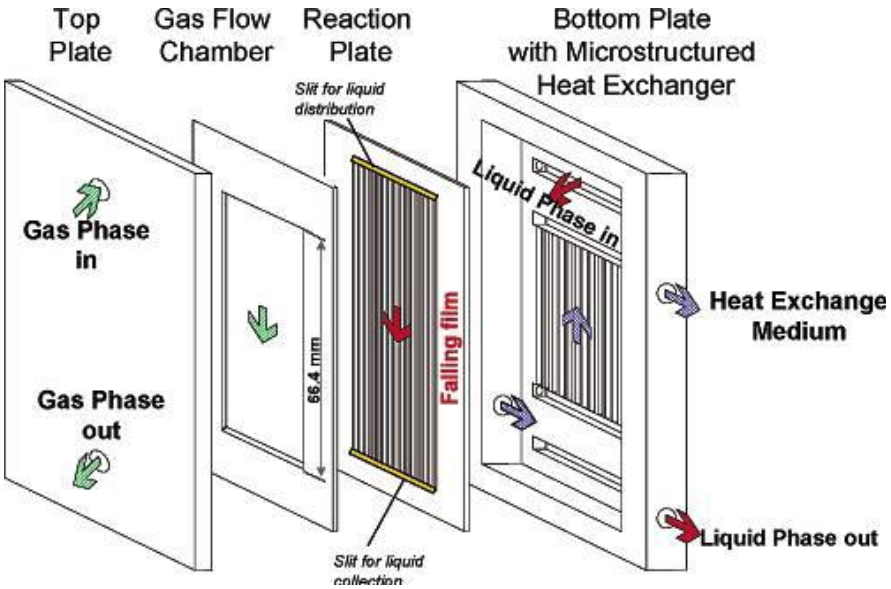

Figure 2. 1 Construction of the falling film microreactor (source: IMM, Mainz).

Another important characteristic of this reactor is that it has high capability for heat removal and minimization of mass transfer resistance in the liquid phase [10]. For conventional units, achievable interfacial area is between 300 and 600 m^2/m^3 [11]. However, recent developments in microtechnology [11] showed that the manufacture of such reactors with interfacial area higher than 10000 m^2/m^3 [11, 12] is possible. Zanfir and Gavriilidis [10] studied carbon dioxide absorbtion in this type of reactor.

An alternative continuous-phase microsystem is the mesh microreactor manufactured by CRL (Central Research Laboratories). The structure of the mesh allows immiscible fluid phases (liquid-liquid or gas-liquid) to come into contact enabling mass transfer and reaction between and within the phases. The two phases are not mixed and are taken away separately at the outlet of the contactor without dispersing the one phase into the other [4]. This reactor was designed for kinetic studies for 2-phase reactions with the ability to handle sequential samples without excessive sample dispersion [4]. Figure 2.2 (a) shows a diagrammatic cross-section of the mesh detailing the reaction chamber regions. Figure 2.2 (b) shows a photograph with the assembled device. The microcontactor has two cavities of a depth of 100 μm each with reaction chamber volume of 100 μl for each phase [4].

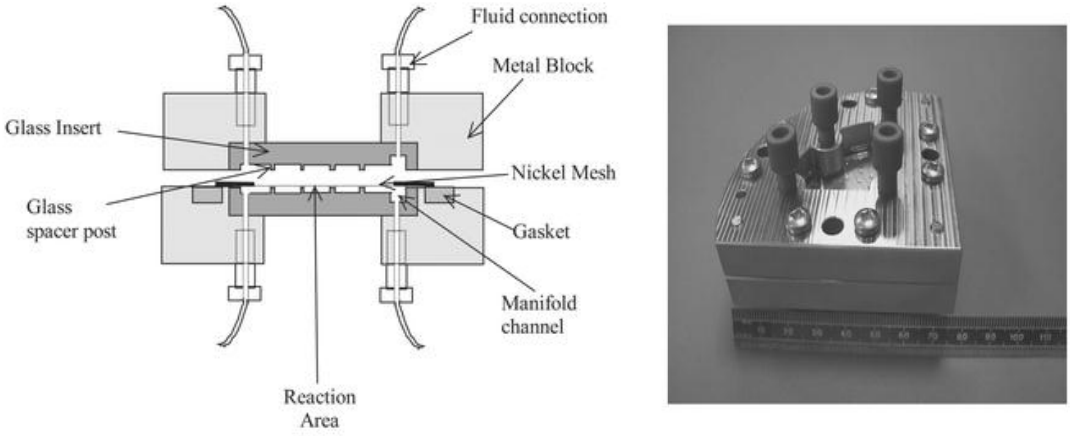

Figure 2. 2 Mesh reactor: (a) diagrammatic cross-section, partially exploded view, (b) assembled device.

Figure 2.3 (a) shows a photograph of a nickel mesh utilized in the mesh microreactor. Micromeshes with pore diameter, depth, and spacing each of approximately 5 μm with open area up to 40% is shown in Figure 2.3.

(a) (b)

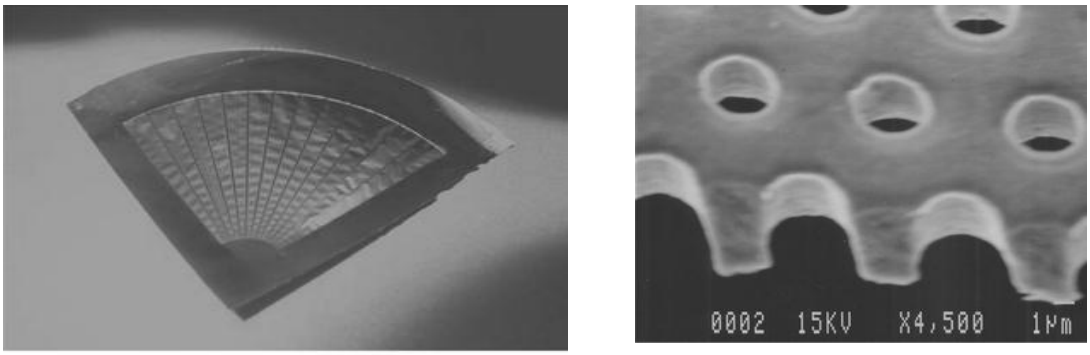

Figure 2. 3 Nickel mesh: (a) Photograph of complete mesh showing frame and struts, (b) scanning electron micrograph of mesh pores.

Furthermore another good example for continuous-phase microsystem is the mesh reactor (see figure 2.4) used by Sun [13]. Acetone stripping and asymmetric transfer hydrogenation was performed in this mesh reactor. A mesh provides an interface for the gas and liquid to be contacted. The reactor measures 3x8 cm in size. The gaskets utilized to define the gas and liquid flow channels are made from brass. The mesh is placed between two gaskets and contains the gas liquid interface. Mesh was made out of stainless (see figure 2.5) by a chemical etching method with average pore size of 76 μm and an open area of 23%.

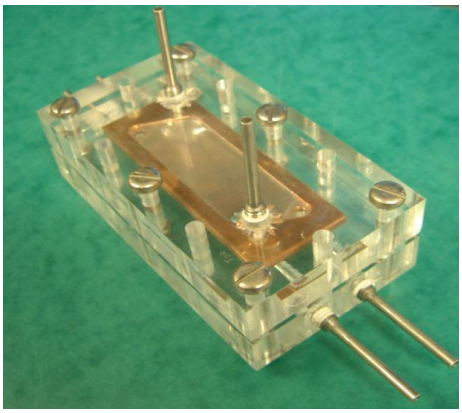

Figure 2. 4 Picture of assembled reactor with Perspex cover plates [13].

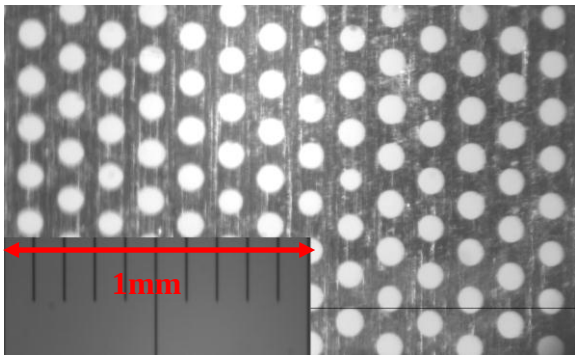

Figure 2. 5 Microscope image of stainless mesh [13].

In addition Brans *et al.* [14] used different microsieve mesh designs in order to investigate the application of yeast-cell filtration. In these microsieve meshes high fluxes are achieved, due to their extremely low flow resistance. The microseive (see figure 2.6) is made with silicon micromachining technology. This microsieve is coated with silicon nitride layer, which after it was etched through with KOH solution forms the mesh of 1 μm thicknes. Two different microsieve meshes were used, one with pores diameter of 1.2μm and porosity of 49% and one with slit shape pores of 0.8μm x 2.5 μm and porosity of 40%. Such a microsieve mesh designs can be used as continuous-phase microsystems for liquid-liquid and gas-liquid separations.

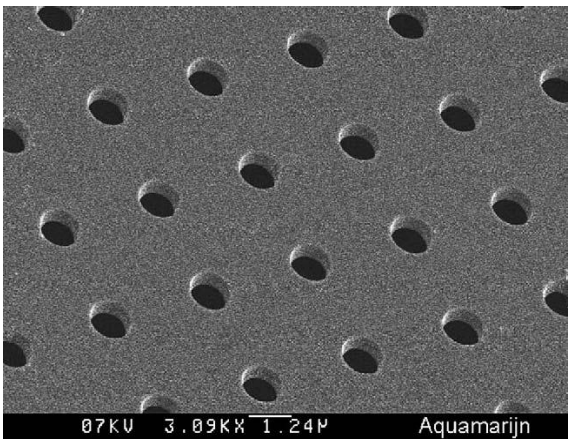

Figure 2. 6 SEM picture of a microsieve mesh [14].

2.3 Phase separation of gas-liquid and liquid-liquid microflows in microchannels

Separations play a significant role in many chemical and biochemical processes at all scales. Future separation needs are primarily related to the pharmaceutical, microelectronics, water, energy (e.g. hydrogen) and life sciences industries [8]. Microprocess engineering is well placed to serve many of these needs, due to the small production scale and unique advantages offered by point of use and intensified operation.

Kralj *et al.* [15] described continuous flow liquid-liquid phase separation in microfluidic devices based on capillary forces and selective wetting surfaces. They achieved liquid-liquid phase separation by using a thin porous fluoropolymer membrane (between microchannels) that selectively wetted non-aqueous solvents, had average pore sizes 0.1-1 μm range, and had a high pore density for high separation throughput. The aqueous phase, which does not wet the PTFE membrane, passes across the membrane surface to outlet 1 while the organic/fluorous phase wets and flows through the pores of the membrane to outlet 2 (see figure 2.7).

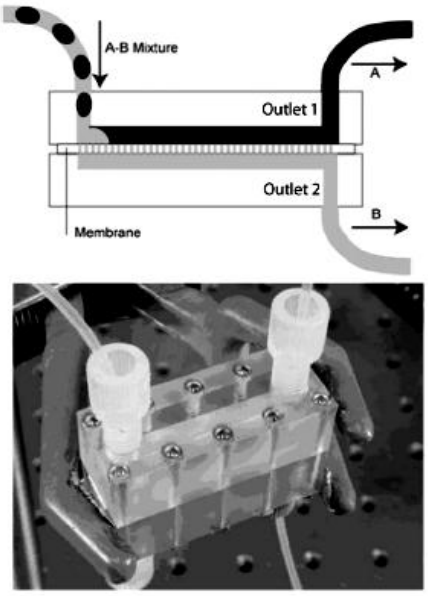

Figure 2. 7 Schematic (top) and photograph (bottom) of the microfluidic device used for the liquid-liquid separation. The device dimensions are 10 mm width, 50 mm length and 20 mm height. Channels dimensions 0.5x0.5x20 mm [15].

Hartman *et al.* [16] performed distillation in microchemical systems using capillary forces and segmented flow. In their system, vapor-liquid equilibrium was achieved using segmented flow (see figure 2.8). A gas-liquid membrane separator was then used to separate vapor from liquid, and thus realized distillation. The membrane separator consisted of a channel (2x2x40 mm) machined into each of two pieces of stainless steel, and a PTFE membrane (0.5 μm pore size) was compressed between both pieces of metal (figure 2.8) using 10 1/6'' cap screws.

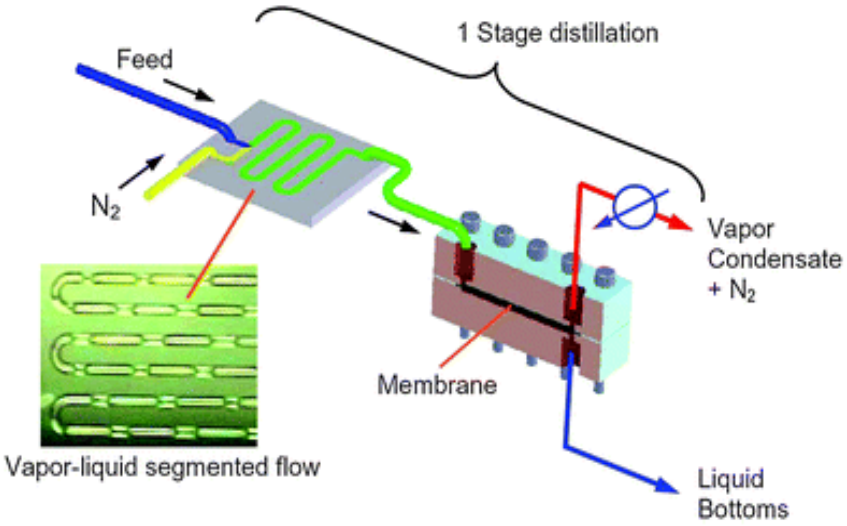

Figure 2. 8 System used to achieve single stage distillation [16].

Membrane distillation in microscale with the aid of sweeping gas for a separation of a mixture of methanol and water was described by Adiche and Sundmacher [17]. The novel micro-separator consists of two horizontal polycarbonate plates (length: 60 mm, width: 30 mm, thickness: 1 mm) which are joined together holding a flat micro-porous polymeric membrane (active area: 17 $1mm^2$) in between (figure 2.9). Polymeric membranes with a range of pore size from 0.22 μm to 0.45 μm were used to establish a stable liquid-vapour contact throughout the micro-channels.

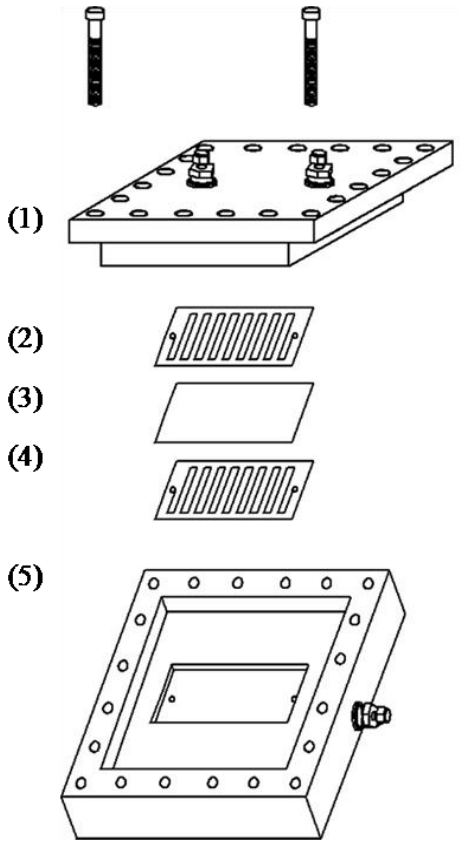

Figure 2. 9 Exploded schematic view of the micro-separator, (1) cover plate for the permeate channel, (2) permeate channel, (3) membrane contactor, (4) feed channel, (5) cover plate for the feed channel [17].

Aota *et al.* [18] examined phase separation of liquid-liquid and gas-liquid microflows in microchannels and characterized by interfacial pressure balance. The phase separation required a single phase flow in each output of the microchannel. They considered as the interfacial pressure the pressure difference between the two phases and the Laplace pressure due to interfacial tension at the interface between the separated phases. When the pressure difference between the two phases was balanced by the Laplace pressure, the contact line between the two phases was static, but when the pressure difference between the phases exceeded the limiting Laplace pressure, one phase dispersed into the output channel of the other phase, and the separation failed Figure 2.10c.

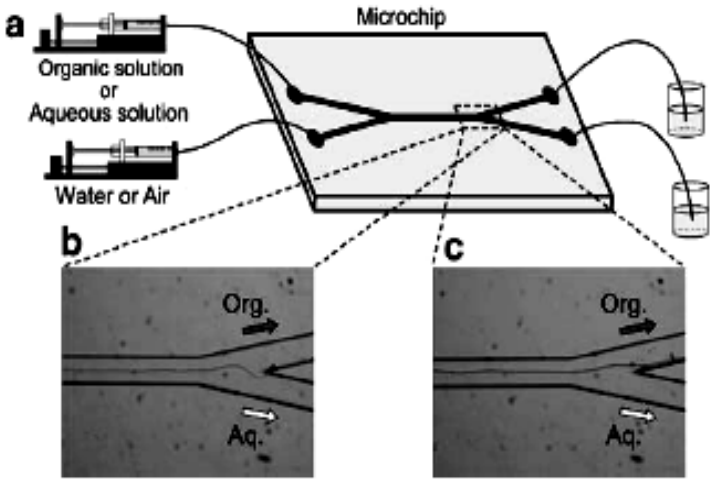

Figure 2. 10 a) Illustration of phase separation (gas-liquid and liquid-liquid) in microchannels whose width, depth and contact length were 215 μm, 34 μm and 20 μm for the liquid-liquid microflows, and 100 μm, 45 μm and 20 μm for the gas-liquid microflows, b) Optical microscope image of the water-ethyl acetate microflow when the phase separation was achieved, c) Image when the phase separation failed [18].

Timmer *et al*. [19] demonstrated an electrolyte concentrator for increasing analyte concentrations in order to improve the detection limit of analytical systems. The concentrator is of the membrane evaporator type (see figure 2.11). The analyte is fed through a channel covered with a hydrophobic (PTFE) membrane of 0.2 μm holes, in order to be permeable for water vapor, but it should be water repellent in order not to let the feed solution through. The concentration effect is enhanced by applying forced convection using dried nitrogen flow over the membrane.

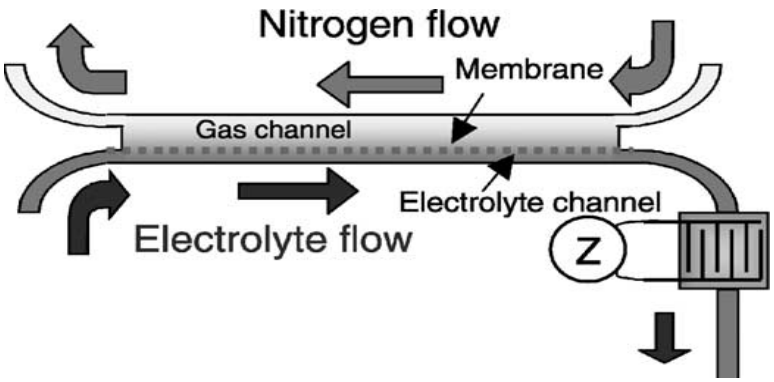

Figure 2. 11 Schematic diagram of the evaporation concentrator, comprising a gas channel, an electrolyte channel and an electrolyte conductivity (EC) sensor [19].

Castell *et al.* [20] exploited the capillary forces on the microscale to continuous flow liquid-liquid phase separator. Segmented flow regimes of immiscible fluids were generated and subsequently separated into their component phases through an array of high aspect ratio, laser machined, separation ducts (36 μm wide, 130 μm deep) in a planar, integrated, polytetrafluoroethylene (PTFE) microdevice (figure 2.12). A controlled pressure differential across the phase separator architecture facilitates the selective passage of the wetting, organic, phase through the separator ducts, enabling separation of microfluidic multiphase flows streams. The reported device is demonstrated to separate water and chloroform segmented flow regimes.

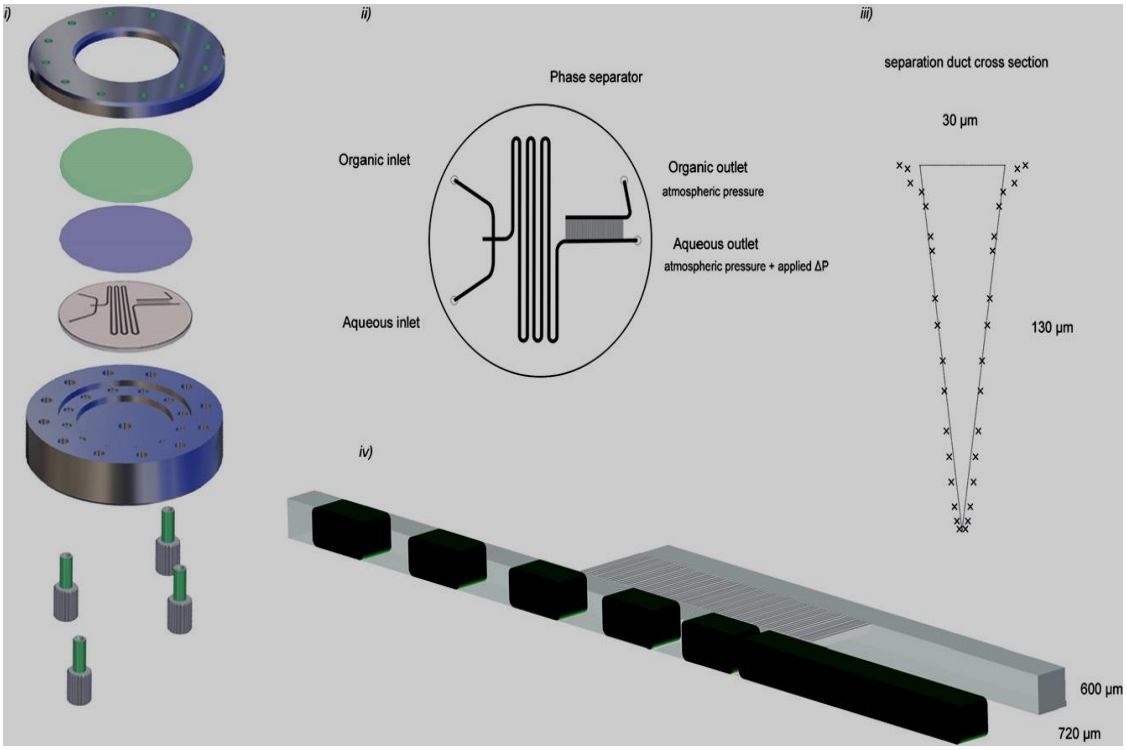

Figure 2. 12 Series of schematic diagrams illustrating (i) device construction (ii) microfluidic channel layout (iii) Cross- sectional Gaussian profile of a single laser machined separation duct as measured by serial z-axis optical microscopy and the approximated triangular geometry (iv) Cartoon illustration of the separator in operation [20].

TeGrotenhuis and Stenkamp [21] used a single channel phase separator device in order to separate liquid from gas. The fundamental approach for their microchannel phase separator is to utilize capillary, surface, and hydrodynamic forces to collect one of the phases into specific flow regions while excluding the other. In this kind of separators, separation is accomplished using combinations of capture, wicking, and pore throat structures within the microchannels

as it can be seen from Figure 2.13. The pore throat/wick structure provides a path for the liquid only to flow to a liquid outlet, while the gas exits from a separate outlet.

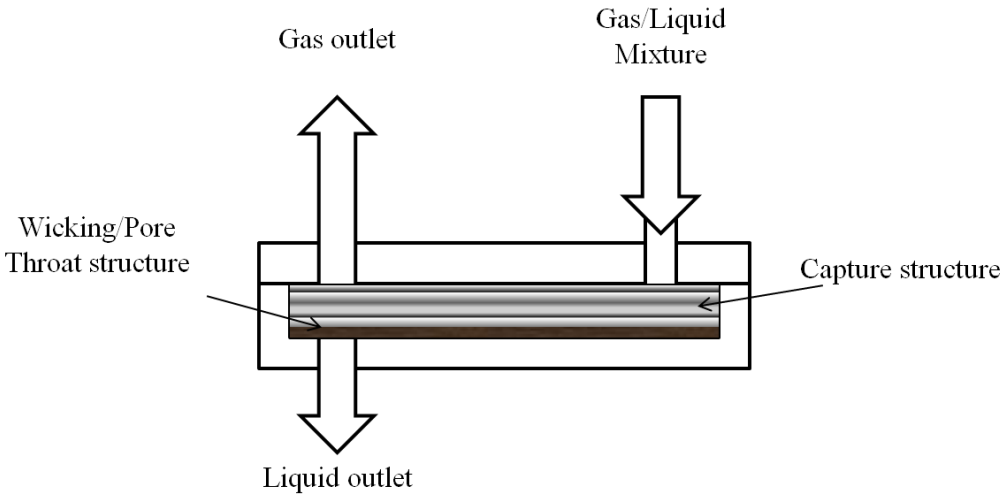

Figure 2. 13 Schematic of the single channel separator [21].

TeGrotenhuis *et al.* [22] used microchannel devices for efficient contacting of liquids in solvent extraction. The micromashined channels are separated by a contactor plate as shown in Figure 2.14. Solvent extraction requires intimate contact of two immiscible liquids to facilitate mass transfer of one or more solutes from one fluid to another. Two micromachined contactor plates of 25 μm and 50 μm thick were used in the micro mesh contactor. The holes were conical and made by laser drilling, averaging 25 μm in diameter on one side and 35 μm in diameter on the other side of the plate. Porosity was estimated at 26%. The micromachined contactors were coated with Teflon to make them more non-wetting to water.

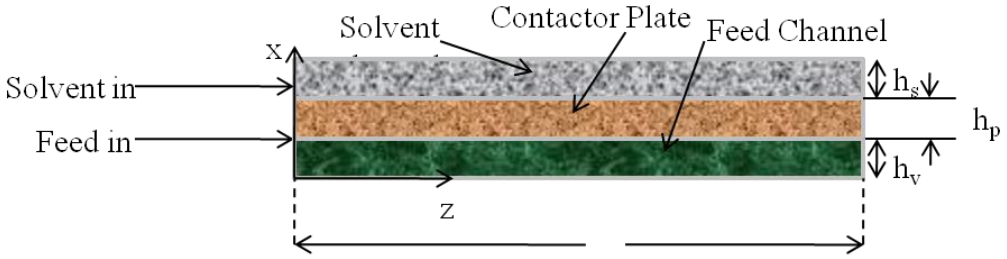

Figure 2. 14 Microchannel contactor device [23].

Chan *et al.* [23] developed a micro-channel contactor-separator for immiscible liquids. The microchannel was made in glass using a photo-chemical etching process, including etching across a gap to produce sections of shallow channel. The device (see figure 2.15) used a

simple T-junction to produce slugs of typically the oil phase in the water phase. The slugs flowed along a straight channel toward a separation section. The separator consisted of small side channels running perpendicular from the main through channel, which carried the water to the water outlet, whilst the oil flowed out along the main channel. The oil phase prevented from entering the side channels by the extra interfacial force associated with the small opening dimension at the junction.

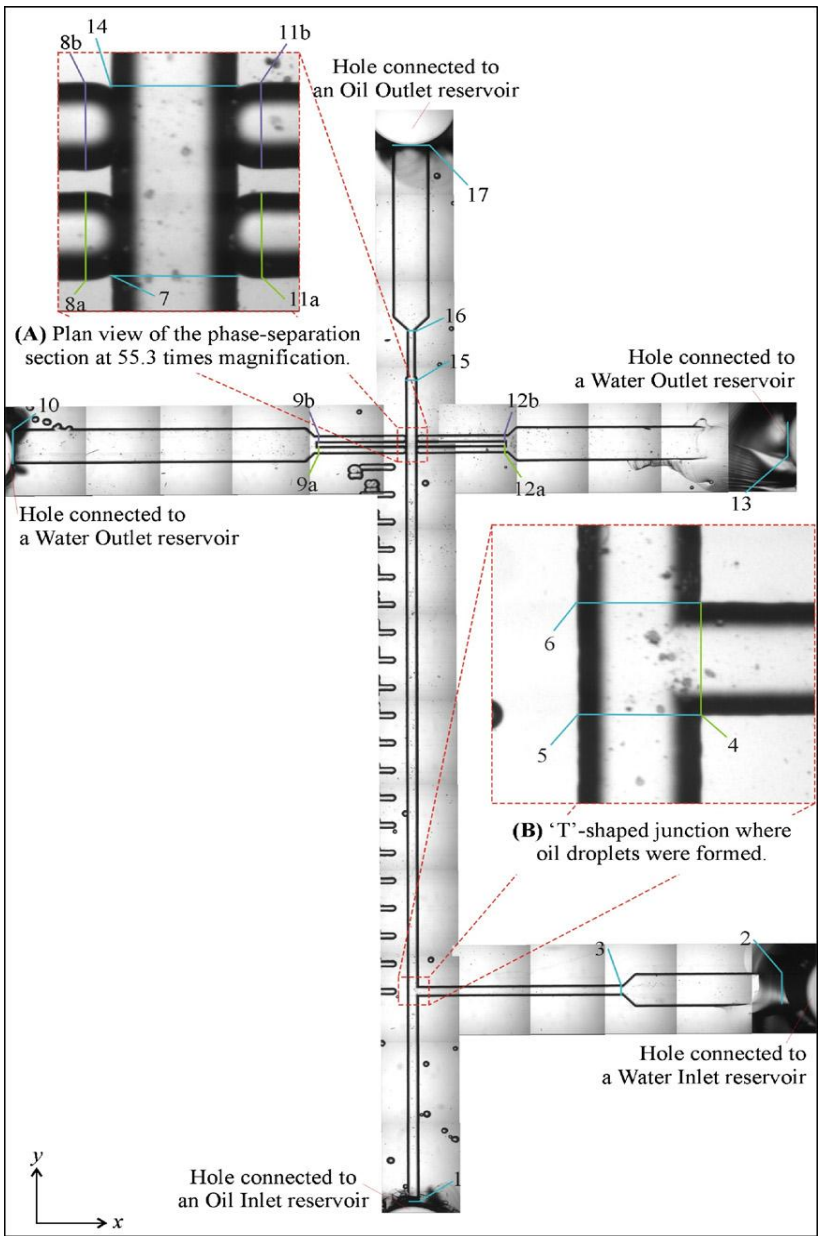

Figure 2. 15 Plan-view of micro-channel network design [23].

2.4 Membrane gas-liquid contactors

Membrane technology is a rapidly emerging field and has since the 1980's been applied in numbers of fields for large scale gas purification. Reliable and selective polymer membranes have been developed for a number of applications such as: absorption, stripping, distillation, pervaporation and extraction. The membrane acts as an interface and keeps the gas/liquid phase separated while the transport of organics can take place through the membrane.

Advantages of membrane contactors compared to the conventional devices including packed tower, venturi scrubber and bubble column are [24]:

- The gas stream flows on one side and the absorbent liquid flows on the other side of the membrane without phase dispersion, thus avoiding problems such as flooding, foaming and emulsion formation which are often encountered in packed/tray columns.

- Interfacial area is known and constant. As a result, it is easier to predict the performance of a membrane contactor [24].

- The compact modular structure of membrane contactors provides much larger gas-liquid interfaces and the flexibility to scale-up or down [24].

- It was reported that hollow fiber contactors are 30 times more efficient for gas absorption than conventional equipment [25].

- More economic. Due to the compact nature of the membrane device, it is less energy-consuming, less voluminous, and hence, more economic. Feron and Jansen [26] found that the membrane contactor could lead to a 10-fold reduction in absorber size compared with packed columns.

- Solvent hold-up is low, which is attractive feature when using expensive solvents [24].

- Modular design of membrane contactor allows flexibility in plant operation and modification. Small and large capacity can be obtained by altering the number of modules [24].

On the other hand membrane contactors have several disadvantages compared to conventional devices [24]:

- The membrane introduces an additional resistance to mass transfer that is not found in conventional methods. This resistance in many cases is not important and there are ways to minimize it.

- Membranes pores may become wetted. In this case, the mass transfer will be reduced because of a liquid stagnant film in the membranes pores.

- Membranes have finite life and generally represent a high investment cost for the replacement of membrane modules.

- The membrane itself is prone to fouling which reduces the mass transfer efficiency. Although it is more critical in pressure-driven processes than concentration-driven process, the problem of membrane fouling needs to be addressed to maintain system performance.

Despite the fact there are a number of disadvantages related to membrane contactors their advantages make them attractive compared to conventional methods often overcome these. Since the introduction of membrane contactors, several studies have been conducted to understand and improve the performance of the process and develop efficient module designs. Membrane contactors have been used in a wide range of applications from medical/pharmaceutical to industrial and environmental engineering processes [27].

As it was mentioned in chapter 1 microfabricated meshes are the microengineered analogue of membranes with various advantages (e.g. heat and mass transfer are intensified). CO_2 absorption in aqueous solutions of NAOH and amines was performed in a microstructured metallic mesh reactor, CRL mesh reactor, PTFE single channel membrane reactor and the silicon nitride mesh reactor in order to understand, evaluate and improve their performance. In the rest of the chapter follows literature review on the hollow fiber membrane reactors which are the only existing membrane reactors which have been used for CO_2 absorption.

2.4.1 Membrane materials and contactor modules

Membranes can be considered as a permselective barrier or interface between two phases and at the heart of every membrane process. Membranes can be thick or thin and their structure can be homogeneous or heterogeneous. Synthetic membranes are generally classified by two groups; 1) organic or polymeric membranes, and 2) inorganic membranes [28], also referred to as ceramic or mineral membranes. The larger group of membranes is by far the polymeric membranes and a wide variety of polymers are used such as; polyvinylidenefluoride (PVDF), polytetrafluoroethylene (PTFE), polypropylene (PP), polyamide, cellulose-esters, polysulfone (PSF), poly (ether-imide), polyetheretherketone (PEEK).

PTFE is highly crystalline and exhibits excellent thermal stability. It is not soluble in any common solvent and hence also shows high chemical resistance. PVDF shows good thermal and chemical resistance however not quite as good as PTFE. PVDF is soluble in aprotic solvents such us dimethylformamide (DMF), dimethylacatamide (DAMC) and in triethylphosphate (TEP). PP is an excellent solvent resistance polymer when it is in the isotactic configuration. The three polymers PTFE, PVDF and PP have some properties which are similar and they all exhibit good to excellent chemical and thermal stability. Because of their hydrophobic nature water cannot wet these membranes spontaneously [13].

Another class of membrane polymers are the polyamides which have outstanding mechanical, thermal, chemical and hydrolytic stability. PSF possess very good chemical and thermal stability and is widely used as basic materials for ultrafiltration membranes and as support materials for composite membranes. Polyetherketones is a new group of chemically and thermally resistant polymers. PEEK is only soluble at room temperature in concentrated inorganic acids such as sulphuric acid or chlorosulfonic acid [13].

Inorganic materials generally possess superior chemical and thermal stability relative to polymeric materials. Four different types of classes, ceramic membranes, glass membranes, metallic membranes and zeolitic membranes are generally used to distinguish inorganic membranes. Polymers are not thermally stable membranes, while the melting point of inorganic membranes is very high and for certain types can have values above 4000^{o}C [13]. This property makes inorganic membranes very interesting and suitable for processes that require high temperature (i.e. gas separation) and also opens for the possibility of cleaning

and sterilization in for example medical/pharmaceutical industrial applications. The chemical stability of inorganic materials is superior and they can generally be applied at any pH and in any organic solvent. All kinds of cleaning agents can be used and at various temperatures which is an important issue from an operation and maintenance perspective for the control of fouling.

All membrane modules are generally based on the two membrane configurations that are available, flat sheets or tubular membranes (figure 2.16). Plate-and-frame and spiral-wound modules involve flat membranes whereas tubular, capillary and hollow fiber modules are based on tubular membrane configurations. The basic principle governing a module design is the objective of achieving the greatest membrane surface area possible per volume.

When choosing a certain membrane module design different criteria are necessary to consider. An economic evaluation is of course required combined with engineering factors such us type of separation problem, ease of operation, maintenance and cleaning requirements, number and size of units and so forth. The characteristics of all modules can be compared qualitatively in Table 2.1 [28].

The costs of the various modules can vary appreciably; each of them has its field applications. Despite being the most expensive configuration, the tubular module is well suited for application with high fouling tendency because of its good process control and ease of membrane cleaning. On the other hand, hollow fiber modules are very susceptible to fouling and are difficult to clean. Pretreatment of the feed stream is most important in hollow fiber systems. Many module concepts for hollow fiber membranes have been developed to reduce the fouling potential and to increase fluxes.

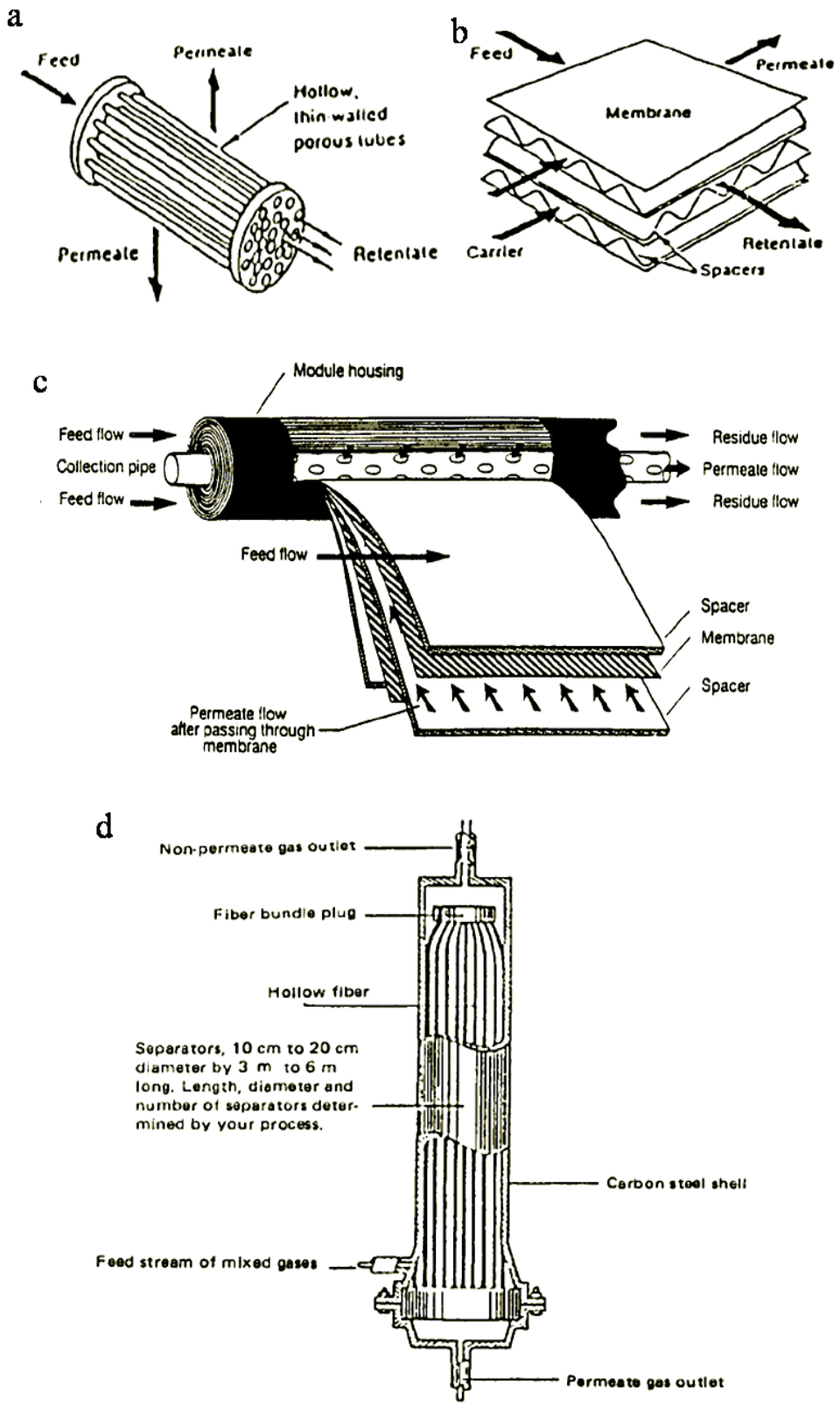

Figure 2. 16 Membrane Modules (a) Plate-and-frame, (b) Tubular, (c) Spiral-wood, (d) Hollow fiber [28].

Table 2. 1 Qualitatively comparison of various membrane configurations [28].

	Tubular	Plate-and-frame	Spiral-wound	Capillary	Hollow fiber
Packing density	Low	⟶			Very high
Investment	High	⟶			Low
Fouling tendency	Low	⟶			Very high
Cleaning	Good	⟶			Poor
Membrane replacement	Yes/no	Yes	No	No	No

2.4.2 Flow patterns in membrane modules

The membrane is a critical component of any membrane separation process. Important design features of a module include the regularity of fibers (polydispersity and spatial arrangements of fibers), packing density and the relative flow directions suchas parallel, i.e., concurrently and countercurrently, and cross flows of the two phases. Membrane modules can be categorised into two groups depending on the relative flow directions of the two phases, the longitudinal-flow module and the cross-flow module [1].

In the longitudinal flow module, the gas and the liquid phases flow in parallel (either concurrently or countercurrently) to each other on the opposite sides of the fibers. Figure 2.17 shows a schematic description of this type of module. The simplicity in manufacturing is the advantage of this module. In contrast, its disadvantage is mainly seen in is mediocre efficiency in mass transfer compared with the cross-flow module.

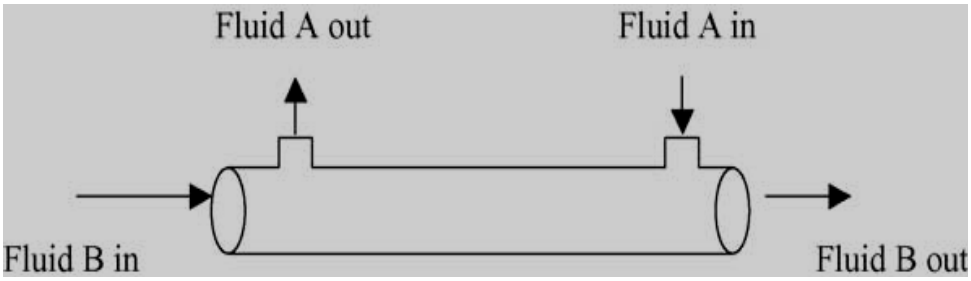

Figure 2. 17 A schematic diagram of a parallel-flow hollow fiber membrane contactor [1].

The characteristic of cross flow module is to integrate some baffles in the module design compared to the longitudinal flow module as it is shown in Fig 2.18. Mass transfer efficiency can be improved with the use of baffles by minimizing shell-side bypass and providing a velocity component normal to the membrane surface. Therefore, the cross flow module can maintain higher mass transfer coefficients; TNO of the Netherlands patented a cross flow membrane module design, which offers good mass transfer characteristic and scale-up potential [26]. In this specific module, CO_2 flows in the shell-side perpendicular to the fiber, but overall, the two phases flow countercurrently through the module. The schematic drawing of the TNO cross –flow module is shown in Fig 2.19.

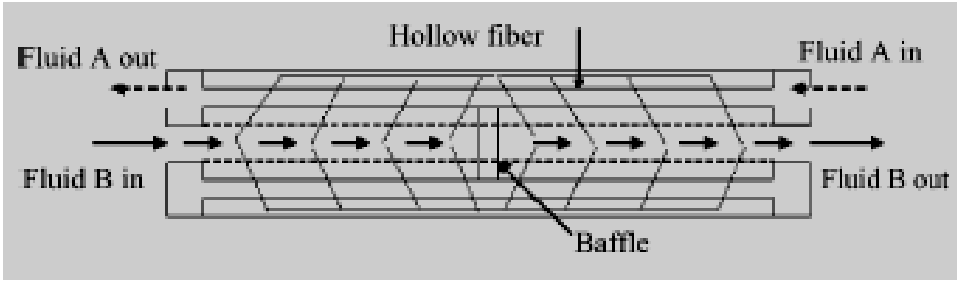

Figure 2. 18 A schematic diagram of a cross-flow hollow fiber membrane contactor [1].

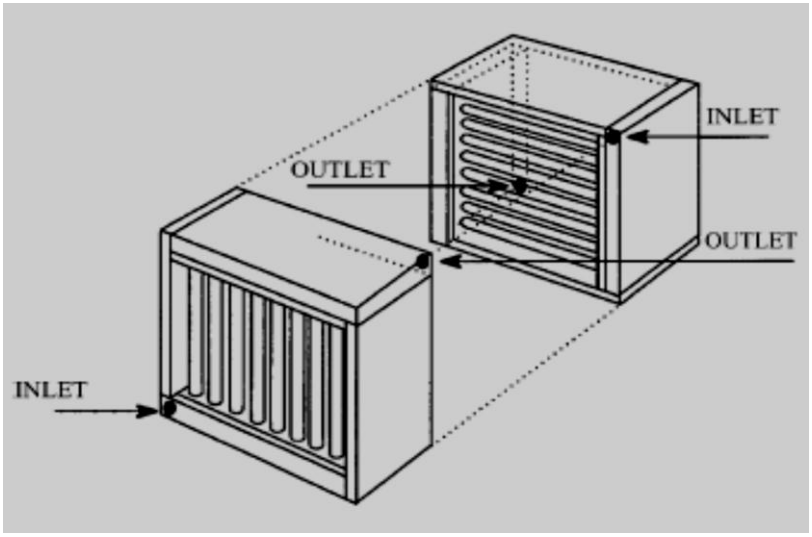

Figure 2. 19 TNO cross-flow membrane module [26].

2.4.3 Applications of membrane contactors

2.4.3.1 Membrane gas absorption and stripping

Membrane gas absorption process is a good alternative to conventional techniques such as column absorption. Various investigators have studied CO_2 absorption in membrane contactors. A membrane contactor acts as a gas absorber, with the gas flowing on one side and the absorbent liquid flowing on the other side of the membrane without either phase being dispersed in the other. Current gas stripping processes operate in an identical manner as the devices used for gas absorption except that species are transferred from the liquid to the gas side. The membranes can be hydrophobic or hydrophilic, and the pores can be either gas filled or absorbent filled. The presence of a membrane adds an additional resistance to the overall mass transfer process. In the ideal case, when the pores are gas filled (non-wetted mode) the mass transfer resistance is negligible. On the other hand, when the pores are liquid filled (wetted mode), the mass transfer resistance is significant. This is due to the fact that the diffusion coefficient of the gas is 3-4 orders of magnitude larger than the diffusion coefficient of liquid. The gas-liquid interface is immobilized at the pore mouth. Through such an interface, one or more gas species may be absorbed into the aqueous solution or one or more gas species may be stripped from the aqueous solution. This mode of nondispersive gas absorption or stripping was first introduced in blood oxygenation. Blood flowed on one side

of a microporous hydrophobic membrane of Teflon [29] or hollow- fiber membranes of polypropylene [30]. On the other side of the membrane, oxygen flowed either as pure oxygen or as air at a pressure slightly lower than the blood pressure. Oxygen was absorbed into the blood, as CO_2 from the blood was stripped out to the O_2-containing gas stream.

Membrane technology is being increasingly investigated for possible application in larger scale gas absorption [31] and gas stripping [32]. Qi and Cussler were the first to use microporous polypropylene membranes for H_2S, SO_2 and CO_2 absorption in a NaOH solution, and NH_3 absorption in water [31, 33]. In the cases of H_2S, SO_2 and NH_3 they found that the absorption is mainly controlled by diffusion across the membrane. However, their results on CO_2 absorption in aqueous NaOH and amine solutions showed that the main resistance to mass transfer existed in the liquid phase, with membrane resistance being very small. They also showed that, for cases where membrane resistance is relatively small, hollow fiber membrane modules have a distinct advantage over the conventional packed columns, due to lower HTUs (Height of Tower Transfer Unit) and independence of gas and liquid flows. Cypes and Engstrom [34] in their analysis of toluene stripping process, they observed that the microfabricated stripping column possesses a higher volumetric efficiency as compared to a conventional packed column. This was attributed to the fact that the obtainable values for the overall mass transfer coefficient were higher for the microfabricated stripping column. In addition they showed that the height of transfer unit is substantially greater in the packed tower than the microfabricated stripping column.

Karoor and Sirkar [35] conducted comprehensive studies on the gas absorption of CO_2, SO_2, CO_2-N_2 and SO_2-air mixtures using distilled water in microporous hydrophobic hollow fiber devices. For CO_2 absorption in water, the wetted mode of operation increased the mass transfer resistance when compared with the non-wetted mode of operation. The experimentally obtained K_La values for the membrane contactors were considerably larger than those for packed columns. In addition they showed that increasing the contact area in a given module for a given fiber size increases the CO_2 removal capacity. Kreulen *et al.* [36, 37] investigated the effects of various factors such as porosity, hollow fiber dimension, liquid viscosity, chemical reaction on the mass transfer in the hollow fiber contactor using the gas-liquid systems of CO_2-water/glycerol and CO_2 (N_2O, H_2S)-NAOH aqueous solutions. Also they developed the modelling of the gas absorption with and without chemical reaction to simulate the mass transfer occurring in the contactor. Rangwala [38] has noted that the overall

mass transfer rates in a hollow fiber membrane contactor can be up to 9 times higher than those found in the conventional packed columns. In their work the membrane transfer coefficient for all the aqueous solutions studied (NaOH 2M, DEA 0.5M), were much lower than those theoretically calculated for a completely non-wetted pore indicating that the pores were partially wetted. In addition to that they showed that even marginal (<2%) wetting of the pores can result in a membrane resistance that can be as high as 60% of the total mass transfer resistance. Kim and Yang [39] used polytetrafluoroethylene (PTFE) microporous membrane contactors to capture CO_2 from CO_2-N_2 mixture with different aqueous amine solutions including 2-amino-2-methyl-l-propanol (AMP), monoethanolamine (MEA) and methyldiethanolamine (MDEA). They found that as temperature rose, the absorption rate of carbon dioxide increased as well. In addition they showed that among the absorbents they used, AMP exhibited a high absorption capacity and moderate absorption rate without the high energy requirement of MEA. Bhaumik *et al.* [40] conducted an experimental study of CO_2 absorption in a hollow fiber device with gas flowing in the fiber lumen and water flowing in the shell side perpendicular to the gas flow. They illustrated that the increase in water flow rate led to an increase in the amount of CO_2 absorbed, which suggested that mass transfer was controlled by the liquid-side film resistance and the gas-phase resistances (gas-side film and pore resistance) were negligible compared to the liquid resistance.

Wang *et al.* [41] performed a theoretical simulation to study CO_2 capture using three alkanolamine solutions of AMP, DEA and MDEA in a hollow fiber membrane contactor. They showed that AMP and DEA solutions have much higher CO_2 absorption fluxes than MDEA, but they exhibit strong radial concentration gradients inside the fibres. Thus the separation efficiency and the consumption of the absorbent should be taken into consideration simultaneously for absorbent selection. Feron and Jansen [42] used (CORAL) absorbents (mixtures of salts and amino-acids) in conjunction with polypropylene membrane contactors for CO_2 removal. The use of salt solutions has the advantage that the vapour pressure of the active components is zero and the solvent is not lost through evaporation. The novel absorption liquids showed an excellent performance in terms of system stability and mass transfer, when used in combination with commercially available, inexpensive polyolefin membranes. The CORAL liquids also showed higher mass transfer when compared with other membrane gas absorption systems, based on MEA and AMP. Dindore *et al.* [43] studied CO_2 absorption into propylene carbonate using hollow fiber membrane contactors at elevated pressures. This work showed that the decrease in the binary gas phase diffusivity and hence

the membrane mass transfer coefficient due to increase in the gas pressures does not have a significant effect on mass transfer coefficient. Thus the overall mass transfer coefficient is controlled by the liquid film resistance even at elevated pressures. Atchariyawut *et al.* [44] investigated the effect of membrane structure on mass-transfer in the microporous PVDF hollow fiber membrane contactors. In that work PVDF microporous hollow fiber membranes fabricated using three different dope solutions containing N-methyl-2-pyrrolidone (NMP) and different additives. The resultant hollow fibers, were used to make membrane modules, which were then applied as gas-liquid membrane contactors for CO_2 absorption in water. Results showed that the different structures of hollow fibers affect CO_2 absorption when used as contactors. All the membranes were partially wetted by water and based on the additives used in each of the three types of membranes the partial wetting was altered as a result to affect CO_2 absorption.

Paul *et al.* [45] studied theoretically CO_2 absorption by different single and blended alkanolamine solvents using flat sheet membrane contactor. The solvents they considered for their work included aqueous solutions of monoethanolamine (MEA), diethanolamine (DEA), N-methyldiethanolamine (MDEA) and 2-amino-methyl-1-propanol (AMP) as well as aqueous blends MEA or DEA with AMP or MDEA. From the theoretical analysis of the absorption of CO_2 in different alkalolamine solvents they showed that the aqueous solution of MEA has the highest absorption flux for CO_2 among the single amine solutions. Finally they showed that the performance of the flat sheet membrane contactor is better than the hollow fiber membrane contactor if only the absorption flux of CO_2 is the amine is considered. Rongwong *et al.* [46] investigated the CO_2 absorption capability and membrane wetting of various types of amine absorbents. Monoethanolamine (MEA), diethanolamine (DEA), and 2-amino-2-methyl-1-propanol (AMP) and their mixtures were used as absorbent solutions. The membrane used for the experiments was a hollow fiber polyvinylidenefluoride (PVDF) membrane. NaCl (inorganic salt) and SG (organic salt) were employed as additives in the amine solutions. It was found that the absorption performance of single absorbents was in the order of MEA>AMP>DEA. The mixed amine absorbents consisting of MEA provided higher absorption flux and CO_2 flux was in the sequence of MEA/AMP>MEA/DEA>DEA/AMP. The addition of NaCl in to MEA introduced the salting out effect (gas solubility in liquid is decreased with increasing salt concentration) leading to the decrease of CO_2 flux. On the other hand the addition of SG into MEA solution enhanced CO_2 flux due to the chemical reaction of both SG and MEA with CO_2.

Rajabzadeh *et al.* [47] studied CO_2 absorption in membrane contactors using MEA solutions as the absorbent by using seven different in-house made PVDF and a commercial PTFE hollow fiber membrane with different structures at the outer surface membrane. Experiments with liquid flowing through the fibers (case 1 operation) and experiments with liquid flowing through the shell side of the module (case 2 operation) were performed. They found that when the absorbent was flown in tube side (case1), the membrane diameter affected CO_2 absorption flux. However, CO_2 absorption rate per fiber was almost the same for all membranes. This behaviour could be explained by the theory of gas absorption with instantaneous chemical reaction, for instantaneous chemical reaction regime (their case) mass transfer k_L is inversely proportional to the membrane diameter, as a result CO_2 absorption rate per fiber remains the same for all membranes. On the other hand, when the absorbent was flown in shell side, CO_2 absorption flux hardly changed with membrane diameter. For the same absorbent volumetric flow rate, CO_2 flux observed in (case1) was about three times higher than those in (case 2) due to the higher absorbent velocity in tube side and thus, the mass transfer coefficient in (case 1) was larger than in (case 2). Delgado *et al.* [48] studied theoretically the absorption of carbon dioxide into aqueous DEA solution using hollow fiber contactor in order to obtain the effect of several operational variables (liquid velocity, fiber length, lean carbon dioxide loading, and amine solution) on productivity and amine solution to carbon dioxide ratio. They found that productivity increases as liquid velocity was increased (which keeps the DEA concentration high as a result, increasing the driving force for CO_2 removal). Increasing the fiber length has a negative effect on performance because of the increase of module size and the enhancement of the mass transfer resistance in the shell side. In addition they found an optimum value of the lean carbon dioxide loading (total$[CO_2]_{in}$/total[DEA], because increasing this parameter has a positive effect (reduction of the regeneration energy) and a negative effect (reduction of productivity) at the same time. Finally they showed that the performance parameter (α.LCL/β, where α=productivity, LCL=lean carbon dioxide loading, β=amine solution to carbon dioxide ratio) improves when the amine concentration is increased within the range of (total[DEA]=2-5M), mainly due to the reduction of the required amine solution to carbon dioxide ratio.

Khaisri *et al.* [49] investigated carbon dioxide absorption into an aqueous solution of monoethaloamine (MEA) using PTFE membrane contactor. Partial membrane wetting was investigated to determine the effect of membrane mass transfer resistance on the absorption performance and the overall mass transfer coefficient. An increase of the percent wetting

decreased the absorption flux and the overall mass transfer coefficient. In addition to that, they compared their experimental results with the model and they showed that the absorption performance dropped roughly 56%, 72%, 85% and 90% at 10%, 20%, 50% and 100% wetting respectively. Finally they showed that the operation temperature had a significant effect on membrane wetting.

Zhang *et al.* [50] studied CO_2 absorption in polypropylene (PP) and polyvinylidene fluoride (PVDF) membrane modules using water and aqueous DEA solutions as absorbents. The simulation results showed that for the physical absorption of CO_2 in water, the proportion of membrane phase resistance in the overall mass transfer resistance increased from less than 5 to 90% when the operation mode was shifted from the non-wetted to wetted. As for the chemical absorption, analysis on the mass transfer resistance revealed that the ratio of the membrane resistance increased sharply from 10 to 70% when only 10% of membrane length was wetted. Aronu *et al.* [51] investigated amine amino acid salts for carbon dioxide absorption. Experimental results showed that amine amino acid salts have similar CO_2 absorption properties to monoethanolamine (MEA) of the same concentration. In addition amino acid salt from an inorganic base, KOH, showed lower performance in CO_2 absorption than the amine amino acid salt (AAAS) mainly due to lower equilibrium temperature sensitivity. AAAS showed better performance than the MEA of same concentration. Finally AAAS from neutralization of sarcosine with 3-(methyllamino) propylamine (MAPA) showed the best performance and the performance could be further enhanced when promoted with excess MAPA. Boucif *et al.* [52] studied numerically CO_2 absorption in a hollow fiber membrane contactor using typical amine solutions of diethanolamine (DEA), 2-amino-2-methyl-1-propanol (AMP), and diisopropanalamine (DIPA). They found that the liquid velocity, external mass transfer coefficient and initial absorbent concentrations as well ass the fiber inner diameter and length have a large effect on the carbon dioxide removal performance. In addition they showed that AMP solution has a higher absorption capacity and a better selectivity than DEA and DIPA.

2.4.3.2 Membrane Distillation

Membrane distillation (MD) [53] is a relatively new process that is being worldwide investigated as a low cost, energy saving alternative to conventional separator process. Membrane distillation is a thermally driven process for separating volatile solvent (or

solvents) from solution on one side of a nonwetted microporous membrane. Generally, the evaporated solvent is condensed or removed on the other side of the microporous membrane. Assume a hot aqueous solution is placed on one side of hydrophobic microporous membrane and a cold aqueous solution is placed on the other side of the membrane, such that neither solution wets the membrane pores Fig 2.20(a). If the pressure of the water vapor of the hot solution is greater than that of the cold solution then water vapor diffuses from the hot solution/membrane interface where the water vapor condenses. In general, water vapor will diffuse in the microporous membrane, through air or any other noncondensable gaseous phase trapped in the pores. If there is no gaseous phase, the pores will have only water vapor. If the cold solution happens to be only water, the process achieves evaporation of water from the hot solution and the condensation of it in the cold liquid in a simple fashion. As long as the two liquids don't wet the membrane pores, they may be at any pressure. As water evaporation continuous the microporous membrane is functioning here as a liquid phase barrier. The membrane distillation process described above is one of the common configurations of the membrane distillation and is identified as direct contact membrane distillation, because the microporous membrane is in direct contact with liquid on both sides. This concept was first proposed by Findley [54], but none of the membranes used by Findley was good enough for extended duration membrane distillation. Sarti and Gostoli [55], Schofield *et al.* [56] have successfully demonstrated membrane distillation using microporous hydrophobic membranes of polytetrafluoroethylene (PTFE), polypropylene (PP), and polyvinylidenefluoride (PVDF).

There are several common configurations for membrane distillation process (Sarti and Gostoli) [55]. These are:

1. Direct contact membrane distillation: It has already been described.

2. Air gap membrane distillation: There is now air gap between the membrane and the condensation surface, instead of using the other side of the membrane as a condensing surface Figure 2.20(b).

3. Vacuum membrane distillation: No condensation surface is provided in the device. The vapor is withdrawn by pulling a vacuum on the other side of the membrane.

4. Sweep gas membrane distillation: A sweep gas is used to carry away the vapor from the MD device. It is a thermally driven process and there is temperature difference

across the membrane, while in the membrane air stripping which often confused with, is isothermal process.

The membrane distillation process has some similarities with the osmotic distillation (OD) process [57, 58]. For example both use hydrophobic microporous membranes with aqueous solutions on the two sides such the pores are not wetted. Another similarity is that, in both cases, water vapour is transferred through the pore due to its partial pressure gradient from the feed to the other side. In contrast, a temperature gradient drives the partial pressure gradient of water in MD in the same direction whereas in OD, with both solutions at the same bulk temperature, an osmotic pressure gradient drives the water vapour in the opposite direction Fig 2.20(c). A highly concentrated brine solution (for example) with a high osmotic pressure is maintained on the other side at the same temperature, instead of the condensate stream in MD. Water vapour is transferred from the feed solution to this high osmotic pressure solution, which has a much lower water vapour pressure.

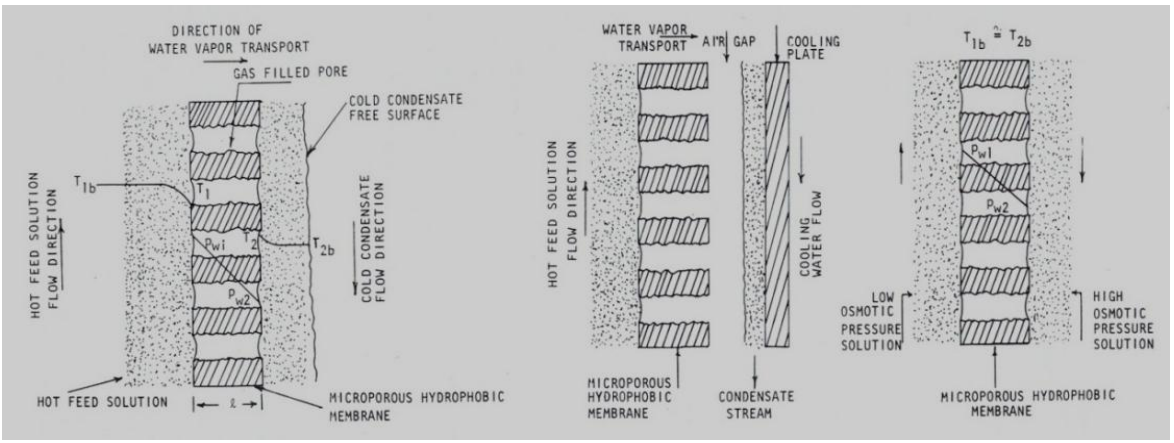

Figure 2. 20 Schematics of (a) direct contact membrane distillation with a hydrophobic microporous membrane (b) air gap membrane distillation and (c) osmotic distillation with a hydrophobic microporous membrane [59].

Separation of aqueous solutions via membrane distillation requires lower operating temperature and pressure, reduces vapor spaces and provides significant interfacial area [60] compared to other more popular separation processes. However, there is lack of general interest in membrane distillation process, because the process solution should not wet the microporous membrane.

2.4.3.3 Membrane Pervaporation

Membrane pervaporation is an effective process tool for separation of liquid mixtures. The process is shown in Figure 2.21.

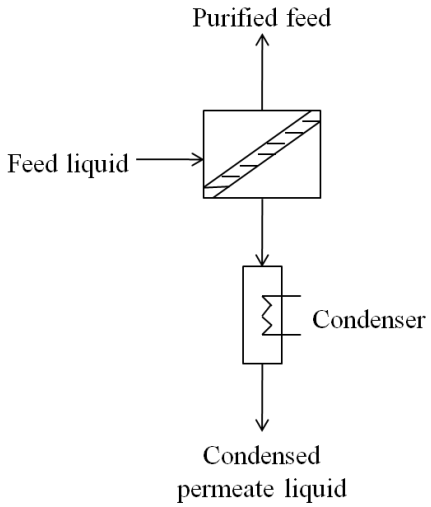

Figure 2. 21 Pervaporation process [59].

Pervaporation is a membrane separation process involving a feed mixture of two or more components passing through a dense membrane, in which one of the components permeates preferentially, and is removed as a vapor from the other side. Transport through the membrane is induced by the vapor pressure difference between the feed solution and the permeate vapor. There are several ways to maintain this vapor pressure difference. In the lab a vacuum pump is usually used to draw a vacuum on the permeate side of the system. Industrially, the permeate vacuum is most economically generated by cooling the permeate vapor, causing it to condense (fig 2.21); condensation spontaneously creates a partial vacuum [61]. The process was first studied in a systematic fashion by Binning and co-workers at American Oil in the 1950s [62]. Binning was interested in applying the process to the separation of organic mixtures.

Pervaporation systems are now commercially available for two applications. The most important is the removal of water from concentrated alcohol solutions. GFT (Germany), the leader in this field, installed its first pilot plant in 1982 [63]. The second commercial application of pervaporation is the removal of small amounts of volatile organic compounds (VOCs) from contaminated water. This technology was developed by Membrane Technology and Research [64]. No commercial pervaporation systems have yet been developed for the

separation of organic/organic mixtures. However, current membrane technology makes pervaporation for separation of organic/organic mixtures possible, and the pervaporation processes is being actively developed by a number of companies. The first pilot-plant results for an organic-organic application the separation of methanol from methyl tert-butyl ether/isobutene mixtures, was reported by Separex in 1988 [65]. More recently ExxonMobil, started a pervaporation pilot plant for the separation of aromatic/aliphatic mixtures [66].

2.4.3.4 Membrane Extraction

Liquid-liquid (L-L) extraction is among the oldest of preconcentration and matrix isolation techniques in analytical chemistry [67]. Supported liquid membrane extraction is the most versatile membrane extraction technique for analytical sample preparation [68]. This technique is based on three-phase system where analytes are extracted from an aqueous sample into another aqueous phase through an organic liquid. The organic phase is held between the aqueous phases by a porous, hydrophobic supporting membrane, immobilized by means of capillary forces. Hence, two different equilibria are involved, which makes the system chemically analogous to extraction and back-extraction in classic liquid-liquid extraction. Supported liquid membrane extraction is applicable to analytes of high or moderate polarity [68]. Also, supported liquid membrane extraction provides unique possibilities extracting polar, ionisable and even permanently charged compounds, including metal ions, which are more difficult to extract with other techniques [68]. Another type of membrane extraction is microporous membrane liquid-liquid extraction, where an aqueous phase and an organic phase are separated by a hydrophobic membrane, and the organic phase also fills the pores of the membrane to provide a direct contact through a liquid-liquid interface without mixing the phases. Figure 2.22 shows examples for typical membrane units for extraction. The membrane extraction units are made of two blocks of inert material with a machined groove in each. The blocks are clamped together with a membrane between them. In principle these membranes are applicable to all versions of membrane extraction for analytical sample preparation or sampling.

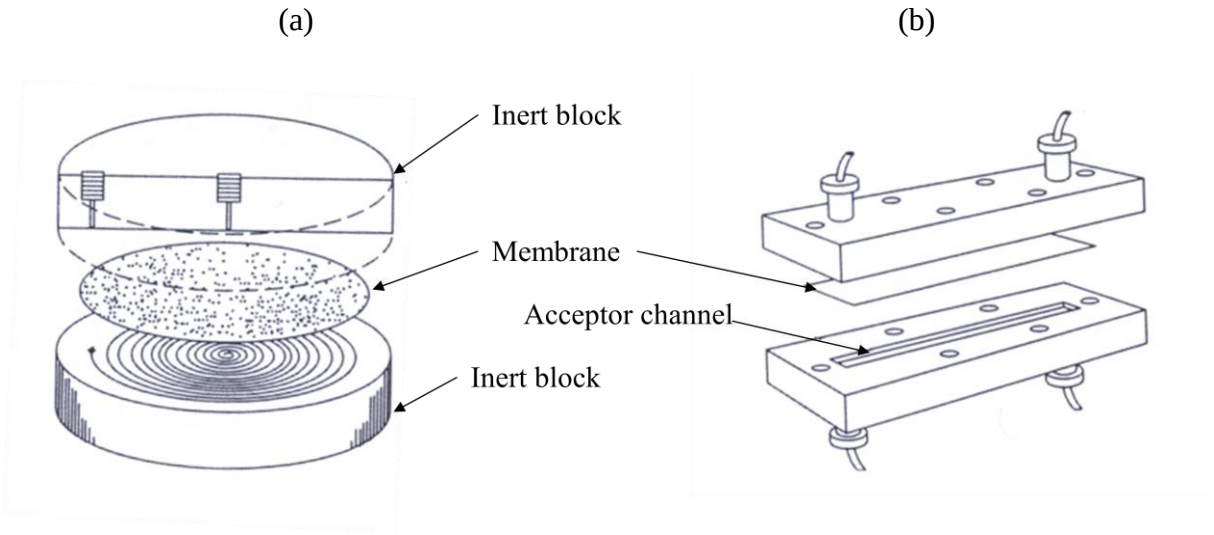

Figure 2. 22 Membrane units for liquid extraction. Shown are flat membrane modules with (a) 1µl and (b) 10µl channel volumes [68].

2.4.4 Mass transfer in membrane contactors

For the local rate of interphase transport of any species being absorbed from the gas into the liquid through a microporous hydrophobic membrane not wetted by the liquid, consider the concentration profile shown in Figure 2.23 (a). Species i diffuse through the gas film, the gas-filled membrane pore, and the liquid film in series. The species I flux expressions for the three regions are [59]:

$$N_I = k_{Ig} \cdot (p_{Igb} - p_{Imi}) = k_{Im} \cdot (p_{Imi} - p_{Ii}) = k_{Il} \cdot (c_{Ii} - c_{Ilb}) \quad (2.1)$$

At the gas/liquid interface, concentration in the two phases is at equilibrium and may be related by Henry's law:

$$C_{Ii} = H_I p_{Ii} \quad (2.2)$$

where H_I is the Henry's constant and p is the partial pressure of I at the gas/liquid interface.

In terms of an overall mass transfer coefficient K_g based on the gas phase, or K_l based on the liquid phase,

$$N_I = K_g \cdot (p_{Igb} - p_I^*) = K_l \cdot (c_I^* - c_{Ilb}) \quad (2.3)$$

where

$c_{Ilb} = H_I p_I^*$ and $c_I^* = H_I p_{Igb}$ (2.4)

where p_I^* is the partial pressure of gaseous I in equilibrium with liquid of concentration c_{Ii} and c_I^* is the liquid concentration of I in equilibrium with gas with partial pressure of p_I.

Recognizing that

$P_{Igb} - p_I^* = (p_{Igb} - p_{Imi}) + (p_{Imi} - p_{Ii}) + (p_{Ii} - p_I^*)$ (2.5)

one can get

$1/K_g = 1/k_{Ig} + 1/k_{Im} + 1/k_{Il}H_I$ (2.6)

The overall resistance to gas transfer comes from three resistances in series: the gas film resistance, the membrane resistance, and the liquid film resistance.

For the case where the membrane's pores are wetted (figure 2.23 (b)) by the liquid absorbent, the flux expressions for species I are:

$N_I = k_{Ig} (p_{Igb} - p_{Imi}) = k_{Im} (c_{Imi} - c_{Ii})$

$= k_{Il} (c_{Ii} - c_{Ilb}) = K_g (p_{Igb} - p_I^*)$

$= K_l (c_I^* - cI_{lb})$. (2.7)

This leads to

$1/K_g = 1/k_{Ig} + 1/k_{Im}H_I + 1/kI_lH_I$ (2.8)

and

$1/K_l = H_I/kI_g + 1/k_{Im} + 1/k_{Il}$ (2.9)

(a) (b)

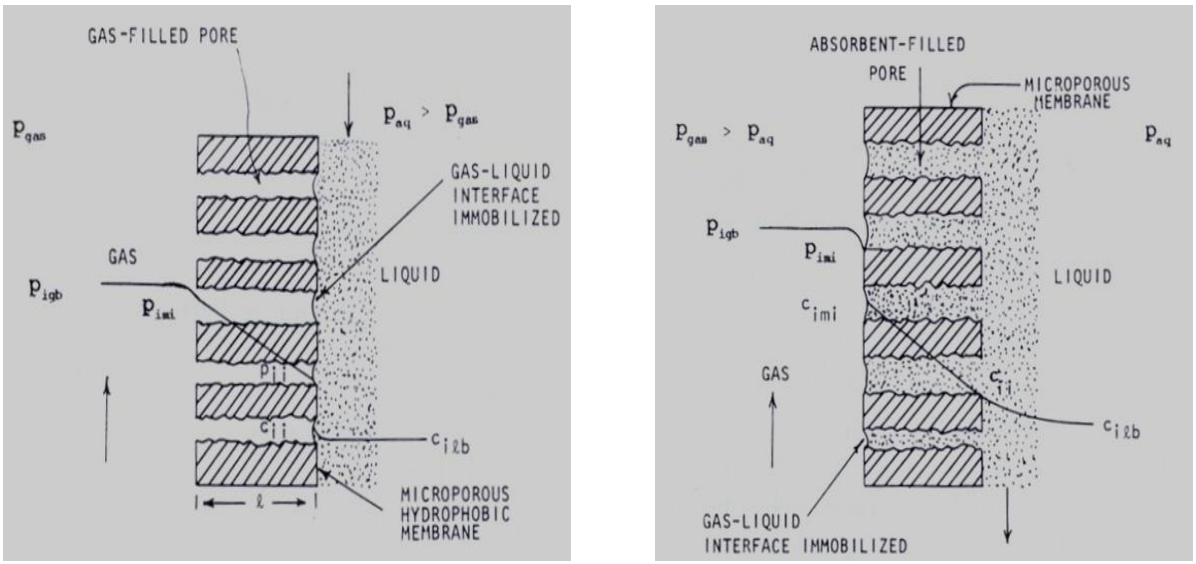

Figure 2. 23 Two operating modes of a hollow fiber membrane contactor: (a) gas-filled pores and (b) absorbent-filled pores [59].

Various correlations are available in the literature [25] to determine the individual mass transfer coefficient K_{Ig} ad K_{Il} , mainly determined by the geometry and the flow conditions in membrane contactor. The membrane mass transfer resistance when the pores are wetted by the absorbent liquid may be described by Eq. (2.10) [69]:

$$K_{Im} = D_{Il}\varepsilon_m/\tau_m\delta \qquad (2.10)$$

where D_{Il} is the diffusion coefficient of species i in the absorbent liquid, ε_m is the membrane porosity, τ_m is the tortuosity of pores in a membrane and δ is membrane thickness.

When the membrane's pores are gas-filled, the membrane transfer coefficient expression will depend on the regime of gas diffusion in the membrane pore. If the ratio of the membrane pore radius r_p to the mean free path of the gas λ, r_p/λ, is much smaller than 1, Knudsen flow regime exists. The membrane transfer coefficient k_{Im} can then be obtained from Knudsen flux expression as [59]:

$$K_{Im} = 2r_p/3\,(8RT/\pi M_I)^{1/2}\,\varepsilon_m/\tau_m\delta \qquad (2.11)$$

where M_I is the molecular weight of the ith gas species .

When r_p/λ is much larger than 1 viscous flow exists. For ratios r_p/λ between the two limits, transitional flow regime conditions are operative. In case of absorption of a species I through

a stagnant gas in the membrane pore under viscous flow conditions, conventional expressions for molecular diffusion may be used for K_{lm} with allowances for ε_m and τ_m [59].

2.4.5 Phase breakthrough

Mesh microcontactors are devices that allow immiscible fluid phases (liquid-liquid or gas-liquid) to come in contact via the pores of the mesh without dispersing one phase into the other. The critical issue in operating the mesh microcontactor is the maintenance of the gas/liquid interface. If the pressure difference exceeds a critical value, then the one phase will break and disperse into the other phase. The breakthrough of one phase into another may cause unwanted froth, foam or emulsion. Such breakthrough can be controlled by applying a higher pressure on the phase which does not wet the pores. In order to avoid the dispersion of one phase into the other the gas-liquid or liquid-liquid interface should remain within the pores for the range of pressure differences existing between the two phases during operation and modified along the membrane due to pressure drop.

In Figure 2.24 we can see a mesh microreactor where a liquid phase comes into direct contact with a fluid phase through the pores of the mesh.

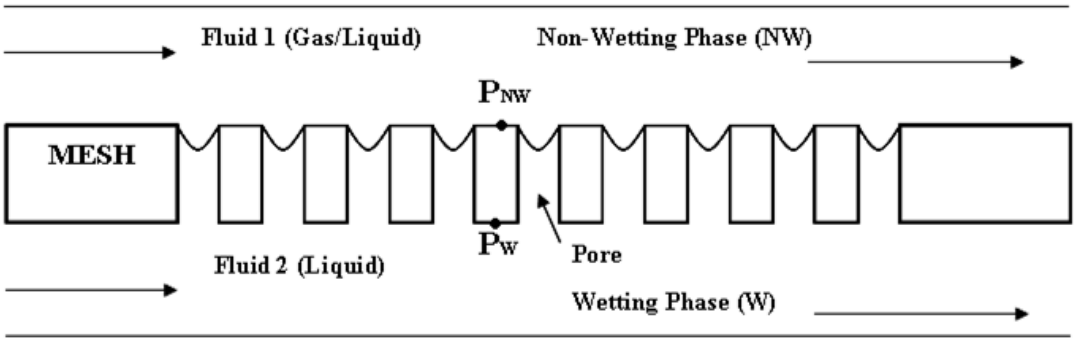

Figure 2. 24 Schematic diagram of mesh microreactor [70].

Based on Adamson and Gast [71] a pore in the mesh can be considered as a capillary and the interface inside each pore can be modelled with capillary rise concept. The mesh breakthrough pressure may be described by the Young-Laplace equation as [72]:

$$\Delta P = \gamma_l \cos\theta \left(\frac{1}{r_1} + \frac{1}{r_2} \right) \tag{2.12}$$

Where γ_1 the liquid surface tension, θ is is the contact angle between the liquid and the solid (the membrane material). r_1 and r_2 are the two characteristic radii of an elliptic shaped pore. For a circular pore the equation is simplified to:

$$\Delta P = \frac{2\gamma\cos\theta}{r} \tag{2.13}$$

with ΔP defined as:

$$\Delta P = P_{NW}\text{-}P_W \tag{2.14}$$

Positive breakthrough pressures (P_w-P_{NW}) of wetting phases in membranes have been reported [73, 74, 75], which seemingly contradict the prediction of the Laplace equation. This is probably due to the fact that the solid wall inclination change at the pores ends (for regular pore membranes) or at pore interior (for tortuous pore membrane) is not accounted for [76]. The above indicates that one needs to use with care the Laplace equation.

The term critical entry pressure of one phase refers to the pressure difference necessary for this phase to enter a pore. Even more important than critical entry pressure is the critical filling pressure of one phase $\Delta P_{C,}$ defined as the pressure difference necessary to completely fill the pores with that phase. Critical and entry and filling pressures are identical for constant cross section pores but they differ for tapered pores when the wetting phase is on the small pore opening side. Thus, there are two critical filling pressures defined as critical filling pressure of the wetting phase $\Delta P_{C,W}$ and the non-wetting phase $\Delta P_{C,NW,}$

$$\Delta P_{C,W} = (P_W\text{-}P_{NW})_{C,W} \tag{2.15}$$

$$\Delta P_{C,NW} = (P_{NW}\text{-}P_W)_{C,NW} \tag{2.16}$$

and two breakthrough pressures $\Delta P_{B,W}$ and $\Delta P_{B,NW}$ for the wetting and the non-wetting phases respectively.

$$\Delta P_{B,W} = (P_W\text{-}P_{NW})_{B,W} \tag{2.17}$$

$$\Delta P_{B,NW} = (P_{NW}\text{-}P_W)_{B,NW} \tag{2.18}$$

The contact angle measured for a liquid advancing slowly across a surface, θ_A, exceeds that of the liquid receding on the surface, θ_R, and all intermediate contact angles correspond to metastable equilibrium states [77]. This phenomenon is called contact angle hysteresis. The contact angle hysteresis is in general attributed to surface roughness and heterogeneity,

solution impurities, swelling, rearrangement or alteration of the surface by the solvent [71]. Because of the contact angle hysteresis, the Laplace-Young equation is written as equation (2.19) to calculate the wetting phase critical filling pressure and equation (2.20) to calculate the non-wetting phase critical filling pressure:

$$\Delta P_{C,W} = -\frac{2\gamma\cos\theta_A}{r} \tag{2.19}$$

$$\Delta P_{C,NW} = \frac{2\gamma\cos\theta_R}{r} \tag{2.20}$$

where θ_A is advancing contact angle and θ_R is receding contact angle. Due to the fact that at the pore end the solid wall changes inclination from vertical to horizontal, an apparent contact angle needs to be defined. For an axisymmetric straight pore, it is defined as the angle that the meniscus forms at the three phase contact line with vertical plane.

There are two mechanisms by which one phase can break through into the other:

1) Breakthrough by spreading, when the apparent contact angle becomes equal to the sum of advancing contact angle and maximum solid wall inclination at the pore ends inclination 90^o,

$\theta_{APP} = \theta_A + 90^o < 180^o$

The wetting phase breaks through into the non-wetting phase by spreading out horizontally along the mesh. In this case, breakthrough pressure difference is calculated by equation 2.21 based on Amador's work [70]:

$$\Delta P_{B,W} = P_L - P_G = -\frac{2\gamma\cos(\theta_A + 90^\circ)}{r} \tag{2.21}$$

Equation (2-21) indicates that $0 \le \Delta P_{B,W} \le \frac{2\gamma}{r}$, which is consistent with positive breakthrough pressure.

2) Breakthrough by maximum curvature, when

$\theta_{APP} = \theta_A + 90^o \ge 180^o$

The meniscus at the non-wetting pore opening will reach its maximum curvature of hemispherical shape, which can accommodate the largest pressure difference between the two

phases. Beyond this point, breakthrough happens by bubble/droplet formation. Breakthrough by maximum curvature is the common mechanism for breakthrough of a non-wetting phase in a wetting phase. The breakthrough pressure of the non-wetting phase can be calculated by equation 2.22:

$$\Delta P_{B,NW} = P_G - P_L = -\frac{2\gamma\cos(0)}{r} = \frac{2\gamma}{r} \quad (2.22)$$

Based on the above discussion, the meniscus position can be determined knowing pore geometry, θ_A, θ_R, as shown in Table 2.2

Table 2. 2 Meniscus position as a function of apparent contact angle (θ_{APP}).

Condition	Meniscus position
$0^o<\theta_{App}< \theta_R$	Wetting pore end
$\theta_R <\theta_{App} < \theta_A$	Any part of the pore
$\theta_A<\theta_{App}< \theta_A+90^o$	Non-wetting pore end

A cylindrical pore and a fluid pair with $\theta_A = 60°$, $\theta_R = 30°$ is considered by Amador work [70] for illustration of the shape and stability of the gas-liquid interface and reproduced in Figure 2.25. Figure 2.25 shows the dimensionless meniscus area and position versus the dimensionless pressure difference between the phases considering that the apparent contact angle can change from 0º at the wetting pore end to θ_A+ 90º= 150º at the non-wetting pore end (see Table 2.2). At contact angles $\theta_R< \theta_{App} < \theta_A$, the meniscus is located at any part within the pore, at $\theta_{App} < \theta_R$ the meniscus is pinned at the wetting end and at $\theta_{App} > \theta_A$ at the non-wetting end. As the contact angle gets closer to 0º at the wetting end, small changes in the pressure difference modify the meniscus area and curvature significantly.

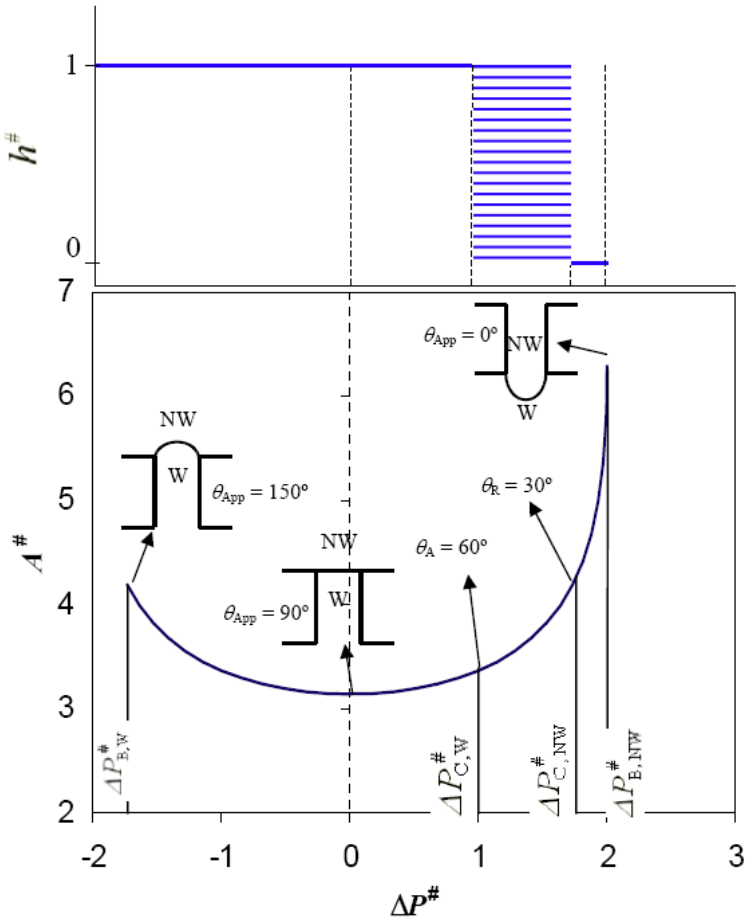

Figure 2. 25 Dimensionless meniscus height $h^{\#}$ and area $A^{\#}$ given as a function of the pressure difference across the meniscus $\Delta P^{\#} = P^{\#}_{NW} - P^{\#}_{W}$ [70].

Microfabricated meshes usually have supports either to keep the mesh from bending or to provide the necessary spacing between the mesh capping plates [4]. It has been experimentally observed that these supports can result in a decrease of the meniscus stability since they increase the effective diameter of the meniscus in the membrane pores adjacent to the supports as shown in Figure 2.26 [70]. A similar effect can happen at the edges of the mesh, where gaskets or O-rings are used for sealing. In addition mesh must be carefully cleaned before use because small particles can rest on it and increase the effective diameter as well. As a result of the increase of effective diameter is the decrease of breakthrough pressure when mesh is wetting by the absorbent liquid. Breakthrough pressure is unaffected by the supports for non-wetting mesh based on Amador work [70].

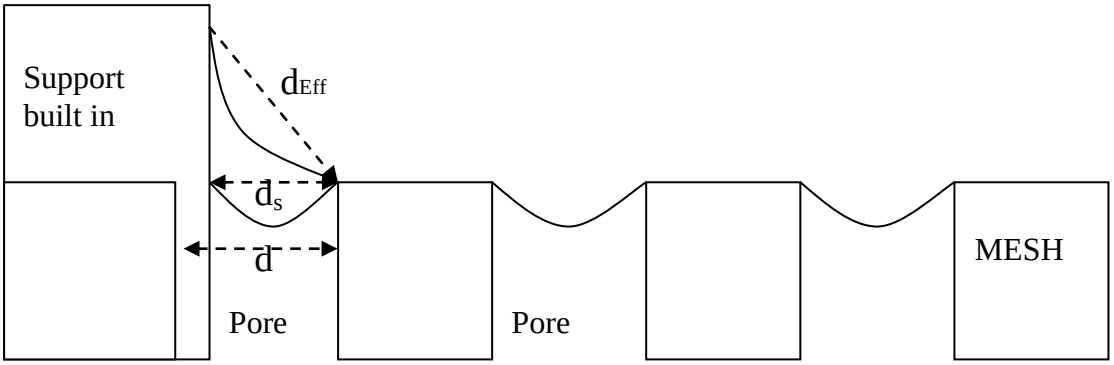

Figure 2. 26 Illustration of effective diameter increase by built in support (edge effect) [70].

In order to prevent wetting of the pores of the membrane as a result less resistance to mass transfer the following measures can be considered:

(a) Using hydrophobic membranes. Since the solvents for CO_2 absorption are aqueous solutions, using hydrophobic membranes minimize the wetting problems [78]. The wettability of different liquid absorbent is summarized in Table 2.3. Due to its higher hydrophobicity, PTFE is more resistance to wetting by aqueous solutions. The disadvantage of using this material is the high production cost and lack of commercial availabilities, especially of those with smaller diameter [1]. PP fibers are less expensive and commercially available in a wider size, but they are not fit for operation with common absorbent liquids. PP is less chemical stable than PTFE. *Wang et al.* [79] examined the impacts of a common solvent used for CO_2 absorption, diethanolamine (DEA) solutions, on two types of PP. They observed that chemical reaction occurred between PP membrane and DEA, which reduced the surface tension and hence its hydrophobicity.

(b) Surface modification of a membrane. Hydrophobic modification of membrane surface can also improve its non-wettability. Nishikawa *et al.* [80] showed that the performance of polyethylene (PE) membrane could be greatly improved by hydrophobic treatment to its surface using fluocarbonic materials. In addition wetting problems can also alleviated by coating the membrane with a very thin permeable layer [81].

(c) Using membranes with a dense top layer and a microporous support effective in preventing wetting problems [1]. The top layer in contact with the liquid phase avails

as a stabilization layer. The material of this layer should be highly permeable to the targeted gas components and be hydrophobic enough to prevent wetting by water.

(d) Using liquids with suitable surface tension, because liquids with lower surface tension have a greater tendency to penetrate into the pores of a hydrophobic membrane owing to less capillary pressure.

(e) Use a smaller pore size. This can be easily concluded from Young-Laplace equation.

Table 2. 3 Wettability of membranes by liquid absorbents [1].

Membrane	Absorption liquid	Wettability	Cause of wetting
PTFE	Aqueous MEA	_	
PE	Aqueous MEA	+	Hydrophobicityof PE is not enough
PP	Aqueous NaOH solutions	+	Possible modification of pores by trace impurities and ionic species
	Aqueous amines solutions	+	
PTFE	Aqueous amines	_	
PP	Aqueous alkanolamines	_	
	Aqueous amino acid salt solutions	_	
PTFE	Aqueous MEA	+	Larger pore size of PTFE
PVDF	Aqueous MEA	_	

PP	Water, aqueous NaOH, Aqueous MEA	+	(MEA) Not given, but possibly due to low surface tension of MEA, Insufficient, Hydrophobicity and chemical instability of membrane
PE		+	(MEA)
PTFE		_	
PE+F		_	
PP	Aqueous amines solutions	+	Cause of wetting was not given; PTFE is more chemically stable
PES+PDMS		+	
PP+PDMS		+	
PTFE		_	
PP	Aqueous NaOH	_	Possibly the low surface tension of aqueous MDEA
	Aqueous MDEA	+	
PTFE	Aqueous KOH solutions	_	

+: wetted; -: non-wetted; F: coated with fluoropolymer; PP: polypropylene; PE: polyethylene; PES: poly (ether sulphone); PDMS: coated with poldimethyl-siloxane (silicon rubber); PTFE: polyTetrafluoroethylene (Teflon); PVDF: polyvinylidenefluoride; AMP: 2-amino-2-methyl-1-prpanol; DEA: methyl-di-ethanolamine; EAE:2-(ethylamino)-ethanol; MEA: momoethanolamine; DEA: Diethanolamine; and TEA: tri-ethanolamine.

2.5 CO_2 Capture systems

There are three basic systems for capturing CO_2 from coal-derived generation.

- Post-combustion capture
- Pre-combustion capture
- Oxy-fuel combustion capture.

These systems are illustrated in Figure 2.27.

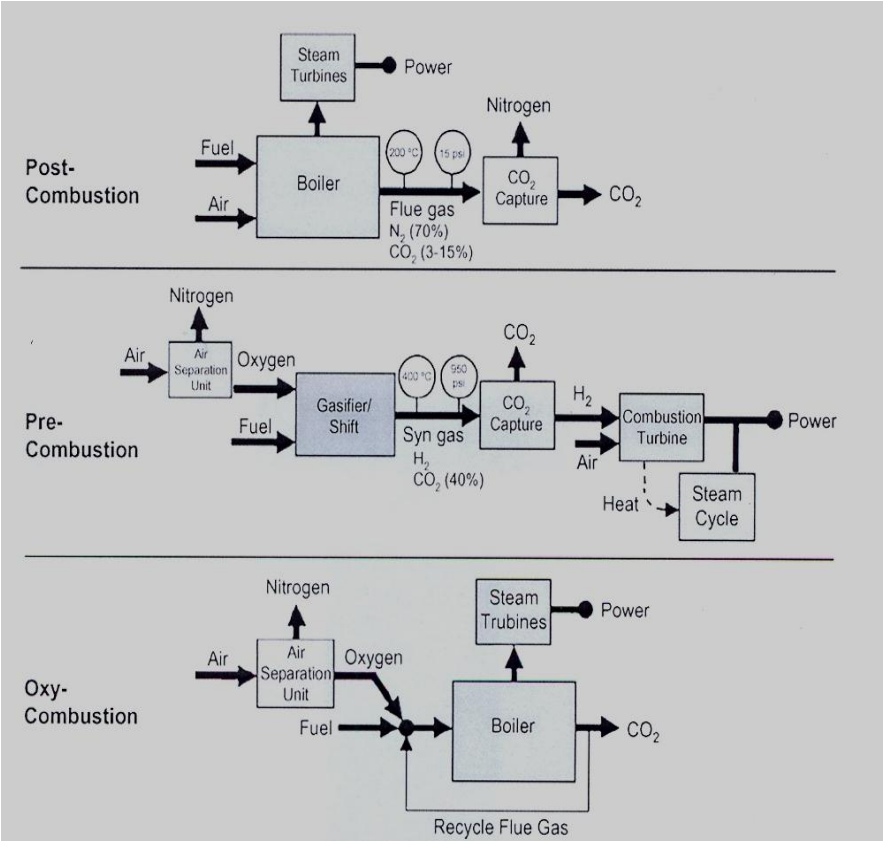

Figure 2. 27 CO_2 capture systems [82].

2.5.1 Post-combustion capture

Post-combustion capture involves the removal of CO_2 from flue gases produced by combustion of fossil fuels in air. Flue gas is passed through equipment which separates most of the CO_2, instead of being discharged directly to the atmosphere. The CO_2 is fed to a storage reservoir and the remaining flue gas is discharged to the atmosphere. A chemical sorbent process would normally be used for CO_2 separation. Other techniques are also being considered but are not at such an advance stage of development. Post-combustion capture can also be applied to coal and oil fired power stations but some additional measures are needed to minimize contamination of the CO_2 capture solvent by impurities in the flue gas, such us sulphur and nitrogen oxides. In many respects, post-combustion capture of CO_2 is analogous to wet flue gas desulphurisation (FGD) techniques, which is widely used on coal and oil fired power stations to reduce emissions of SO_2 [83].

2.5.2 Pre-combustion capture

In pre-combustion capture a fuel reacts with oxygen or air and/or stream to give mainly a‘synthesis gas (syngas)’ or ‘fuel gas’ a mixture of mainly CO and H_2. The syngas, with added steam, is then sent to a catalytic reactor (shift converter), to convert CO to CO_2 and give more H_2. CO_2 is then separated, usually by a physical or chemical absorption process, resulting in a hydrogen-rich fuel which can be used in many applications such as boilers, furnaces, gas turbines, engines and fuel cells. These systems are considered to be strategically important but the power plant systems of reference today are $4GW_e$ of both oil and coal-based, integrated gasification combined cycles (IGCC) which are around 0.1% of total installed capacity worldwide [83].

2.5.3 Oxy-fuel combustion capture

In oxy-fuel combustion capture the fuel is burned with nearly pure oxygen mixed with recycled flue gas (mainly CO_2 and H_2O). The pure oxygen is mixed with recycled flue gas to maintain combustion conditions similar to an air fire configuration. This is necessary because,

if the fuel is burnt in pure oxygen, the flame temperature is excessively high. Oxygen is usually produced by low temperature (cryogenic) air separation and novel techniques to supply oxygen to the fuel, such as membranes and chemical looping cycles are being developed [82]. The advantage of this technology is the elimination of NO_x control equipment and the CO_2 separation step [84]. The main systems for reference for oxy-fuel combustion are the same as those mentioned above for post-combustion capture.

2.5.4 Advantages and Disadvantages of the CO_2 capture systems

Table 2.4 shows a summary of the advantages and disadvantages of each of these systems.

Table 2. 4 Advantages and Disadvantages of different CO_2 capture approaches [82].

	Advantages	**Barriers to implementation**

Post-combustion	• Applicable to the majority of existing coal-fired power plants
	• Retrofit technology option
		• Flue gas is:
		• Dilute in CO_2
		• At ambient pressure
		Resulting in:
		• Low CO_2 partial pressure
		  • Significantly higher performance or circulation volume required for high capture levels
		  • CO_2 produced at low pressure compared to sequestration requirements

Pre-combustion	Synthesis gas is: • Concentrated in CO_2 • High pressure	• Applicable mainly to new plants, as few gasification plants are currently in operation • Barriers to commercial application of

	Resulting in:
	• High CO_2 partial pressure
	  • Increased driving force for separation
	  • More technologies available for separation
	• Potential for reduction in compression costs/loads
		gasification are common to pre-combustion capture
		  • Availability
		  • Cost of equipment
		  • Extensive supporting systems requirements

Oxy-combustion	• Very high CO_2 concentration in flue gas
	• Retrofit and repowering technology option
		• Large cryogenic O2 production requirement may be cost prohibitive
		• Cooled CO_2 recycle required to maintain temperatures within limits of combustor materials
		  • Decreased process efficiency
		  • Added auxiliary load

2.5.5 Types of CO_2 capture technologies

2.5.5.1 CO_2 capture with sorbents

A number of solids can be used to react with CO_2 to form stable compounds under a set of conditions, and then under a different set of conditions, be regenerated after being heated, after a pressure decrease or after any other change in the conditions around the sorbent, to release the absorbed CO_2 and reform the original compound. After the regeneration step the sorbent is sent back to capture more CO_2 in a cyclic process. In some variants of this process the sorbent is solid and does not circulate between vessels because the sorption and regeneration are achieved by cyclic changes (in pressure or temperature) in the vessel where

the sorbent is contained [85]. A make-up flow of fresh sorbent is always required to compensate for the natural decay of activity and/or sorbent losses. No solid sorbent systems for large scale recovery of CO_2 from flue gas have yet been commercialized, because solids are inherently more difficult to work with than liquids, although molecular sieve systems are used to remove impurities from a number of streams, such as in the production of pure H_2. Figure 2.28 shows the separation process [82].

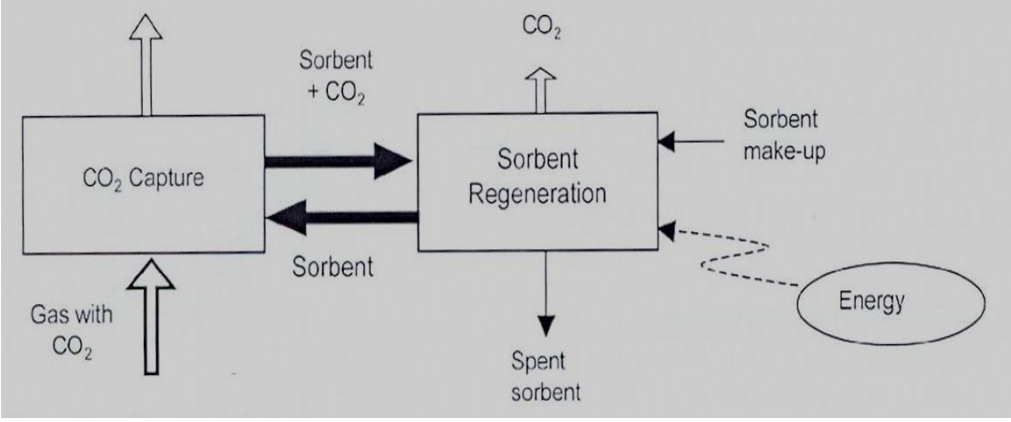

Figure 2. 28 Separation with sorbents.

2.5.5.2 Chemical solvent scrubbing

Currently the favoured method to remove CO_2 from flue gases is using chemical solvents. The most common solvents for capturing CO_2 from low pressure flue gas, is monothanolamine (MEA) and tertiary methyldiethanolamine (MDEA), due to the high CO_2 loading possible and the low regenerator heating load, relative to other solvents [85]. The solvent removes CO_2 from flue gas by means of chemical reaction, which can be reversed by pressure reduction and heating. Prior to CO_2 removal the flue gas is cooled and particulates and other impurities are removed as far as possible. After that, it is passing into an absorption vessel where it comes into contact with the chemical solvent, which absorbs much of the CO_2 by chemically reacting with it to form a loosely bound compound. To reverse the CO_2 absorption reactions the CO_2 – rich solvent from the bottom of the absorber is passing into a stripping column where it is heated with steam. After the release of CO_2 in the striper is compressed for transport and storage and the CO_2 free solvent is recycled to the absorption vessel [85]. Around 98% CO_2 recovery can be achieved, though around 90% capture is usually proposed for power stations, and product purity can be excess of 99% [86].

2.5.5.3 Physical solvent process

A physical solvent selectively absorbs CO_2 without chemical reaction. Physical solvent processes are mostly applicable to gas streams which have a high CO_2 partial pressure and/or a high total pressure. They are mostly used to remove the CO_2 from the mixed stream of CO_2 and H_2 that comes from the shift reaction in pre-combustion CO_2 process (see figure 2.22), such as product from partial oxidation of coal and hydrocarbons [85]. The regeneration of solvent is carried out by release of pressure at which CO_2 evolves from the solvent, in one or more stages. If further regeneration is needed the solvent would be stripped by heating. The energy consumption for the process is low, as only the energy for pressurizing the solvent (liquid pumping) is required. In a pre-combustion capture process the use of high sulphur fossil fuels result in syngas with H_2S. Acid gas components must be removed. If transport and storage of mixed CO_2 and H_2S is possible then both components can be removed together. Sulphinol was developed to achieve significantly higher solubilities of acidic components compared to amine solvents, without added problems of excessive corrosion, foaming, or solution degradation [85]. It consists of a mixture of sulpholane (tetrahydrothiophene 1,1-dioxide), an alkanolamine and water in various proportions depending on the duty. The main physical solvents that could be used for CO_2 capture are cold methanol (Rectisol process), dimethylether of polyethylene glycol (Selexol process), propylene carbonate (Fluor process) and sulpholane [82].

2.5.5.4 Chemical looping combustion

In chemical looping process, no air separation unit is required for the production of concentrated CO_2 stream. In this process oxygen is supplied by a suitable metal oxide as an oxygen carrier, rather than by air or gaseous oxygen. Chemical looping is used to carry out in two fluidized beds [87]. In the first bed (oxydiser), a metal compound (Me) is oxidised with air to form an oxide (MeO) and produce a hot flue gas (reaction (1-7)), which is necessary to raise steam for the steam turbines that runs the generator. In the second bed reactor (reducer) the MeO is reduced to its initial state by the fuel (reaction (1-8)), while producing a gas with a high concentration of CO_2 that can be captured and sequestered. The effect of having combustion in two reactors compared to conventional combustion in a single stage is that the CO_2 is not diluted with nitrogen gas, but is almost pure after separation from water, without requiring any extra energy demand and costly external equipment for CO_2 separation [85].

Air Reactor: $O_2 + 2Me \rightarrow 2MeO$ (2.23)

Fuel Reactor: $C_nH_{2m} + (2n + m)\ MeO \rightarrow nCO_2 + mH_2O + (2n + m)Me$ (2.24)

Chemical looping is in the early stage of process development. Bench and laboratory-scale experimentation is currently being conducted. Key hurdles include the handling of multiple solid streams and the development of adequate oxygen carrier materials [82].

CHAPTER 3

OPTIMAL DESIGN FOR FLOW UNIFORMITY IN MICROCHANNEL PLATE

3.1 Introduction

Fluid flow distribution in the geometry of a single microreactor plate plays a crucial role in the performances of the latter in chemical reaction. An uneven distribution of fluid flow over the channels would introduce dispersion, leading to loss in conversion and selectivity. In addition, a non-uniform flow distribution would increase the pressure drop over a microstructured plate leading to strong limitations in the throughput of the microdevice [88].

The use of microreactors for industrial-scale production of chemicals requires a large number of reactors in parallel, since each reactor provides only a small volume dedicated to reaction. Unfortunately, process design based on this ‘‘numbering-up’’ approach, is not exempt from some of the same difficulties encountered in traditional scale-up [89]. In particular, the parallel process structures may exhibit poor uniformity in the fluid distribution between microchannels, which is generally undesirable and can limit severely the inherent advantages of microchannel reactors [89]. Therefore, it is important, to design reactor geometries enabling narrow velocity distributions between channels.

In this Chapter fluid flow distribution in the geometry of a single microreactor is investigated in order to approach a design which allows the flow distribution to be as uniform as possible over the plate. For this purpose, 3D CFD models were formulated by varying in turn geometrical parameters such as: width of inlet and outlet flow distribution regions, different shapes of inlet and outlet flow distribution regions, shifting the channels in parallel, effect of the channels and the results of the simulations are presented in terms of fluid bypass and the uniformity of the fluid flow into the channels area.

3.2 Simulation Conditions

The fluid flow in microchannels is considered to be laminar. In this work, the density and the dynamic viscosity of the gas stream used for all the simulations (20vol% CO_2/N_2) have been set to ρ_{gas}=1.327 Kg/m^3 and μ_{gas}=1.69e^{-5} Pa.s respectively and for the liquid stream (2M NaOH) ρ_{liquid}=1088 Kg/m^3 and μ_{liquid}=1.67e^{-3} Pa.s respectively. For laminar flow in the microchannels to be applicable, Reynolds numbers should be lower than 2,000 for a Reynolds number defined as:

$$Re = \frac{\rho_i u_i D_H}{\mu_i} \tag{3.1}$$

where u_i is the characteristic velocity of the gas or liquid stream, and D_H the hydraulic diameter.

The Reynolds numbers for the channels were well below the critical value in all cases (a maximum value of Re=21 for each of the channels was found for a velocity of 0.162 m/s for the gas stream and a maximum value of Re=1.3 was found for a velocity of 5.0x10^{-3} m/s for the liquid stream, the highest figure taken into account,(these velocities were chosen based on the experimental gas and liquid flowrates, which will be used in the next chapters for CO_2 absorption)), allowing the flow to be regarded to as laminar.

The governing equations for this model are the Navier-Stokes equations [90]:

$$\rho_i\left(\frac{\partial\vec{u}}{\partial t}+\vec{u}\cdot\nabla\vec{u}\right)=-\nabla p+\mu_i\nabla^2\vec{u}+\rho_i\vec{g} \tag{3.2}$$

combined with the equation of continuity,

$$\frac{\partial\rho_i}{\partial t}=-\left(\nabla\cdot\rho_i\vec{u}\right) \tag{3.3}$$

where $\vec{u}$ is the fluid velocity vector, t , time, p , pressure and $\vec{g}$, gravity vector.

For incompressible fluids at steady state hydrodynamics and isothermal conditions with negligible gravity, equations (3.2) and (3.3) become respectively:

$$\vec{u}\cdot\nabla\vec{u}=-\nabla p+\mu_i\nabla^2\vec{u} \tag{3.4}$$

And

$$\nabla\cdot\vec{u}=0 \tag{3.5}$$

Equations (3.4) and (3.5) are to be solved in the fluid domain in order to obtain the velocity distribution within the channels.

Comsol 3.5a®, specific modelling software for finite element analysis of partial differential equations, was used to solve equations (3.4) and (3.5). A mesh consisting of 66273 number of elements and 163887degrees of freedom was used to execute the simulations in Windows XP with Pentium 4 processor 3.00GHz and 4GB RAM. Increasing the numbers of degree of freedom in the computentional domain from 66273 to 402300, no significant variation in the results could be detected meaning that the calculated distribution was not influence by the mesh grid.

3.3 3D Simulations

In order to calculate the velocity distribution over the microplate, preliminary 3D simulations have been carried out. Four different simplified 2D plates, namely A_1, A_2, A_3, A_4 (see figure

3.1-3.4), have been considered in order to study the fluid flow over the microplate. In addition three-dimensional computational domain of the plates A_1 and A_2 are shown in Figures 3.5-3.6. In order to solve the Navier-Stokes and the continuity equations, (3.4) and (3.5), for the 3D model, no-slip boundary conditions have been set at all walls, being the fluid treatable as a continuum medium. At the outlet, a fixed pressure has been specified (P=0 $N \cdot m^{-2}$). The solution was checked from 66273 to 402300 number of Degrees of Freedom, and no significant variation in the results could be detected indicating that the solution was mesh independent. By considering four different plates A_1 (4 channels), A_2 (8 channels) and A_3, A_4 (channels are shifted in parallel), the goal was to examine the effects of those on the velocity profile along the channels, in order to attain the most favourable design of microstructured plate that allows the fluid to be distributed equally into each channel.

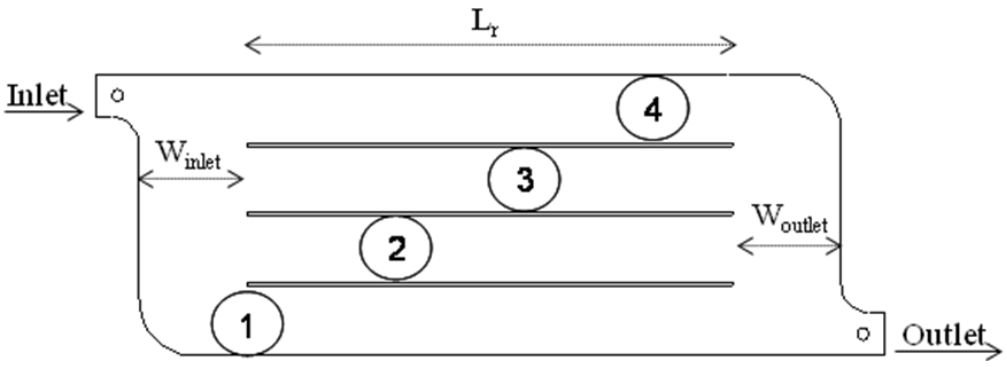

Figure 3. 1 Microplate geometry A_1. The dimensions are: 850 μm chamber thickness for the gas side and 200 μm for the liquid side, 90 mm channel length (L_r). The inlet and outlet widths are 20mm (W_{inlet} and W_{outlet}, respectively).

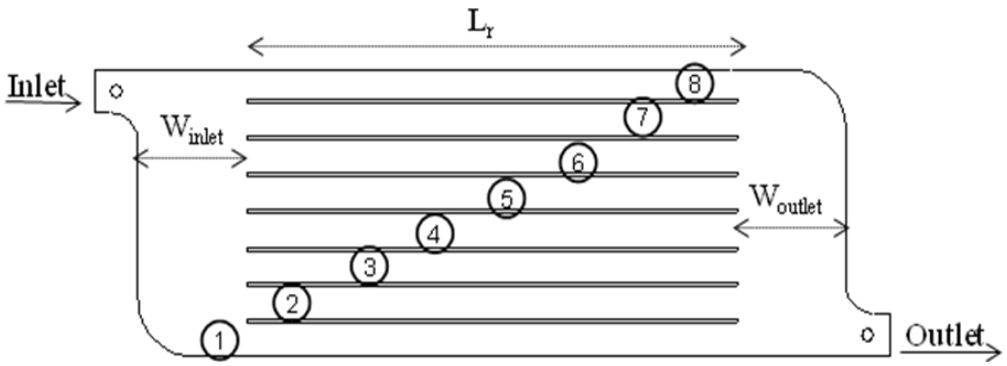

Figure 3. 2 Microplate geometry A_2. The dimensions are 850 μm chamber thickness for the gas side and 200 μm for the liquid side with 90 mm channel length (L_r). The inlet and outlet widths are 20 mm (W_{inlet} and W_{outlet}, respectively).

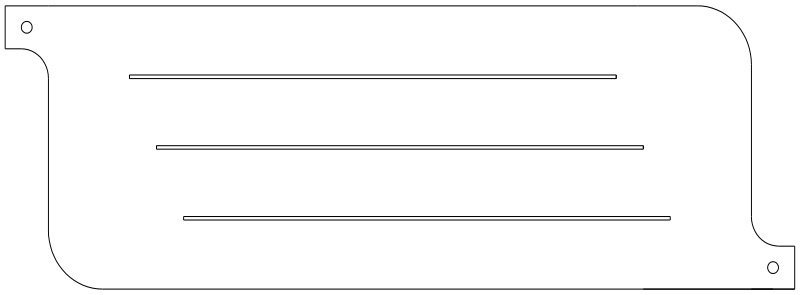

Figure 3. 3 Microplate geometry A_3. The dimensions are 850 μm thickness and 90 mm channel length (L_r).

Figure 3. 4 Microplate geometry A_4. The dimensions are 850 μm thickness and 90 mm channel length (L_r).

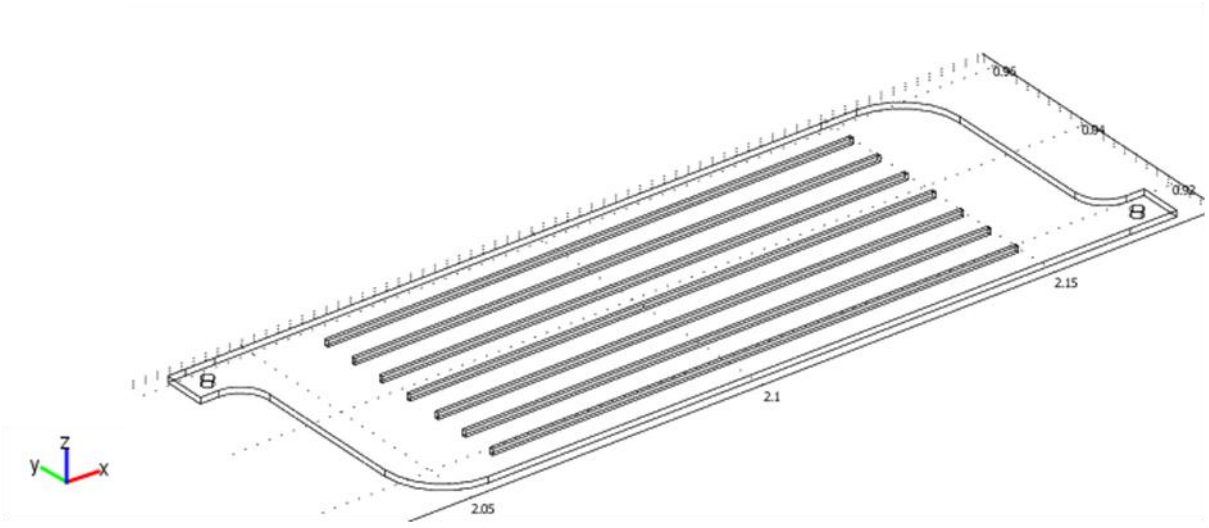

Figure 3. 5 Three-dimensional computational domain of the microplate A_1.

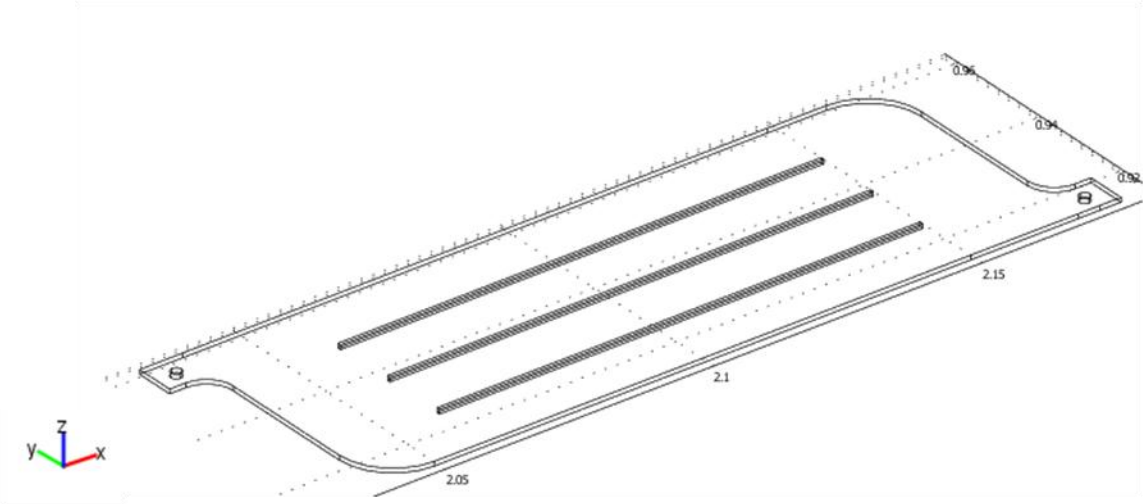

Figure 3. 6 Three-dimensional computational domain of the microplate A_2.

3.4 Results and discussion

As already mentioned, the main objective of this work is to consider the effect of geometrical parameters of the microplate in order to approach a design which allows the flow distribution to be as uniform as possible over the plate for the gas and liquid phase. As it can be seen from Figure 3.7 and 3.8 (velocity profiles at the mid-height of the gas chamber from the CFD simulation for the maximum gas flowrate used in the experiments) the number of channels affect the flow distribution in the same way. In both geometries (A_1 and A_2) it is clear that two small regions appear at each corner of the plates, where the fluid has significantly smaller velocity compared to the velocity inside the channels (fluid bypass). However, since the gas-liquid contact occurs only in the channel area these stagnation regions are not detrimental and they will not affect the performances of the plate. In order to compare the quality of flow distribution within the channels, average velocities u(i) within each channel are calculated by integration of the velocity profiles in y and z plane. In Figures 3.9 and 3.10 normalized average velocities $u(i)/u_{mean}$ in geometries A_1 and A_2 are shown where the mean velocity is given by equation (3.5):

$$u_{mean} = \frac{1}{n}\sum_{i=1}^{n} u(i) \qquad (3.5)$$

The maximum difference between average velocities was found to be [ui(max)- ui(min)] / u_{mean}< 0.1% for both geometries (A_1 and A_2) confirming flow uniformity within the channels. Simulations were performed on geometries A_1 and A_2 for the minimum gas flowrate used in the experiments (V_{gas}=177 ml/min). Maximum difference between average velocities was found to be <0.1% as well.

Comparing the geometries A_3, A_4 with A_1, A_2 plates apart from the fluid bypassing that exists (more in geometry A_4 less in geometry A_3) see Figures 3.11 and 3.12 a maldistribution of the fluid appears among the channels. As it can be seen from normalized velocity distribution within microchannels for geometries A_3 and A_4 (figures 3.13 and 3.14), fluid tends to flow with higher velocity in the middle channels for geometry A_3 and with lower for geometry A_4 as shown in Figures 3.11 and 3.12. Thus, it leads to worsening the performance of the plate. In addition it can be seen that the velocity is higher at the beginning and at the end of the supporting bars in comparison with the velocity inside the channels. This is due to the fact that these are the areas where the fluid hits or leaves the solid boundaries of the supporting bars, hence there is a velocity change.

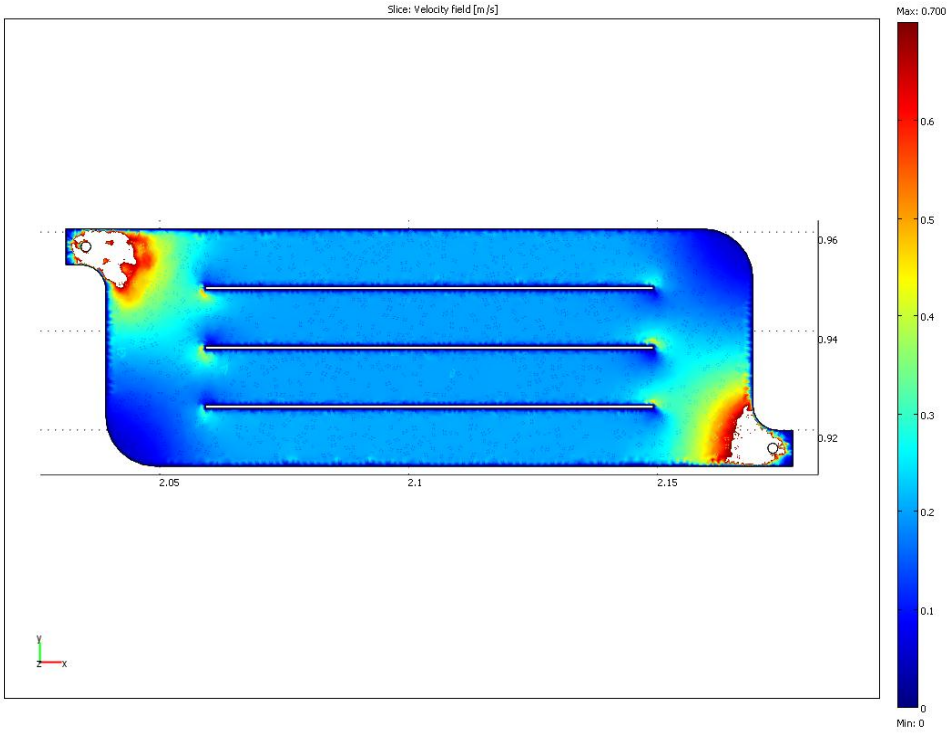

Figure 3. 7 Velocity profile in geometry A_1 in the gas chamber at channel mid-height=425 μm. Inlet gas flowrate Y_g=354 ml/min.

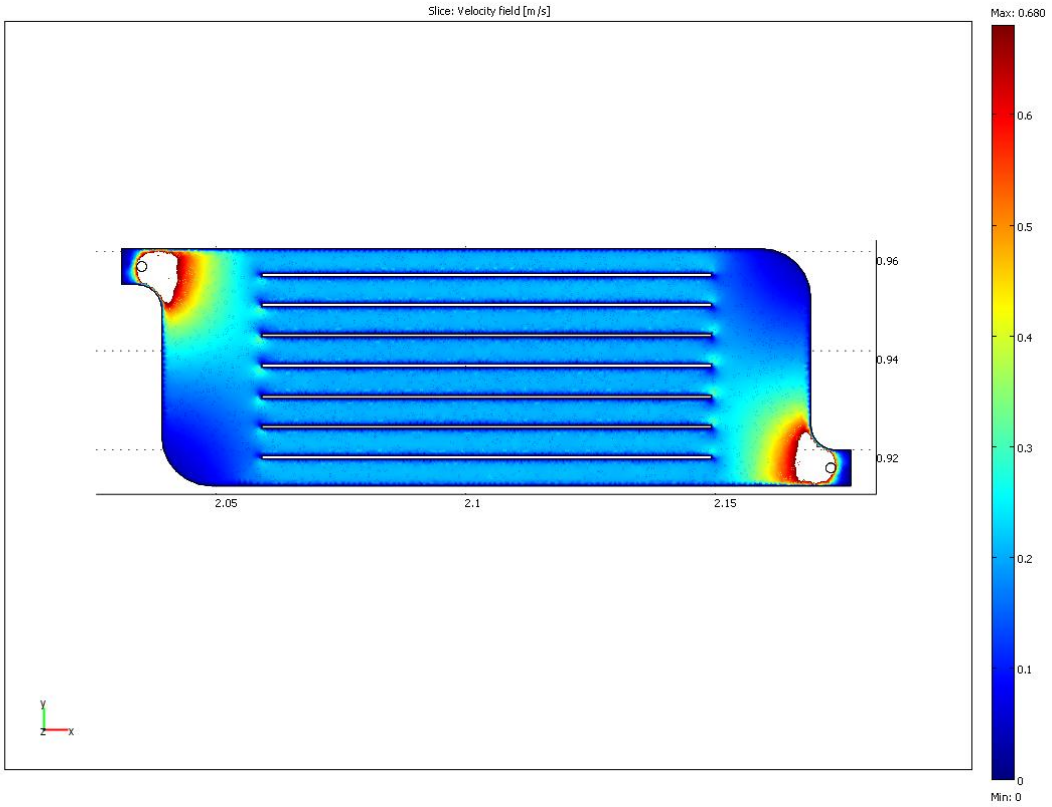

Figure 3. 8 Velocity profile in geometry A_2 in the gas chamber at channel mid-height=425 μm. Inlet gas flowrate Y_g=354 ml/min.

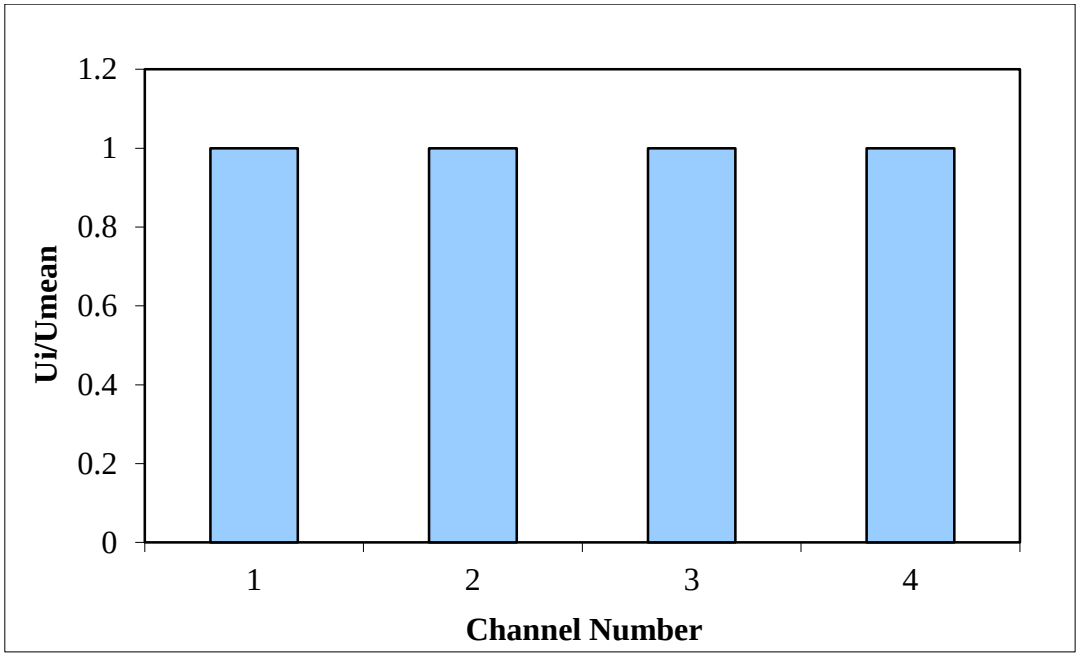

Figure 3. 9 Normalized velocity distribution in geometry A_1 within microchannels at inlet gas flow rate Y_g=354 ml/min and Re=21.

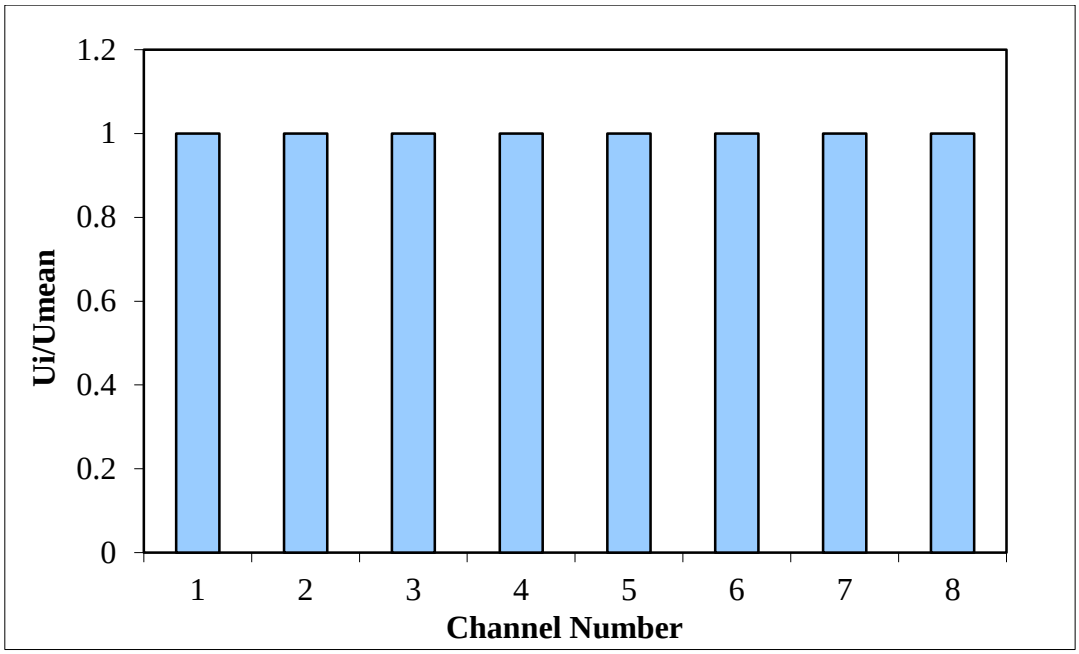

Figure 3. 10 Normalized velocity distribution in geometry A_2 within microchannels at inlet gas flow rate Y_g=354 ml/min and Re=20.

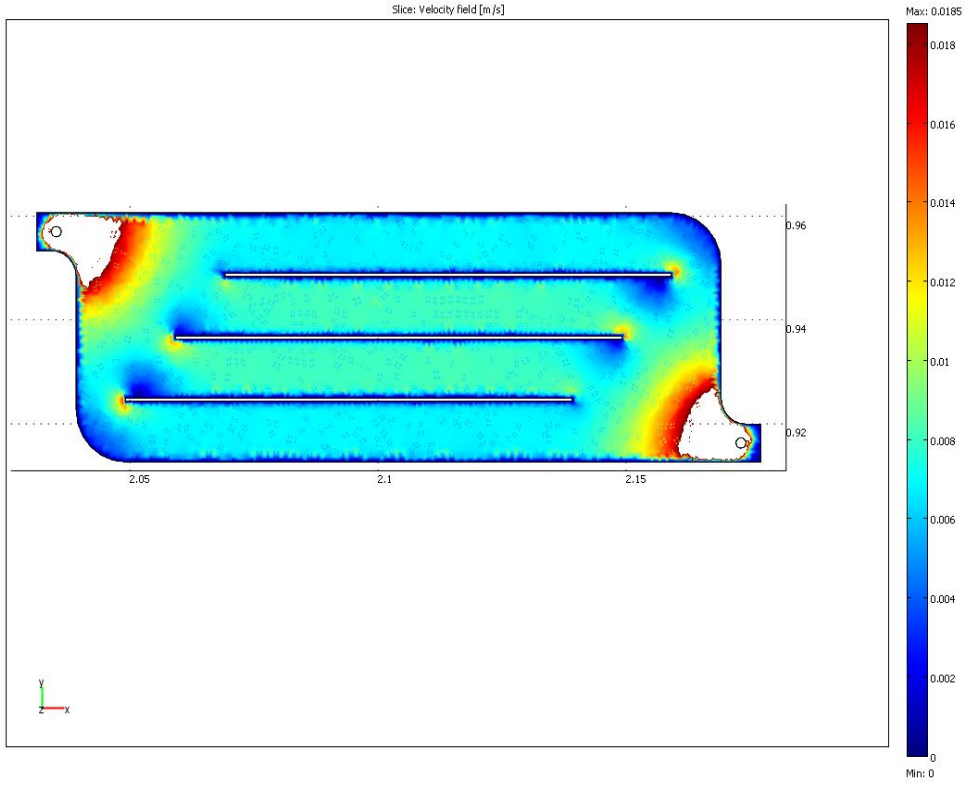

Figure 3. 11 Velocity profile in geometry A_3 in the gas chamber at channel mid-height=425 μm. Inlet gas flowrate Y_g=354 ml/min.

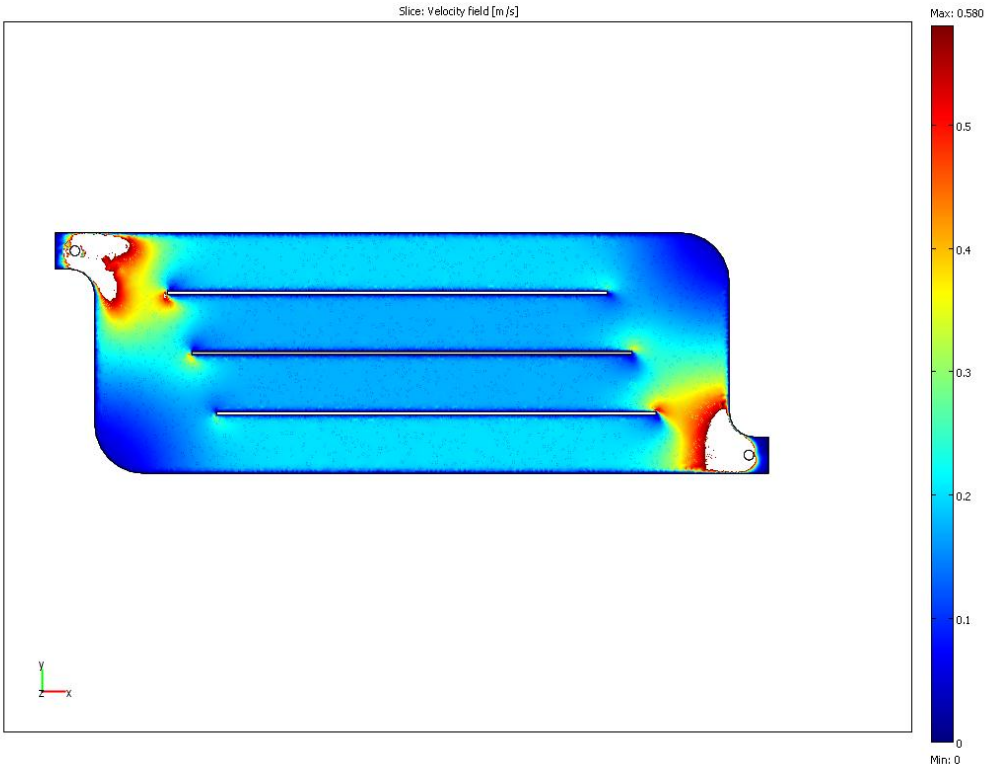

Figure 3. 12 Velocity profile in geometry A_4 in the gas chamber at channel mid-height=425 μm. Inlet gas flowrate Y_g=354 ml/min.

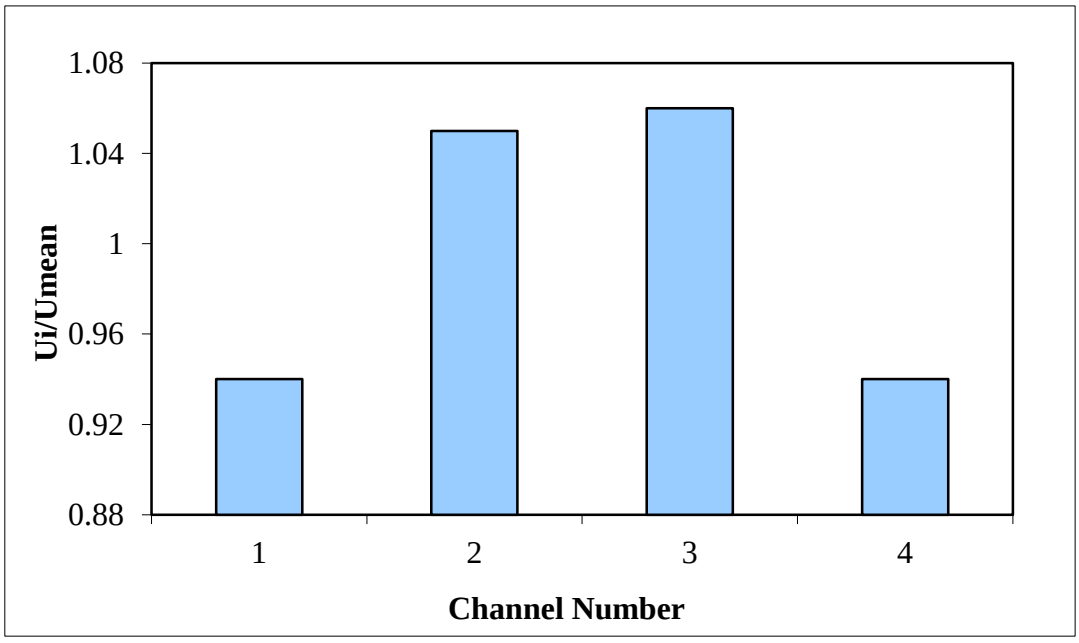

Figure 3. 13 Normalized velocity distribution in geometry A_3 within microchannels at inlet gas flow rate Y_g=354 ml/min.

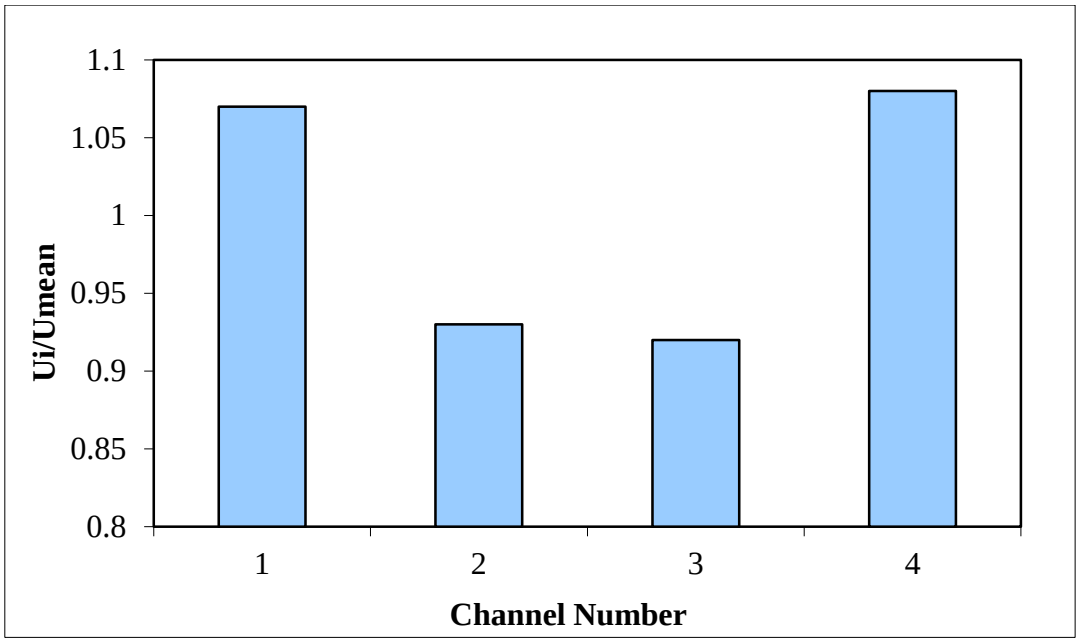

Figure 3. 14 Normalized velocity distribution in geometry A_4 within microchannels at inlet gas flow rate Y_g=354 ml/min.

3.4.1 Effect of the width of inlet and outlet flow distribution chambers

The influence of the width of inlet and outlet flow distribution regions is discussed in this section. Two microplates have been considered, namely A_5 and $A_{6,}$ in which the width of both inlet and outlet flow distribution chambers was 10 mm, in order to study the effects of these modifications on the fluid arrangement within the microchannels. In contrast, all other geometrical parameters have been kept equal to those given in Figure 3.1 and 3.2, for plate A_1 and A_2 respectively. As it can seen from Figure 3.15 and 3.16 by decreasing the width of the inlet and outlet chamber the fluid tends to flow on the top and the bottom channels with a higher velocity compared to the middle area of the plate (see normalized velocity distribution within microchannels as well, Figures 3.17 and 3.18). In both plates the velocity distribution becomes much worse than in plates A_1 and A_2, as it was discussed above that the fluid distribution inside the channels was uniform.

Tonomura *et al*. [90] examined the influence of manifold area on flow distribution over microstructured plates by means of CFD-calculations. They considered microplate geometries

with constant inlet and outlet flow distribution chamber widths where water was fed at a uniform inlet velocity of 0.5 m/s. They observed that by doubling both inlet and outlet manifold areas the flow distribution became more uniform, the same trend was shown in the present work (see section 3.4 where the inlet and outlet widths are double).

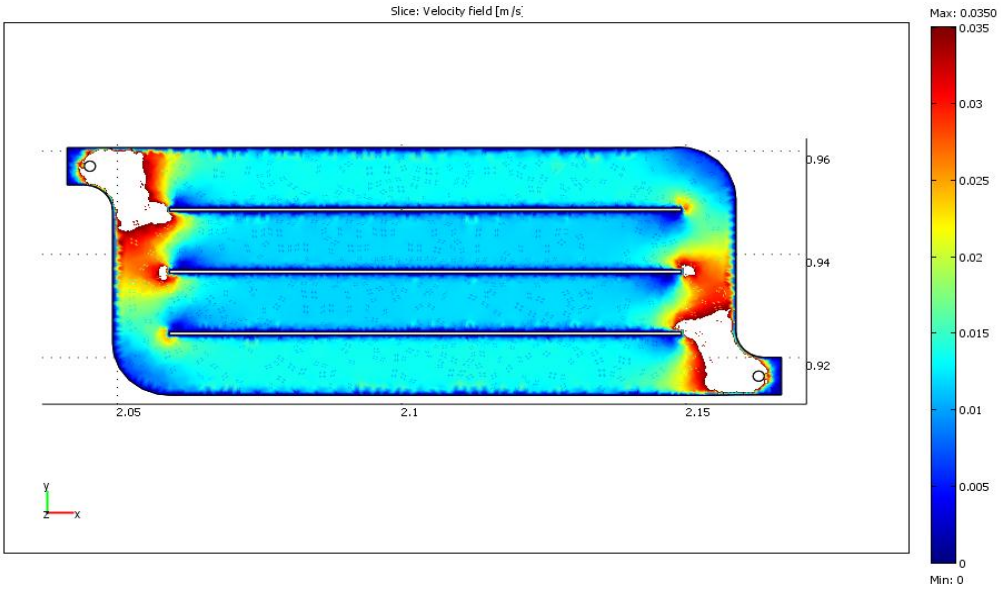

Figure 3. 15 Velocity profile in geometry A_5 in the gas chamber at channel mid-height=425 μm. Inlet gas flowrate Y_g=354 ml/min.

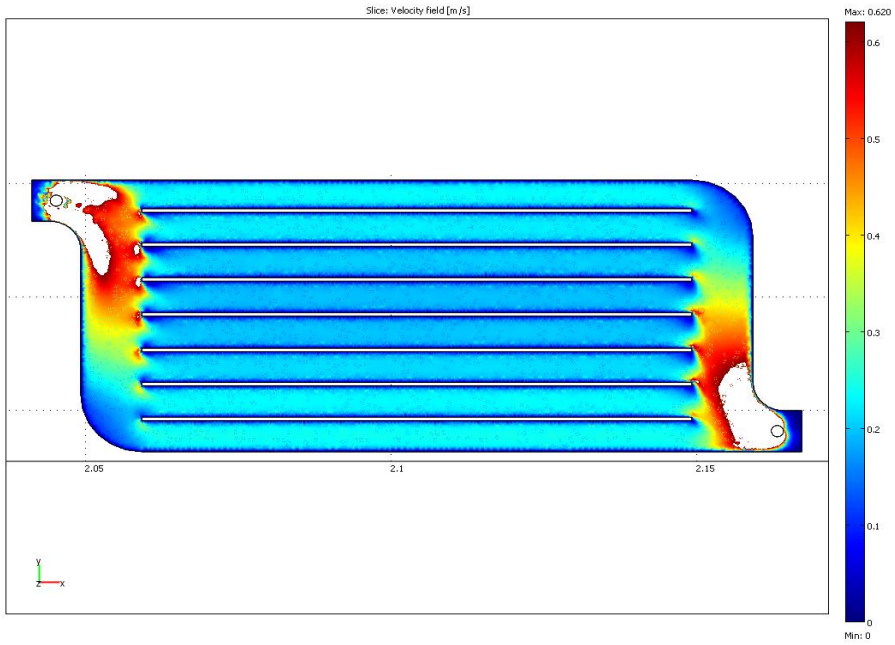

Figure 3. 16 Velocity profile in geometry A_6 in the gas chamber at channel mid-height=425 μm. Inlet gas flowrate Y_g=354 ml/min.

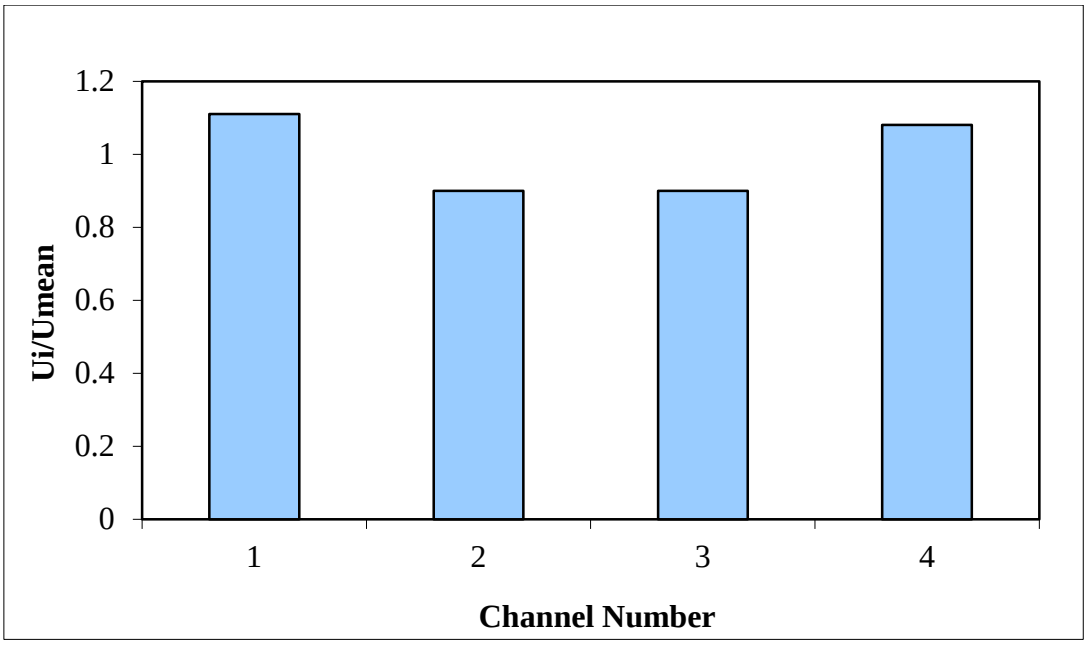

Figure 3. 17 Normalized velocity distribution in geometry A_5 within microchannels at inlet gas flow rate Y_g=354 ml/min.

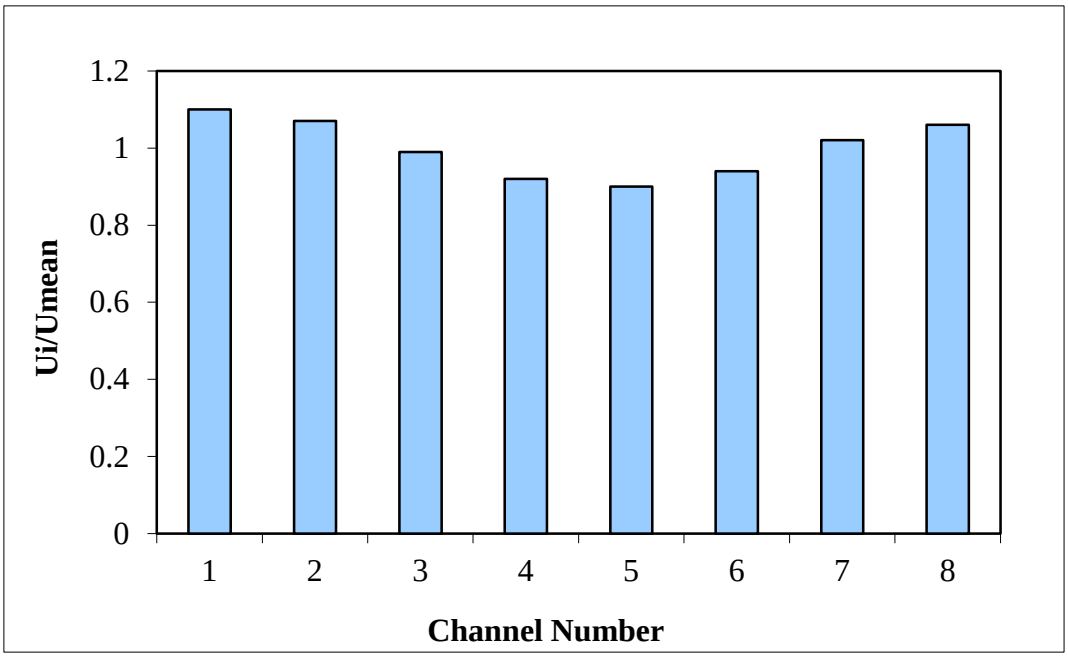

Figure 3. 18 Normalized velocity distribution in geometry A6 withmicrochannels at inlet gas flow rate Yg=354 ml/min.

3.4.2 Effect of the shape of flow distribution chambers

This section examines the effects of different shapes of inlet and outlet flow distribution regions on the flow uniformity through the microchannels. Along these lines two new microplate outlines have been designed, namely B_1 and B_2, shown in Figures 3.19 and 3.20.

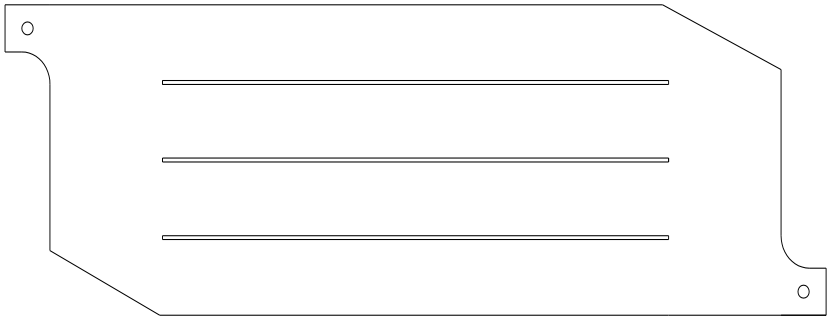

Figure 3. 19 Microplate geometry B_1. The dimensions are 850 μm plate thickness and 90 mm channel length (L_r).

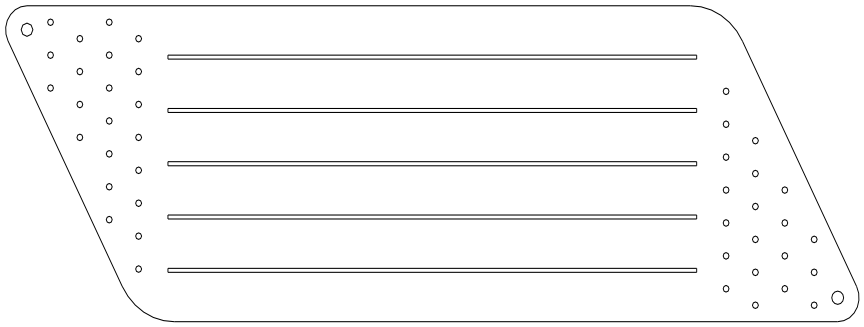

Figure 3. 20 Microplate geometry B_2. The dimensions are 850 μm plate thickness and 90 mm channel length (L_r).

As it can been seen from the Figure 3.21 and Figure 3.22, the shape of the inlet and outlet manifolds is an important factor to take into consideration as it can significantly affect the quality of the flow distribution within the microchannels. As it emerges from these two Figures the uniformity of the fluid flow is very good (see also figures 3.23 and 3.24 for normalized average velocities) and in addition fluid bypass was managed to be eliminated. Furthermore Figure 3.22 shows that by increasing the profile angle at the sides of the plate

more than the plate B_1 fluid bypassing can be eliminated completely. Tonomura *et al*. [86] in their work trimmed away 25% of the corners of their initial design in order to eliminate the dead volumes of the corners.

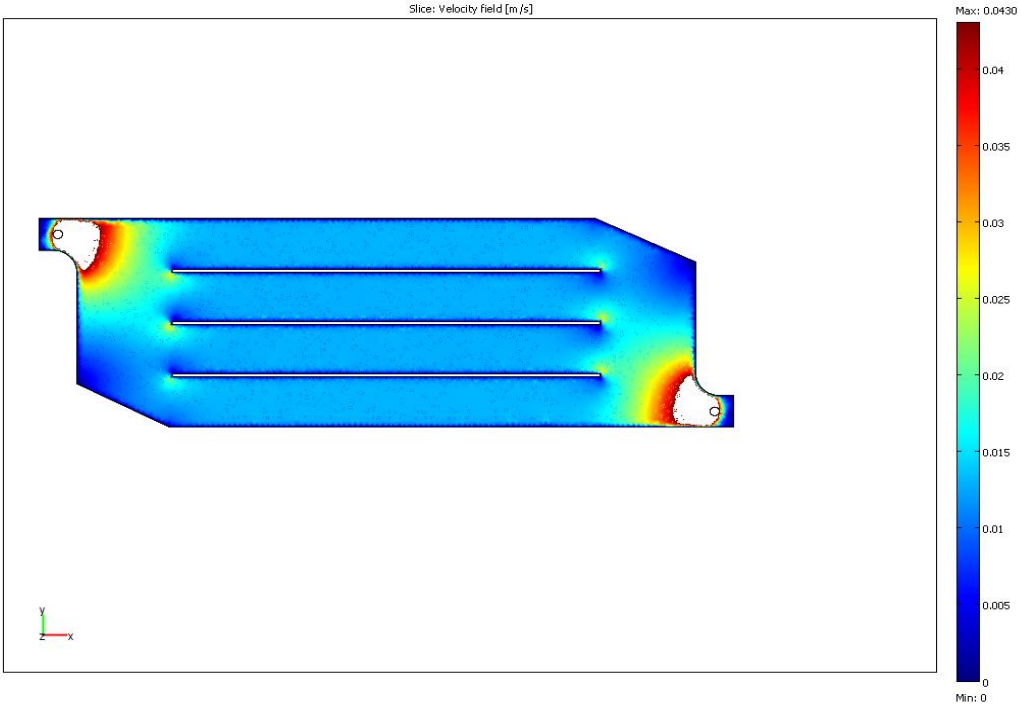

Figure 3. 21 Velocity profile in geometry B_1 in the gas chamber at channel mid-height=425 μm. Inlet gas flowrate Y_g=354 ml/min.

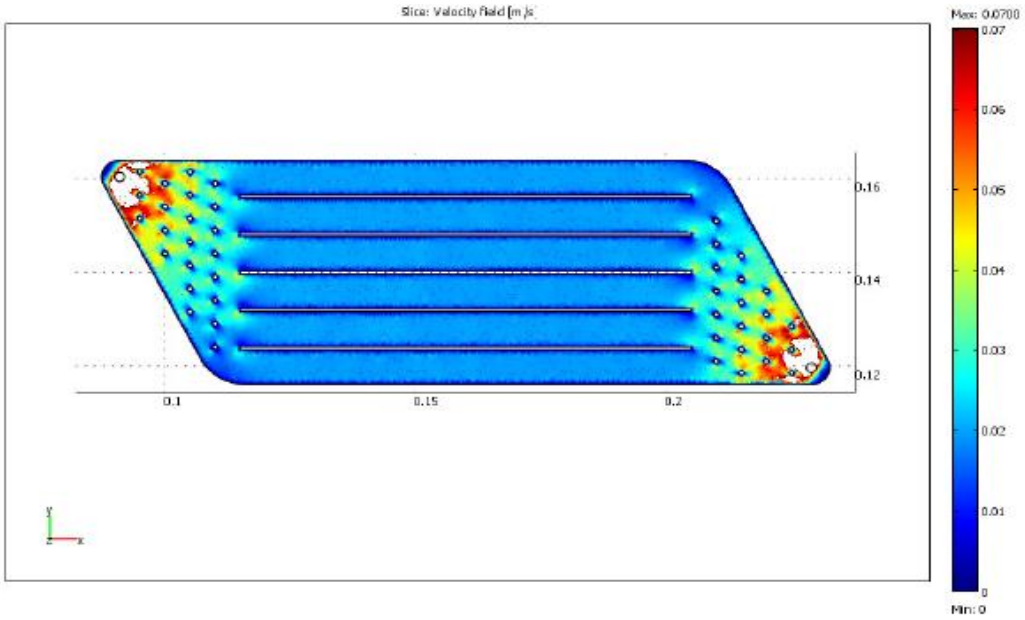

Figure 3. 22 Velocity profile in geometry B_2 in the gas chamber at channel mid- height=425 μm. Inlet gas flow rate Y_g=354 ml/min.

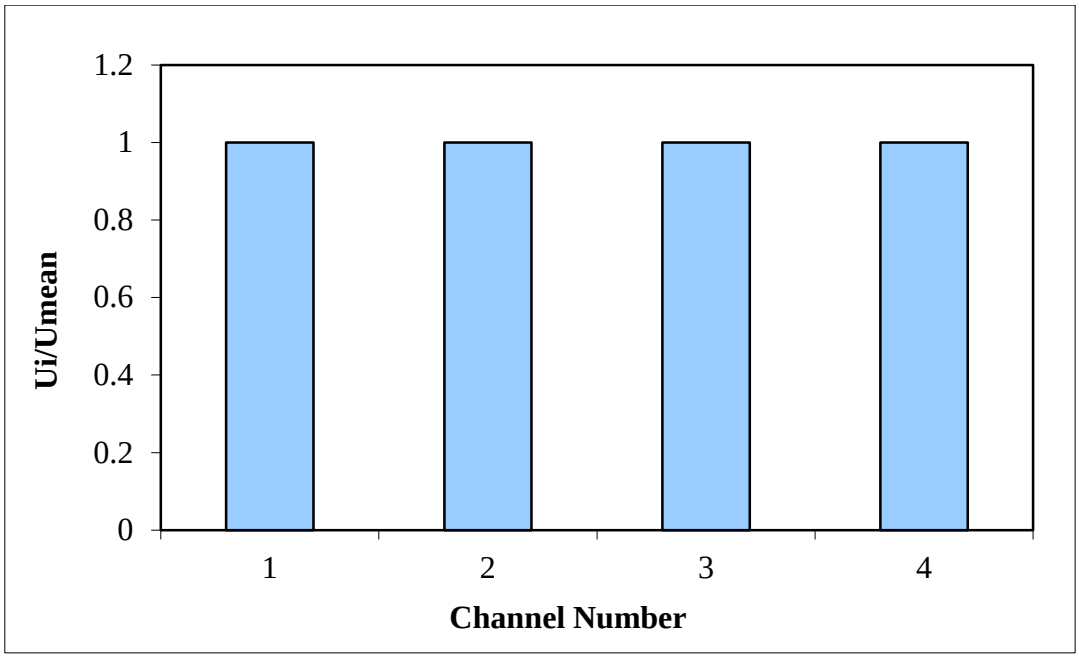

Figure 3. 23 Normalized velocity distribution in geometry B_1 within microchannels at inlet gas flow rate Y_g=354 ml/min.

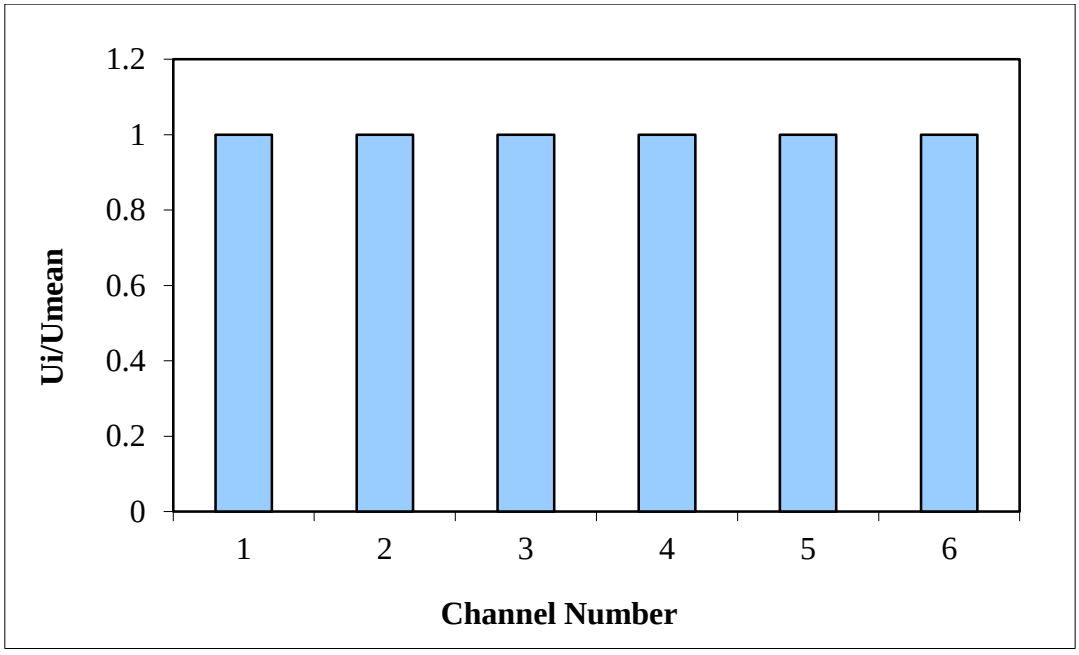

Figure 3. 24 Normalized velocity distribution in geometry B_2 within microchannels at inlet gas flow rate Y_g=354 ml/min. Re=20.

3.4.3 Effect of the number of channels on the flow distribution

A preliminary investigation was carried out on a microplate without channels, so that the role of these on the uniformity of the fluid flow distribution over the plate can be examined. For this purpose the geometry of the microplate B_2 was used in simulations, except that no channels have been employed for B_2, so that the fluid is not constrained in any way and is free to flow over the whole microplate.

It is clear from Figure 3.25 that fluid bypass exists, which causes the two zones highlighted to show very low fluid velocities compared to the central part of the plate.

This means that the fluid tends to cover the middle area of the plate with higher velocity compared to that in the stagnation regions. As a result, a particularly uneven flow distribution emerges over the plate, hence leading to worsening in the performances of the plate. This analysis shows that is important to use channels when the fluid must be distributed over the microplate with uniform velocity. Griffini and Gavriilidis [91] showed that the flow distribution improves by including fins in the plate to guide the flow. Their simulations in a blank microreactor showed that fluid by-pass existed.

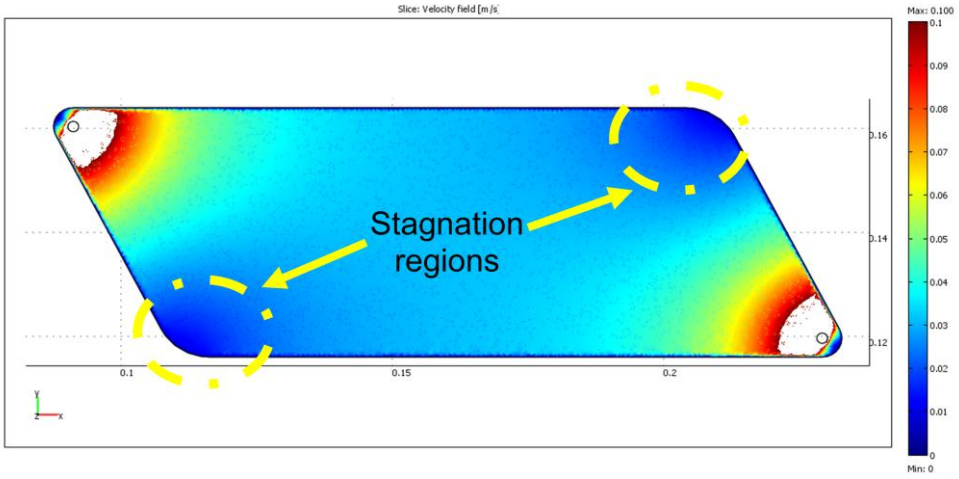

Figure 3. 25 Velocity profile in geometry B_2 in the gas chamber at channel mid-height=425 μm. Inlet gas flowrate Y_g=354 ml/min.

3.4.4 Flow distribution in the microplate when the fluid is liquid

Similar simulations were performed for the liquid chamber, where channel height was 200 μm and maximum liquid flowrate was 2.56 ml/min (Re=1.3).

The geometries of the microplates A_1 and A_2 were used in our simulations to investigate the uniformity of the fluid flow distribution over the plate when liquid (2M NaOH) was used. It can be seen from Figures 3.26 and 3.27 that the uniformity of the liquid flow is the same with the gas flow (examined in section 2.3.4) and the maximum difference between average velocities was found to be <0.1% as it was found for gas fluid. In addition simulations were performed for the minimum liquid flowrate used in the experiments (Y_{liquid}=1.28 ml/min). Maximum difference between average velocities was found to be <0.1% as well (see figures 3.28 and 3.29 for normalized average velocities).

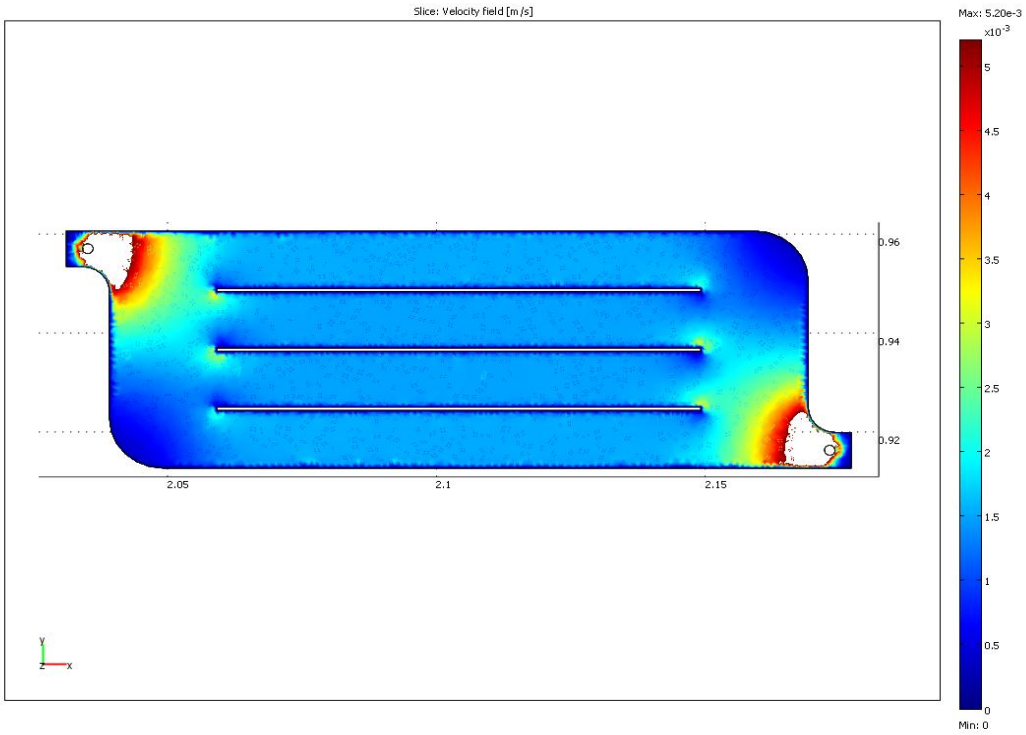

Figure 3. 26 Velocity profile in geometry A_1 in the liquid chamber at channel mid-height=100 μm. Inlet liquid flowrate Y_l=2.56 ml/min.

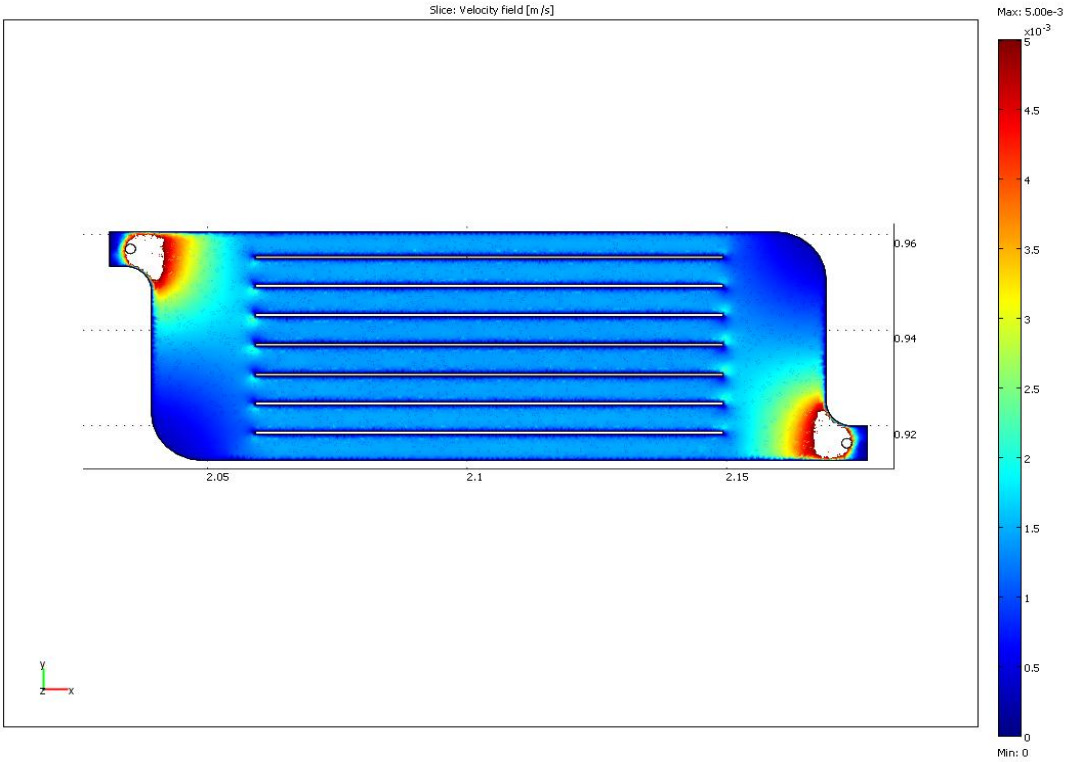

Figure 3. 27 Velocity profile in geometry A_2 in the liquid chamber at channel mid-height=100 μm. Liquid flowrate Y_l=2.56 ml/min.

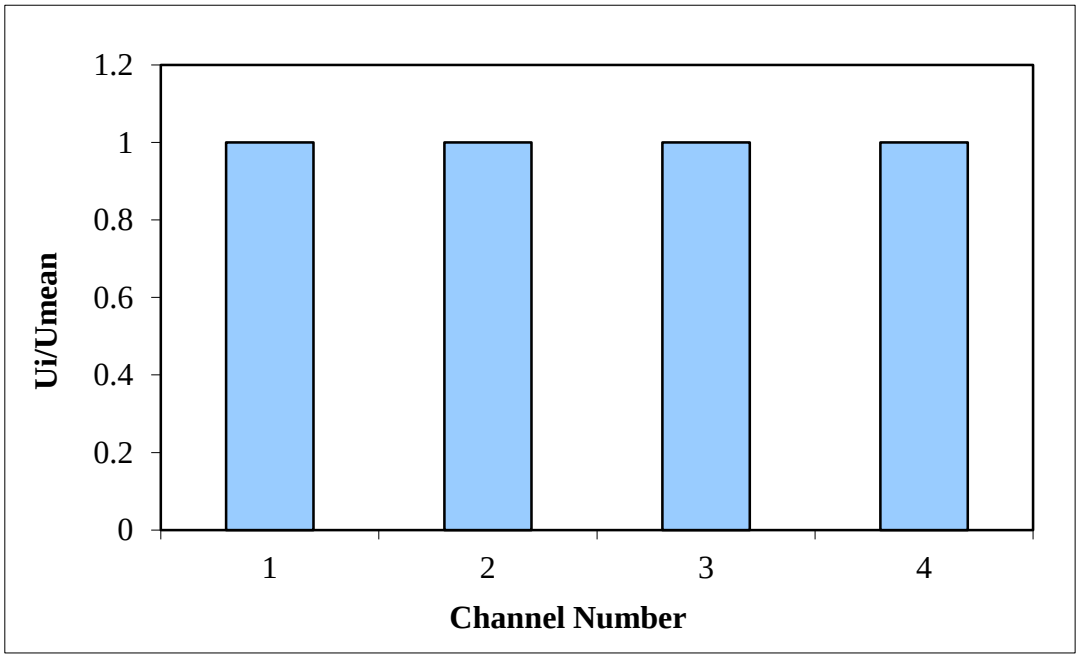

Figure 3. 28 Normalized velocity distribution in geometry A_1 within microchannels at inlet liquid flow rate Y_l=2.56 ml/min.

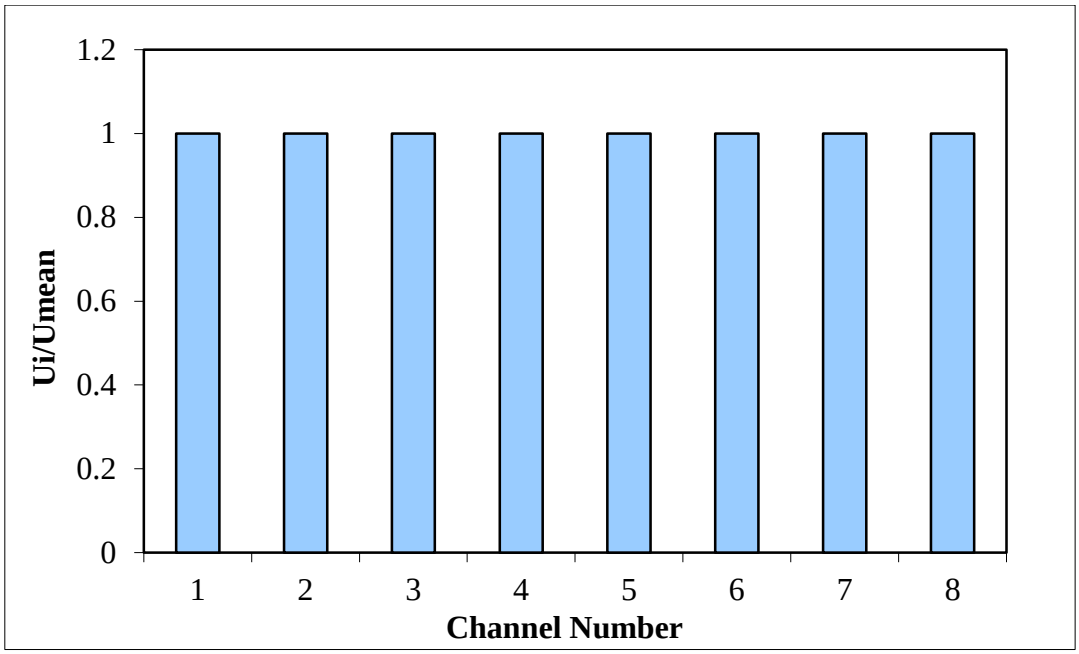

Figure 3. 29 Normalized velocity distribution in geometry A_2 within microchannels at inlet liquid flow rate Y_l=2.56 ml/min.

3.5 Conclusions

The distribution of fluids has been calculated using 3D CFD models in order to develop a design which allows the flow distribution to be as uniform as possible over the plate, by changing the geometrical parameters of the microplate.

A preliminary investigation was carried out on a microplate without channels and the calculations have revealed that fluid bypass exists, leading to the formation of two stagnation regions (figure 3.25) with very low fluid velocities compared to the central part of the plate. As a result, a particularly uneven flow distribution emerges over the plate, hence leading to worsening in the performances of the plate.

As a result, the use of channels over the microplate appears to be crucial when the fluid must be distributed over the microplate with uniform velocity, so that fluid bypass can be avoided and even distribution of flow achieved.

Then by taking the original plates A_1 and A_2 as a starting point, geometrical parameters such as: width of inlet and outlet flow distribution regions, different shapes of inlet and outlet flow

distribution regions, shifting the channels in parallel, have been varied in turn and the results of the simulations have been presented in terms of fluid bypass and the uniformity of the fluid flow into the channels area.

It has been shown by decreasing the width (plates A_4, A_5) of the inlet and outlet chamber the fluid tends to cover the top and the bottom channels with a higher velocity compared to the middle area of the plate. In both plates the velocity distribution becomes much worse than in plates A_1 and A_2, where the fluid distribution inside the channels was found to be uniform.

Furthermore, the shape of the flow distribution chambers was investigated and the results showed that the shape of the inlet and outlet manifolds is an important factor to take into consideration as it can significantly affect the quality of the flow distribution within the microchannels. As it emerged from Figure 3.21 and Figure 3.22 the uniformity of the fluid flow is perfect and in addition we managed to eliminate the fluid bypass. In addition Figure 3.22 shows that by increasing the profile angle at the sides of the plate more than the plate B_1 fluid bypassing can be eliminated completely.

It can be finally concluded that the best results were obtained by using plate B_2, but for reasons that they will be explained in the next chapter plate A_2 was chosen for the micromesh contactor.

CHAPTER 4

CO_2 ABSORPTION IN METALLIC MESH REACTOR USING AQUEOUS SOLUTION OF NaOH

4.1 Introduction

In recent years, chemical engineers have been able to create devices with the help of microfabrication principles that open a new way of performing traditional chemistry. A microreactor has traditionally mean a small tubular reactor for testing catalytic performance, but with the widening use of microfabrication technologies it is now used to designate a reactor built with techniques used for electronic circuits [92]. The main advantages of microreactors are that due to its large surface to volume ratio, mass and heat transfer are intensified, this allows achieving isothermal conditions very easily resulting in greater conversions and selectivities than in conventional reactors [93]. Carbon dioxide capture followed by sequestration, is one of the solutions being explored at international level, to achieve the necessary deep reductions in greenhouse gas emissions.

In this Chapter, CO_2 absorption in sodium hydroxide solution was conducted in a metal microstructured mesh reactor. Breakthrough was investigated first in the microreactor in order to establish the operation pressure difference between gas and liquid phase. Carbon dioxide absorption in sodium hydroxide solution was then conducted in the metal mesh microreactor in order to evaluate, understand and improve its performance. For this reason, various

conditions such as gas and liquid flowrates, gas film thickness, mesh open area, type of the flow and gas residence time were investigated.

4.2 Reactor design and experimental conditions

The reactor was conceived by examining previous designs and attempting to improve on the previous drawbacks. One of the problems in the past designs (see figure 4.1) was the blockage of the inlet/outlet posts by the membrane (membrane sag) when we were tightening the two plates together in order to get the appropriate sealing. To eliminate the blockage problem supporting posts were incorporated in the inlet/outlet locations creating a support structure for the membrane (see figure 4.1). Another improvement was achieved in sealing by changing the plate profile from plate B_2 (see figure 3.20) to plate A_2 (see figure 4.2). With design A_2 where the sides of the plates are nearly vertical, the gasket material was more firmly supported and compressed, providing better sealing, whereas with design B_2 the gasket is not supported/compressed as fully by the upper and lower plates, allowing liquid to migrate between the gasket and the plate, resulting to stagnant liquid regions in the gasket areas (see figure 4.1). The final version of the mesh microreactor is shown in Figure 4.1.

The reactor used in this work comprises of a microstructured mesh placed between two 18 mm thick acrylic plates (S.I.M, UK), containing inlet and outlet ports for the fluids. Channels are machined in the acrylic plates with 0.85 mm and 0.2 mm depth forming the areas where gas and liquid flow respectively. The reactor measures 192 mm x 97 mm (see figure 4.1). Two viton gaskets 0.5 mm thick (Altec, UK) are placed in 0.4 mm deep grooves machined (using miiling machine SM 1500, UK) in the acrylic plates to provide the sealing. The mesh is made from nickel by electroforming (Tecan, UK). It is 25 μm thick and contains holes 25 μm diameter in a hexagonal pore arrangement (see figure 4.2a). The pores are concentrated in eight rectangular areas separated by seven bars and correspond to the eight channels of the acrylic plates. The porous area of the mesh is 43.8 mm x 90 mm (figure 4.1) with an open area of 15% and defines the reaction area between the two fluids. To investigate the effect of the open area on CO_2 removal two other nickel meshes were used, also with 25 μm thickness. One with slit-type pores (25 μm x 75 μm), and an open area of 25% (see figure 4.2b) and the other one with square pores (35 μm x 35 μm) and an open area of 20% (see figure 4.2c). It

was necessary to include supports in the acrylic plates to prevent the mesh buckling, which is a consequence of its large surface area. Seven supporting bars were designed with 0.6 mm width and with a distance of 5.48 mm from each other. In addition 36 posts were incorporated in the entrance and outlet regions of the acrylic plates (see figure 4.1). Two pin holes were employed in both plates and mesh for alignment, while 16 screws were used for clamping all components together. A picture of the assembled reactor and a schematic of all components of the reactor are shown in Figure 4.1. In order to investigate the influence of the gas film thickness on CO_2 removal an additional stainless steel gasket (0.1 mm) thick, and an additional viton gasket were used to increase the gas flow channel depth from 0.85 mm to 1.45 mm.

(a)

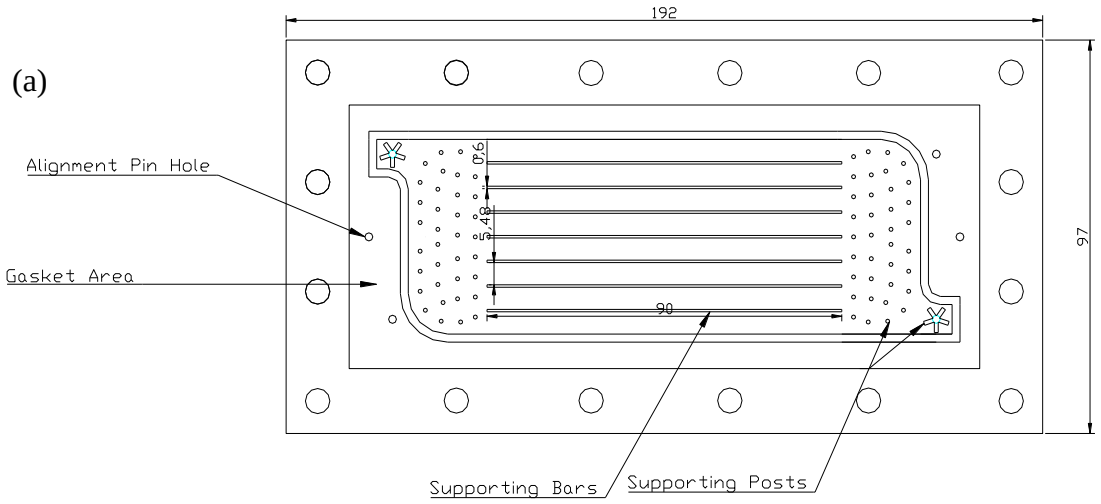

(b)

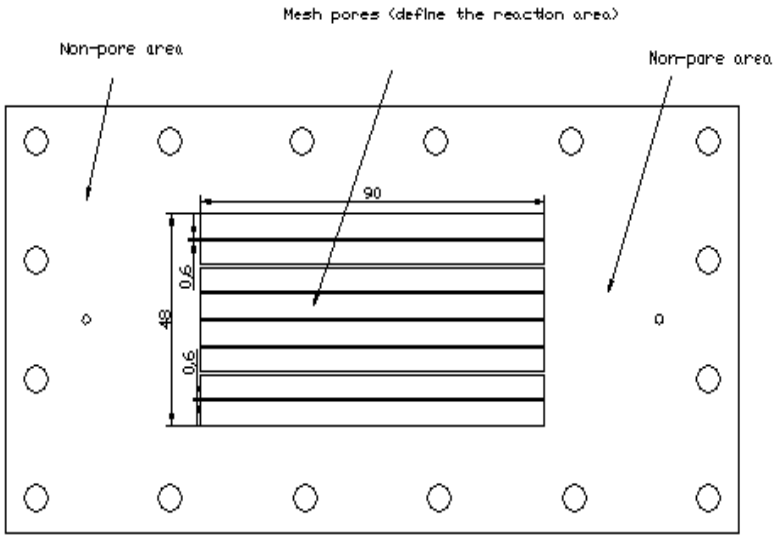

(c)

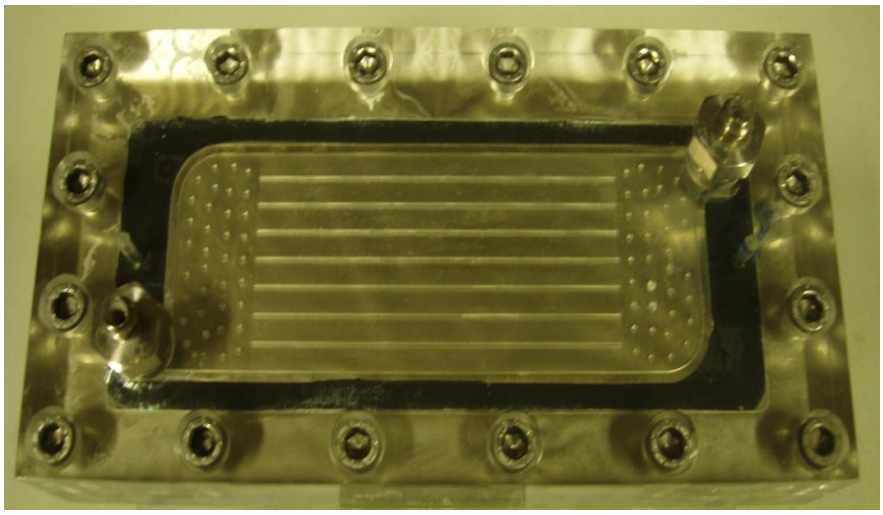

(d)

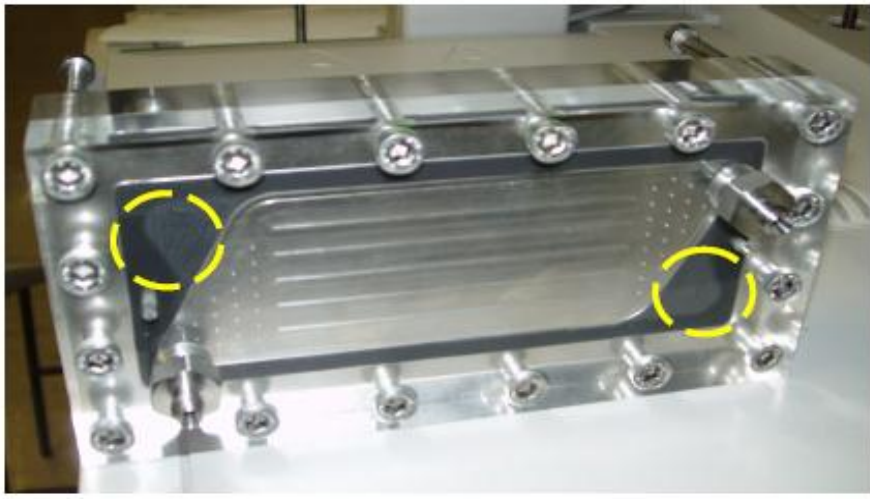

(e)

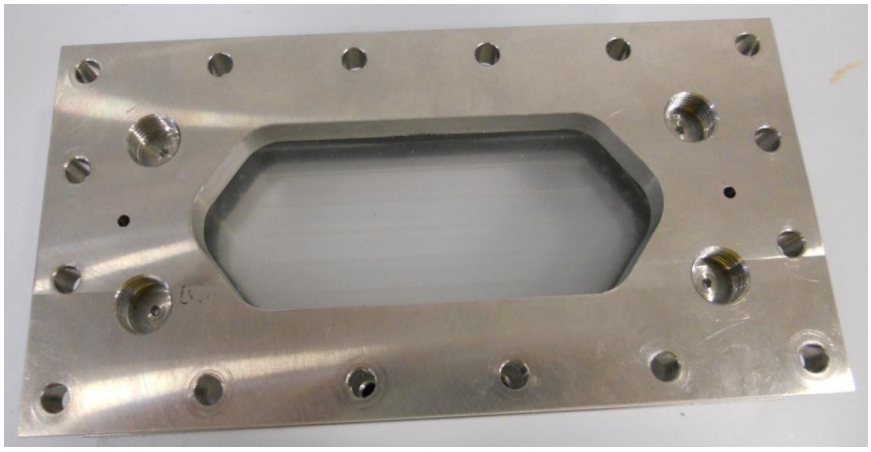

(f)

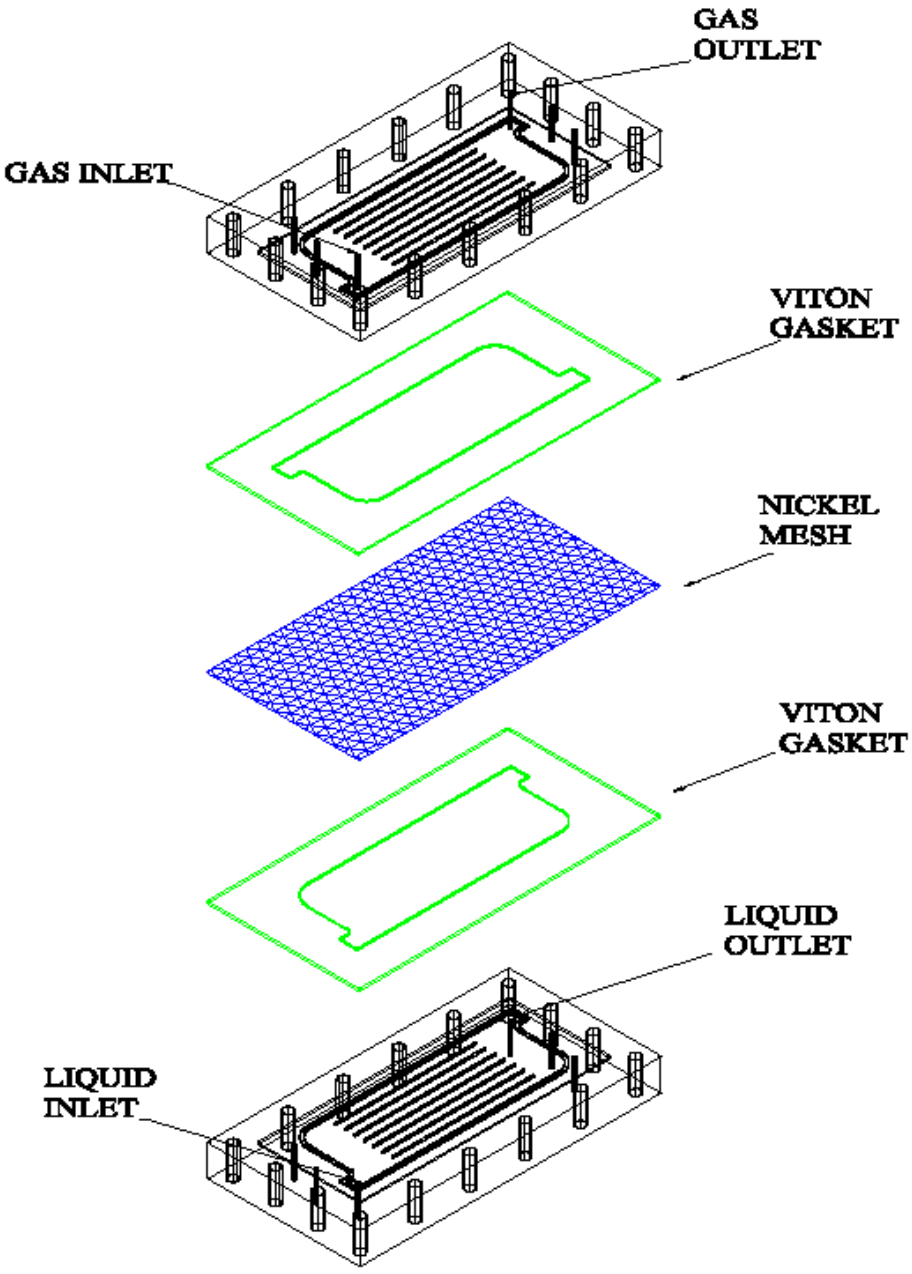

Figure 4. 1 Mesh microstructured reactor: (a) Schematic of acrylic plate (b) Schematic of mesh, (c) Picture of assembled device (d) Picture of assembled device based on plate B_2 (e) Picture of the assembled device of the preliminary design. (f) Exploded schematic view of the reactor. Dimensions are in mm.

(a)

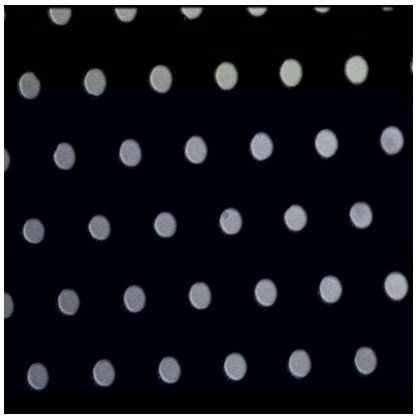

(b)

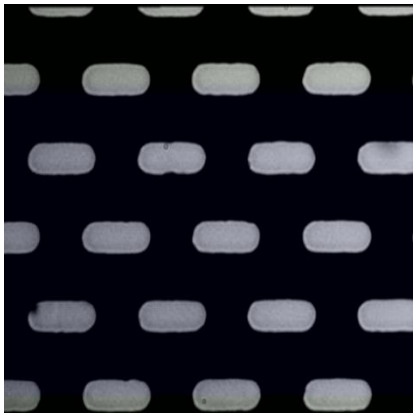

(c)

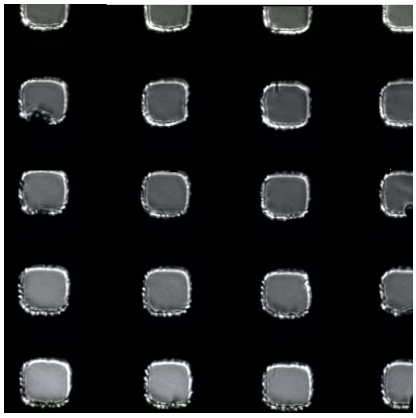

Figure 4. 2 Microscope images of the microstructured meshes: (a) Pore diameter=25 µm, open area=15%, thickness=25 µm (b) Pore 25 µm x 75 µm, open area=25%, thickness=25 µm (c) Pore 35 µm x 35 µm , open area=20%, thickness 25 µm.

A schematic of the experimental set up for CO_2 absorption is shown in Figure 4.3. An HPLC pump (Waters 5100) was used to drive the liquid 2M NaOH in the bottom chamber of the reactor, while the gas 20vol% CO_2/N_2 was controlled by a mass flow controller (Brooks 5850) and flowed above the mesh. The differential pressure between the two phases was controlled by a metering valve (Swagelok) at the outlet of the liquid phase. The gas phase pressure and liquid phase pressures were measured by pressure sensors (Honeywell; pressure range 0-15psi, power supply; Traco 5V, use of the Labview program running by computer for pressure readings). The outlet of the gas phase passed through a liquid trap to avoid any liquid getting into the gas chromatograph (GC) in case of breakthrough of the liquid in the gas phase, and then connected to a GC (Shimadzu GC-14B) for carbon dioxide concentration determination. Experimental data were obtained varying the liquid flow rate in the range 1.28-2.56 ml/min and gas flowrate in the range 177-354 ml/min. These flowrates resulted to residence times, based on the gas/liquid volumes in contact with the perforated mesh area, 0.56-1.12 s for the gas and 18-36 s for the liquid respectively. All the experiments were carried out at room temperature (approximately 20^{o}C). Based on carbon balance below:

$$F_{in} - F_{out} - X_{CO_2} F_{in} = 0 \quad (4.1)$$

The CO_2 removal efficiency was calculated from:

$$X_{CO_2} = 1 - \frac{F_{CO_2 out}}{F_{CO_2 in}} \quad (4.2)$$

where F is the molar flowrate of CO_2. The experimental error in CO_2 removal was assessed to be ± 5%. Two to three chromatographs were taken for each measurement and the deviation between them was about ± 5%.

In addition a preliminary investigation of the mesh microreactor manufactured by CRL (Central Research Laboratories) for CO_2 absorption was performed. The CRL microreactor consists of the mesh in an enclosure formed from glass and copper. Figure 2.2 (Chapter 2) shows a diagrammatic cross-section of the reactor detailing the reactor regions, and the assembled device, while Figure 2.3 shows a photograph of a nickel mesh utilized in the CRL microreactor. More details about CRL microreactor are described in section 4.5.7. The experimental set-up used for CRL microreactor, is the same to the one described previously for the metallic mesh microstructured reactor (see figure 4.3), except that the gas phase pressure and the liquid phase pressures were measured by a manometer.

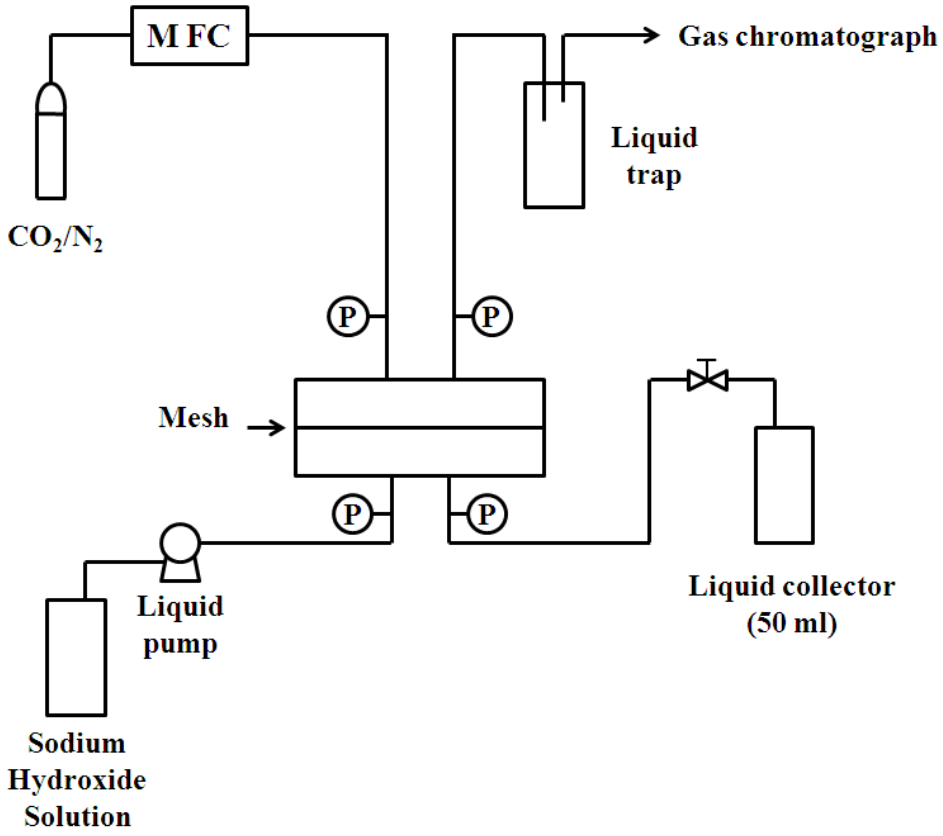

Figure 4. 3 Schematic diagram of the experimental set-up used in this work. P indicates pressure sensor. Experiments were carried out at room temperature (approximately 20^0C).

4.3 Mathematical Model Development

A two-dimensional model of the microstructured mesh reactor was formulated and the following assumptions were made: (1) The system is at steady state (system was allowed to reach steady state conditions, no change of pressure, temperature with time). (2) Ideal gas behavior is valid for the gas phase. (3) Henry's Law is applicable (Henry's law is applied to connect CO_2 interfacial concentrations in the liquid and gas phase). (4) Plug flow profiles are assumed in the gas and liquid phases. (5) Mesh pores are completely filled by the liquid (NaOH solution wets the hydrophilic mesh), so that the gas-liquid interface is situated at the same location as the mesh-gas interface. (6) Pressure drop along the reactor is neglected (pressure drop for gas and liquid phase was found experimentally and it was trivial see Figure 4.6). The reactor model is divided in three main domains: the gas phase, the mesh, and the liquid phase (figure 4.4). The differential mass balances to describe the concentration profiles

of components in the three domains are given below, and they were solved with COMSOL 3.a.

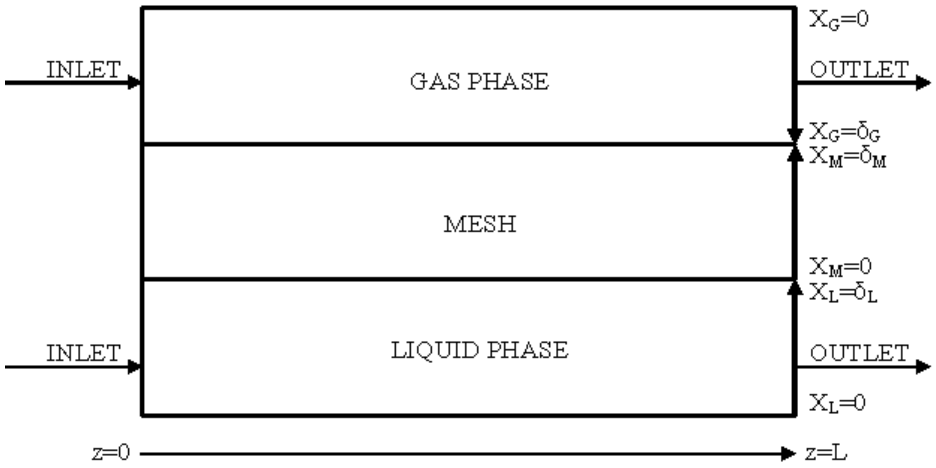

Figure 4. 4 Mathematical model domains with coordinates and boundaries.

Mass balances in the liquid phase:

The differential mass balances of components in the liquid phase along with the associated boundary conditions are [35]:

$$u_L \frac{\vartheta}{\vartheta z} C^L_{CO_2} = D^L_{CO_2}\left(\frac{\partial^2 C^L_{CO_2}}{\partial z^2} + \frac{\partial^2 C^L_{CO_2}}{\partial x_L^2}\right) + R_{CO_2} \tag{4.3}$$

$$u_L \frac{\vartheta}{\vartheta z} C^L_{NaOH} = D^L_{NaOH}\left(\frac{\partial^2 C^L_{NaOH}}{\partial z^2} + \frac{\partial^2 C^L_{NaOH}}{\partial x_L^2}\right) + R_{NaOH} \tag{4.4}$$

where R is the reaction rate, D is the diffusion coefficient, c is the concentration, and u the velocity.

at z=0, $$C^L_{CO_2} = 0, C^L_{NaOH} = C_{NaOH,initial} \tag{4.5}$$

at z = L, $$\frac{\vartheta C_{CO_2}}{\vartheta z} = 0 \ , \frac{\vartheta C_{NaOH}}{\vartheta z} = 0 \tag{4.6}$$

at $x_L=\delta_L$ $$C^L_{CO_2} = C^M_{CO_2}, D^L_{CO_2} \frac{\vartheta C^L_{CO_2}}{\vartheta x_L} = D^M_{CO_2} \frac{\vartheta C^M_{CO_2}}{\vartheta x_M} \tag{4.7}$$

$$C^{L}_{NaOH} = C^{M}_{NaOH} \qquad D^{L}_{NaOH}\frac{\vartheta C^{L}_{NaOH}}{\vartheta x_L} = D^{M}_{NaOH}\frac{\vartheta C^{M}_{NaOH}}{\vartheta x_M},$$

$$\text{at } x_L = 0, \qquad \frac{\vartheta C_{NaOH}}{\vartheta x_L} = 0, \ \frac{\vartheta C_{CO_2}}{\vartheta x_L} = 0 \tag{4.8}$$

Mass balances in the mesh:

The differential mass balances of components in the mesh, along with the associated boundary conditions are:

$$D^{M}_{CO_2}\frac{\vartheta^2 C^{M}_{CO_2}}{\vartheta x^2_M} + R_{CO_2} = 0 \tag{4.9}$$

$$D^{M}_{NaOH}\frac{\vartheta^2 C^{M}_{NaOH}}{\vartheta x^2_M} + R_{NaOH} = 0 \tag{4.10}$$

$$\text{at } x_M = 0, \ C^{M}_{CO_2} = C^{L}_{CO_2}, \ D^{M}_{CO_2}\frac{\vartheta C^{M}_{CO_2}}{\vartheta x_M} = D^{L}_{CO_2}\frac{\vartheta C^{L}_{CO_2}}{\vartheta x_L}$$

$$C^{M}_{NaOH} = C^{L}_{NaOH}, \ D^{M}_{NaOH}\frac{\vartheta C^{M}_{NaOH}}{\vartheta x_M} = D^{L}_{NaOH}\frac{\vartheta C^{L}_{NaOH}}{\vartheta x_L} \tag{4.11}$$

$$\text{at } x_M = \delta_M, \ C^{M}_{CO_2} = mC^{G}_{CO_2}, \ D^{M}_{CO_2}\frac{\vartheta C^{M}_{CO_2}}{\vartheta x_M} = D^{G}_{CO_2}\frac{\vartheta C^{G}_{CO_2}}{\vartheta x_G}, \ \frac{\vartheta C_{NaOH}}{\vartheta x_M} = 0 \tag{4.12}$$

where m is dimensionless Henry's law constant.

Mass balances in the gas phase:

The differential mass balances in the gas phase, along with the associated boundary conditions are:

$$u_G\frac{\vartheta}{\vartheta z}C^{G}_{CO_2} = D^{G}_{CO_2}\left(\frac{\vartheta^2 C^{G}_{CO_2}}{\vartheta z^2} + \frac{\vartheta^2 C^{G}_{CO_2}}{\vartheta x^2_G}\right) \tag{4.13}$$

$$\text{at } x_G = 0 \quad => \frac{\vartheta C_{CO_2}}{\vartheta x_G} = 0 \tag{4.14}$$

$$\text{at } x_G = \delta_G, \quad mC^G_{CO_2} = C^M_{CO_2} \quad , \quad D^G_{CO_2} \frac{\vartheta C^G_{CO_2}}{\vartheta x_G} = D^M_{CO_2} \frac{\vartheta C^M_{CO_2}}{\vartheta x_M} \tag{4.15}$$

$$\text{at z = L,} \quad \frac{\vartheta C^M_{CO_2}}{\vartheta z} = 0 \tag{4.16}$$

$$\text{at z=0,} \quad C^G_{CO_2} = C_{CO_2,\text{initial}} \tag{4.17}$$

Two variations of the model were implemented. The first one, called “segregated model”, where the solid part of the perforated area is neglected and the open area of the mesh is utilised to modify the effective length of the reactor, i.e. the reactor length in this case is “εL”, and the second one, called “pseudo-homogeneous model”, where the mesh is considered as a homogeneous medium with diffusivities “εD”. The solution was checked from 109219 to 227947 number of Degrees of Freedom, and no significant variation in the results could be detected indicating that the solution was mesh independent.

4.4 Reaction System

The reaction system considered refers to the absorption of CO_2 from a 20vol% CO_2/N_2 mixture within a solution of 2M NaOH. Three steps occur during the absorption of CO_2 into aqueous hydroxide solutions (Pohorecki and Moniuk) [94]:

$$CO_{2(g)} \leftrightarrow CO_{2(l)} \tag{4.18}$$

$$CO_{2(l)} + OH^- \rightarrow HCO_3^- \tag{4.19}$$

$$HCO_3^- + OH^- \leftrightarrow CO_3^{2-} + H_2O \tag{4.20}$$

The overall reaction can be written as:

$$2NaOH + CO_2 \rightarrow Na_2CO_3 + H_2O \tag{4.21}$$

The rate of reaction (4.19) is significantly slower than reaction (4.20), and hence it governs the overall rate of absorption:

$$R_{CO_2} = -kC_{CO_2}C_{NaOH} \quad (4.22)$$

$$R_{NaOH} = -2kC_{CO_2}C_{NaOH} \quad (4.23)$$

All the parameters used in the calculations were taken from previous CO_2/NaOH studies and are reported in table 4.1.

Table 4. 1 Values of parameters used in the simulations for T=20^0C.

Parameter	Value	Reference
$D^G_{CO_2}$ (m^2/s)	$1.64x10^{-5}$	Cussler [95]
$D^L_{CO_2}$ (m^2/s)	$2.35x10^{-6}\exp(-2119/T)$	Versteeg and Van Swaaij [96]
D^L_{NaOH} (m^2/s)	$1.67 \times D^L_{CO_2}$	Nijsing *et al.* [97]
m (dimensionless)	0.8314	Zanfir *et al*. [10]
k (m^3/mol s)	$10^{(11.916-2382/T)}$	Pohorecki and Moniuk [94]

4.5 Results and Discussion

4.5.1 Phase Breakthrough

Breakthrough was investigated in order to establish the acceptable operational pressure difference between gas and liquid which keeps the two phases separated. If the pressure difference exceeds a critical value, then one phase will break through and disperse into the other phase [1]. Figure 4.5 shows an experiment where liquid from the bottom chamber has entered the gas-phase channel when increasing the liquid phase pressure beyond the

breakthrough pressure. The theoretical breakthrough pressure of NaOH, can be calculated by equation 4.24 which is equation 2.21 based on Amador's work [70]:

$$\Delta P_{B,_{NaOH}} = P_L - P_G = -\frac{2\gamma\cos(0+90)}{r} = 0 \quad (4.24)$$

where γ is the surface tension of NaOH, r the radius of the mesh.

The breakthrough pressure of CO_2/N_2 can be calculated by equation 4.25 which is derived from equation 2.22:

$$\Delta P_{B,_{CO_2/N_2}} = P_G - P_L = -\frac{2\gamma\cos(0)}{r} = \frac{2\gamma}{r} \quad (4.25)$$

Table 4.2 shows a comparison of breakthrough pressure between the experimental results and the prediction from equations (4.24) and (4.25) for different meshes. The theoretical values are higher than the experimental ones. These discrepancies between theoretical and experimental results might be explained by the edge effect (see section 2.5.3.1). In the case of CRL mesh the supports which keep the mesh from bending can cause the edge effect. The supports can decrease the meniscus stability since they are increasing the effective diameter of the meniscus in the membranes pores adjacent to the supports. Similar discrepancies between theoretical and experimental values of breakthrough pressures were observed from Amador [70] when he performed experiments using CRL mesh for water/air system. Amador [70] pointed out that the edge effect or particles resting on the mesh may cause these discrepancies. In addition similar effect of meniscus stability can take place at the edges of the membrane, where gaskets are used for sealing. In all the experiments with nickel membranes, breakthrough of liquid in the gas phase firstly occurred at the locations where the gaskets were in contact with the membrane and at the locations where the membrane were in contact with the supporting bars of the microplate. Furthermore SEM images of the meshes have to be taken in order to ensure that there are no defective pores in the mesh. Breakthrough occurs first on the pore with the largest diameter [98] and hence defective pores can reduce the breakthrough pressure.

Table 4. 2 Breakthrough pressure of different membranes for the NaOH - CO_2/N_2 system.

Membrane	**Breakthrough pressure (G→L) P_G-P_L (cm H_2O)**		**Breakthrough pressure (L→G) P_L-P_G (cm H_2O)**	
	Experiment	**Equation (4.25)**	**Experiment**	**Equation (4.24)**
Nickel Mesh Pore size (35μm)	15-20	85	0-3	0
Nickel Mesh Pore size (25μm)	27-31	118	0-3	0
Nickel Mesh (CRL) Pore size (5μm)	40-44	595	0-3	0

During typical operation (Y_G=354 ml/min, Y_L=2.56 ml/min) in the acrylic mesh microreactor, the pressure drop in the gas phase was 1.6cm H_2O and in the liquid phase was 1.9 cm H_2O. The pressure difference between gas and liquid phase was kept at $(P_G\text{-}P_L)_{inlet}$=30 cm H_2O and $(P_G\text{-}P_L)_{outlet}$=30.2 cm H_2O (see figure 4.6) when the nickel mesh of 25 μm pores diameter was used.

The theoretical values for gas and liquid phase pressure drop were 0.1 cm H_2O and 2.3 cm H_2O respectively, based on the equation below [99]:

$$\Delta P = \frac{12u\mu L}{d^2} \tag{4.26}$$

where u is the velocity, d is the hydrolic diameter, μ is the viscosity and L is the length of the channel.

The discrepancy between the theoretical and experimental value for the gas phase pressure drop, might be due to the fact that the equation does not count for the pressure drop along the fittings of inlet/outlet, while the pressure sensors used in the experiments measured the pressure drop along the fittings of inlet/outlet (see figure 4.7). Also blockage of the outlet of the gas phase due to the deposition of sodium carbonate (product of the reaction between $CO_2 + NaOH \rightarrow Na_2CO_3$, which was observed in the outlet of the gas phase during the experiment) could increase the pressure drop along the gas phase and cause the discrepancy.

In addition fluctuations of flowrates, which was caused by the mass flow controller, might cause this deviation.

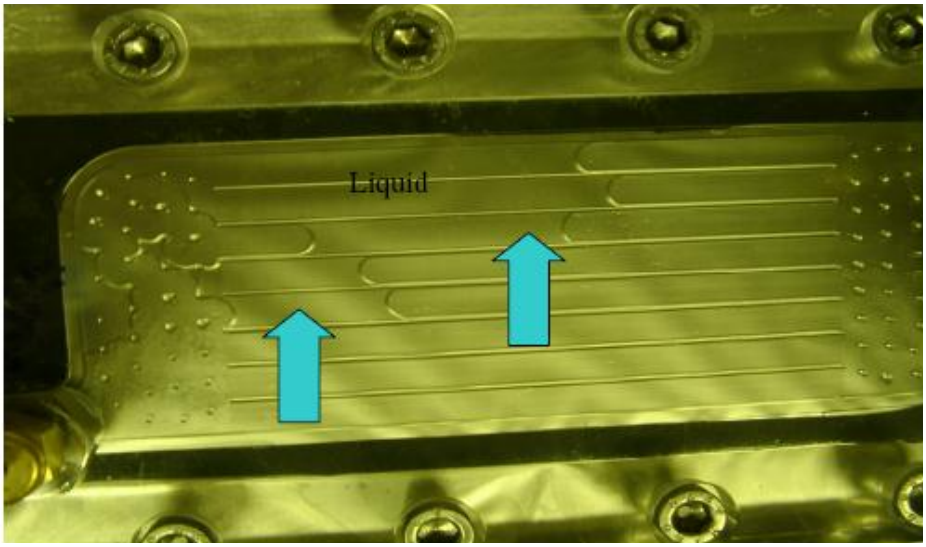

Figure 4. 5 Picture of the top (gas) side of the reactor, during a breakthrough experiment. The arrows indicate breakthrough of the liquid into the gas phase.

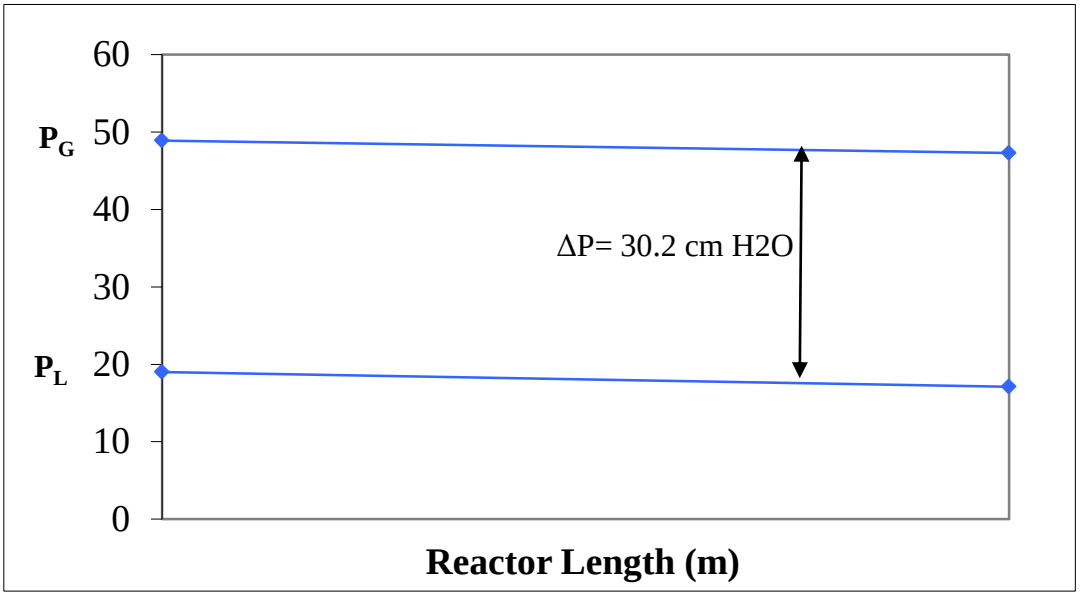

Figure 4.6 Pressure profile in gas liquid phases in (a) co-current operation membrane contactor.

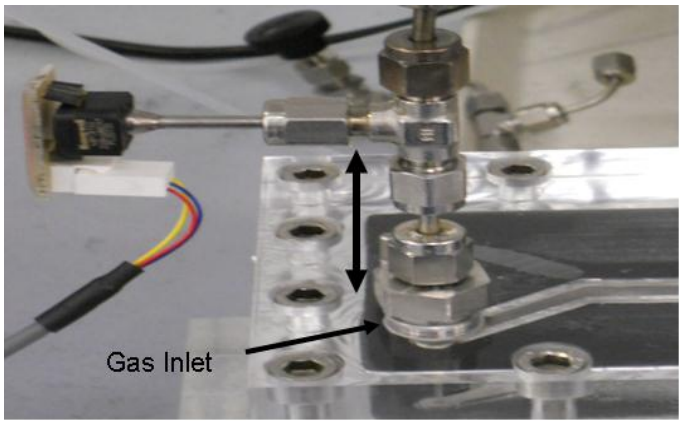

Figure 4.7 Picture of a part of the top (gas) side of the reactor, showing the distance of the pressure sensor from the inlet of the reactor.

4.5.2 Model prediction for CO_2 absorption in NaOH solution

The predictions of the segregated model and pseudo-homogeneous model are compared with experimental results, obtained from carbon dioxide absorption in sodium hydroxide solution. The pseudo-homogeneous model has been used by various investigators for the modelling of membrane contactors [100, 101]. However, as shown in Figure 4.8 this model shows significant deviation from the experimental results. The segregated model shows a much better agreement with the experimental results. 18-30% of the carbon dioxide contained in the inlet stream was removed within 0.5-1.2 s experimental gas residence time.

These results are comparable with similar research where CO_2 absorption was investigated in microchannel separated-flow contactors. In a falling film microreactor, 69% of CO_2 from a 26vol% CO_2 stream was absorbed in ca. 11 s gas residence time, using 2M NaOH [10]. In that case, the liquid film and gas film thickness were 100 μm and 5.5 mm respectively, and the inlet molar ratio CO_2:NaOH was 0.4, while in our work the inlet molar ratio CO_2:NaOH is 0.6. TeGrotenhuis *et al.* [102] observed that in a microchannel membrane device with 100μm thick gas and liquid layers, using polymeric membranes of 10-50 μm thick, with pore size of 0.1-5 μm, more than 30% of CO_2 from a 25%vol CO_2 stream was absorbed in ca. 3 s residence time in 20% diethanolamine solution.

It is worth noting that even though the CO_2 removal decreases with increasing gas flowrate, the CO_2 flux remains constant at almost $2x10^{-3}$ mol/m^2·s (based on the mesh area) indicating the absence of mass transfer resistance in the gas phase. In addition to that, if there was a resistance in the gas phase by increasing the gas flowrate, CO_2 flux should increase due to the fact that the gas boundary layer resistance decreases. Simulations were performed also with laminar flow profiles and the results were practically the same with the results when plug flow profiles were used (figure 4.8) for gas and liquid phase. This proves that our assumption for plug flow in both phases was reasonable. Sensitivity analysis of the model was carried out where $D^G_{CO_2}$, $D^L_{CO_2}$, D^L_{NaOH} and *k* were varied by ±20%. While in Figure 4.8 average deviation from experimental data is 3.3%, varying $D^G_{CO_2}$ by ±20% did not produce any detectable changes. When varying $D^L_{CO_2}$ by ±20% or D^L_{NaOH} by ±20%, the average deviation became 4% and 4.1%, respectively. When varying the rate constant by ±20% the average deviation was still found to be 3.3%.

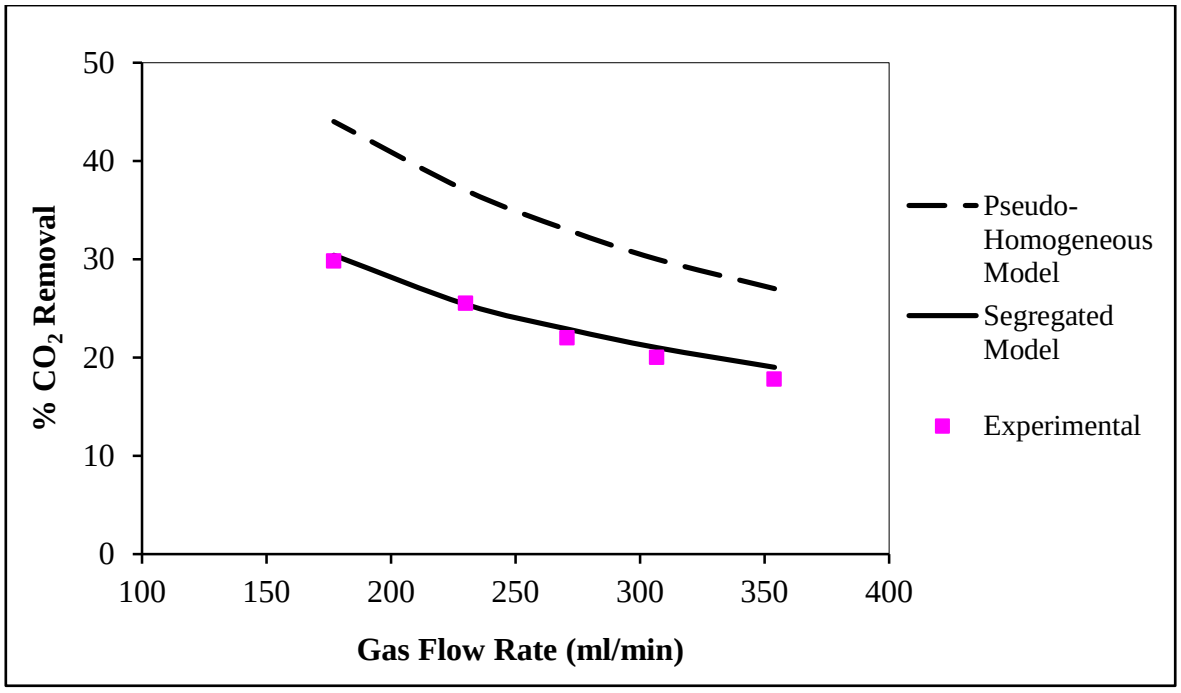

Figure 4.8 Amount of CO_2 removed from the gas phase as a function of gas flowrate, obtained experimentally and by the segregated and pseudo-homogeneous models. Mesh open area=15%, δ_G=850 μm, δ_L=200 μm, Y_G/Y_L=139.5, NaOH=2M.

4.5.3 Influence of liquid and gas flowrates

Figure 4.9 shows the comparison of the model with the experimental results for CO_2 removal as a function of gas and liquid flowrates. For each of these plots (figure 4.9) the gas flowrate was kept constant while the liquid flowrate was varied. The percentage of CO_2 removal increases by increasing the liquid flowrate and decreasing the gas flowrate. The increase of the gas flowrate reduces the residence time in the reactor; hence, it results in a lower rate of removal of carbon dioxide as shown in Figure 4.8. On the other hand, as the liquid flowrate increases, the concentration of NaOH inside the mesh is kept higher, increasing the driving force for CO_2 removal. The increase of CO_2 absorption is however relatively small, in agreement with similar trends observed by Al-Marzouqi *et al.* [100] for CO_2 absorption in NaOH in wetting hollow fiber membranes. This work further indicated that increase of CO_2 removal with liquid flowrate became more significant for non-wetting membranes. By filling the pores with the absorbent liquid, the membrane-phase resistance is increased as the liquid offers additional resistance to the transport; this behaviour indicates the existence of mass transfer resistances in the bulk liquid phase. Zhang *et al.* [103] observed a small increase in CO_2 flux as liquid velocity increased at low velocities but no effect at larger velocities, for CO_2 absorption in DEA solution in non wetting hollow fibers. In that work, the rate-determining step was located in the gas phase, as demonstrated by the increase of CO_2 flux with gas velocity. In our case, CO_2 flux remains constant not only with gas flowrate (as discussed previously) but also with liquid flowrate (e.g. the CO_2 flux was approximately $2x10^{-3}$ $mol/m^2 \cdot s$ for 354 ml/min gas flowrate).

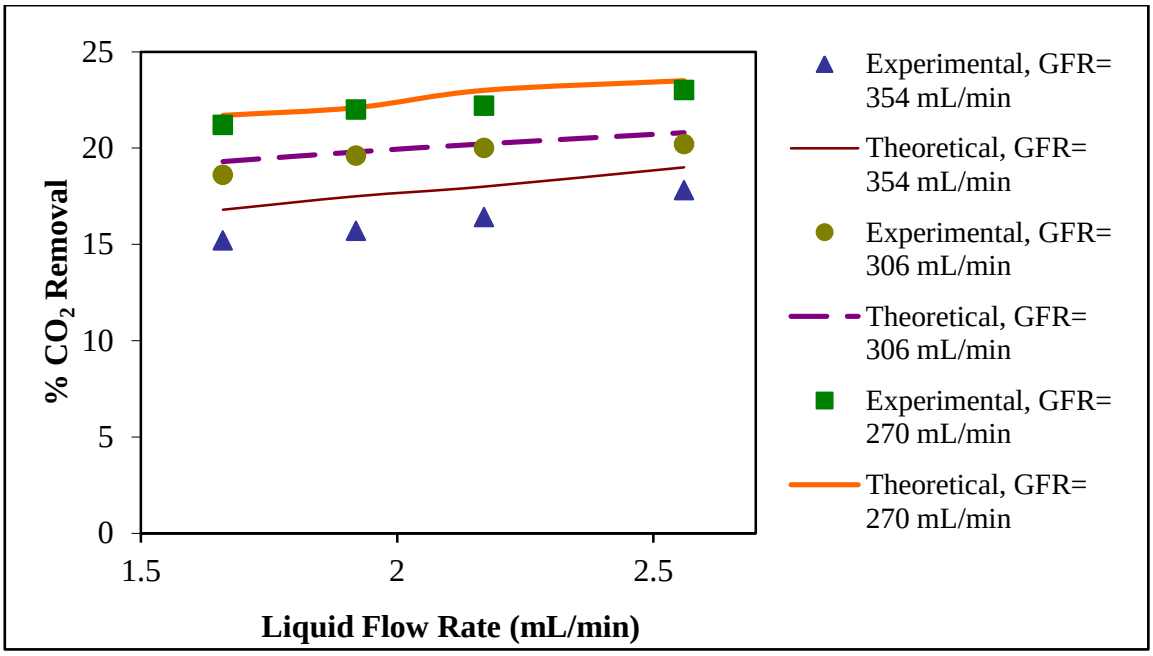

Figure 4.9 Amount of CO_2 removed from the gas phase as a function of liquid flowrate obtained experimentally and theoretically by the segregated model, for various gas flowrates. Mesh open area=15%, δ_G=850 μm, δ_L=200 μm, NaOH=2M.

4.5.4 Influence of mesh open area

The results so far indicated that there is no mass transfer resistance in the gas or bulk liquid phases. Since the mesh is wetting, one would expect mass transfer resistance to exist in the mesh. In order to investigate this, experiments and simulations were performed for meshes with different open contact area. As shown in Figure 4.10, increasing open area significantly increases CO_2 removal. For example by increasing open area from 15% to 25%, CO_2 removal increases almost linearly from 17.8% to 27% (see figure 4.10 for gas flowrate=354 ml/min). The agreement with the segregated model and the experiments is good, providing further confidence on the model predictive behaviour. Next, the segregated model was used to calculate transverse concentration profiles (see section 4.3 for mass balances) in the mesh. As can be seen in Figure 4.11 there is a sharp decrease in CO_2 concentration in the mesh liquid, confirming that mass transfer resistance exists in the mesh. In addition the model indicates that the carbon dioxide is consumed within 3.5 μm from the gas–mesh liquid interface. For lower NaOH concentration provides lower reaction rate and leads to penetration of carbon dioxide deeper in the mesh liquid. Such small penetration distances were also observed for CO_2 absorption in NaOH solution in a falling film microstructured reactor [10]. Figure 4.12

shows the transverse concentration profiles for 2M and 1M NaOH in the mesh liquid, confirming that lower NaOH concentrations lead to lower reaction rates and hence, less NaOH consumption.

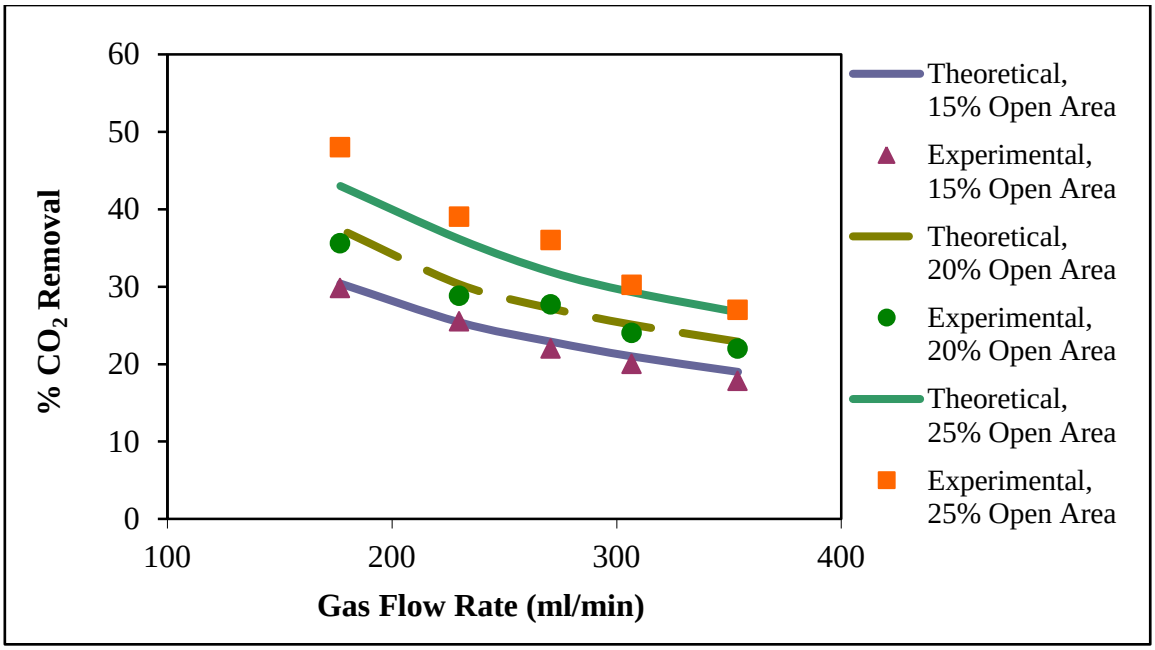

Figure 4.10 Amount of CO_2 removed from the gas phase as a function of gas flowrate obtained experimentally and theoretically by the segregated model, for meshes with different open areas. δ_G=850 μm, δ_L=200 μm, Y_G/Y_L=139.5, NaOH=2M.

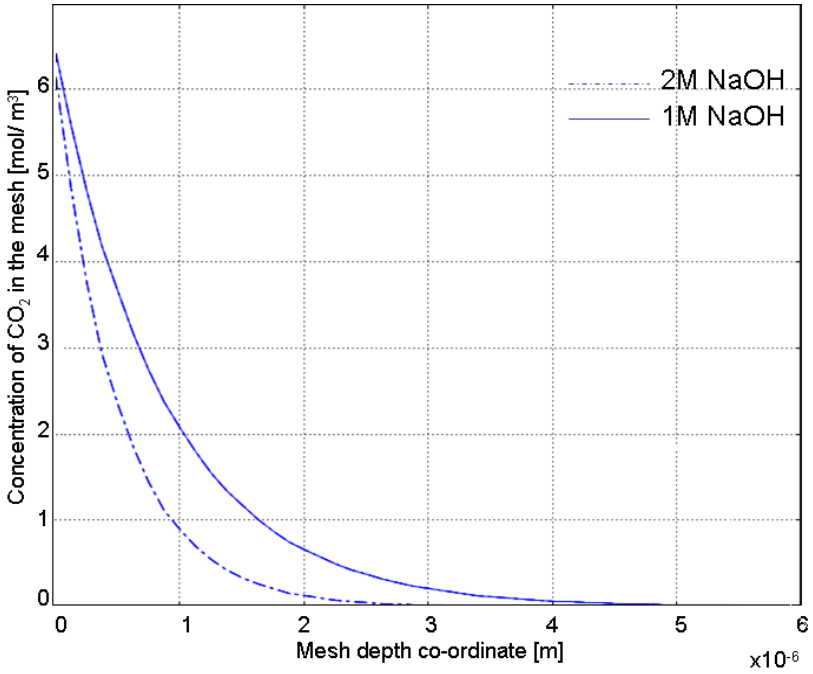

Figure 4.11 Transverse concentration profile of CO_2 in the mesh. Mesh open area=15%, δ_G=850 μm, δ_L=200 μm, Y_G/Y_L=139.5, gas flowrate =354 ml/min, z=4.5 cm, mesh thickness=25 μm.

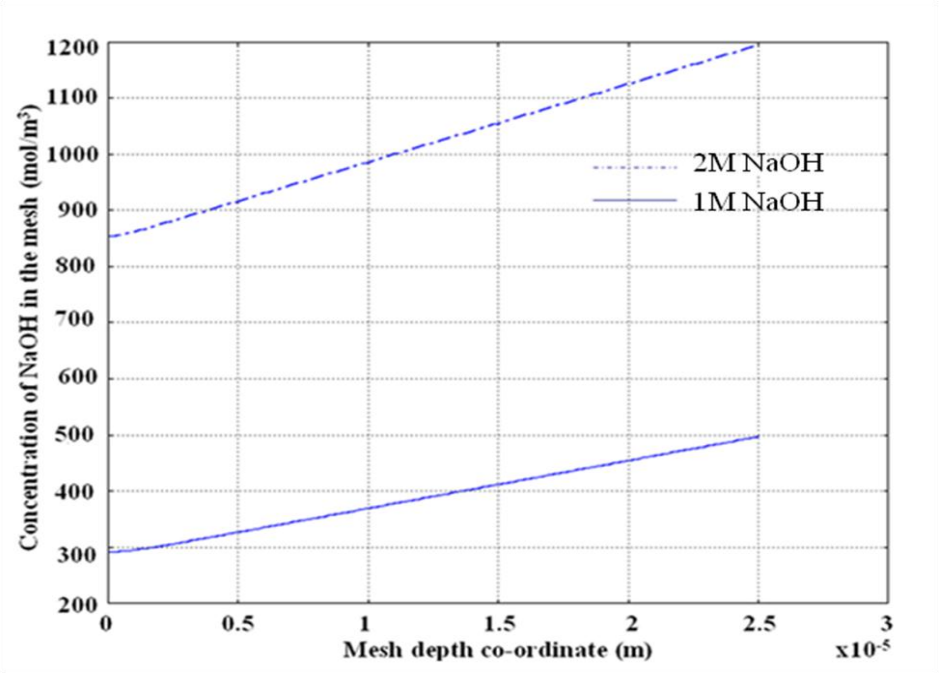

Figure 4.12 Transverse concentration profile of NaOH in the mesh. Mesh open area=15%, δ_G=850 μm, δ_L=200 μm, Y_G/Y_L=139.5, gas flowrate =354 ml/min, z=4.5 cm, mesh thickness=25 μm.

4.5.5 Influence of gas film thickness

Figure 4.13 shows the CO_2 removal for two different gas chamber heights, 850 μm and 1450 μm as a function of gas residence time. The percentage of CO_2 removal increases by increasing the gas residence time. Both experimental and modelling results demonstrate lower CO_2 removal for the higher, gas chamber height. This is related to the fact that as chamber height increases the ratio of gas volume over gas-liquid surface area increases. This is expected to be a key parameter for such a mass-transfer limited system.

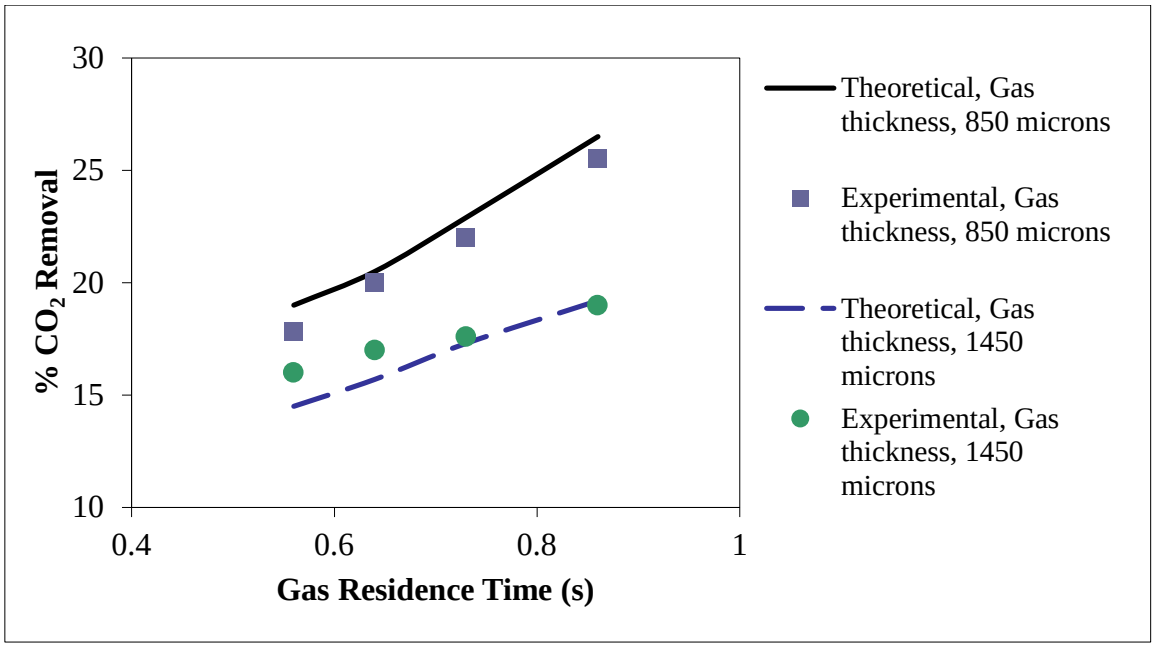

Figure 4.13 Amount of CO_2 removed from the gas phase as a function of gas flowrate obtained experimentally and theoretically by the segregated model, for different gas chamber thickness. Y_G/Y_L=139.5, mesh open area=15%, δ_L=200 μm, NaOH=2M.

4.5.6 Influence of the type of flow

Figure 4.14 shows the performance of the mesh microreactor when the gas flow is counter or co-current to the liquid flow. As it can be seen from Figure 4.14 the operating flow patterns become unimportant as both co-current and counter current flow patterns show the same results for CO_2 removal. This could be due to the fact that the mesh is wetting, hence the dominant resistance for mass transfer is located in the mesh, and this, in turn, minimises the effect of flow patterns on the CO_2 removal. In addition to that, laminar flow and plug flow profiles showed the same influence on CO_2 removal, since the mass transfer resistance exists in the mesh. Li and Teo [104] showed that when gas and liquid flow in parallel, the difference between cocurrent and counter-current flows are much less significant in the membrane absorption compared to conventional gas permeation.

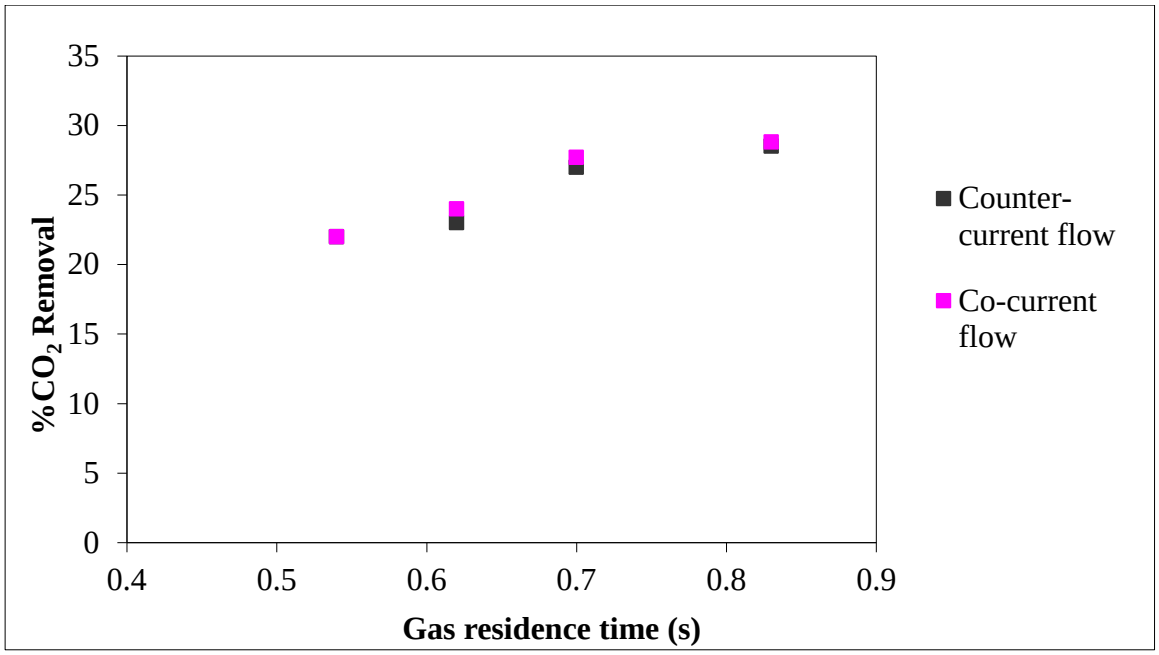

Figure 4.14 Effect of the flow (counter or co-current) on CO_2 removal obtained experimentally. Mesh open area=20%, δ_G=850 μm, δ_L=200 μm, Y_G/Y_L=139.5, NaOH=2M.

4.5.7 Preliminary investigation of CO_2 absorption in NaOH solution using CRL microreactor

4.5.7.1 Reactor design and experimental conditions

The mesh microreactor consists of the mesh in an enclosure formed from glass and copper. Figure 2.2 in chapter 2 shows a diagrammatic cross-section and the assembled device of the mesh microreactor detailing the reaction chamber regions [4]. The reaction chamber depth is set at 100 μm in the active area on each side of the mesh by supports formed on the chamber walls. Mesh area was chosen so that the reaction chamber volume for each phase to be 100 μl, and the surface area of the mesh to be 5.23 cm^2. Each chamber wall has a milled low flow resistance manifold channel (cross-section of 0.7 mm by 1 mm, with volume 37 μl). Due to its chemical inertness and transparency glass material was chosen for the reaction chamber wall.

Copper blocks were milled to form the structural components, which included provision for fluid connections and heaters, with a recess in each to accept the glass chamber wall components [4]. The blocks were electroplated with nickel in order to obtain chemical

compatibility similar to that of the mesh. Finally, a glass component was fixed into each copper block with Epotek 353ND-T epoxy. The complete device comprises of two blocks (mentioned above) with a mesh between them. A viton gasket is placed in a recess in one of the copper blocks to provide the sealing. The mesh was made from nickel (see figure 2.3) using a two stage-stage electroplating method. The pore diameter, depth, and the spacing between the hexagonal pores were approximately 5 μm with an open area of 20% is shown in Figure 2.3.

The experimental set-up was identical to the one described in section 4.2, except that a single- syringe pump (Cole- Palmer 74900 series) was used to drive the liquid fluid (NaOH 2M) into the bottom of the reactor. Experimental data were obtained varying the liquid flow rate from 10-20 ml/h using NAOH inlet concentration of 2M and gas flow rate of 23-45 ml/min for CO_2 inlet concentration of 20%vol. These flow rates resulted to residence times, 0.13-0.26 s for the gas and 18-36 s for the liquid respectively. All the experiments were carried out at room temperature (approximately 20°C).

4.5.7.2 Experimental results and conclusions

Figure 4.15 shows the performance of CRL mesh microreactor in CO_2 absorption. Over 75% of the carbon dioxide was absorbed in less than 0.3s experimental gas residence time from a stream containing 20vol% CO_2. In the micromesh reactor studied before 30% of CO_2 from a 20vol% CO_2 stream was absorbed in 1.2 s gas residence time. In that case the gas film and the liquid film thickness were 850 μm and 200 μm respectively, while in the CRL mesh reactor the liquid film and gas film thickness were 100 μm each. Since both reactors operate in the wetted mode the main resistance is inside the mesh. CRL mesh is 5 μm thick, while in the microstructured reactor mesh is 25 μm thick. This is expected to be the key parameter for having more CO_2 removal in the CRL mesh reactor since the thickness of the CRL mesh is 5 times thinner than the mesh of the microstructured reactor, hence less resistance to mass transfer.

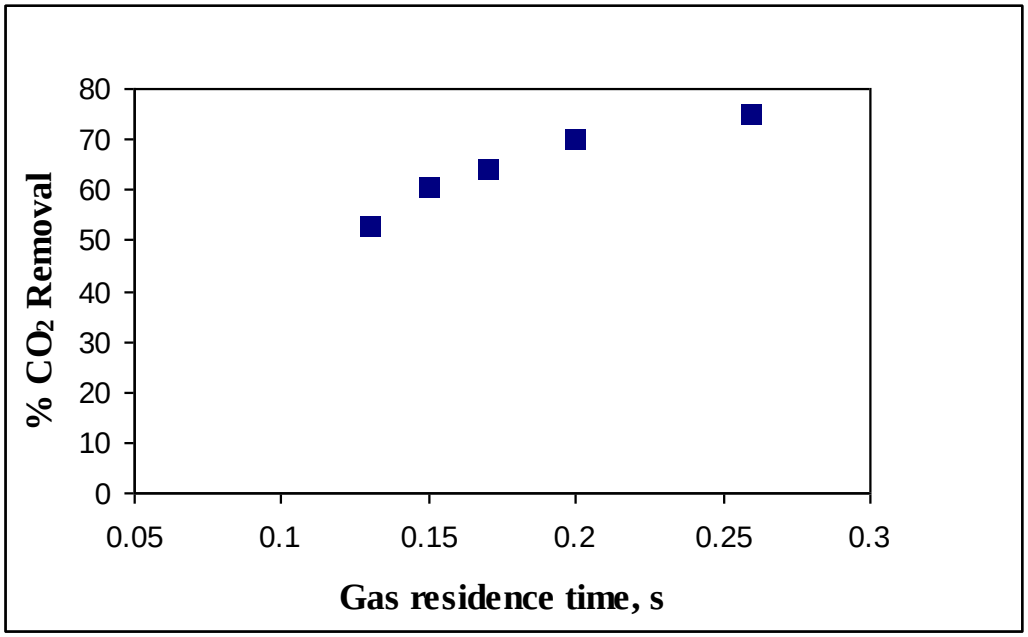

Figure 4.15 Amount of CO_2 removed from the gas phase as a function of gas residence time, obtained experimentally. Mesh open area=20%, δ_G=100 μm, δ_L=100 μm, Y_G/Y_L=139.5, NaOH=2M.

4.6 Conclusions

A microstructured mesh reactor was used for studying carbon dioxide absortion in NaOH solution, which is an example of a fast gas-liquid reaction. Four different nickel meshes were used: (a) Pore diameter 25 μm, open area 15%, thickness 25 μm (b) Pore 25 μm x 75 μm, open area 25%, thickness 25 μm (c) Pore 35 μm x 35 μm, open area 20%, thickness 25 μm, (d) Pore 5 μm, open area 20%, thickness 5 μm. The mesh helped to stabilize the gas/liquid interface and keep the two phases separated. Significant absorption was observed with gas residence times below 1 s. Two models with no adjustable parameters were formulated utilizing the open area of the membrane either to adjust the effective reactor length (segregated model) or to adjust the effective diffusivity in the mesh. The segregated model showed much better agreement with experimental data. Parametric studies showed that the percentage of CO_2 removal increases by increasing the liquid flowrate and decreasing the gas flowrate. The model indicated that the carbon dioxide is consumed within few microns from the gas – liquid interface, and the dominant resistance for mass transfer is located in the mesh

because is wetted by the liquid reactant. Increase of the open area of the mesh from 15% to 25% increases the CO_2 removal significantly. In addition the operating flow patterns are unimportant as both co-current and counter current flow patterns show the same results for CO_2 removal. Finally CO_2 removal was increased using CRL reactor. This related to the fact that in the CRL reactor the thickness of the mesh was 5 times thinner from the mesh used in the acrylic reactor, hence less resistance to mass transfer.

CHAPTER 5
CO_2 ABSORPTION IN PTFE MEMBRANE REACTOR USING AQUEOUS SOLUTIONS OF AMINES

5.1 Introduction

For technical, economical and environmental concerns, aqueous solutions of alkanolamines are widely applied for: (a) acid gases (CO_2, H_2S) removal during natural gas sweetening and (b) CO_2 capture from fossil-fuel-fired power plants, as well as some other important industries such chemical and petrochemical, steel, and cement production. Industrially more often used alkanolamines are monoethanolamine (MEA), diethanolamine (DEA), diisopropalamine (DIPA), N-methyldiethanolamine (MDEA), 2-amino-2-methyl-1-propanol (AMP) [105]. The choice of a certain amine (single or blended amine) is mainly based on the absorption capacity, reaction kinetics and regenerative potential and facility. In recent years, the efficiency of membrane contactor for CO_2 capture has been extensively studied. Results showed that the membrane gas absorption process is a good alternative to conventional techniques as it was explained extensively in the literature review.

In this Chapter, CO_2 absorption in solutions of monoethanolamine (MEA) and diethanolamine (DEA) was performed in a membrane PTFE microstructured reactor. In order to evaluate, understand and improve the performance of the membrane microreactor, various conditions

such as gas flowrates, membrane contact area between the gas and the liquid, different amine solutions, and liquid concentrations were investigated.

5.2 CO_2 Absorption in Amine solutions

5.2.1 Reactor design and experimental conditions

The reactor used in this work comprises of a microstructured membrane placed between two 18 mm thick acrylic plates (S.I.M, UK), containing inlet and outlet ports for the fluids. One channel is machined in each acrylic plate with 0.85 mm and 0.2 mm depth forming the areas where gas and liquid flow respectively. The reactor measures 192 mm x 97 mm (see figure 5.1). Two viton gaskets 0.5 mm thick (Altec, UK) are placed in 0.4 mm deep grooves machined in the acrylic plates to provide the sealing. The membrane (see figure 5.2) is made from pure PTFE (Teflon) (Sterlitech, US) laminated onto a polypropylene layer. The pure PTFE is 20 μm thick and contains holes approximately 0.5-5 μm diameter as observed by SEM. The polypropylene layer is 80 μm thick and consists of holes in an approximately rectangular shape with dimensions of 0.8 x 0.324 mm (see figure 5.2). The porous area of the membrane is 5.48 mm x 90 mm with an open area of 67-70% and defines the reaction area between the two fluids. Two pin holes were employed in both plates and membrane for alignment, while 16 screws were used for clamping all components together. A picture of the assembled reactor and a schematic of all components of the reactor are shown in Figure 5.1. In order to investigate the influence of the gas/liquid contact area experiments were performed with the 8 channel reactor using the PTFE membrane (see figure 5.1). The 8 channel reactor uses the same top/bottom plates as the reactor used with metallic mesh in chapter four, for CO_2 absorption in NaOH solution. The 8 channel reactor has approximately 11.3 times larger contact area (gas/liquid contact area 55.9 cm^2) between gas and liquid, than the contact area of the single channel reactor (gas/liquid contact area 4.9 cm^2).

A picture of the experimental set up for CO_2 absorption is shown in Figure 5.3. An HPLC pump (Waters 5100) was used to drive the liquid solution in the bottom chamber of the reactor which were aqueous amine solutions of 10%w.t MEA, 16.6%w.t DEA. These concentrations were chosen in order to compare equal molarities of DEA and MEA, which in

our case correspond to 1.62M. The gas 20vol% CO_2/N_2 was controlled by a mass flow controller (Brooks 5850) and flowed above the mesh. The differential pressure between the two phases was controlled by a metering valve (Swagelok) at the outlet of the liquid phase. The gas phase and liquid phase pressures were measured by a digital manometer (Comark; pressure range 0-30psi). The outlet of the gas phase passed through a liquid trap to avoid any liquid getting into the gas chromatograph (GC) in case of breakthrough of the liquid in the gas phase, and then connected to a GC (Shimadzu GC-14B) for carbon dioxide concentration determination. Experimental data were obtained varying the liquid flow rate in the range 1.66-2.56 ml/min and gas flowrate in the range 160-247 ml/min. These flowrates resulted to residence times, (based on the gas/liquid volumes in contact with the membrane area), 0.10-0.16 s for the gas and 2.3-3.54 s for the liquid respectively. All the experiments were carried out at room temperature (approximately 20°C). The CO_2 removal efficiency was calculated from:

$$X_{CO_2} = 1 - \frac{F_{CO_2 out}}{F_{CO_2 in}} \qquad (5.1)$$

where F is the molar flowrate of CO_2. The experimental error in CO_2 removal was assessed to be ± 5%. Two to three chromatographs were taken for each measurement and the deviation between them was about ± 5%.

(a)

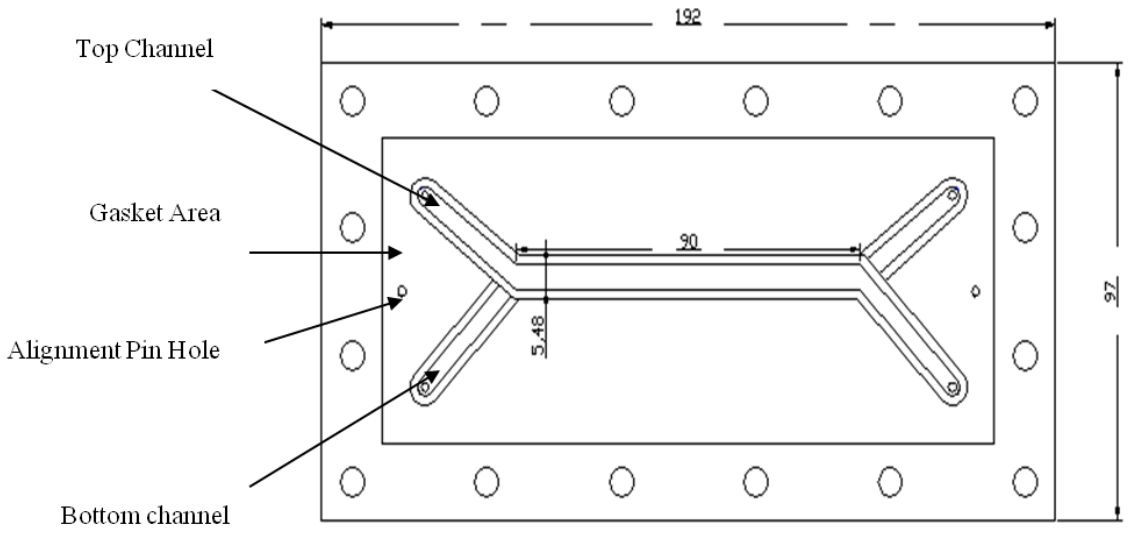

(b)

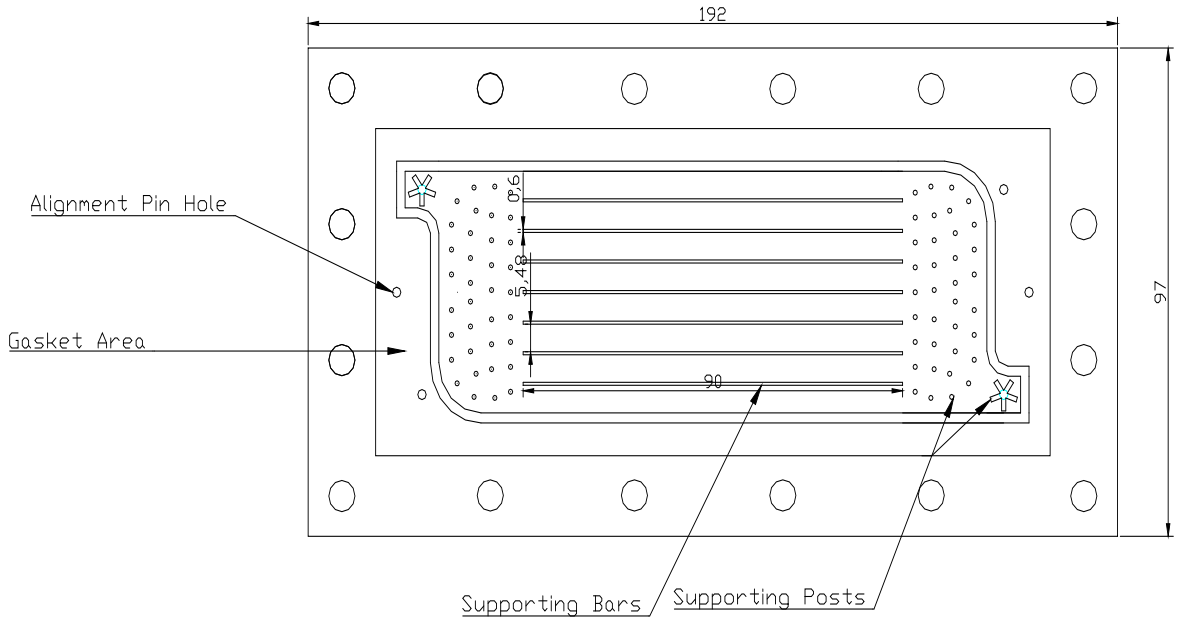
192
97
Alignment Pin Hole
Gasket Area
0.6
5.48
90
Supporting Bars
Supporting Posts

(c)

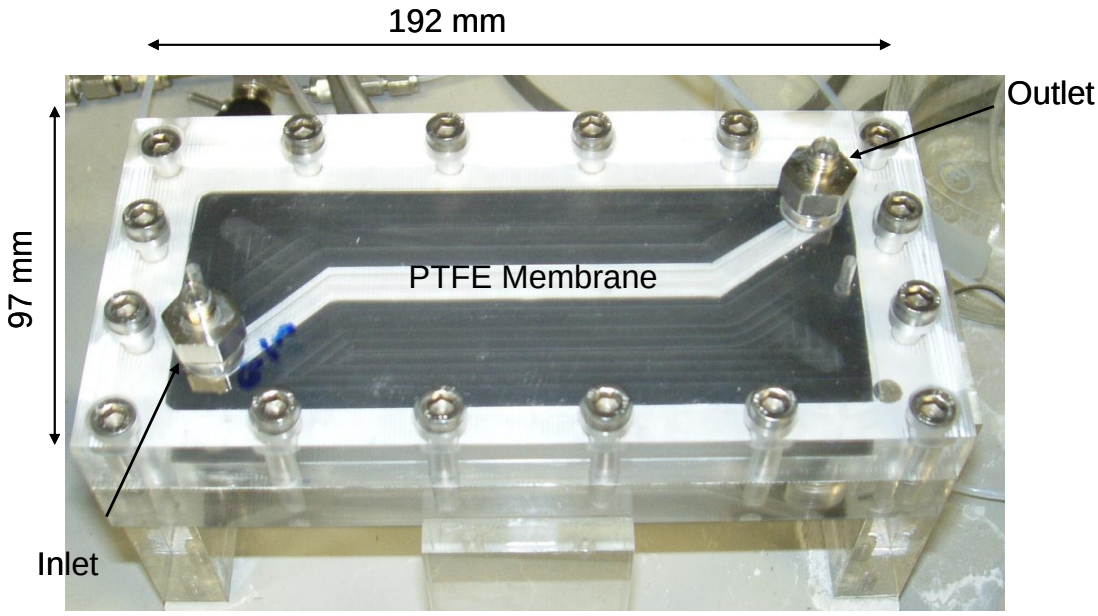
192 mm
97 mm
Outlet
PTFE Membrane
Inlet

(d)

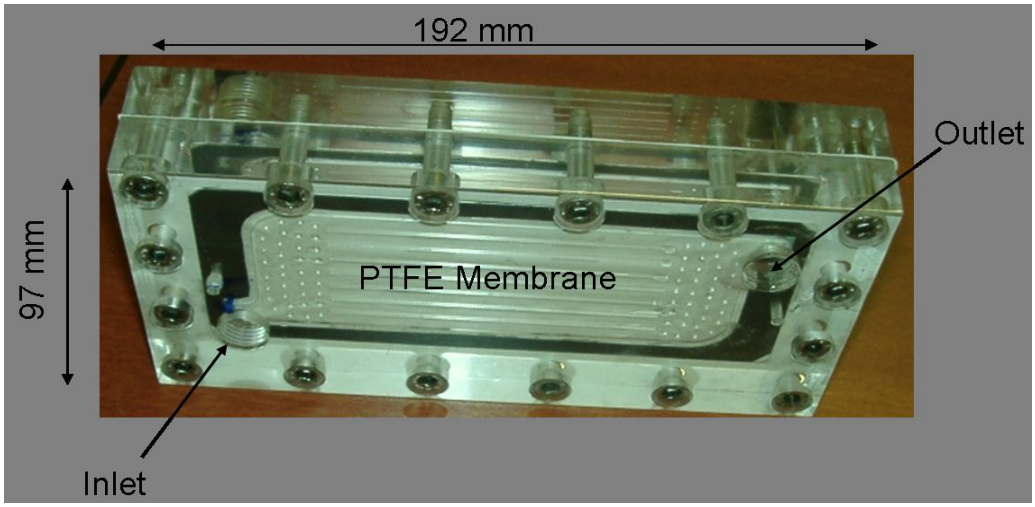

(e)

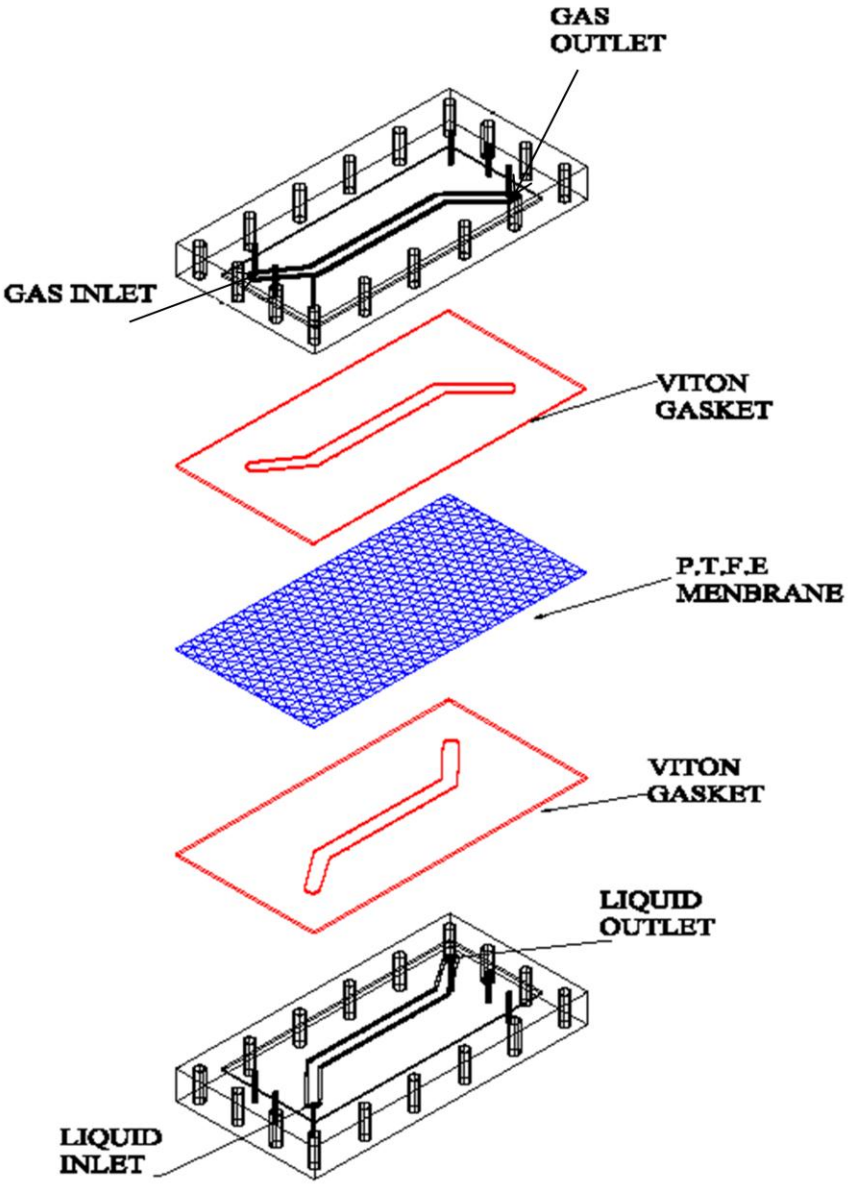

Figure 5. 1 Membrane microstructured reactors: (a) schematic of acrylic plate (b) schematic of the 8 channel PTFE reactor (c) picture of assembled device of the PTFE single

channel reactor and (d) picture of the assembled device of the 8 channel PTFE reactor (e) Exploded schematic view of the reactor. Dimensions are in mm.

(a)

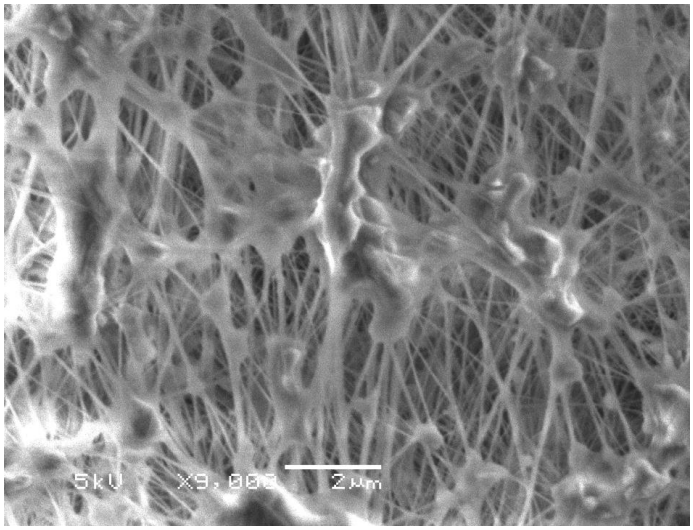

(b)

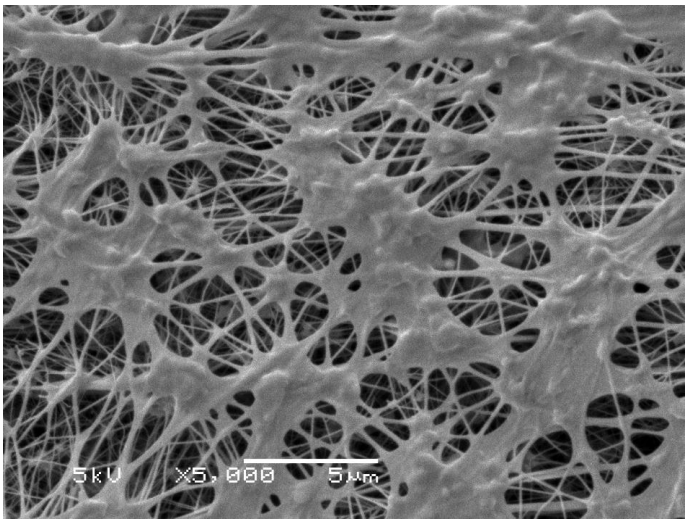

(c)

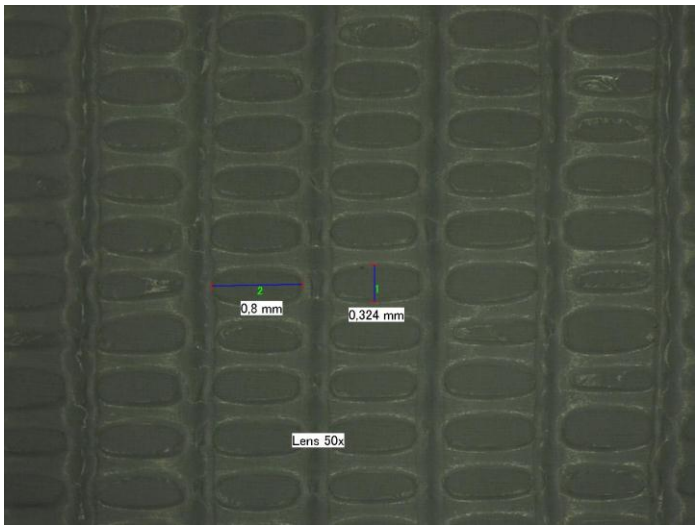

Figure 5. 2 (a) SEM picture of pure PTFE membranes with magnification of x9000, non-coated, (b SEM picture of pure PTFE membranes with magnification of x5000, gold coated, (c) Optical image of the laminated part of the PTFE membrane (polypropylene).

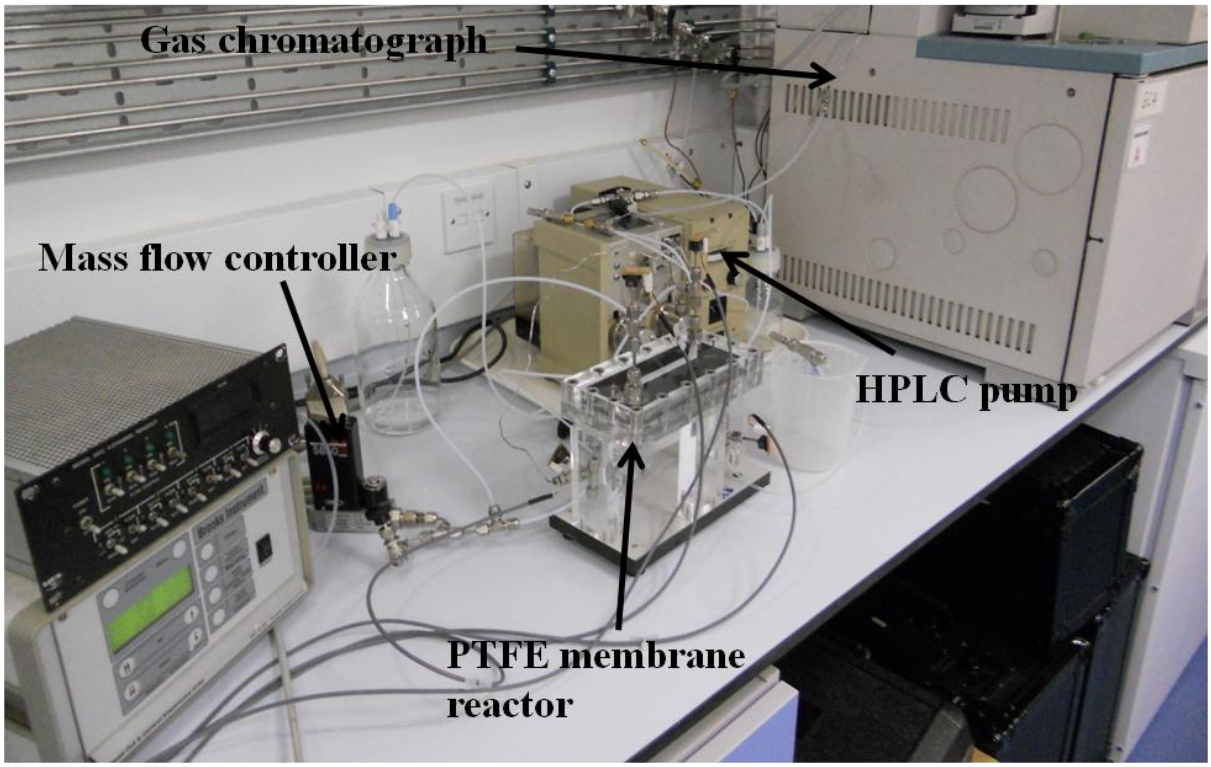

Figure 5. 3 Picture of the experimental set-up used in this work.

5.2 Mathematical Model Development

A two-dimensional model of the microstructured membrane reactor was formulated and the following assumptions were made: (1) The system is at steady state (system was allowed to reach steady state conditions, no change of pressure, temperature with time). (2) Ideal gas behavior is valid for the gas phase. (3) Henry's Law is applicable (4) No evaporation of water in the gas phase is assumed. (5) Plug flow profiles are assumed in the gas and liquid phases. (6) Membranes pores considered as gas filled. (7) No change in gas flowrate along channel. The reactor model is divided in three main domains: the gas phase, the membrane, and the liquid phase (figure 5.4). The differential mass balances to describe the concentration profiles of components in the three domains are given below, and they were solved with COMSOL 3.5a.

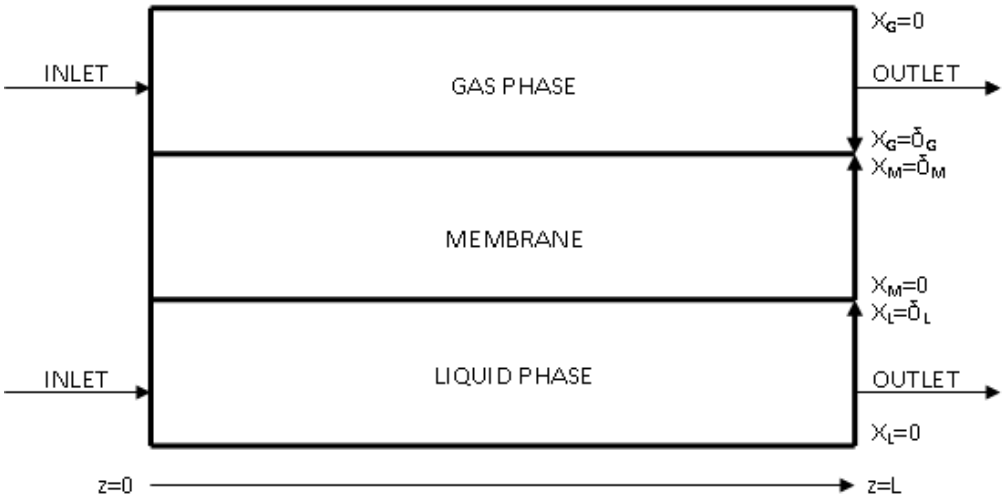

Figure 5.4 Mathematical model domains with coordinates and boundaries.

Mass balance in the liquid phase:

The differential mass balance of components in the liquid phase along with the associated boundary conditions are:

$$u_L \frac{\vartheta}{\vartheta z} C^L_{CO_2} = D^L_{CO_2} \left(\frac{\partial^2 C^L_{CO_2}}{\partial z^2} + \frac{\partial^2 C^L_{CO_2}}{\partial x_L^2} \right) + R_{CO_2} \tag{5.2}$$

$$u_L \frac{\vartheta}{\vartheta z} C^L_{Ami} = D^L_{Ami} \left(\frac{\partial^2 C^L_{Ami}}{\partial z^2} + \frac{\partial^2 C^L_{Ami}}{\partial x_L^2} \right) + R_{Ami} \tag{5.3}$$

$$\text{at } z=0,\ C^L_{CO_2} = 0, C^L_{Ami} = C_{Ami,\,initial} \tag{5.4}$$

$$\text{at } z = L, \frac{\vartheta C_{CO_2}}{\vartheta z} = 0\ ,\ \frac{\vartheta C_{Ami}}{\vartheta z} = 0 \tag{5.5}$$

$$\text{at } x_L=\delta_L \text{ , } C^L_{CO_2} = m\, C^M_{CO_2} \text{ , } \frac{\vartheta C_{Ami}}{\vartheta x_L} = 0 \text{ , } D^L_{CO_2} \frac{\vartheta C^L{}_{CO_2}}{\vartheta x_L} = D^M_{CO_2} \frac{\vartheta C^M_{CO_2}}{\vartheta x_M} \tag{5.6}$$

$$\text{at } x_L = 0, \quad \frac{\vartheta C_{Ami}}{\vartheta x_L} = 0 \text{ , } \frac{\vartheta C_{CO_2}}{\vartheta x_L} = 0 \tag{5.7}$$

Mass balance in the membrane:

The differential mass balance of components in the mesh, along with the associated boundary conditions are:

$$D^M_{CO_2} \frac{\vartheta^2 C^M_{CO_2}}{\vartheta x^2_M} = 0 \tag{5.8}$$

$$\text{at } x_M = 0 \text{ , } C^L_{CO_2} = m\, C^M_{CO_2} \text{ , } \frac{\vartheta C_{Ami}}{\vartheta x_M} = 0 \text{ , } D^M_{CO_2} \frac{\vartheta C^M{}_{CO_2}}{\vartheta x_M} = D^L_{CO_2} \frac{\vartheta C^L_{CO_2}}{\vartheta x_L} \tag{5.9}$$

$$\text{at } x_M = \delta_M \text{ , } C^M_{CO_2} = C^G_{CO_2} \text{ , } \quad D^G_{CO_2} \frac{\vartheta C^G_{CO_2}}{\vartheta x_G} = D^M_{CO_2} \frac{\vartheta C^M_{CO_2}}{\vartheta x_M} \tag{5.10}$$

Mass balance in the gas phase:

The differential mass balances in the gas phase, along with the associated boundary conditions are:

$$u_G \frac{\vartheta}{\vartheta z} C^G_{CO_2} = D^G_{CO_2} \left(\frac{\vartheta^2 C^G_{CO_2}}{\vartheta z^2} + \frac{\vartheta^2 C^G_{CO_2}}{\vartheta x^2_G} \right) \tag{5.11}$$

$$\text{at } z=0, \; C^G_{CO_2} = C_{CO_2,initial} \tag{5.12}$$

$$\text{at } z = L, \; \frac{\vartheta C_{CO_2}}{\vartheta z} = 0 \tag{5.13}$$

$$\text{at } x_G = 0 \;\Rightarrow\; \frac{\vartheta C_{CO_2}}{\vartheta x_G} = 0 \tag{5.14}$$

$$\text{at } x_G = \delta_G,\ C^G_{CO_2} = C^M_{CO_2},\ D^G_{CO_2}\frac{\vartheta C^G_{CO_2}}{\vartheta x_G} = D^M_{CO_2}\frac{\vartheta C^M_{CO_2}}{\vartheta x_M} \quad (5.15)$$

The model is a "pseudo-homogeneous model", where the membrane is considered as a homogeneous medium with $D^M_{CO_2} = \frac{\varepsilon}{\tau}D^G_{CO_2}$, where ε is the membrane porosity and τ is the tortuosity (an adjustment parameter which corrects for the pore geometry). COMSOL Myltiphysics 3.5.a was used to solve the differential mass balances. A mesh consisting of 52000 number of elements and 313983 degrees of freedom was used to execute the simulations in Windows XP with Pentium IV 2.93GHz CPU and 4GB of RAM. At this number of elements the solution was found to be mesh independent.

5.3 Reaction System

For monoethanolamine (MEA) and diethanolamine (DEA) the overall reaction system can be written as [106, 107]:

$$CO_2 + 2MEANH_2 \rightarrow MEANHCOO^- + MEANH_3^+ \quad (5.16)$$

where MEA formula is = $NH_2 – CH_2 – CH_2$

$$CO_2 + 2DEANH_2 \rightarrow DEANHCOO^- + DEANH_3^+ \quad (5.17)$$

where DEA formula is = $HN(CH_2CH_2OH)_2$

The overall rate of absorption can be written as [108]:

$$R_{CO_2} = k_{Ami}[CO_2][A_{mi}] \quad (5.18)$$

$$R_{Ami} = 2k_{Ami}[CO_2][A_{mi}] \quad (5.19)$$

All the parameters used in the calculations were taken from previous CO_2/Amines studies and are reported in table 5.1

Table 5. 1 Values of parameters used in the simulations**.** All the parameters were taken for T=20^{o}C.

Parameter	Value	Reference
$D^{G}_{CO_2}$ (m^2/s)	$1.64x10^{-5}$	Cussler [95]
$D^{L}_{CO_2}$ (m^2/s)	$1.4x10^{-9}$	Dankwerts [107]
D^{L}_{MEA} (m^2/s)	$7.7x10^{-10}$	Dankwerts [107]
m_{MEA} (dimensionless)	0.76	Paul *et al.* [109]
k_{MEA} ($m^3/mol \cdot s$)	3.8	Rivera *et al.* [110]
$D^{L}_{CO_2}$ (m^2/s)	$1.05x10^{-9}$	Zhang *et al.* [50]
D^{L}_{DEA} (m^2/s)	$4.97x10^{-10}$	Zhang *et al.* [50]
m_{DEA} (dimensionnelles)	0.8	Paul *et al.* [109]
k_{DEA} ($m^3/mol \cdot s$)	2.3	Zhang *et al.* [50]

5.4 Results and Discussion

5.4.1 Membrane characterisation

The porosity of the membrane was measured using the helium pycnometer method and it was found to be approximately 67-70%. The helium pycnometer method uses helium. The pycnometer consists of two chambers, connected by a tube with a valve in it. The rationale is to measure the pressure difference between the two containers, one of which has the sample material in it. The porosity is determined by the difference in the pressures caused by the opening of the valve at constant temperature.

In order to examine the pores of the membrane scanning electron microscopy (SEM) was exploited. A scanning electron microscope (SEM) is a type of electron microscope that images a sample by scanning it with a high- energy beam of electrons in a raster scan pattern. Figure 5.2 shows SEM images with magnification of x5000 and x9000, gold coated and non-coated and the accelerating voltage used was 5kV. Gold coating improvs the quality of the image and avoids scanning faults, since the surface of the membrane is a more electrically conductive than a non-coated membrane. From Figure 5.2 it can be seen that the diameter of the pores varies from 0.5-5 μm or even larger.

5.4.2 Breakthrough studies

Breakthrough experiments identified that the breakthrough of liquid in the gas phase for DEA solution occurred at a pressure difference P_L-P_G of about 180-210 cm H_2O. During typical operation (Y_G=247 ml/min, Y_L=2.56 ml/min) the pressure difference between liquid and gas phase was kept at P_L-P_G≈90 cm H_2O. The theoretical breakthrough pressure of DEA was calculated based on equation (6.23) and it was found 166.3 cm H_2O, with surface tension γ=0.066 N/m, pore diameter 5 μm and contact angle approximately 108° which is in agreement with the experimental values. The experimental and theoretical breakthrough values for MEA solution were similar with DEA solution, due to the fact that the solutions were dilute (DEA, MEA =1.62M) and hence, surface tension and apparent contact angle were similar.

5.4.3 Contact angle measurement

The value of the contact angle of aqueous solution of DEA 1.62M was measured on the porous PTFE membrane and pure PTFE. A droplet of the solution was placed on a piece of porous PTFE membrane and then on the pure PTFE and the analysis was performed with Keyence microscope (VHX-600) see chapter 6. The apparent contact angle on porous PTFE was found to be around 140° (see figure 5.5a) while the contact angle on pure PTFE was found around 108° (see figure 5.5b). The apparent contact angle measured experimentally is in a good agreement with Cassie and Baxter equation [111], was found around 142°, which proposed that the apparent contact angle θ formed by liquid droplet on a porous surface is related to the contact angle φ_1, for the homogeneous solid material, by:

$$\cos\theta = \alpha_1\cos\varphi_1 - \alpha_2 \qquad (5.20)$$

where α_1 is the fraction of the surface which is solid and α_2 the fraction which is open area.

(a)

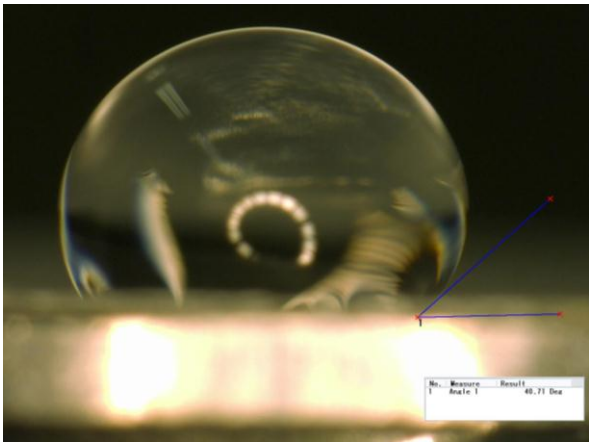

(b)

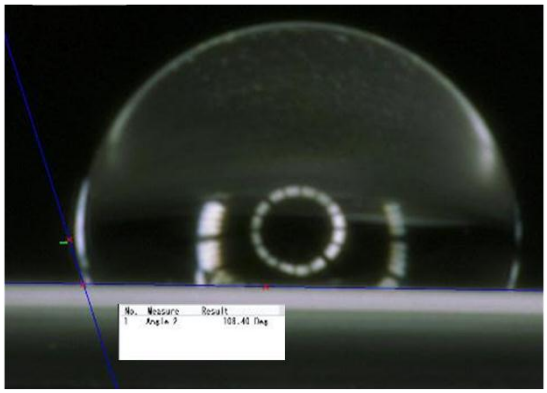

Figure 5. 5 Optical image of a droplet of DEA 1.62M solution on (a) porous PTFE membrane (b) pure PTFE.

5.4.4 Model prediction for CO_2 absorption in amine solutions

The predictions of the pseudo-homogeneous model are compared with experimental results, obtained from carbon dioxide absorption in DEA (diethanolamine) solution. As it can be seen from Figure 5.6 the experimental results are in a very good agreement with model's prediction. Figure 5.6 shows the comparison of the model with the experimental results for CO_2 removal as a function of gas flowrates. It can be seen that the percentage of CO_2 removal decreases by increasing the gas flowrate. The increase of the gas flowrate reduces the residence time in the reactor; hence, it results to lower removal of carbon dioxide. In addition

it shows that 11-14% of the carbon dioxide contained in the inlet stream was removed within 0.1-0.16 s experimental gas residence time, based on 0.419 cm^3 volume of contact area. These results are comparable with similar research where CO_2 absorption was investigated in microchannel separated-flow contactors. As it was mentioned in section 4.5.2 TeGrotenhuis *et al.* [102] observed that in a microchannel membrane device with 100 μm thick gas and liquid layers, using polymeric membranes of 10-50μm thick, with pore size of 0.1-5 μm, more than 30% of CO_2 from a 25vol%CO_2 stream was absorbed in ca. 3 s residence time in 20% diethanolamine solution. Furthermore, in the metallic mesh microreactor used in Chapter 4 approximately 30% of the carbon dioxide contained in the inlet stream was absorbed in ca.1.12 s residence time in 2M NaOH solution.

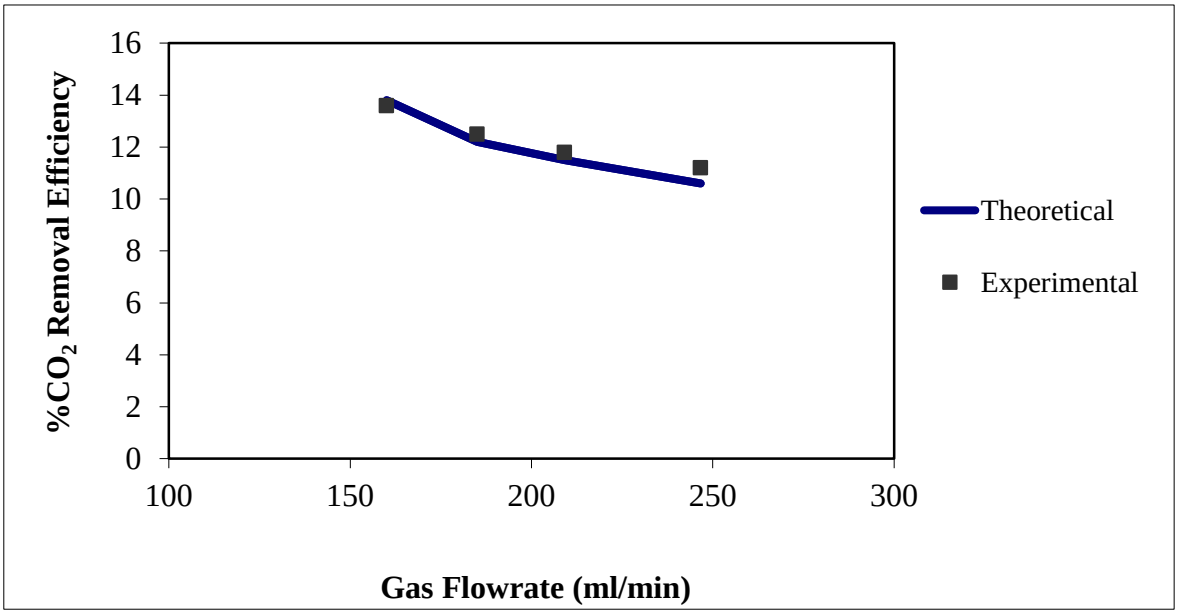

Figure 5. 6 Amount of CO_2 removed from the gas phase as a function of gas flowrate, obtained experimentally and by the pseudo-homogeneous model. Membrane porosity≈67-70%, δ_G=850 μm, δ_L=200 μm, Y_{CO_2}/Y_{DEA}=96.4, DEA=16.6%w.t.

5.4.5 Influence of different amine solutions in CO_2 removal

Figure 5.7 shows the CO_2 removal for two different amine solutions DEA, MEA (diethanolamine, monoethanolamine). Both experimental and modelling results show that MEA solution absorbed more CO_2 than DEA. Based on Rongwong *et al.* [46] this is due to the fact that MEA has higher reaction rate constants than DEA. In their work they studied

CO_2 absorption using PVDF hollow fiber membrane with three different amine solutions (MEA, DEA, AMP, all of them 1M). They showed that CO_2 absorption fluxes were increased in the following order MEA>AMP>DEA. Paul *et al.* [45] in their work about theoretical studies on separation of CO_2 by single and blended aqueous alkanolamine solvents in flat sheet membrane reactor they showed that the aqueous solution of MEA has the highest CO_2 flux followed by AMP, DEA and MDEA in sequence, which is again due to the fact MEA has the highest reaction rate constant than the other amine solutions.

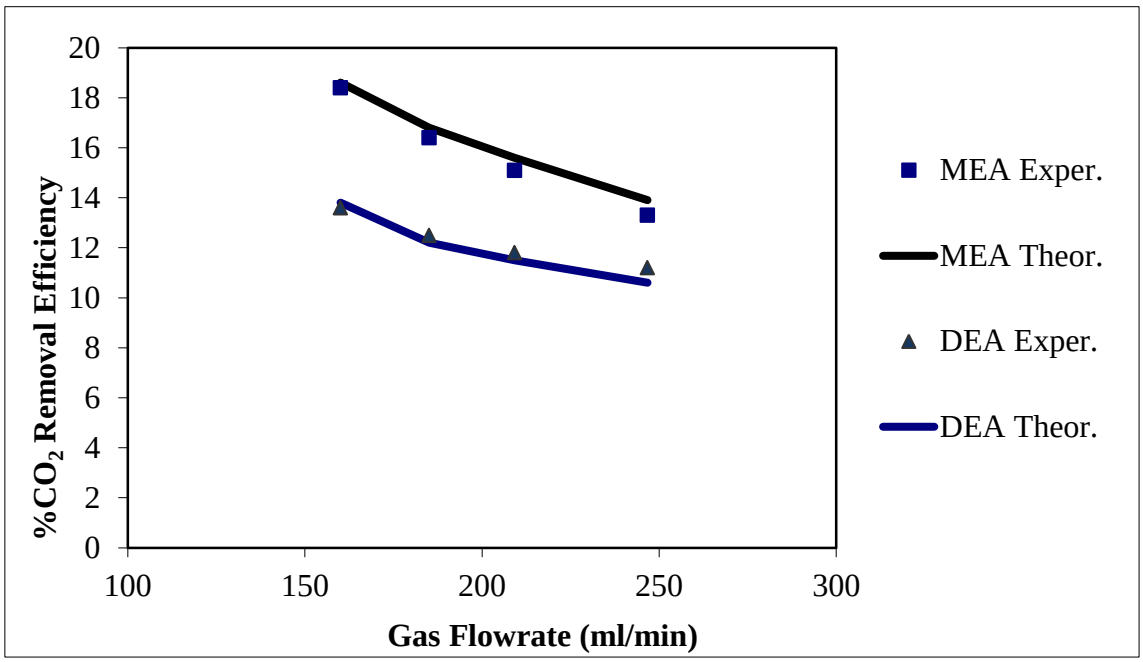

Figure 5. 7 Amount of CO_2 removed from the gas phase as a function of gas flowrate, obtained experimentally and theoretically by DEA and MEA solutions. Membrane porosity≈67-70%, δ_G=850 μm, δ_L=200 μm, MEA=10%w.t, DEA=16.6%w.t, Y_{CO_2}/Y_{Ami} =96.4.

5.4.6 Influence of MEA concentration in CO_2 removal

Experiments were also performed with 6%w.t (0.97M) MEA concentration. Figure 5.8 shows the comparison of the model with the experimental results for CO_2 removal as a function of gas flowrates. As it can be seen from Figure 5.8 for lower MEA concentration, less CO_2 removal efficiency was obtained. This is because lower MEA concentration provides lower reaction rate, hence results to less CO_2 removal efficiency. Rongwong et al. [47] performed experiments with different concentrations of MEA and they showed that by increasing the

concentration of MEA from 0.25M to 1M the CO_2 flux was increased for the same reason explained above. Marzouqi and Faiz [112] performed mathematical modeling for the simultaneous absorption of CO_2 and H_2S using MEA in hollow fiber membrane contactors and they showed by increasing the MEA concentration from 1M to 3M, CO_2 removal efficiency was increased due to higher reaction rates.

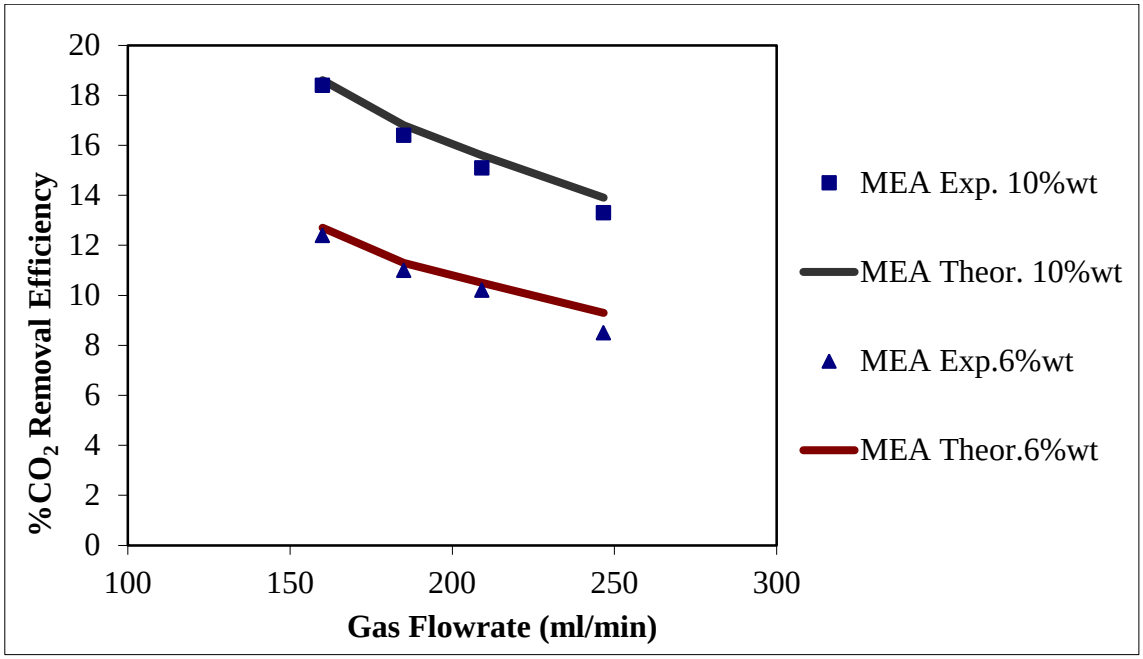

Figure 5. 8 Amount of CO_2 removed from the gas phase as a function of gas flowrate, obtained experimentally and theoretically by MEA 6%w.t and MEA 10%w.t. Membrane porosity≈67-70%, δ_G=850 μm, δ_L=200 μm, Y_{CO_2}/Y_{MEA}=96.4.

5.4.7 Influence of the gas liquid contact area

In order to examine the influence of the gas/liquid contact area on CO_2 removal efficiency experiments were performed with the 8 channel PTFE reactor (55.9 cm^2 gas/liquid contact area) and the single channel PTFE reactor (4.9 cm^2 gas/liquid contact area). Figure 5.9 shows the CO_2 removal for the 8 channel PTFE reactor (see chapter 4 for more information) and the single channel PTFE reactor as a function of gas flowrates. 63-76% of the carbon dioxide contained in the inlet stream was removed within 1.15-1.78 s experimental gas residence time, while in the single channel reactor 13-19% of carbon dioxide was removed within 0.1-0.16s experimental gas residence time. From Figure 5.9 it can be seen that both model and experimental results

demonstrate higher CO_2 removal for the 8 channel reactor. This is due to the fact the reaction area between CO_2 and MEA for the 8 channel reactor is much larger (approximately the contact area between gas and liquid is 11.3 times larger than the contact area of the single channel reactor) than the single channel reactor. Hence higher gas residence times for CO_2 to react with MEA solution results to higher CO_2 removal efficiency.

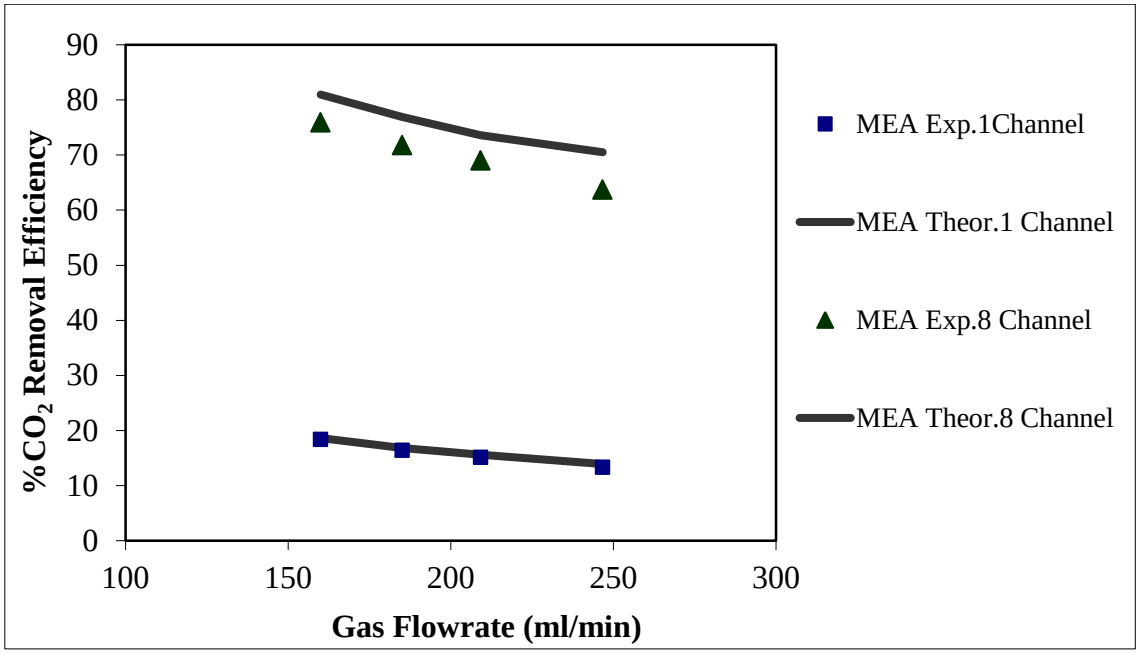

Figure 5. 9 Amount of CO_2 removed from the gas phase as a function of gas flowrate, obtained experimentally and theoretically by the single channel reactor and the 8 channel reactor. Membrane porosity≈67-70%, δ_G=850 μm, δ_L=200 μm, MEA 10%w.t, Y_{CO_2}/Y_{MEA}=96.4.

5.6 Conclusions

Carbon dioxide absorption in amine solutions was studied in a membrane PTFE microstructured reactor. Experimental data were obtained for aqueous amine solutions of (10%w.t MEA, 16.6% DEA) and 20vol%CO_2 inlet concentration, for various liquid and gas flowrates, while keeping the molar flowrate ratio CO_2/Amine at 0.4 in order to keep amine solution in excess (25%). Significant absorption was observed with gas residence times below 0.2 s. A two dimensional model with no adjustable parameters was formulated to simulate the reactor, and experimental results were compared to model predictions in terms of CO_2 removal efficiency. The model shows very good agreement with experimental data. Both

model and experimental results showed that, MEA solution absorbed more CO_2 than DEA. In addition experiments were performed with 6%w.t MEA concentration. Both model and experiments showed less CO_2 removal efficiency with lower MEA concentration. Finally experiments performed with larger contact area between gas and liquid. CO_2 removal efficiency increases by increasing the contact area between gas and liquid when keeping the gas and liquid flowrates the same.

CHAPTER 6

CO_2 ABSORPTION IN PTFE MEMBRANE REACTOR USING AQUEOUS SOLUTION OF NaOH

6.1 Introduction

Carbon dioxide absorption in NaOH solution is an example of a fast gas-liquid reaction. Sodium hydroxide is well used for actual industrial absorption processes of CO_2 [113]. Due to the fast chemical reaction between the CO_2 and NaOH reduces the liquid film resistance with respect to CO_2 transfer [104]. Atchariyawut *et al.* [114] in their work for separation of CO_2 from CH_4 by using gas-liquid membrane contactors, they showed that, in the case of chemical absorption, a higher CO_2 flux was achieved using aqueous NaOH solution than aqueous amine solutions of monoethanolamine (MEA) with the same concentration. This result can be explained by the fact that the reaction rate constant of CO_2 and OH^- is higher than that of CO_2 and MEA, as reported by many researchers.

In this Chapter, CO_2 absorption in sodium hydroxide solution was conducted in a PTFE microstructured membrane reactor. Breakthrough was investigated first in the microreactor in order to establish the operation pressure difference between gas and liquid phase. Various conditions such as gas flowrates, membrane contact area between the gas and the liquid and

liquid concentrations, acceptable distance between the pores were investigated, in order to evaluate, understand and improve its performance of the PTFE membrane reactor.

6.2. CO_2 Absorption in NaOH solutions

6.2.1 Reactor design and experimental conditions

The reactor design and the experimental set-up used for CO_2 absorption in aqueous solution of NaOH are identical to the ones used in Chapter 5 for the single channel PTFE membrane reactor (see figure 5.1c and 5.3). During typical operation the pressure difference between liquid and gas phase was kept at P_L-P_G≈100 cm H_2O. Experimental data were obtained varying the liquid (NaOH 2M) flow rate in the range 1.66-2.56 ml/min and gas (20%vol CO_2) flowrate in the range 160-247 ml/min. These flowrates resulted to residence times, (based on the gas/liquid volumes in contact with the membrane area), 0.10-0.16 s for the gas and 2.3-3.54 s for the liquid respectively. All the experiments were carried out at room temperature (approximately 20^{o}C). The CO_2 removal efficiency was calculated from:

$$X_{CO_2} = 1 - \frac{F_{CO_{2out}}}{F_{CO_{2in}}} \qquad (6.1)$$

where F is the molar flowrate of CO_2. The experimental error in CO_2 removal was assessed to be ± 5%. Two to three chromatographs were taken for each measurement and the deviation between them was about ± 5%.

6.2.2 Mathematical Model

In order to compare the experimental results with theory a two-dimensional model of the microstructured membrane reactor was formulated. The model is a "pseudo-homogeneous model", where the membrane is considered as a homogeneous medium with $D^M_{CO_2} = \frac{\varepsilon}{\tau} D^G_{CO_2}$, where ε is the membrane porosity and τ is the tortuosity (an adjustment parameter which corrects for the pore geometry).

Two variations of the model were implemented. One which considered the membrane pores as gas filled (see Chapter 5) and the second as liquid filled (see Chapter 4). The differential mass balances to describe the concentration profiles of components in the three domains can be seen in Chapters 4 and 5. In addition, the reaction system of NaOH with CO_2 along with all the parameters used for the calculations, are shown in Chapter 4.

6.3 Results and Discussion

6.3.1 Model Prediction for CO_2 Absorption in NaOH Solution

The predictions of the pseudo-homogeneous model for the wetted (pores are considered 100% liquid filled) and the non-wetted (the pores are considered 100% gas filled) mode are compared with experimental results, obtained from carbon dioxide absorption in sodium hydroxide solution using the single channel PTFE membrane reactor. From Figure 6.1 it can be seen that the percentage of CO_2 removal decreases by increasing the gas flowrate, due to the decreasing of the residence time in the reactor. In addition it shows that 14.7-20% of the carbon dioxide contained in the inlet stream was removed. Although CO_2–NaOH system with PTFE membrane has often considered to be non-wetting, partial wetting (some pores are completely filled with liquid and some pores are completely gas filled) is considered in this work. As it can be seen from Figure 6.1 the experimental results have better agreement with the wetted-mode conditions. This is due to the fact that the pores of the PTFE membrane during the experiments were partially wetted and not 100% gas filled. Marzouqi *et al.* [94] in their modelling studies of CO_2 absorption in NaOH solution using membrane contactors showed a partial wetting of the polypropylene membrane. Although CO_2-NaOH with polypropylene hollow fiber membrane is considered to be non-wetting, their experimental results showed agreement with the theoretical results when 20% of the membrane was considered to be wetted. SEM image of their polypropylene (PP) membrane showed large pores, which expected to be easily filled with the solution, which might explain the partial wetting of NaOH solution. Same observation we noticed with our membranes after SEM analysis. Figure 5.2 in Chapter 5 shows SEM pictures of the PTFE membranes used for our

experiments. Despite the fact the membranes pore diameters should be around 1μm, pores with bigger diameter can be seen. Dindore *et al.* [43] in their work of CO_2 absorption at elevated pressures using hollow fiber contactors, they observed that the long-term application results in changes in the membrane surface morphology and consequently wetting behaviour of the polypropylene fiber. SEM analysis of the hollow fiber before and after the use, showed that the number of smaller pores present in the membrane are reduced significantly after use, while the larger pores seemed to have increased in size. This can be explained by the intrusion of solvent into larger pores and subsequent enlargement of larger pores. It is easier to have intrusion into the larger pores than into the smaller pores. After the larger pores are wetted by the solvent, the additional intrusion into the larger pores exerts lateral force on the pore walls causing the displacement of these walls. This displacement of the pore walls of larger pores results in the decrease in the size of smaller pores and possibly blocking of these pores. Similar observations were made by Barbe *et al*. [98] after they examined the membranes using scanning electron microscope (SEM). They observed that the surface morphology of the polypropylene membranes change permanently after they were exposed to water for 72 h, due to the intrusion of the water meniscus into some pores resulting to enlargement of pore entrance. However, membrane wettability also depends on several factors such as contact angle, surface tension, membrane pore size, and breakthrough pressure [1].

Kaisri *et al.* [49] developed a mathematical model for carbon dioxide absorption membrane (PTFE) contactors that studied the effect of partially wetted membranes. Partial membrane wetting was modelled to investigate the effect of membrane mass transfer resistance on the absorption performance and the overall mass transfer coefficient. They showed that, an increase in the percentage of the membrane wetting decreased the absorption flux and the overall mass transfer coefficient significantly. In addition to that, they compared their experimental results with the model and they showed that the absorption performance dropped roughly 56%, 72%, 85% and 90% at the 10%, 20%, 50% and 100% wetting respectively.

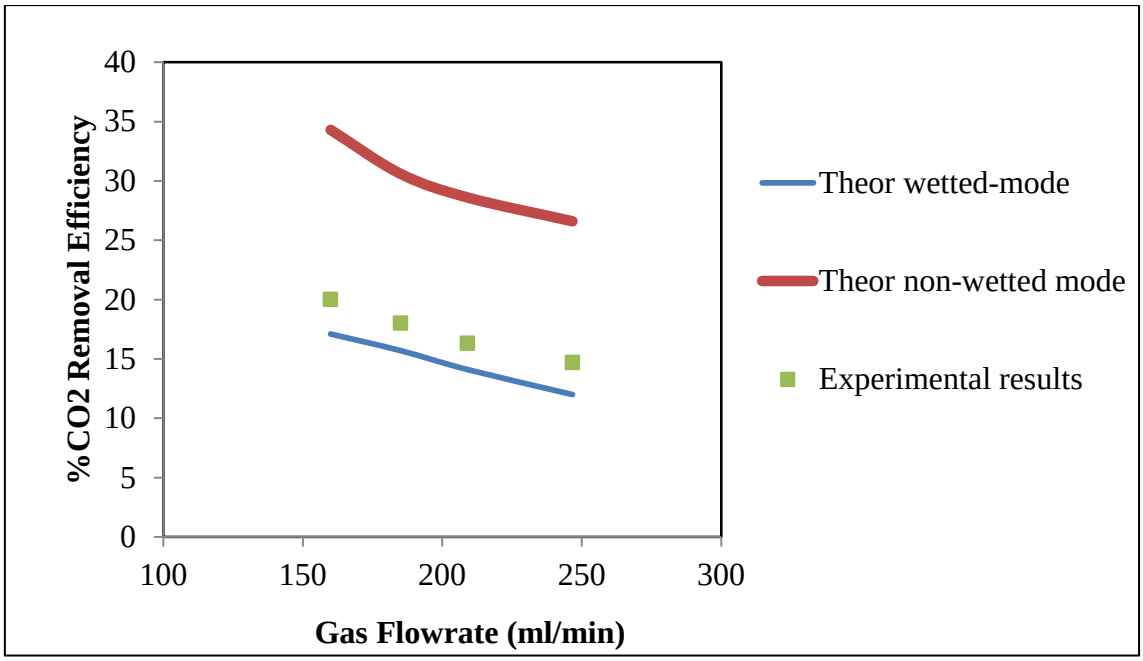

Figure 6. 1 Amount of CO_2 removed from the gas phase as a function of gas flowrate, obtained experimentally and by pseudo-homogeneous model for the wetted and the non-wetted mode using the single channel PTFE membrane reactor. PTFE porosity≈67-70%, δ_G=850 μm, δ_L=200 μm, NaOH 2M, $\mathbf{Y_{CO_2}}/Y_{NaOH}$=96.4.

6.3.2 Influence of membrane's wetting on CO_2 removal

Figure 6.2 shows the experimental results of the 8 channel (PTFE) membrane microreactor (see figure 5.1d) and mesh (metallic) microreactor (see figure 4.1b) in CO_2 absorption as a function of gas residence time. Experimental data were obtained varying the liquid flowrate in the range 1.66-2.56 ml/min and gas flowrates in the range of 230-354 ml/min for both of the reactors. The gas/liquid contact area is 55.9 cm^2 for the 8 channel reactor and 38.7 cm^2 for the metallic mesh reactor. As it can be seen increasing the gas residence time in the reactor increases the CO_2 removal efficiency. Despite the fact that the residence times are only slightly larger in the membrane reactor, the CO_2 removal efficiency is much higher than the mesh reactor. This is due to the fact that the pores of the metallic mesh are completely liquid filled and hence, there is more resistance to mass transfer than the PTFE membrane whose pores are considered to be partially wetted (some pores are completely liquid filled and some pores are completely gas filled). In addition the PTFE membrane used in the experiments consisted of 20 microns thick pure PTFE and 80 microns thick polypropylene layer for

support (see figure 5.2c). As it was shown in Figure 5.2c the pores of the polypropylene layer are very large and hence, they are considered to be liquid filled. From the Figure below it can be seen that CO_2 removal efficiency is higher when the polypropylene layer is on the gas side, than when it is on the liquid side. This is because the polypropylene layer is on the liquid side, since the polypropylene layer is considered to be liquid filled and hence, increases the resistance to mass transfer.

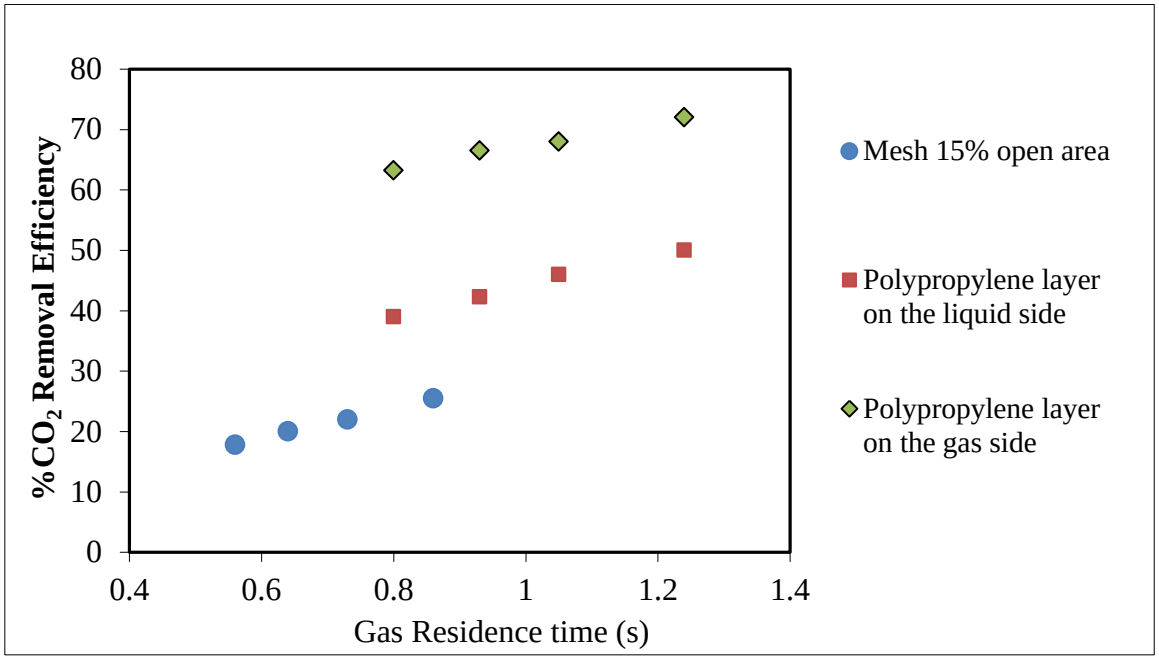

Figure 6. 2 Experimental comparison between the 8 channel (PTFE) membrane reactor with mesh (metallic) reactor. PTFE porosity 65-70%, Mesh porosity=15%, δ_G=850 μm, δ_L=200 μm, NaOH 2M, Y_G/Y_L=139.5.

6.3.3 Influence of the gas liquid contact area

Figure 6.3 shows the experimental results of CO_2 removal for the 8 channel PTFE membrane reactor as a function of gas flowrates. Experimental results were compared with the predictions of the pseudo-homogeneous model for the wetted and the non-wetted conditions. As it can be seen from Figure 6.3 the experimental results have better agreement with the wetted-mode conditions for the same reasons explained in section 6.3.1. In addition the percentage of CO_2 removal increases by decreasing the gas flowrate. Furthermore, from the comparison between the experimental results of Figure 6.3 and 6.1 it can be seen that the CO_2 removal efficiency is much higher for the 8 channel reactor than the single channel reactor.

63-72% of the carbon dioxide contained in the inlet stream was removed within 0.8-1.24 s experimental gas residence time for the 8 channel reactor, while in the single channel reactor 14.7-20% of carbon dioxide was removed within 0.1-0.16 s experimental gas residence time. This is due to the fact the gas/liquid contact area (55.9 cm^2) between CO_2 and NaOH for the 8 channel reactor is much larger (approximately 11.3 times larger than the contact area of the single channel reactor) than the single channel reactor (4.9 cm^2 gas/liquid contact area) and hence, higher gas residence times for CO_2 to react with NaOH solution as a result higher CO_2 removal efficiency.

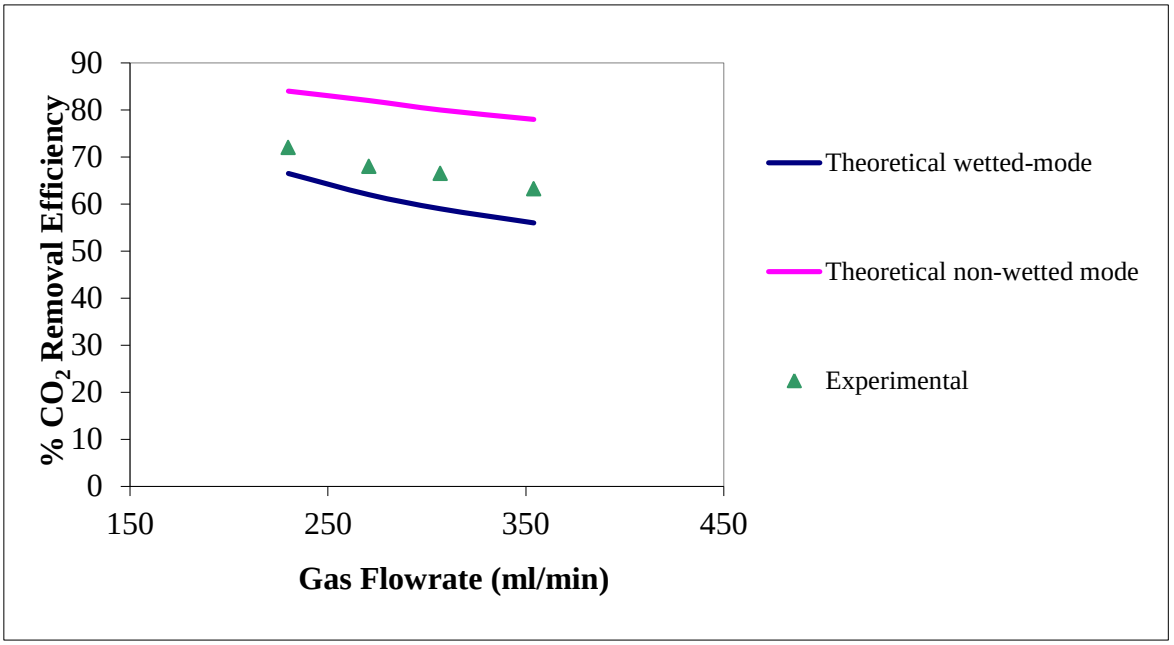

Figure 6. 3 Amount of CO_2 removed from the gas phase as a function of gas flowrate, obtained experimentally and theoretically by the 8 channel PTFE reactor. Membrane porosity≈67-70%, δ_G=850 μm, δ_L=200 μm, NaOH 2M, Y_G/Y_L=139.5, Polypropylene layer in the gas side.

6.3.4 Influence of NaOH concentration on CO_2 removal

Experiments also performed with 1M NaOH concentration. Figure 6.4 shows the experimental comparison between two different NaOH concentrations for CO_2 removal as a function of gas flowrates. Lower NaOH concentration, leads to less CO_2 removal efficiency. This is due to the fact lower NaOH concentration provides lower reaction rate, hence less CO_2 removal efficiency. Same observation was reported from Marzouqi *et al*. [100] in their work

of chemical absorption of CO_2 in polypropylene membrane contactors. They showed that by increasing the concentration of NaOH from 0.005M to 0.01M, $\%CO_2$ removal efficiency was increased. Aroonwilas *et al.* [115] in their studies 'behaviour of the mass transfer coefficient of structured packings in CO_2 absorbers with chemical reactions', showed that increasing the NaOH concentration induces higher CO_2 absorption performance.

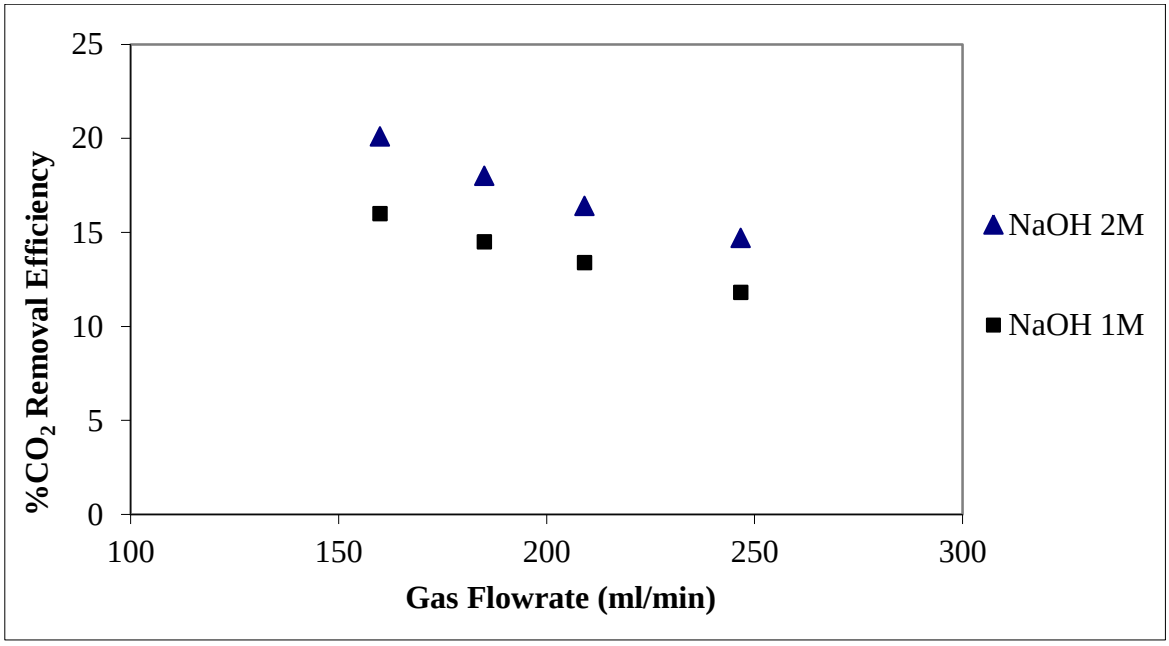

Figure 6. 4 Amount of CO_2 removed from the gas phase as a function of gas flowrate, obtained experimentally. Membrane porosity≈67-70%, δ_G=850 μm, δ_L=200 μm, Y_{CO_2}/Y_{NaOH}=96.4.

6.3.5 Influence of the absorbent type

Figure 6.5 shows the experimental prediction of CO_2 removal using aqueous solutions of NaOH (2M) and DEA (1.62M) as a function of gas flowrate. It can be seen that CO_2 removal efficiency is higher when NaOH is used as an absorbent liquid. The reason for that is not only due to the fact that NaOH concentration is slightly higher than DEA concentration, but is mainly because the reaction rate constant of CO_2 and OH^- is higher than that of CO_2 and DEA, as a result higher CO_2 removal efficiency. Similar trends were observed from other researchers. Aroonwilas *et al.* [115] they examined the behaviour of mass-transfer coefficient of structured packings in CO_2 absorbers with chemical reactors, and they observed that the

use of NaOH as an absorbent gives higher mass transfer than when AMP (2-amino-2-methyl-1-1-propanol) was used as an absorbent for CO_2.

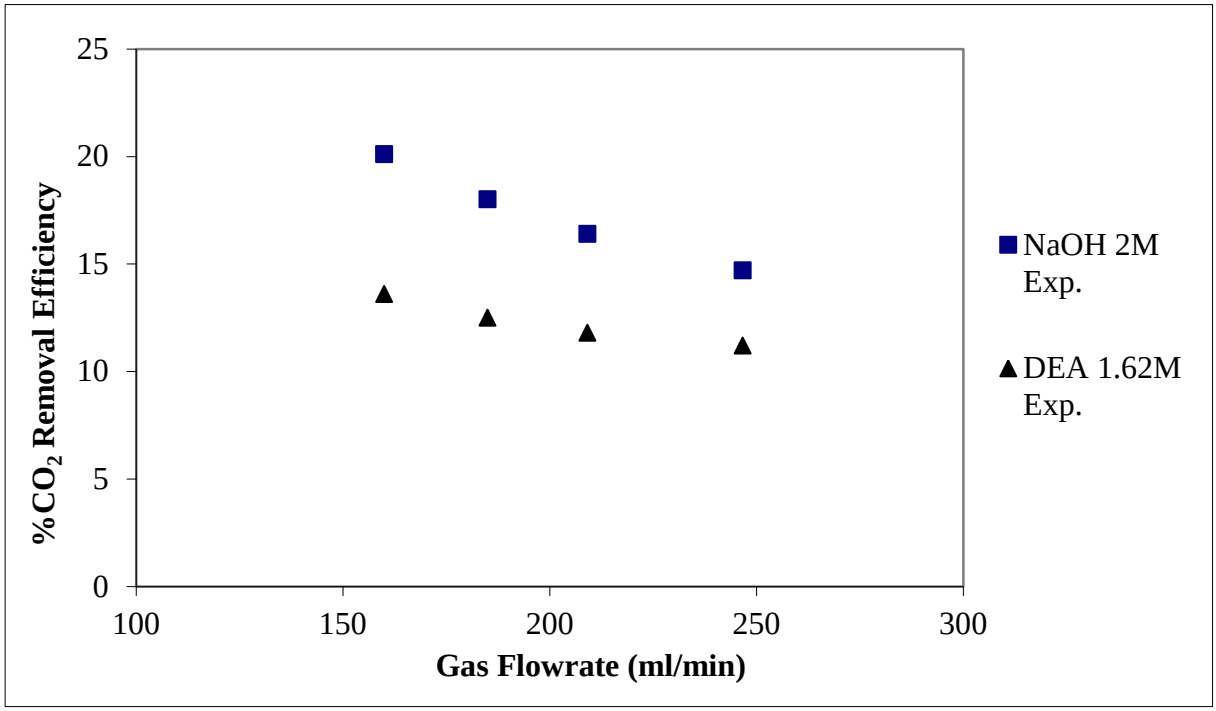

Figure 6. 5 Amount of CO_2 removed from the gas phase as a function of gas flowrate, obtained experimentally using NaOH 2M and DEA 1.62M as absorbent liquids in the single channel PTFE membrane reactor. Membrane porosity≈67-70%, δ_G=850 μm, δ_L=200 μm, Y_{CO_2}/Y_{NaOH}=96.4.

6.3.6 Comparison between PTFE membrane reactor with hollow fiber reactors from literature

In this paragraph a comparison of our experimental results obtained by the PTFE membrane reactor with hollow fiber membrane reactors from literature is shown. Table 6.1 shows the governing properties of the various reactors. In the single channel PTFE membrane microreactor used in this chapter, 20% of CO_2 from a 20 vol% CO_2 stream was absorbed in ca. 0.16 s gas residence time, using 2M NaOH . The membrane used in our experiments was made out of PTFE, with pore size of 0.5-5 μm and porosity of 67-70%. In addition, membrane's length was 9 cm with a contact area of 4.9 cm^2. Furthermore, experiments were performed also with the 8 channel PTFE membrane reactor (see figure 5.1 Chapter 5).

Approximately 72% of the CO_2 was captured using the same liquid and gas concentrations as above in 1.24s gas residence time. The characteristics of the membrane were the same as above except that the length and the contact area of the membrane change to 13 cm and 55.9 cm^2 respectively. Shirazian and Ashrafizadeh [113] observed that in a hollow-fiber membrane contactor 52% of CO_2 was removed from a stream of 10vol% CO_2/N_2 in 50 s gas residence time in 2M diethanolamine (DEA) solution. They used polypropylene membranes with pore size of 0.04 μm, porosity of 40%, and fiber length of 113 mm, diameter of 0.3 mm, and a contact area of 0.09m^2. Kim and Yang [39] investigated absorption of carbon dioxide through hollow fiber using various aqueous absorbents. They almost reached 100% capture of CO_2 from a stream of 40vol% CO_2/N_2 in 16 s gas residence time in 2M monoethanolamine (MEA) solution. They used PTFE membranes with pore size of 0.8 μm, porosity of 62%, and fiber length of 240 mm, diameter of 0.9 mm, and a contact area of 0.034 m^2. Marzouqi *et al.* [100] performed experiments with polypropylene (PP) hollow fiber membrane contactors. They removed up to 80% of CO_2 from a stream of 10 vol% CO_2/CH_4 in 57 s gas residence time in 0.01M NaOH solution. The characteristics of their membrane were: pore size of 0.36 μm, porosity of 40%, and fiber length of 228.86 mm, diameter of 0.3 mm and a contact area of 0.57 m^2. In order to compare all the modules together, modified residence times were calculated. Modified gas residence time is defined as the surface area of gas/liquid contact area over inlet volumetric gas flowrate. As it can be seen from the Figure 6.6 the 8 channel PTFE membrane reactor has the best performance among the modules, since for the smallest modified gas residence time has removed 72% of CO_2.

Table 6. 1 Comparison between the PTFE membrane reactor with hollow fibre membrane reactors from literature.

Reactor type/ Governing properties	**Single channel PTFE membrane reactor**	**Eight channel PTFE membrane reactor**	**Hollow fibre membrane reactor [113]**	**Hollow fibre membrane reactor [39]**	**Hollow fibre membrane reactor [100]**
CO_2 removal (%)	20	72	52	100	80
Gas Residence Time (s)	0.16	1.24	50	16	57
Membrane's pore size (µm)	1	1	0.04	0.8	0.36
Membrane porosity (%)	67-70	67-70	40	62	40
Membrane length (cm)	9	13	11.3	24	22.9
Fibre diameter (mm)			0.3	0.9	0.3
Gas-liquid contact area (m^2)	0.00049	0.00559	0.09	0.034	0.57
Absorbent type (in M)	2 NaOH	2NaOH	2DEA	2MEA	0.01NaOH
Gas mixture (%vol.)	20 CO_2/N_2	20 CO_2/N_2	20 CO_2/N_2	40 CO_2/N_2	10 CO_2/CH_4

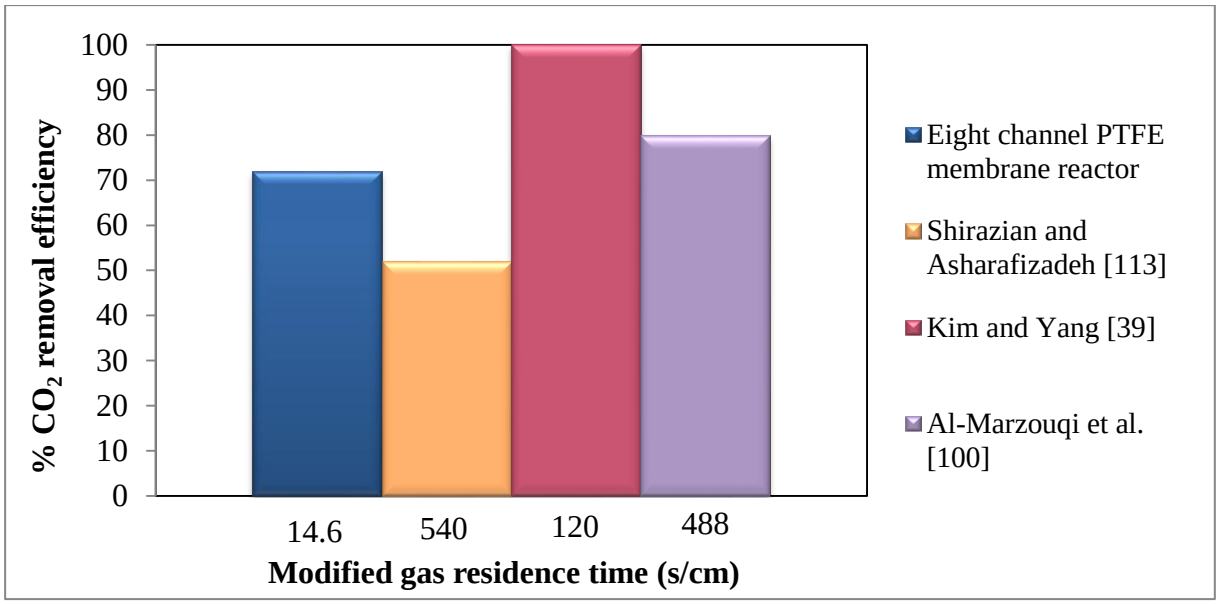

Figure 6. 6 Amount of CO_2 removed from the gas phase as a function of modified gas residence times. Comparison between the 8 channel reactor with hollow fiber membrane reactors from literature.

6.3.7 Phase Breakthrough

6.3.7.1 Contact angle measurements

The value of the contact angle of the aqueous solution of NaOH 2M was measured on the porous PTFE membrane and on pure PTFE. A drop of the solution was placed on a piece of porous PTFE membrane and on a pure PTFE and the analysis was performed with Keyence microscope (VHX-600). The apparent contact angle on the porous PTFE membrane was found around 145° (see figure 6.7b) while the contact angle on pure PTFE was found around 115.18° (see figure 6.7c). The apparent contact angle measured experimentally is in a good agreement with Cassie and Baxter equation (see chapter 5 equation 4) and it was found around 145.7°. Figure 6.7 shows the experimental set-up used for the measurements, and the optical image of the NaOH droplet on the porous and pure PTFE membrane.

(a)

(b)

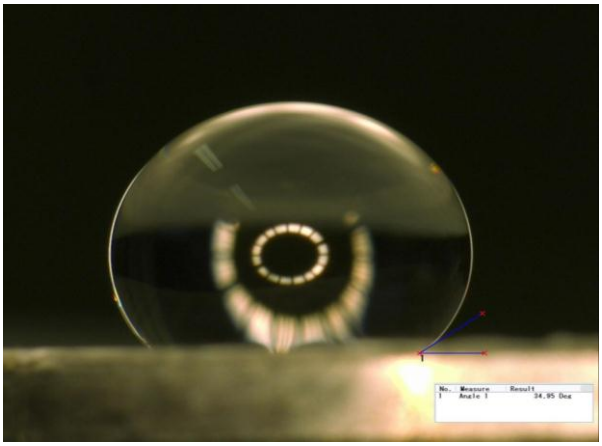

(c)

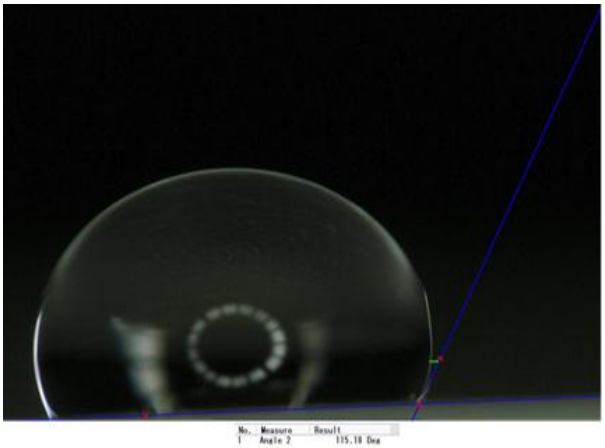

Figure 6. 7 (a) Experimental set-up for the contact angle measurement (b) Optical images of a 2M NaOH droplet on the porous PTFE membrane (c) Optical images of a NaOH droplet on the pure PTFE membrane.

6.3.7.2 Breakthrough studies

Breakthrough was investigated in order to establish the acceptable operational pressure difference between gas and liquid which keeps the two phases separated. Figure 6.8 shows an experiment where liquid from the bottom chamber has entered the gas-phase channel when increasing the liquid phase pressure beyond the breakthrough pressure. The theoretical breakthrough pressure of NaOH solution can be calculated by the Young-Laplace equation as:

$$\Delta P = \frac{-2\gamma\cos\theta}{r} \qquad (6.23)$$

where γ is the surface tension of 2M NaOH, r is the radius of the membrane pore, and θ is the contact angle of the liquid with the membrane material.

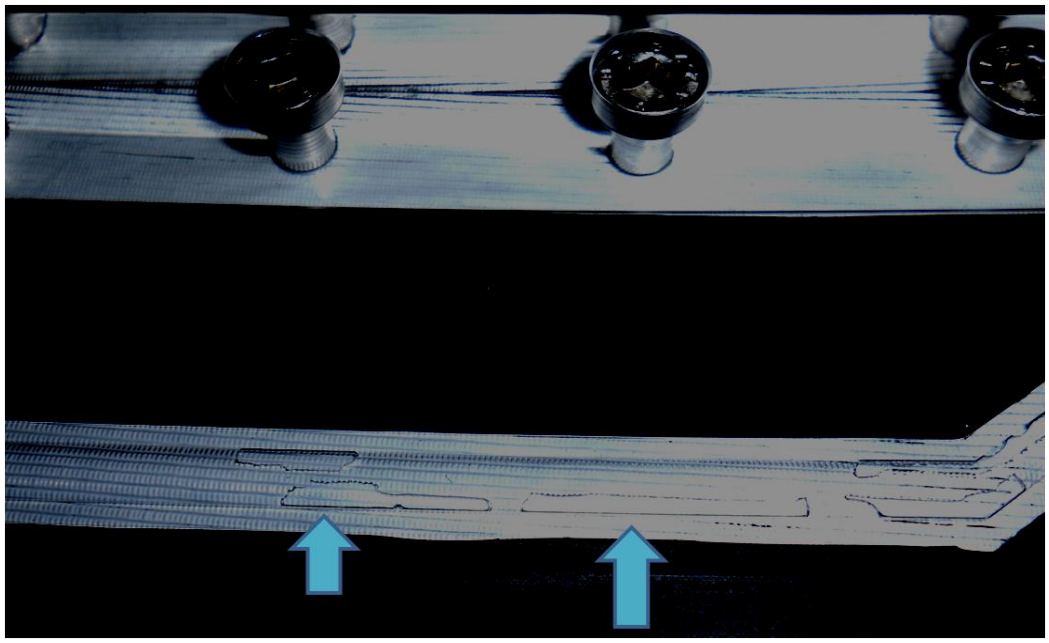

Figure 6. 8 Picture of the top (gas) side of the single channel reactor, during a breakthrough experiment. The arrows indicate breakthrough of the liquid into the gas phase.

Breakthrough experiments identify that the breakthrough of liquid in gas the phase occurred at pressure difference P_L-P_G of about 200-220 cm H_2O. Based on equation (6.23) the theoretical value of breakthrough should be 247 cm H_2O, with surface tension γ=0.073 N/m, pore diameter 5 μm and contact angle approximately 115.18° which is in agreement with the experimental values.

6.3.8 One pore model

In order to examine the influence of the distance between the pores (i.e how close the pores can be to each other without causing overlap of the diffusion fields around the individual pores) in the PTFE membrane, on the performance of the microreactor. 2D simulations of a single pore were performed in order to examine the concentration profiles of CO_2 and NaOH in the liquid side of the microreactor. The differential mass balances to describe the concentration profiles of components in the three domains (gas/pore/liquid) were the convection-diffusion-reaction equations coupled with the Navier-Stokes equation (Navier-Stokes for the liquid side). Non-slip boundary conditions were applied to all boundary walls. The differential mass balances and the assumptions used in this model are identical with the ones used for the absorption of CO_2 in the PTFE membrane reactor and are reported in section 5.2, except that laminar flow profile was considered in the liquid phase instead of plug flow. The pore is considered to be gas filled. Figure 6.9 shows the concentration profile of CO_2 in the liquid phase (pore and liquid phase are enlarged in order to observe the concentration profiles adjacent to the pore). From Figure 6.9 and 6.10 (transverse concentration profile of CO_2 in the liquid phase at z_2) it can be seen that CO_2 was consumed approximately within 2-3 μm from the pore-liquid interface. Such small penetration distances were also observed for CO_2 absorption in NaOH solution in a falling film microstructured reactor by Zanfir and Gavriilidis [10].

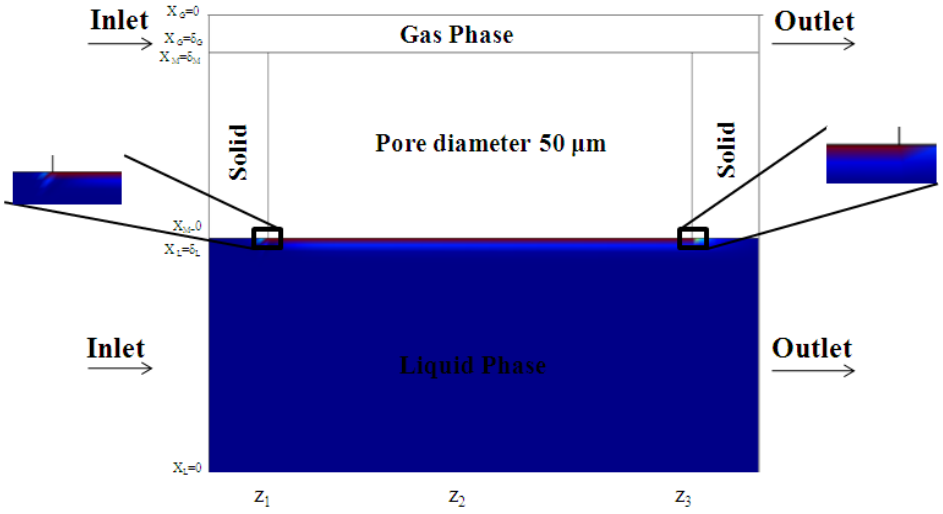

Figure 6. 9 Concentration map of CO_2 in the liquid phase at z_2. Pore diameter≈50 μm, δ_G=850 μm, δ_L=200μm, δ_M=20 μm, Y_{CO_2}/Y_{NaOH}=96.4, NaOH=2M.

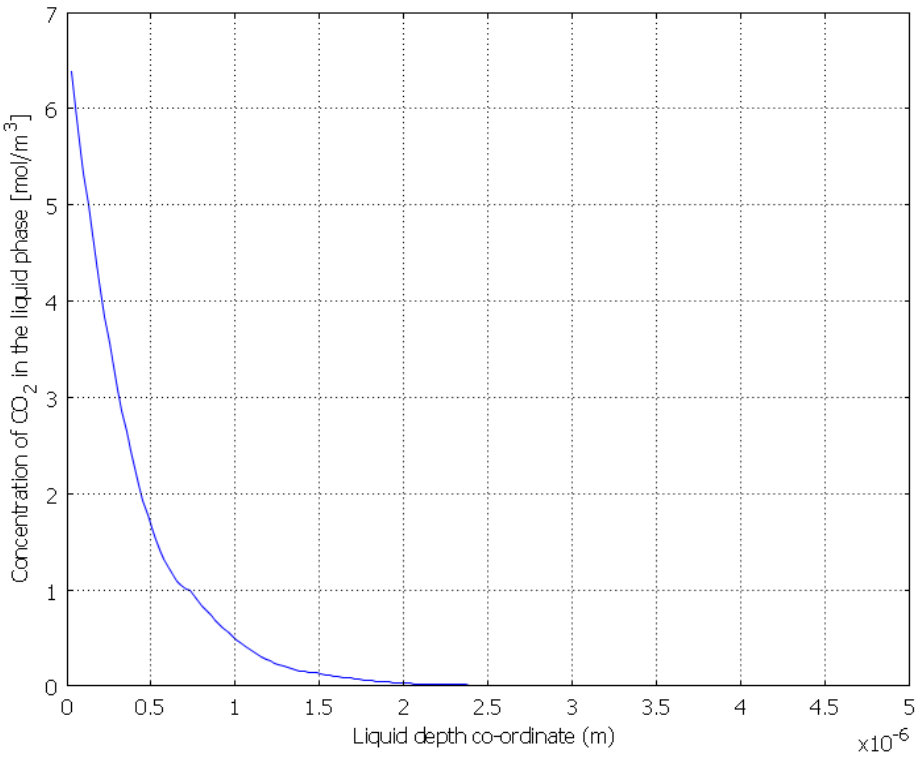

Figure 6. 10 Transverse concentration profiles of CO_2 in the liquid phase at z_2. Pore diameter≈50 μm, δ_G=850 μm, δ_L=200 μm, Y_{CO_2}/Y_{NaOH}=96.4, NaOH=2M.

Furthermore it can be seen that CO_2 exists in a distance of approximately 2-3 μm (z direction) adjacent to the pore walls, which means that when the micropores in the membrane are in a distance of more than 2-3 μm they do not cause overlap of diffusion fields (around the individual pores), which might affect the $\%CO_2$ removal effeciency. Similar results were observed when simulations were performed with plug flow profile in the liquid phase (results are not shown). In addition the model was used to calculate the concentration profile of NaOH in the liquid phase. Figure 6.11 shows the concentration map of NaOH and Figure 6.12 the transverse concentration profile of NaOH in the liquid phase at z_2. As it can be seen from Figure 6.12 the NaOH concentration is almost constant and drops just 1% in 0.1μm distance from the pore/liquid interface, while as it was reported above CO_2 was consumed 100% in 2-3μm from the liquid-pore interface. Finally transverse concentration profiles of CO_2 and NaOH in the liquid phase were calculated along the pore at positions z_1 and z_3 (results are not shown). The transverse concentration profiles of CO_2 and NaOH do not change signifigantly compared to Fig 6.10 and Figure 6.12 (at position z_2), due to the fact that the distance between z_1 and z_3 is very small (50 μm).

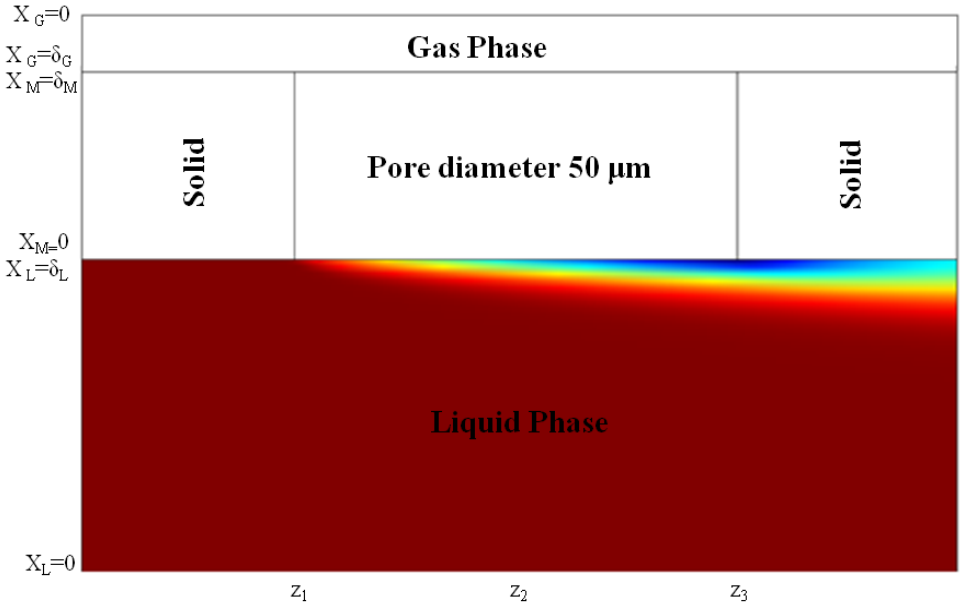

Figure 6. 11 Concentration map of NaOH in the liquid phase. Pore diameter=50 µm, δ_G=850 µm, δ_L=200 µm, Y_{CO_2}/Y_{NaOH}=96.4, NaOH=2M.

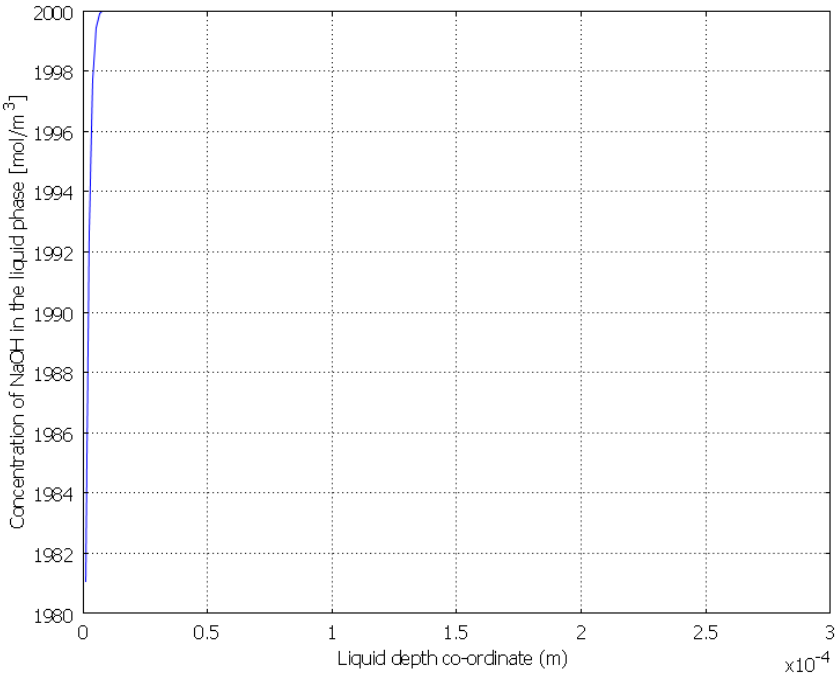

Figure 6. 12 Transverse concentration profiles of NaOH in the liquid phase at z_2. Pore diameter=50 µm, δ_G=850 µm, δ_L=200 µm, Y_{CO_2}/Y_{NaOH}=96.4, NaOH=2M.

Finally to examine the effect of the pore diameter, simulations were performed with pore diameters larger than 50 µm. Figure 6.13 shows the concentration map of CO_2 in the liquid

side for 100 μm pore diameter incorporated by the velocity profile (red arrows in figure 6.13). From Figure 6.13 it can be seen that the concentration profile adjacent to the pore walls remains the same with the concentration profile examined before for 50 μm pore diameter. In addition it can be seen from the velocity profile that by increasing the pore diameter a small circulation of the fluid starts to be created below the membrane area, which might help in mass transfer enhancement.

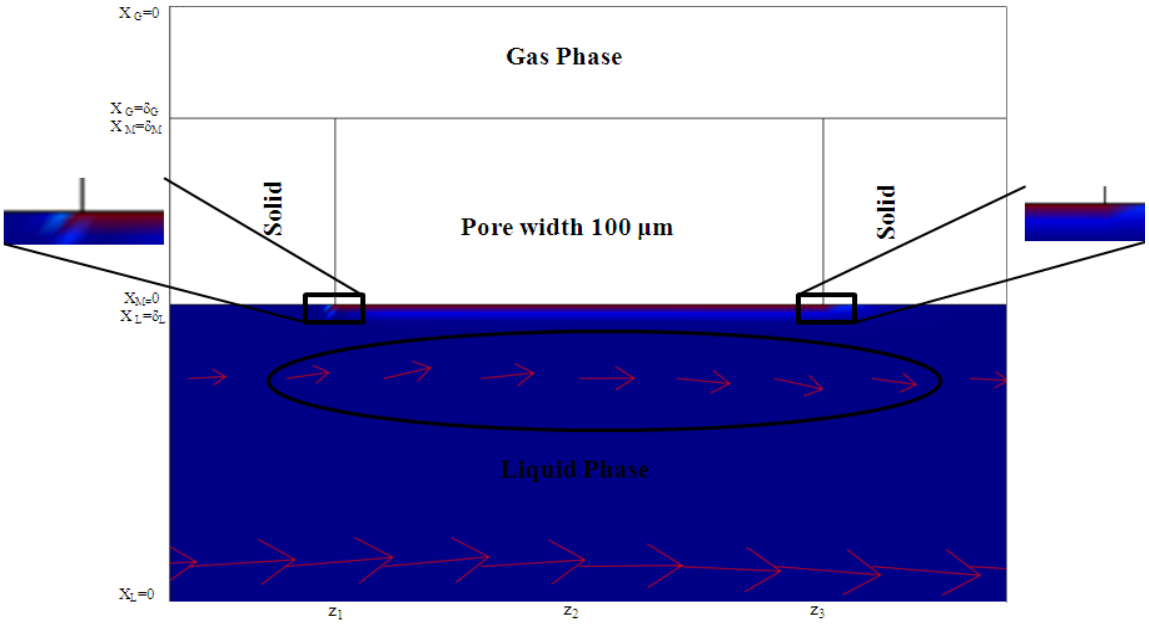

Figure 6. 13 Concentration map of CO_2 in the liquid phase, incorporated by the velocity profile (red arrows). Pore diameter 100μm, δ_G=850 μm, δ_L=200 μm, Y_{CO_2}/Y_{NaOH}=96.4, NaOH=2M.

6.4 Conclusions

Carbon dioxide absorption in NaOH solution was studied in a PTFE membrane microstructured reactor. Significant absorption was observed with gas residence times below 0.2s. A two dimensional model with no adjustable parameters using wetted and non-wetted operation conditions was formulated to simulate the reactor, and experimental results were compared to model predictions in terms of CO_2 removal efficiency. Experimental results showed better agreement with the wetted-mode conditions than the non-wetted conditions. An explanation to that might be the fact that the pores of the PTFE membrane are partially wetted

and not 100% gas filled. Comparison between (PTFE) microreactor and mesh (metallic) microreactor showed much higher CO_2 removal efficiency for the PTFE membrane reactor than the mesh microreactor. This is due to the fact that the pores of the PTFE membrane are considered to be partially wetted (some pores are completely liquid filled and some pores are completely gas filled) and hence, there is less resistance to mass transfer than the metallic mesh which the pores of the mesh are completely liquid filled. Experiments showed that the CO_2 removal efficiency reduces with lower concentration of NaOH, since lower concentration provides lower reaction rate. Furthermore, experiments performed with larger contact area between gas and liquid. CO_2 removal efficiency increases by increasing the contact area between gas and liquid. Using NaOH as an absorbent liquid showed higher CO_2 removal efficiency than when DEA was used as an absorbent liquid. Finally simulations were performed using just a single pore in order to understand the effect of the distance between the pores (i.e how close the pores can be to each other without causing overlap of the diffusion fields around the individual pores) in the PTFE membrane, on the performance of the microreactor. 2D simulations showed that CO_2 exists in a distance of approximately 2-3μm (z direction) adjacent to the pore walls, which means that when the micropores in the membrane are in a distance of more than 2-3μm they do not cause overlap of diffusion fields, which might affect the CO_2 removal efficiency. In addition CO_2 was consumed 100% approximately within 2-3μm from the liquid-pore interface, while the NaOH concentration was almost constant and dropped just 1% in 0.1 μm distance from the pore/liquid interface. Furthermore, simulations were performed with pore diameter of 100 μm. The concentration profiles of CO_2 in the liquid phase adjacent to the pore walls remained the same with the concentration profiles examined for 50 μm pore diameter. Finally from the velocity profile in the liquid phase it was showed that by increasing the pore diameter more than 100 μm a small circulation of the liquid starts to be created below the membrane area.

CHAPTER 7
EFFECT OF STAGGERED HERRINGBONES ON CO_2 ABSORPTION USING AQUEOUS SOLUTION OF NAOH IN PTFE MEMBRANE REACTOR

7.1 Introduction

The minimization of chemical processes is becoming a popular trend in the chemical engineering field. Due to the small dimensions of the microchannels, the surface to volume ratio is several orders of magnitude higher compared to conventional equipment. Based on this the rates of heat and mass transfer are high, resulting to a greater reaction yield and selectivity. However, for applications with high Peclet number, Pe=ud/D>100, radial mass transfer is purely diffusive, thus, ways of stirring to intensify mass transfer are necessary.

Stroock *et al*. [116] in their work for chaotic mixing in microchannels proposed the staggered herringbone micromixer, which has been shown to be effective for mixing applications [117, 118, 119, 120, 121, 122, 123, 124, 125, 126]. Recently it was shown that the presence of staggered herringbones in a channel has a higher mass transfer rate compared to a standard

rectangular channel. Kirtland *et al.* [127] simulated mass transfer on the top wall of a channel with floor staggered herringbone structures by tracking passive tracers over a range of Peclet number with an instantaneous kinetics at the reactive boundary. They found that the staggered herringbones leads to increased rates of mass transfer compared to a standard rectangular channel. Yoon *et al.* [128] described 3 methods to overcome mass transfer limitation to reactive surfaces: (i) removing the depleted zone through multiple periodically-placed outlets, (ii) adding fresh reactants through multiple periodically-placed inlets along the reactive surface, or (iii) producing a spiralling, transverse flow through the integration of herringbone ridges along the channel walls. They showed that approaches (i) and (ii) are better at improving the reactant conversions rate; on the other hand the space required for operation and the pressure drop is higher than approach (iii). Golden *et al.* [129] used grooves for redirecting the flow and enhancing delivery of the molecules from the bulk to the surface and preventing the formation of a depletion layer at the surface. Comparing assay results in grooved and plain channels showed that the mixers improved assay results by 26-46%. Lopez and Graham [130] have shown that the shear induced diffusion in flowing suspensions can also enhance mass transfer to boundaries. They showed that the most effective way to enhance mass transfer is through a combination of both herringbones structures and shear-induced diffusion. The shear-induced diffusion was found to enhance transport across the boundary layer, while the herringbones structures were found to be effective at circulating fluid between the bulk and the boundary layer.

In this chapter carbon dioxide absorption in sodium hydroxide solution was studied in a PTFE membrane microstructured reactor with and without the use of staggered herringbones on the floor of the liquid channel of the reactor, in order to examine the effect of staggered herringbones in CO_2 removal efficiency. In addition a 3D model was formulated in order to compare theoretically the CO_2 removal efficiency between a channel with the staggered herringbones on it and a channel without the herringbones. Furthermore, analytical model which describes acetone mass transfer from water solution to the nitrogen stream flowing co-currently was formulated in order to examine the effect of staggered herringbones on stripping of acetone from water. Further information about the experimental part of this work can be found elswere [131].

7.2 Reactor design and experimental conditions

The reactor design and the experimental set-up used for CO_2 absorption in aqueous solution of NaOH with and without the used of staggered herringbones are identical to the ones described in detail in previously (chapter 5) for the absorption of CO_2 in aqueous solutions of amines and NaOH in the acrylic single channel PTFE membrane microreactor. The herringbone structures employed on the microchannel floor of the liquid channel are presented in figure 7.1 and are similar to the ones proposed by Stroock *et al.* [116]. In our case the channel width is 5.47 mm and the channel height is 200 μm, while in Stroock's paper channel width is 200 μm and channel height is 85 μm. In our case groove depth is 60 μm, groove width is 100 μm, and the groove length is 400 μm. The grooves are placed at an angle of θ=45° with respect to the channel width. In Stroock's work groove depth is 30 μm, groove width is 50 μm, and the groove length is 200 μm. The grooves are placed at an angle of θ=45°. By factor of two groove depth, width and length are larger than Strook's herringbones. Furthermore, multiple herringbones exist along the channel width in order to cover the entire channel width with herringbones (since herringbone groove's length is 400 μm and the channel width is 5.47 mm). In addition the channel is divided in cycles, each one consisting of 13 herringbones (in the entire width of the channel) of twelve asymmetric grooves along length (AB structure) Figure 7.1, for our case while in Stroock's work each cycle consists of one herringbone in the entire width of twelve asymmetric grooves. The position of the asymmetry changes every half cycle. An alternative herringbone structure (ABCD) suggested by Cantu-Perez [137], is shown in Figure 7.1. The ABCD structure is the AB herringbone structure with CD herringbone structure, combined together to form ABCD herringbone structure. Each cycle changes form AB structure to CD structure. In the CD structure instead of having 13 herringbones spanning the entire width of the channel, there are 26 herringbones, covering the entire width. The fabrication of the herringbones structures at the microchannel floor of the acrylic reactor was done by using a milling machine (SM 1500, UK). The fabrication of such small grooves (depth=60 μm, width=100 μm) on the acrylic microchannel floor has it limits, as a result an alternative fabrication method has to be considered to improve the quality of herringbones. In order to improve the imperfections of the staggered herringbones (see figure 7.1c,d) during the fabrication on the floor of the acrylic plate, which could make the staggered herringbones insufficient to create sufficient stirring, silicon inserts (525 μm thick) with the staggered herringbones on it were fabricated using conventional semi-conductor processing

techniques (see Appendix B) and placed in 725 μm deep liquid channel of the acrylic reactor in order to provide 200 μm liquid channel thickness (see figure 7.1f,g). In order to compare the staggered herringbones with a channel without herringbones on CO_2 removal efficiency, flat silicon insert of 525 μm thick with dimensions of 90 mm x 5.47 mm (LxW) was fabricated as well.

Experimental data were obtained varying the liquid (NaOH 2M) flow rate in the range 1.66-2.56 ml/min and gas (20%vol CO_2) flowrate in the range 160-247 ml/min. During typical operation (Y_G=247 ml/min, Y_L=2.56 ml/min) the pressure difference between liquid and gas phase was kept at P_L-P_G≈90 cm H_2O.

(a)

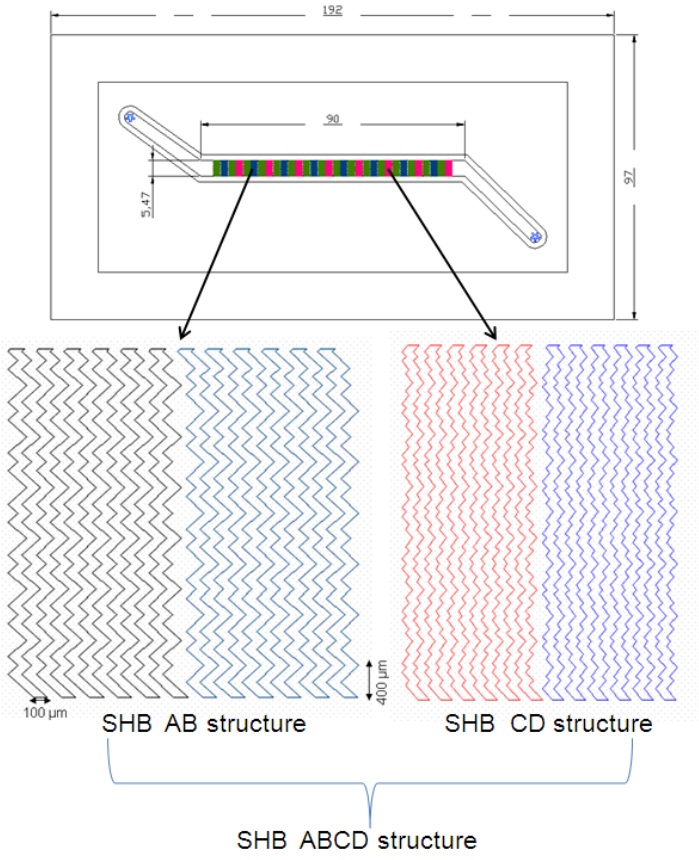

(b)

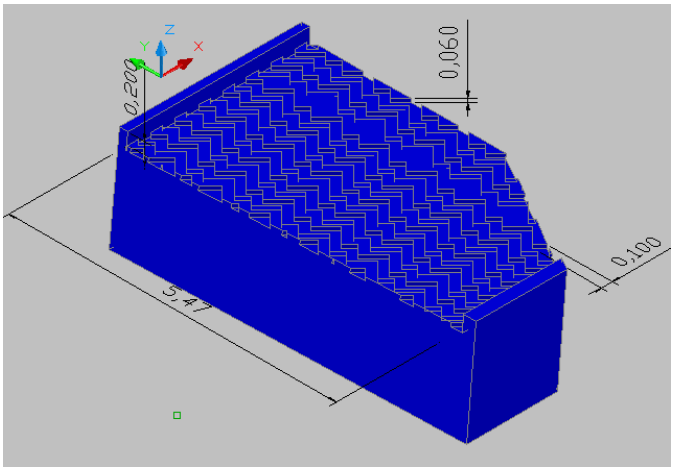

(c)

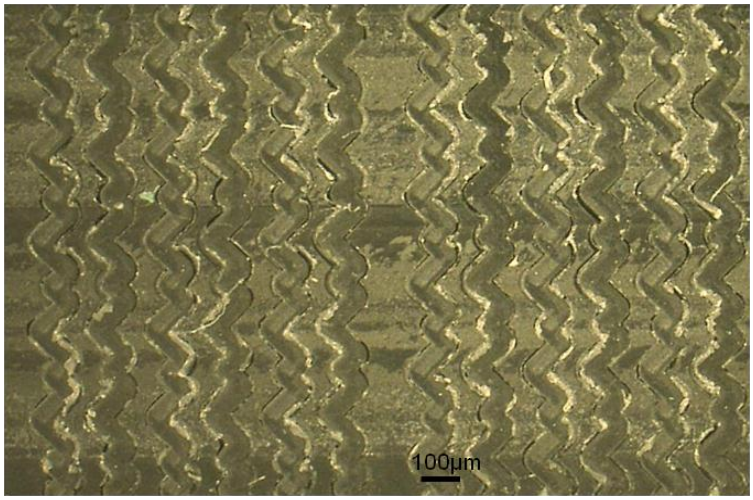

(d)

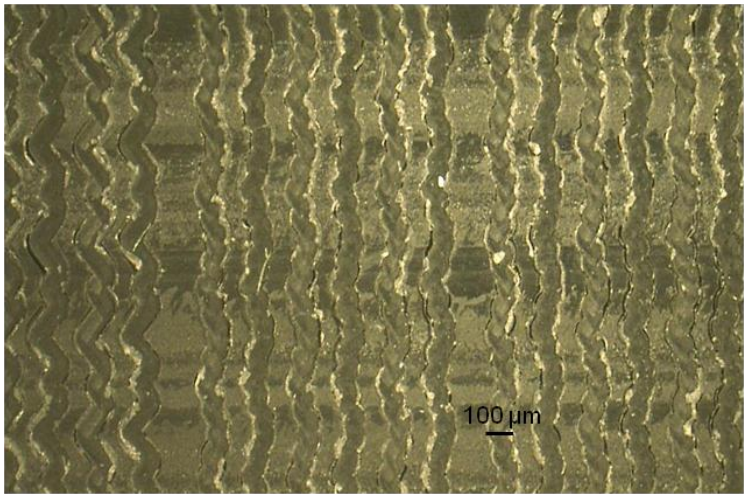

(f)

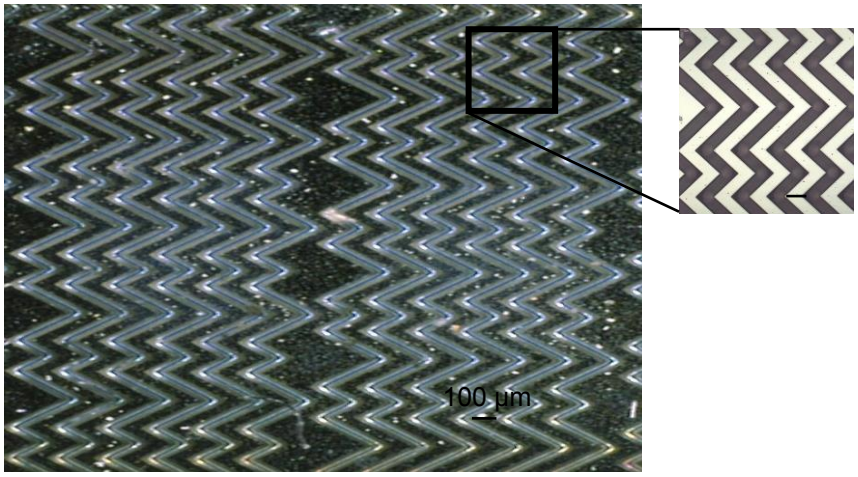

(g)

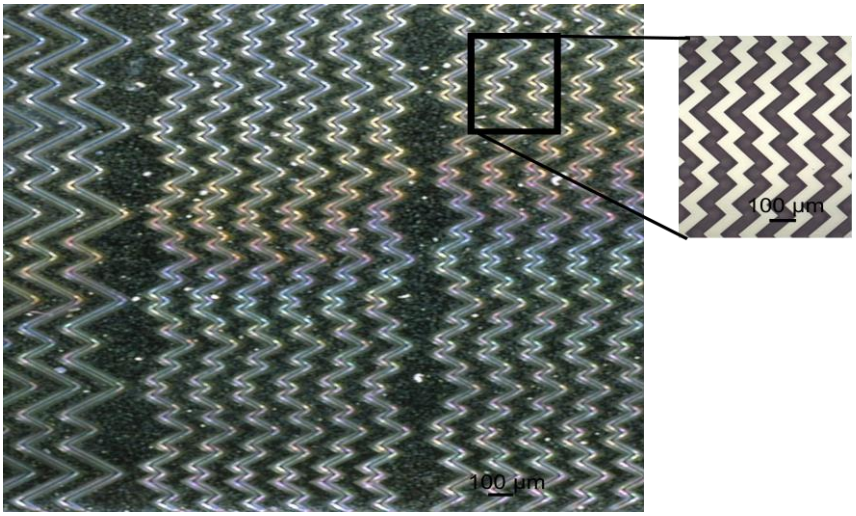

(h)

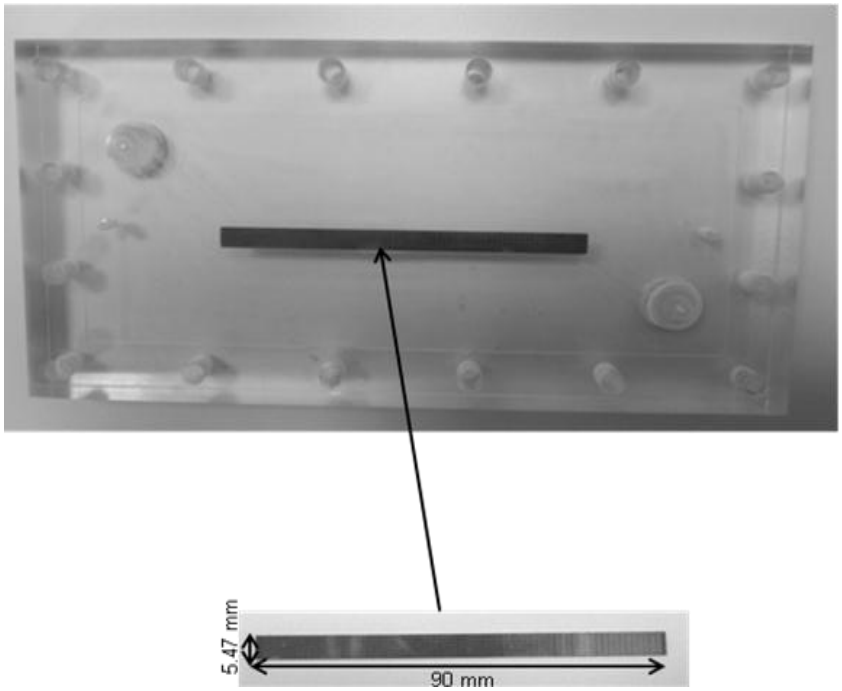

Figure 7. 1 (a) Schematic of the acrylic plate with the staggered herringbones structures (AB), (CD) and (ABCD) (b) 3D schematic of a part of the liquid channel with the staggered herringbones on the floor of the channel. Dimensions are in mm (c) Optical image of the SHB AB structure on the floor of the acrylic liquid channel (d) Optical image of the SHB ABCD structure on the floor of the acrylic liquid channel (f) Optical image of silicon insert of the SHB AB structure (g) Optical image of silicon insert of the SHB ABCD structure (h) Bottom plate (liquid side) of the acrylic reactor with silicon insert.

7.3 Mathematical model development

7.3.1 Numerical model for CO_2 absorption with and without the use of herringbones

In order to study the effect of the staggered herringbones on the CO_2 removal efficiency a three-dimensional model (see figure 7.2 for the geometries used in the 3D models) of the microstructured membrane reactor was formulated with and without the use of the staggered herringbones on the floor of the liquid side. The numerical simulations were performed with COMSOL Multiphysics 3.5.a, commercial modelling software based on the finite element method that solves the Navier-Stokes and mass conservation equations simultaneously. The velocity field is solved using periodic boundary conditions so that the velocity at the outlet boundary is the same as the inlet one, with a constant flowrate throughout the channel. This allows using the simulated velocity field for one cycle, over many successive cycles if entrance effects are neglected (Very small entrance length of 0.01 cm, while the total length is 9 cm). The volumetric flowrate is calculated by integrating the velocity profile which is obtained after specifying a pressure drop across the cycle and setting the outlet pressure equal to the inlet minus the pressure drop. Non-slip boundary conditions are applied to all boundary walls. The differential mass balances to describe the concentration profiles of components for the reaction occurring, can be found by solving the convection-diffusion-reaction equations coupled with the Navier-Stokes equation. The differential mass balances used to describe the concentration profiles of the components in the three domains gas/membrane/liquid phase are identical with the ones used in Chapter 5 for CO_2 absorption by NaOH solution using non-

wetted conditions. A mesh consisting of 561421 number of elements and 1252378 degrees of freedom is used to execute the simulations in Windows XP with Pentium IV 2.93GHz CPU and 24GB of RAM. At this number of elements the solution was found to be mesh independent. Cell peclet number was checked and it was found 1.4 which implies that we had stable model without numerical errors (often called numerical diffusion) [132].

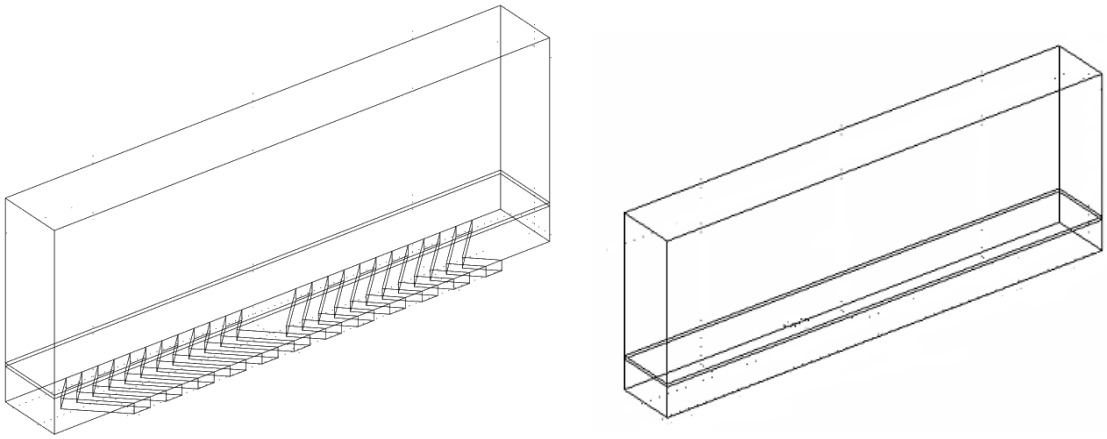

(a) (b)

Figure 7. 2 3D geometry used in the simulations (a) SHB for AB structure (b) Single channel without SHB.

7.3.2 Analytical model of stripping of acetone from water

Analytical model which describes acetone mass transfer from water solution to the nitrogen stream flowing co-currently was formulated under the assumptions of (a) constant gas and liquid flowrates, (b) dilute mixtures, (c) isothermal and isobaric conditions and (d) constant mass transfer coefficient. The analytical model solution of the model provides the outlet actone concentration in the liquid phase of the PTFE membrane contactor $C_{Ac,out}$ as function of the inlet concentration $C_{Ac,in}$, the contactor length L and two dimensionless parameters β and Ω (for more details see Appendix C):

$$\frac{C_{Ac,out}}{C_{Ac,in}} = \frac{1}{1+\Omega}\left\{1+\Omega\cdot\exp\left[-\beta\cdot\left(1+\frac{1}{\Omega}\right)L\right]\right\} \tag{7.1}$$

$$\Omega = \frac{F_g}{F_l}\cdot\frac{1}{H} \tag{7.2}$$

$$\beta = \frac{K_T \cdot \tau_l}{\delta_l \cdot L} \tag{7.3}$$

where F_g and F_l are gas and liquid volumetric flowrates, H, is the Henry's law coefficient (defined as ratio of liquid to gas concentrations), K_T , overall mass transfer coefficient based on the liquid phase, τ_l , liquid residence time, δ_l , liquid channel thickness. The overall mass transfer coefficient is calculated from [59]:

$$\frac{1}{K_T} = \frac{1}{k_l} + \frac{H}{k_m} + \frac{H}{k_g} \tag{7.4}$$

where k_l, k_m, k_g, re the mass transfer coefficients in the liquid phase, the membrane phase and the gas respectively. When the Graetz number, $Gz=Re\cdot Sc\cdot 2\delta/L<20$ the laminar flow can be considered as fully developed in rectangular channels [133]. Then the Nusselt number has a constant value of 4.86 [134] for one wall transferring heat. Due to heat-mass transfer analogy this will be the same value for the Sherwood number ($k\cdot 2\delta/D$) and can be used for the calculation of the gas and liquid mass transfer coefficients. The Gz number for nitrogen flowrates studied (160-280 ml/min) was in the range of 0.4-0.7 and for liquid flowrates used (0.13-0.3 ml/min) was in the range of 0.8-1.8. The mass transfer coefficient in the membrane was calculated from equation (7.5) for gas filled membranes pores.

$$\frac{H}{K_m} = \frac{H \cdot \delta_m \cdot \tau}{D_g \cdot \varepsilon} \tag{7.5}$$

where D_g is the diffusion coefficient of the gas, ε is the porosity, δ_m is the thickness and τ is the tortuosity of the membrane(calculated as $\tau=(2-\varepsilon)^2/\varepsilon$ [135]). The model was formulated in order to study theoretically the effect of staggered herringbones on $\frac{C_{Ac,out}}{C_{Ac,in}}$ for the stripping of acetone from water.

7.4 Results and Discussion

7.4.1 Influence of different structures of staggered herringbones fabricated in acrylic plates on CO_2 removal effciency

Figure 7.3 shows the experimental results on CO_2 removal efficiency with and without the use of staggered herringbones on the liquid channel floor of the single channel PTFE membrane contactor. The different structures of staggered herringbones (AB and ABCD) shown in Figure 7.3 are the ones fabricated on the acrylic microchannel floor. From the graph it can be seen that CO_2 removal efficiency is slightly lower for the AB structure compared with the channel without herringbones (flat channel) and the ABCD structure, while CO_2 removal efficiency is almost the same for the flat channel and ABCD structure. The experimental results obtained from the staggered herringbones show that staggered herringbones did not have the effect on mass transfer as reported in literature [127, 136]. A reason that might explain this behaviour is that the PTFE membrane is partially wetted and not fully gas filled and hence, the use of staggered herringbones will not improve the mass transfer coefficient, since the wetting in the pores of the membrane will increase the mass transfer resistance in the membrane. In addition imperfections of the staggered herringbones on the acylic floor of the reactor (see figure 7.1c,d) during the fabrication might prevent the fluid of penetrating in the herringbone grooves, as a result the staggered herringbones might be insufficient to create sufficient stirring of the fluid, which is necessary for the enhancement of mass transfer. Despite the imperfections of staggered herringbones, from Figure 7.4 it can be seen that the fluid penetrates inside the staggered herringbones grooves (gas air bubbles in liquid fluid). Furthermore considering the 60 μm of the depth of the staggered herringbone grooves on the total volume of the liquid phase it can be said that a slight improvement was achieved with the ABCD structure, because by increasing the volume of the liquid side the residence time in the liquid chamber is increased. In Chapter 4 it was showed that by increasing the liquid residence time CO_2 removal efficiency decreases. Based on that the advantage of ABCD structure is that, an increase of the residence time (10-15%) in the liquid side can be acheived without decreasing CO_2 removal efficiency compared with the flat channel. Finally,

experiments were performed using 1M NaOH. Figure 7.5 shows the comparison between the flat channel with the AB herringbone structure. The idea of using lower NaOH concentration is due to the fact that NaOH will be consumed slower near the membrane/liquid interface and leads to penetration of carbon dioxide deeper in the liquid phase, hence the staggered herringbones might help to move the unreacted NaOH from the bottom of the liquid chamber to the membrane/liquid interface, and hence more CO_2 will be consumed. In Figure 7.5 it can be seen that CO_2 removal is slightly higher when AB structure was used compared with the flat channel. This might be due to the reason mentioned above or due to experimental error which was found to be ± 5%. Further explanations of the reasons why staggered herringbones are insufficient to improve mass transfer in our case will be discussed more in next sections.

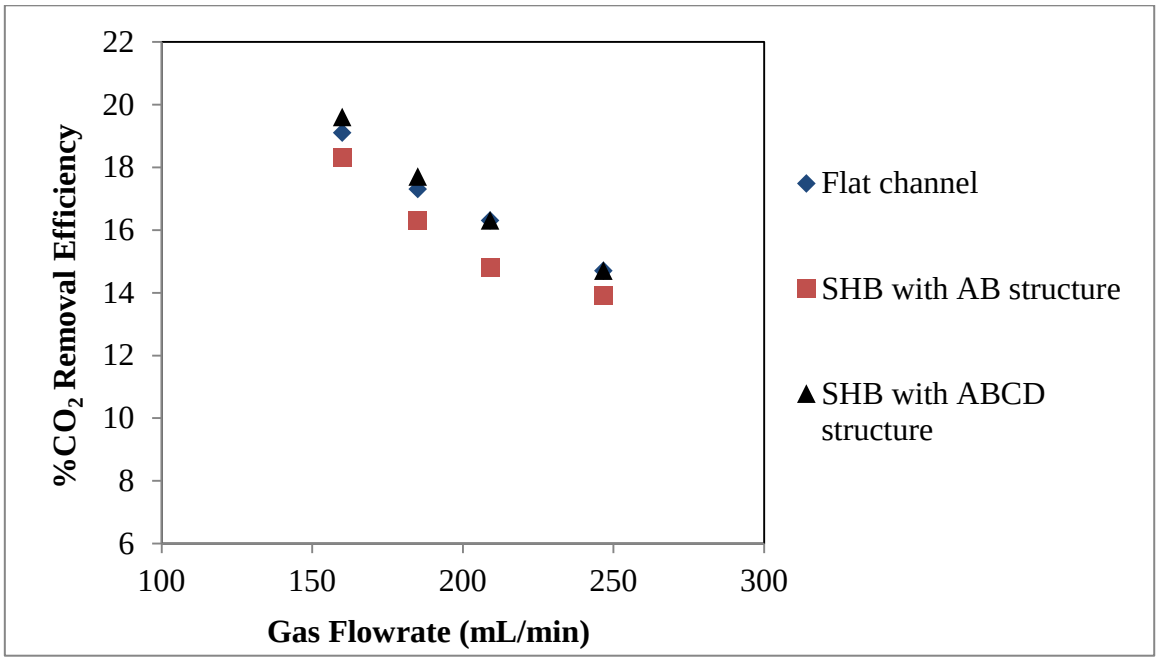

Figure 7. 3 Experimental comparison between the flat channel with two different structures of staggered herringbones (AB and ABCD) engraved on the liquid channel floor of the acrylic reactor. PTFE porosity=65-70%, δ_G=850 µm, δ_L=200 µm, Y_{CO_2}/Y_{NaOH}=96.4, NaOH 2M.

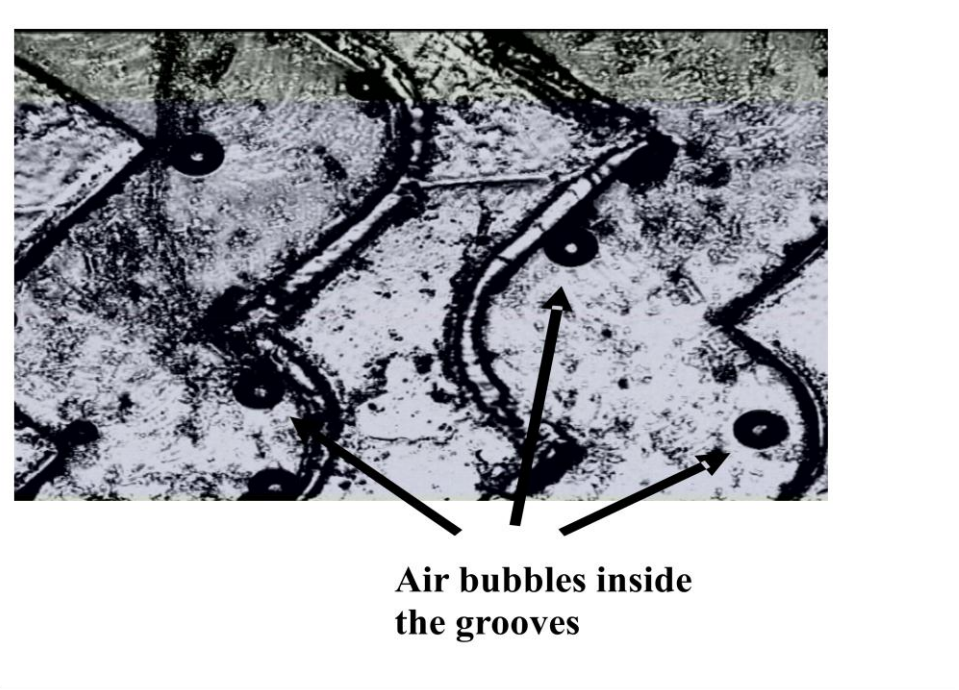

Figure 7. 4 Optical picture of a section of staggered herringbones on the acrylic floor of the liquid channel indicating the existence of liquid (see gas air bubbles) in the grooves of herringbones.

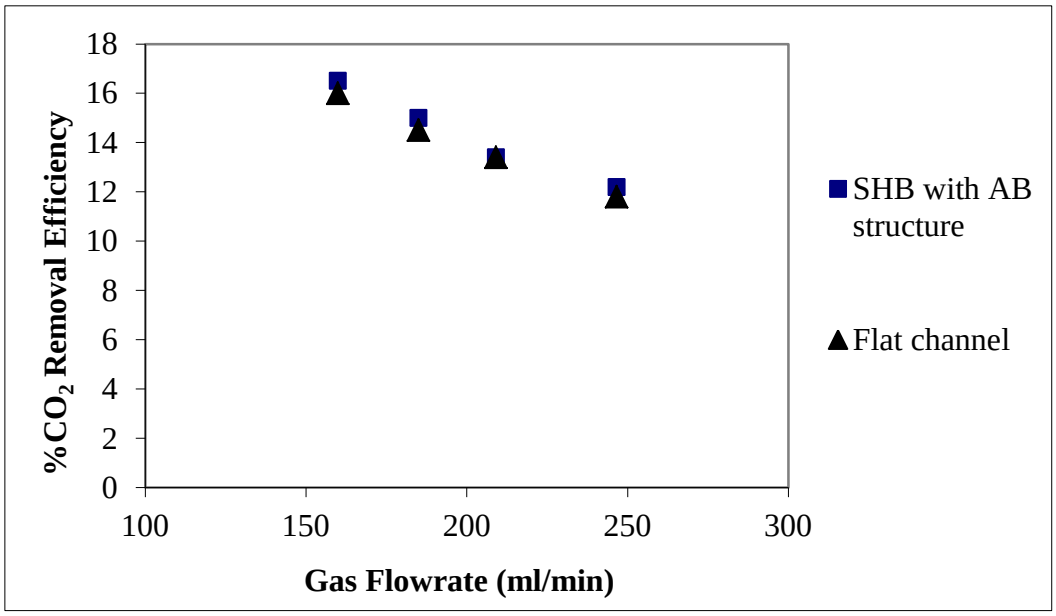

Figure 7. 5 Comparison between the flat channel with the staggered herringbones (AB structure) engraved on the liquid channel floor of the acrylic reactor. PTFE porosity≈65-70%, δ_G=850 µm, δ_L=200 µm, Y_{CO_2}/Y_{NaOH}=96.4, 1M NaOH.

7.4.2 Influence of different structures of staggered herringbones fabricated in silicon inserts on CO_2 removal effciency

In order to examine if the imperfections of the staggered herringbones on the floor of the acrylic plate (see figure 7.1 b, c) was the reason of the non improvement of the mass transfer due to insufficient stirring, silicon inserts silicon (525 μm thick) with and without the staggered herringbones were placed in 725 μm deep liquid channel (see figure 7.1 f) in order to provide 200 μm liquid channel thickness. As it can be seen from Figure 7.1 f and g, the staggered herringbones are much more precisely made on the silicon inserts than the floor of the acrylic plates (figure 1c, d). Figure 7.6 shows the comparison between the flat silicon insert with two different silicon inserts structures of staggered herringbones (AB and ABCD). It can be seen that CO_2 removal efficiency is slightly lower for the ABCD structure compared with the flat insert and the AB structure, while CO_2 removal efficiency is slightly higher for the AB structure compared with the flat insert. As it can be seen from the results the imperfections of the staggered herringbones on the acrylic plates was not the reason of the non improvement of the mass transfer. A reason might explain this behaviour of non improvement of mass transfer is that the staggered herringbones are too far from the liquid/membrane interface where the reaction takes place, and hence, the staggered herringbones do not influence the mass transfer near the liquid/membrane interface. Cantu Perez [137] showed in his work that the highest stirring intensity, therefore higher convecting mass transfer was found close to the channel floor. In the following sections follow further explanations for the reasons that might cause the non improvement of mass transfer with the use of staggered herringbones are provided.

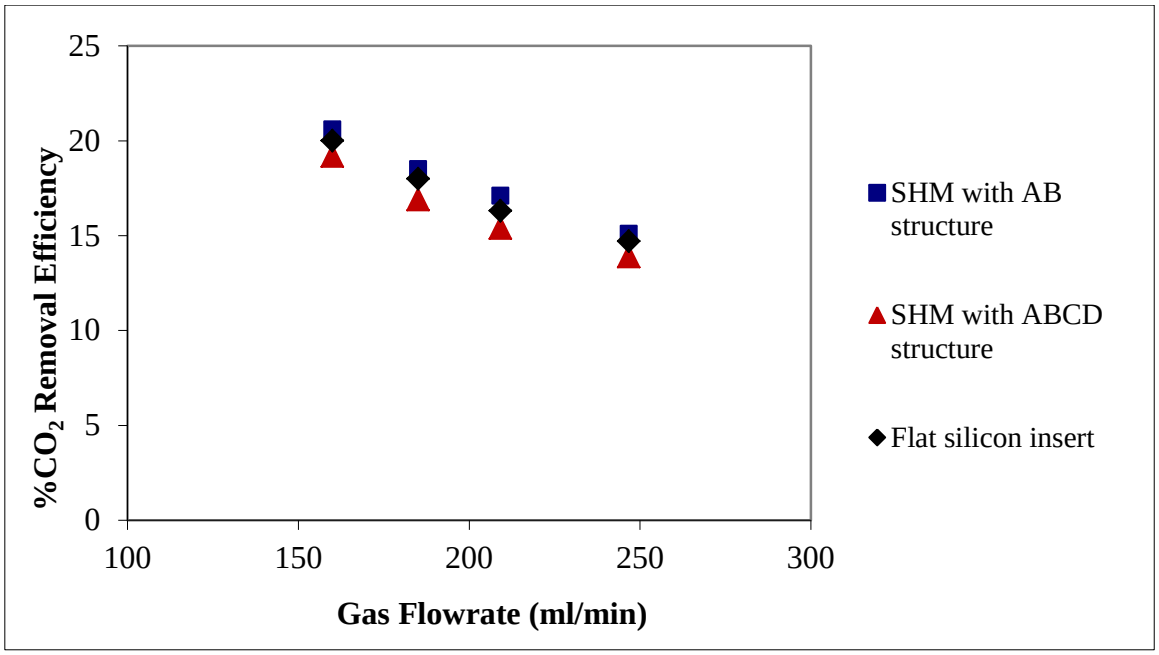

Figure 7. 6 Experimental comparison between two different structures of staggered herringbones (AB and ABCD) fabricated on silicon inserts with a flat silicon insert. PTFE porosity≈65-70%, δ_G=850 μm, δ_L=200 μm, Y_{CO_2}/Y_{NaOH} =96.4, NaOH 2M.

7.4.3 Model prediction for CO_2 removal with and without the use of staggered herringbones

In order to investigate the reasons of the non improvement of staggered herringbones in mass transfer, theoretical simulations were executed with and without the use of staggered herringbones. Figure 7.7 shows the comparison between a channel with staggered herringbones AB structure with a flat channel for CO_2 removal efficiency as a function of gas flowrate. It can be seen that the staggered herringbones do not show any improvement on CO_2 removal efficiency compared with the flat channel. Figure 7.8 and 7.9 show the cross-sectional concentration profiles of NaOH in the liquid side with and without the use of staggered herringbones at a length of (z/δ_L =77.5). It can be seen that the herringbones stir the liquid so that the reacted material from the liquid/membrane interface is distributed along the centre of the channel compared to the channel without herringbones where the liquid is not distributed along the cross section (see figure 7.9). This trend for the staggered herringbone channel is in agreement with literature [137]. In addition Figure 7.10 shows the cross-sectional concentration profile of CO_2 in the liquid side at a length of (z/δ_L =77.5) which is

the same for both cases (with and without staggered herringbones). Since the penetration of CO_2 in the liquid side takes place only for few microns from the liquid/membrane interface as it can be seen from Figure 7.10 the use of staggered herringbones on the floor of the liquid side does not have any effect on the concentration profile of CO_2. This is why the cross-sectional concentration profile of CO_2 with and without the herringbones is identical as shown in Figure 7.10.

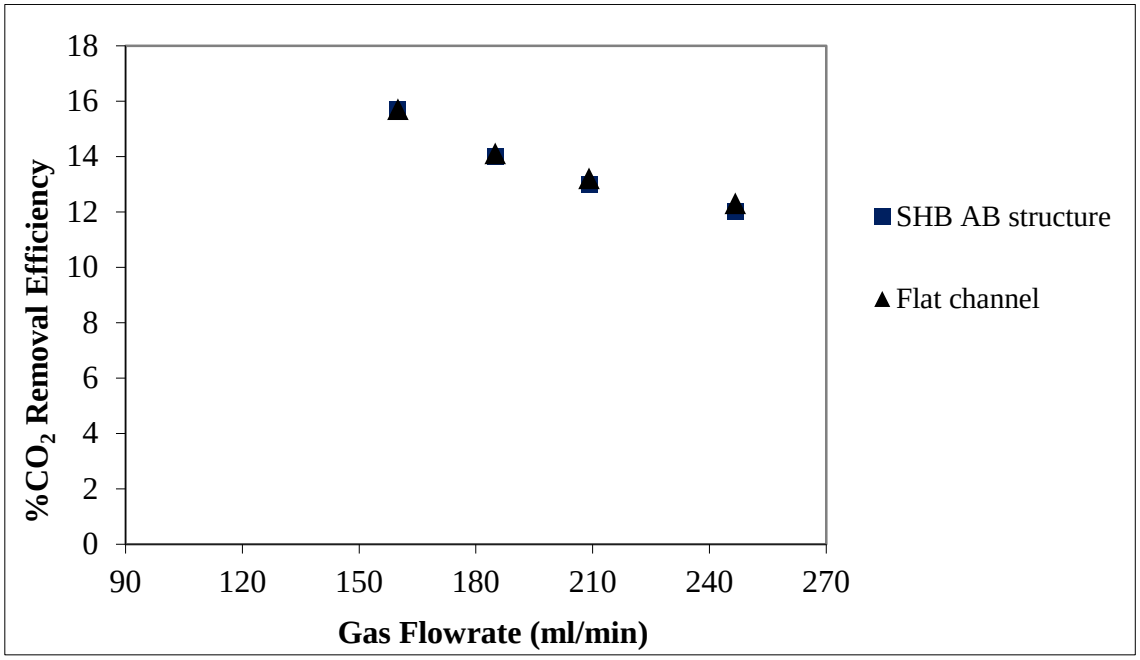

Figure 7. 7 Theoretical simulations with and without the staggered herringbones for CO_2 removal efficiency at a length of (z/δ_L =77.5). PTFE porosity≈65-70%, δ_G=850 μm, δ_L=200 μm, NaOH 2M, Y_{CO_2}/Y_{NaOH}=96.4.

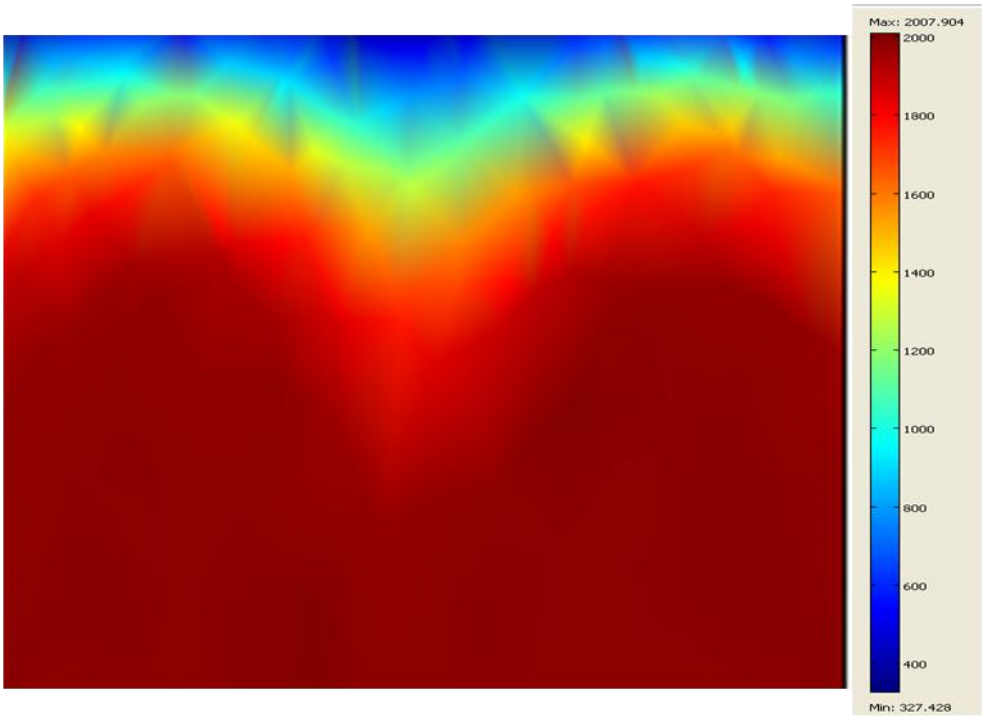

Figure 7. 8 Cross-sectional concentration map of NaOH in the liquid side at a length of (z/ δ_L =77.5) with the use of staggered herringbones. PTFE porosity≈65-70%, δ_G=850 μm, δ_L=200 μm, NaOH 2M, Y_{CO_2}/Y_{NaOH}=96.4, Pe~10^3.

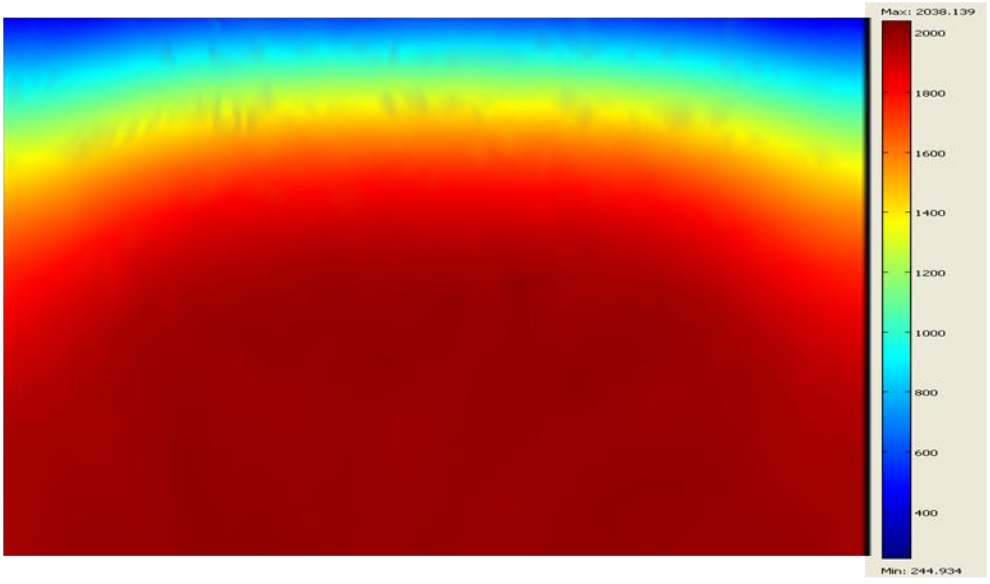

Figure 7. 9 Cross-sectional concentration map of NaOH in the liquid side at a length of (z/ δ_L =77.5) without the use of staggered herringbones. PTFE porosity≈65-70%, δ_G=850 μm, δ_L=200 μm, NaOH 2M, Y_{CO_2}/Y_{NaOH}=96.4, Pe~10^3.

Figure 7. 10 Cross-sectional concentration profile of CO_2 in the liquid side at a length of (z/ δ_L =77.5) with the use of staggered herringbones. PTFE porosity≈65-70%, δ_G=850 μm, δ_L=200 μm, NaOH 2M, Y_{CO_2}/Y_{NaOH}=96.4, Pe~10^3.

7.4.4 Model prediction for stripping of acetone from water with and without the use of staggered herringbones

In order to investigate more the effect of staggered herringbones on mass transfer, an analytical model for the stripping of acetone from water was formulated. Furthermore, the idea is to calculate the mass transfer coefficient of acetone k_l in the liquid phase (with and without the staggered herringbones) according to Sherwood numbers from Kirtlands paper [127] and then to see the effect of the k_l on the ratio $\frac{C_{Ac,out}}{C_{Ac,in}}$. Figure 7.12 shows the calculated k_l using the Sherwood numbers from Kirtlands paper (figure 6) [127] with and without the use of staggered herringbones for Peclet number~10^3 as a function of length (z/H). As it can be seen the k_l number with SHB diverges from the k_l without the SHB at z/ δ_L ~20. k_l reaches its plateau at earlier and higher value than without SHB which is in agreement with kirtland's results [127] . Furthermore, from equation (7.1) $\frac{C_{Ac,out}}{C_{Ac,in}}$ was calculated with the use of k_l from Figure 7.12 for (z/ δ_L) from 20-100. As it can be seen from Figure 7.12 the ratio $\frac{C_{Ac,out}}{C_{Ac,in}}$ is not improved by the k_l values with the staggered herringbones and is

almost the same for both cases (k_l with and without SHB). This observation of the non improvement of the ratio $\frac{C_{Ac,out}}{C_{Ac,in}}$ with the use of staggered herringbones is in agreement with the theoretical and experimental studies on CO_2 absorption (showed before) with and without the use of staggered herringbones which showed no improvement on CO_2 removal with the use of SHB.

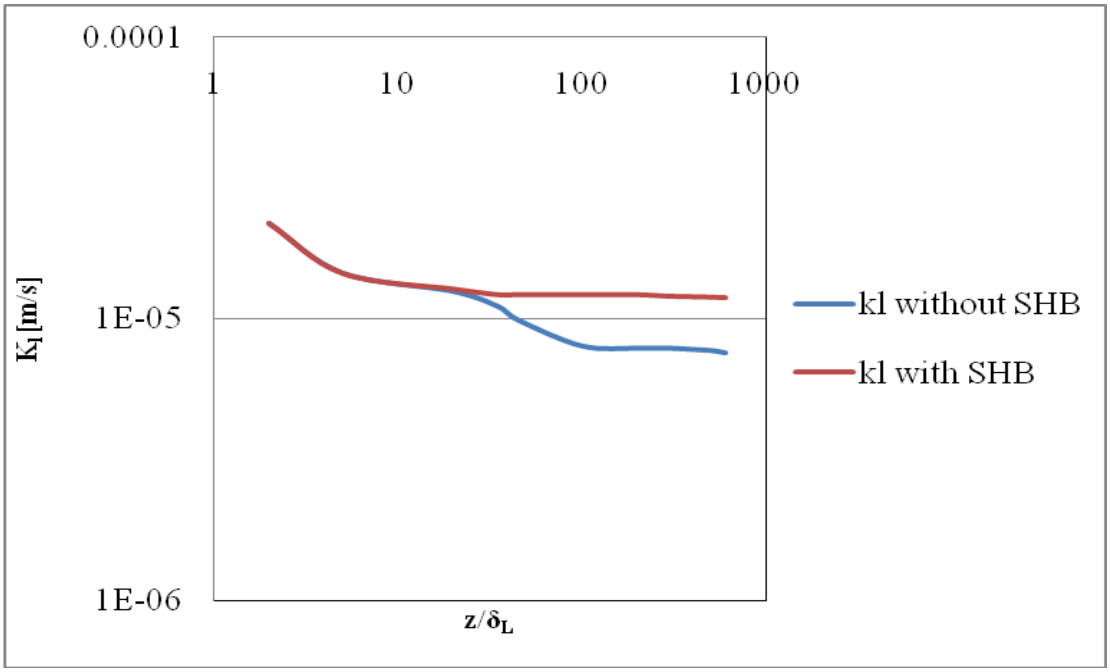

Figure 7. 11 Acetone mass transfer k_l as a function of axial distance ($z/\ \delta_L$). PTFE porosity≈65-70%, δ_G=850 µm, δ_L=200 µm, Acetone 1M, Pe~10^3, D_{Ac}=1.16x10^{-9} m^2/s, L_e=0.002 cm.

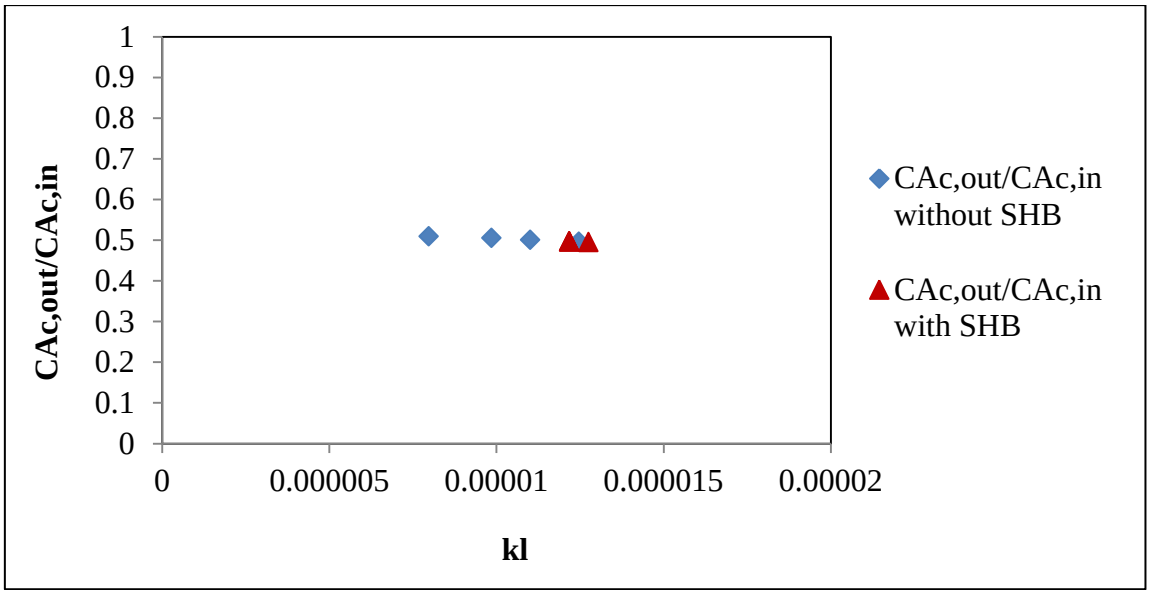

Figure 7. 12 Model prediction for acetone stripping in PTFE membrane contactor for k_l values with and without the use of SHB. PTFE porosity≈65-70%, δ_G=850 μm, δ_L=200 μm, Acetone 1M, Pe~10^3, D_{Ac}=1.16x10^{-9} m^2/s, D_{N2}=1.15x10^{-5} m/s, L_e=0.002 cm, τ_l=50 s, Y_{N2}/Y_{Ac}=1200, H=1127.

7.4.5 Hatta number analysis for CO_2 into 2M NaOH

In order to understand the reasons for the non improvement of mass transfer when staggered herringbones were used in our experiments the Hatta number (M_H) and Enhancement factor (E) were calculated. Hatta number was calculated from equation 7.1 [138] for second order reaction:

$$M_H = \frac{\sqrt{D_A k C_B}}{k_l} \qquad (7.6)$$

where D_A is the diffusivity of CO_2 in the liquid phase, k is the second order reaction rate constant, C_B is the initial concentration of NaOH, and k_1 is the mass transfer of CO_2 in the liquid phase. The Sherwood number $\left(\frac{k \cdot 2\delta}{D}\right)$ has constant value of 4.86 for a fully developed flow based on Shah and London [134] and can be used for the calculation of gas and liquid mass transfer coefficients. The calculated values for Hatta number and Enhancement factor are reported in Table 7.1 [138].

Table 7. 1 Estimated values for Hatta number and Enhancement factor with all the parameters used in the calculations.

$M_H=(D_A k C_B)^{1/2}/k_{Al}$	$E_i = 1+D_B C_B H_A/bD_A p_{Ai}$		NaOH	E (Enhancement factor)	
292	221.23		2M	≈150	
k_l	D_A	D_B	k	H_A (defined as $p_{Ai} = H_A C_{Ai}$)	p_{Ai}
$1.56x10^{-5}$ (m/s)	$1.7x10^{-9}$ (m^2/s) [96]	$2.8x10^{-9}$ (m/s) [97]	6.1 (m^3/mol.s) [94]	0.026 (m^3atm/mol) [10]	0.2 (atm)

According to the Figure 7.13 and from the calculated values from Table 7.1 for M_H=292 and E_i=221.23 the enhancement factor is around 150, which indicates that enhancement factor is almost in the plateau of the graph for the fast second-order reaction. For second order reactions when Hatta number exceeds a specific value (see Hatta diagram) the Enhancement factor reaches a limit (plateau of the graph), which does not happen for first order reactions (Kirtland's case)[127] where Enhancement goes to infinity. For second order fast reactions in liquid film with high concentration of NaOH the apparent rate equation is independent from k_l [138]. Any change of mass transfer k_l achieved by staggered herringbones will not increase the apparent rate equation and consequently will not increase the CO_2 removal efficiency as it was shown also from our experimental results in previous sections. In addition, the transverse concentration profiles of CO_2 and NaOH in the liquid phase were calculated (see figure 7.14) from the model for CO_2 removal at a length of (z/δ_L =77.5) without the use of SHB on the floor of the liquid channel and are in agreement with Levenspiel's plot [128] (case D: Fast Reactions; High C_B) where the apparent rate equation is independent from k_l.

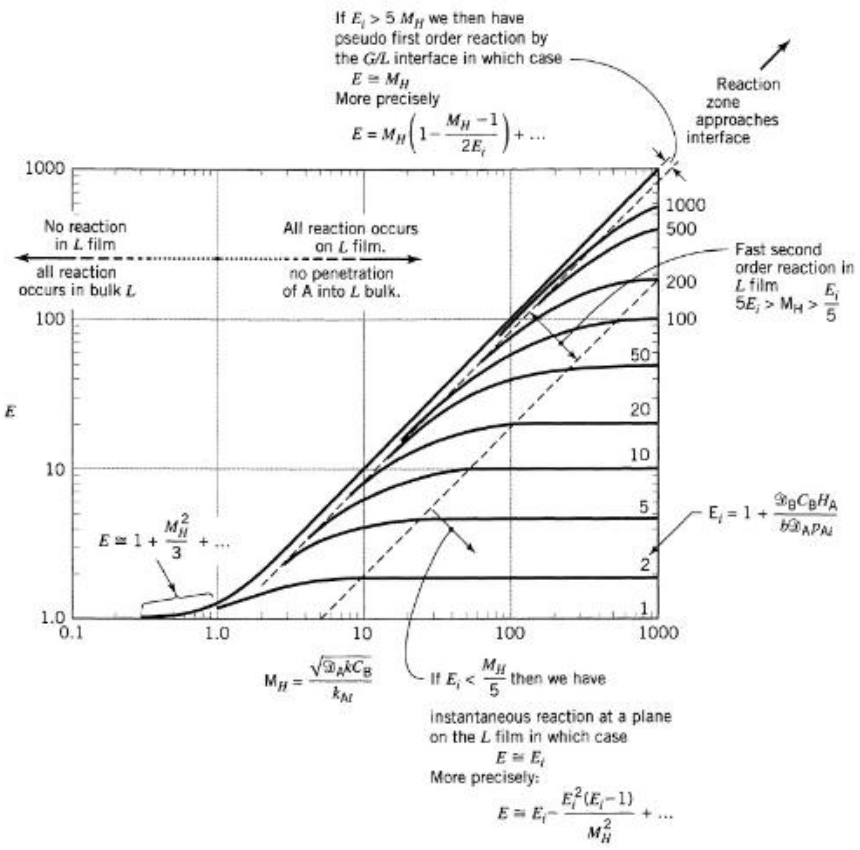

Figure 7. 13 The enhancement factor for fluid-fluid reactions as a function of M_H and E_i [138, p.530].

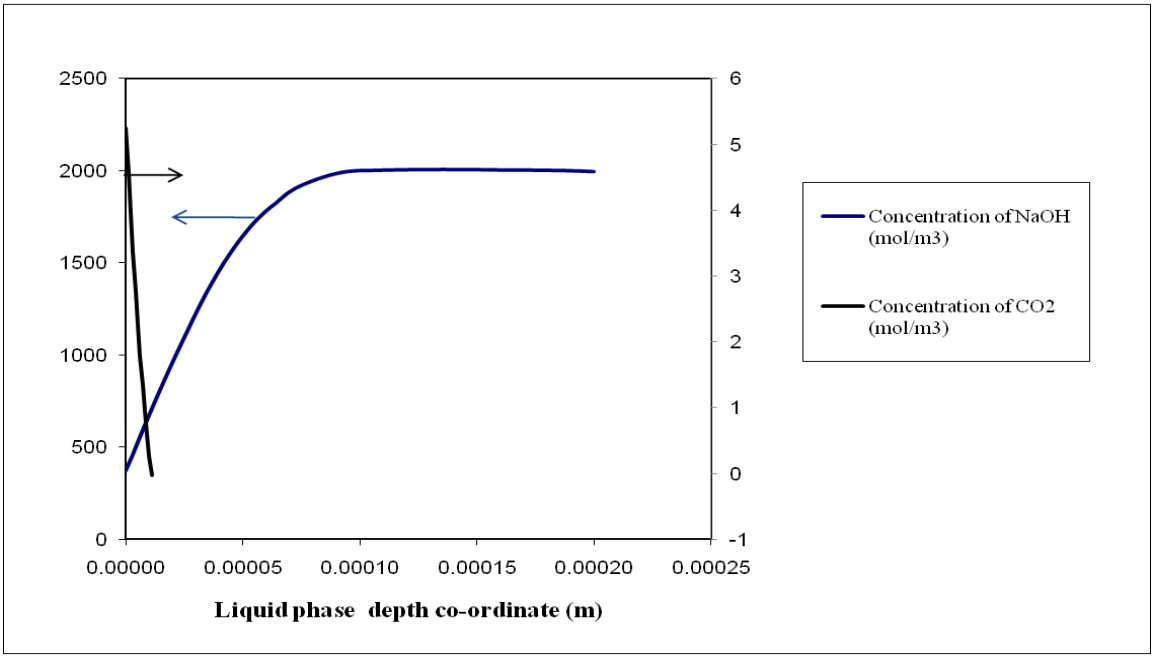

Figure 7. 14 Transverse concentration profiles of CO_2 and NaOH in the liquid phase at a length of (z/δ_L =77.5) for the flat channel. PTFE porosity≈65-70%, δ_G=850 µm, δ_L=200 µm, NaOH 2M, Y_{CO_2}/Y_{NaOH}=96.4.

7.5 Conclusions

Carbon dioxide absorption in sodium hydroxide was studied in a membrane microstructured reactor with and without the use of staggered herringbones on the floor of the liquid channel of the reactor. Experimental comparison between the flat channel with two different structures of staggered herringbones (AB and ABCD) when the staggered herringbones were engraved in the acrylic plate were performed. The experimental results obtained from the staggered herringbones showed that staggered herringbones did not have any effect on mass transfer compared to the flat channel. In order to examine if the imperfections of the staggered herringbones on the floor of the acrylic plate was the reason of the non improvement of the mass transfer due to insufficient stirring, silicon inserts (525 μm thick) with and without the staggered herringbones on them were placed in 725 μm deep liquid channel. Despite the fact that the staggered herringbones were much more precisely made on the silicon inserts than the herringbones on the floor of the acrylic plates CO_2 removal efficiency was similar as the flat channel. Tree-dimensional simulations were executed with and without the use of staggered herringbones which showed that the staggered herringbones on the floor of the liquid channel do not have any improvement on CO_2 removal efficiency compared with a flat channel.

In addition, in order to investigate more the effect of staggered herringbones on mass transfer, an analytical model for the stripping of acetone from water was formulated. Non improvement of the ratio $\frac{C_{Ac,out}}{C_{Ac,in}}$ was observed with the use of staggered herringbones compared with the flat channel.

A Hatta number analysis was carried out in order to understand the reasons for the non improvement of mass transfer when staggered herringbones were used in our work. The analysis showed that enhancement factor is almost in the plateau of the graph for the fast second-order reaction. For fast second order reactions in liquid film with high concentration of NaOH the apparent rate equation is independent from k_l and hence, any change of mass transfer k_1 achieved by staggered herringbones will not increase the apparent rate equation and consequently will not increase the CO_2 removal efficiency.

CHAPTER 8

PRELIMINARY INVESTIGATION OF THE EFFECT OF ULTRASOUND ON CO_2 ABSORPTION

8.1 Introduction

Ultrasound has found numerous applications in the field of sonochemistry [139]. For example with the use of ultrasound the reactivity of metal powders can be increased by more than 100000 times. The main reason responsible for this activation is cavitation [140]. Through a series of compression and expansion cycles created by acoustic waves, gas bubbles in the liquid may grow larger than 100 μm. The bubbles eventually become unstable and implode, producing high-speed microjets of liquid, intense localized heating and high pressure shock waves [141]. Ultrasound has also been shown to improve mass transport in gas and liquid systems by acoustic streaming [142]. It has been reported for many researches that the use of ultrasound can enhance mass transfer [143,144,145,146,147].

Sohbi *et al.* [148] studied the effect of vibration on the absorption of CO_2 with chemical reaction in aqueous solution of calcium hydroxide. They found that the vibration with a higher frequency increased the mass transfer coefficient, but vibration with lower frequency did not improve it. Schueller and Yang [149] in their work of ultrasound enhanced adsorption and desorption of phenol on activated carbon and polymeric resin, they observed that for

adsorption in a batch adsorber, ultrasound was found to act like a mixer, improving the mass-transfer coefficient through cavitation and acoustic streaming. For desorption ultrasound was found to enhance the surface diffusivity. Yamashita *et al.* [150] in their studies for enhanced mass transfer in peritoneal dialysis with application of ultrasound they observed that the ultrasound of an ultrasonic cleaner enhanced the rate of the peritoneal mass transfer and the effects were dependent on the frequency of ultrasound. Riera *et al.* [151] they used high-intensity ultrasound to produce a small scale agitation in order to enhance mass transfer on supercritical fluids (SF) extraction processes. They observed from their results that power ultrasound significantly accelerates the kinetics of the process and improves the final extraction yield. These improvements may be basically attributed to an increase in the mass transfer coefficient. Ben Yi and Yi Gang [152] developed a mathematical model of the mass-transfer enhanced factor which shows that the ultrasound enhances the mass-transfer in the supercritical carbon dioxide extraction process. The results calculated by the model are in a good agreement with experimental results. In addition they showed that mass-transfer enhanced factor is in direct proportion to the ultrasonic power, and in inverse proportion to the ultrasonic frequency, i.e. when using the ultrasonic to enhance the mass transfer process, we must choose an ultrasonic instrument with high power and low frequency.

In this Chapter carbon dioxide absorption in sodium hydroxide was studied in the PTFE membrane microstructured reactor with and without the use of ultrasound, in order to investigate if ultrasound has an effect in CO_2 removal efficiency.

8.2 Experimental set-up and conditions

The reactor used for CO_2 absorption in aqueous solution of NaOH with and without the used of ultrasound is the same single channel PTFE membrane microreactor showed in previous chapters for the absorption of CO_2 in aqueous solutions of amines and NaOH. For the ultrasound experiments the membrane reactor was completely submerged in a water bath of an ultrasonic cleaner (UW, UK) of 30kHz as shown in Figure 8.1. An HPLC pump (Waters 5100) was used to drive the liquid 2M aqueous NaOH solution in the bottom chamber of the reactor, while the gas 20vol% CO_2/N_2 was controlled by a mass flow controller (Brooks 5850) and flowed above the membrane. The outlet of the gas phase passed through a liquid trap to avoid any liquid getting into the gas chromatograph (GC) in case of breakthrough of

the liquid in the gas phase, and then connected to a GC (Shimadzu GC-14B) for carbon dioxide concentration determination. A water bath (Julabo F25, Germany) was used to keep the temperature inside the ultrasonic cleaner at 20°C. Experimental data were obtained varying the liquid flow rate in the range 1.66-2.56 ml/min and gas flowrate in the range 160-247 ml/min. Figure 8.2 shows the experimental set-up used for the ultrasound experiments. Furthermore, an aluminium foil was used to dermine the distribution of the cavitation intensity in the ultrasonic cleaner [153].

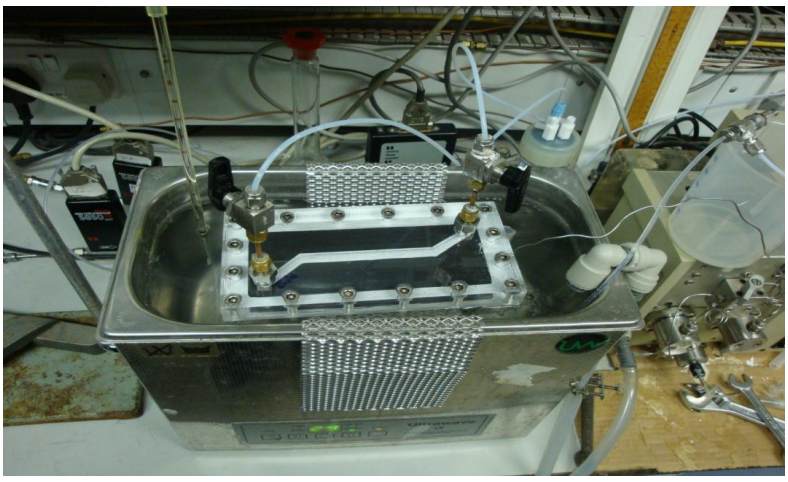

Figure 8. 1 Membrane microreactor submerged completely in a water bath of an ultrasound cleaner.

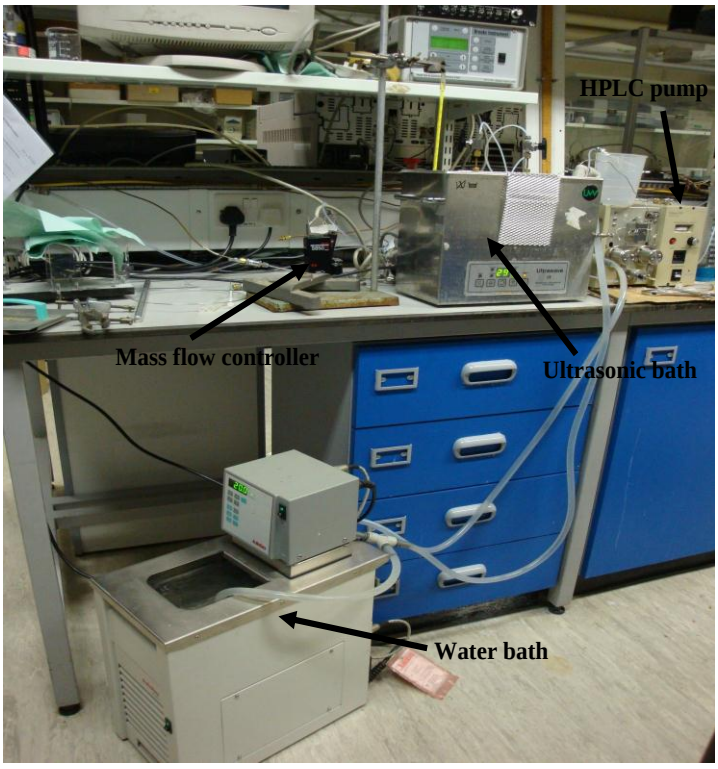

Figure 8. 2 Experimental set-up for the ultrasound experiments.

8.3 Results and Discussion

In order to determine the distribution of cavitation intensity in the ultrasonic cleaner, an aluminium foil (same height with the level of the water inside the ultrasonic bath) was submerged into the ultrasonic bath [153]. After the application of ultrasound for 5-10 minutes the aluminium foil (see figure 8.3) was eroded in different positions. From the erosion pattern that was created on the aluminium foil the cavitation intensity of the ultrasonic cleaner can be determined. From Figure 8.3 can be inferred that the cavitation intensity is concentrated at the midheight of the ultrasonic cleaner (see dashed line of figure 8.3), as a result the liquid chamber of the PTFE membrane reactor was located at the midheight of the ultrasonic cleaner in order to see the effect of cavitation on CO_2 removal.

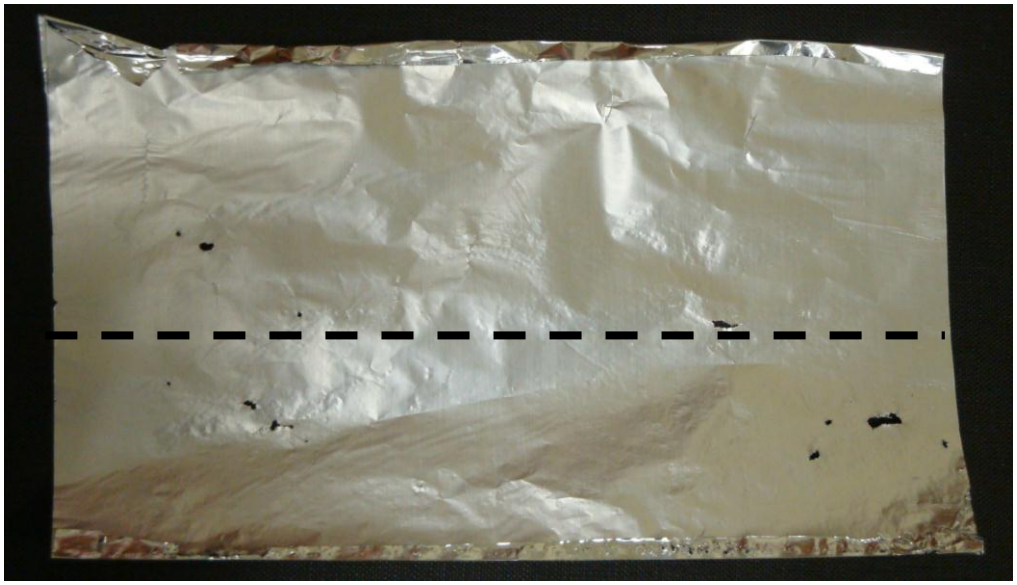

Figure 8. 3 Aluminium foil used to determine the distribution of cavitation intensity in the ultrasonic cleaner.

8.3.1 Influence of ultrasound on CO_2 removal efficiency

Figure 8.4 shows the performance of the membrane (PTFE) microreactor with and without the use of ultrasound in CO_2 absorption efficiency as a function of gas flowrate. As it can be seen from Figure 8.4, with and without the use of ultrasound the experimental results for CO_2 removal efficiency were the same. Despite the fact that the cavitation intensity was determined at the mid-height of the ultrasonic bath, hence the liquid chamber of the

membrane contactor was located at the mid-height of the ultrasonic bath, no enhancement of CO_2 removal efficiency with the use of ultrasound was observed. Schueller and Yang [149] showed that cavitation has only a slight effect on the mass- transfer coefficient, compared to the increase due to acoustic streaming. Based on the observation of Schueller and Yang that cavitation might not have an effect on mass transfer it might be a good explanation for our case that ultrasound did not have any effect on mass transfer and hence, the CO_2 removal efficiency did not improve. Another reason that might explain the non improvement of mass transfer with the use of ultrasound is that the acrylic plate which the liquid chamber is engraved on it is quite thick 15 mm, so the ultrasound cannot create acoustic streaming strong enough inside the liquid chamber in order to increase mass transfer and hence CO_2 removal.

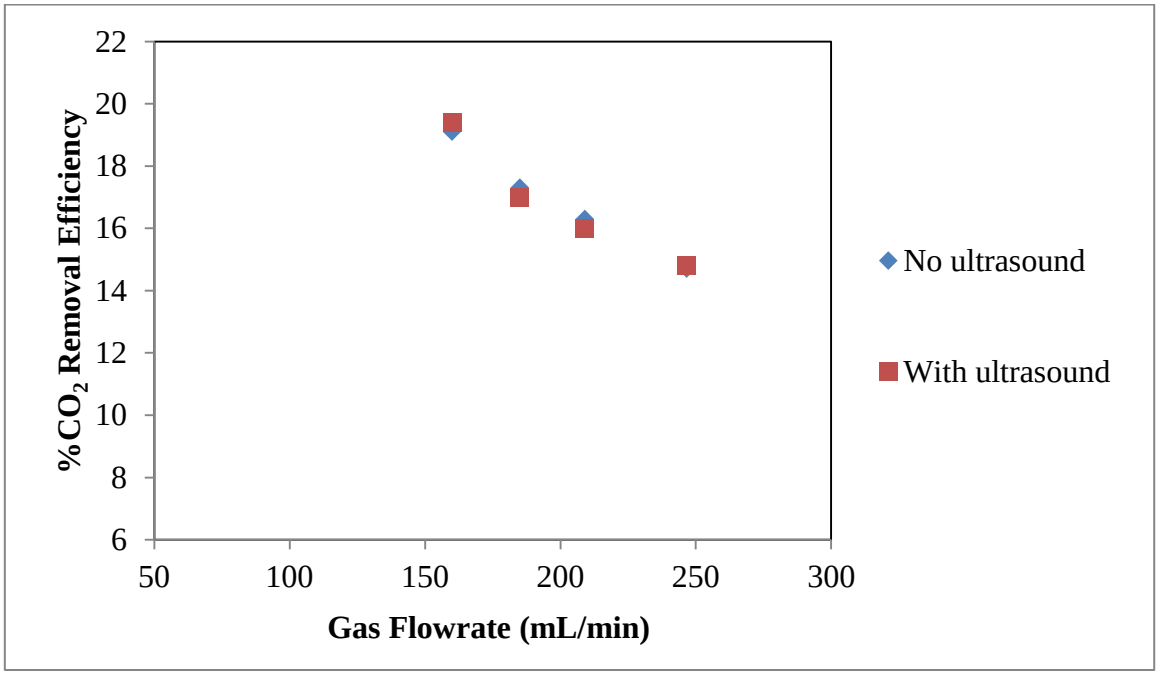

Figure 8. 4 CO_2 removal efficiency as a function of gas flowrate with and without the use of ultrasound. PTFE open area≈65-70%, δ_G=850 μm, δ_L=200 μm, NaOH 2M, Y_{CO_2}/Y_{NaOH}=96.4.

8.3.2 Influence of different orientations of the membrane reactor inside the ultrasonic bath

Since the behaviour of the acoustic field in the ultrasound bath is unknown experiments were performed with different orientations of the membrane reactor inside the ultrasonic bath, in order to achieve streaming in the liquid side of the membrane reactor. Figures 8.5 and 8.6 show the different orientations of the membrane reactor used for the ultrasound experiments. Despite the different orientation of the membrane reactor inside the ultrasonic bath the experimental results for CO_2 removal efficiency did not improve and are identical with the results obtained for Figure 8.4. Further investigation and understanding of the acoustic field inside the ultrasonic cleaner is worth carrying out in order to achieve acoustic streaming in the liquid side of the membrane reactor which might enhance mass transfer and hence CO_2 removal.

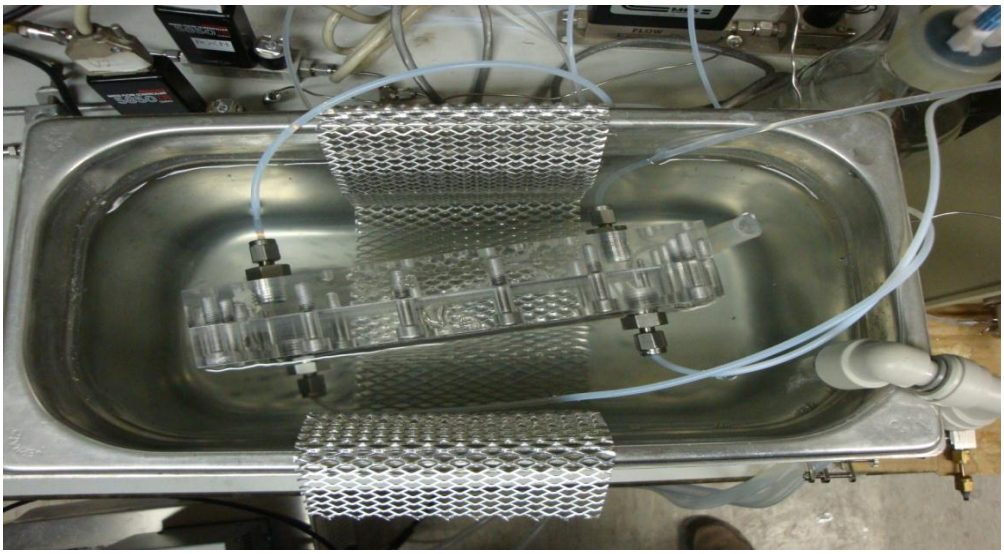

Figure 8. 5 The reactor is placed vertically inside the ultrasonic bath.

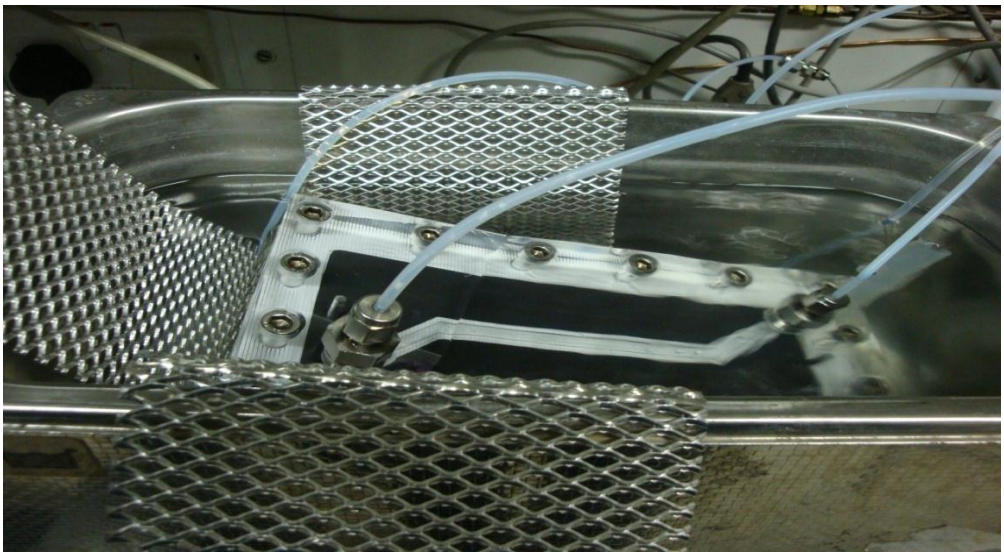

Figure 8. 6 The reactor is placed in an inclined position inside the ultrasonic bath.

8.4 Conclusions

Carbon dioxide absorption in sodium hydroxide was studied in the single channel membrane microstructured reactor with and without the use of ultrasound in order to examine the effect of ultrasound on the CO_2 removal efficiency. The experimental results obtained from the use of ultrasound did not have any effect on mass transfer compared to the experimental results without the use of ultrasound and hence, no improvement on CO_2 removal efficiency was observed. A possible explanation for that might be the fact that cavitation does not have an effect on the mass- transfer coefficient or due to the fact that the acrylic plate which the liquid chamber is engrave on it is quite thick 15mm, so the ultrasound cannot create acoustic streaming strong enough inside the liquid chamber in order to increase mass transfer and hence, enhance CO_2 removal efficiency. Furthermore, experiments were performed with different orientations of the membrane reactor inside the ultrasonic bath, in order to achieve streaming in the liquid side of the membrane reactor. Despite the different orientation of the membrane reactor inside the ultrasonic bath, we did not achieve any enhancement of mass transfer and the experimental results for CO_2 removal efficiency did not show any improvement compare with results without the use of ultrasound.

CHAPTER 9
INVESTIGATION OF SCALE-OUT OF THE METALLIC MESH REACTOR

9.1 Introduction

In some cases the amount of reaction product may not meet a required output, even though the reaction yield may be improved by using a microreactor. To increase production volume, the number of reactors is simply increased using an approach referred as scale out or numbering up. Numbering-up can be performed in two ways. External numbering-up [154] is reffered to as the connection of many devices in parallel fashion and internal numbering-up means the parallel conection of the functional elements only, rather than of the complete devices [154]. When using micro-fluidic systems, a reaction is first optimised using a single microreactor. Therefore, a reaction is only optimised once and then all sequential reactors are controlled using the same operating conditions. This approach is therefore cost-effective, time-efficient, and flexible, enabling changes in production volume by simply increasing or decreasing the number of reactors employed [155, 156, 157, 158, 159, 160, 161]. However, in the scale out approach uniform flow distribution must be achieved so that each parallel unit shows identical reagent flow rates.

There are two different structures used for distributing flows. The consecutive type manifold (our case) consists of a header distributing to a number of outlets while in the bifurcation manifold structure flow is split into two streams repeatedly. In general there are two main approaches to achieve even flow distribution in consecutive headers. The first approach

achieves uniform flow distribution by careful design of the shapes of both distributing and collecting header geometries. Optimal header geometries were obtained via CFD investigations, taking into consideration among other things, the effects of header shape and channel geometry [89, 90]. In the second approach uniform flow distribution is achieved by making the average pressure drop across the microchannel outlets substantially larger than the preesure variation along the length of the distribution header [162]. Although the second approach is simpler the first approach which involves careful design of distributing and collecting header geometries might be preferable.

Kikutani *et al.* [163] made a pile up microreactor in which ten levels of microchannel circuits were integrated to form a single glass entity. An amide formation reaction between amine in aqueous solution and acid chloride in organic solution was carried out using the pile-up reactor. The maximum throughput for ten-layered pile-up reactor was ten times larger than that of a single-layered one. They suggested that many conventional plants producing fine chemicals can be replaced by microreactors through the numbering-up technology based on their results. Tonkovich *et al.* [164] in their studies microchannel technology scale-up to commercial capacity they pointed out that the keys to success transition from lab-scale to industrial-scale are: solving challenges around device fabrication, flow distribution and catalyst integration. Kikutani *et al.* [165] performed 2 x 2 amide formation reactions using a microchip and the possibility of the parallel micro-flowreactor system for combinatorial chemistry was demonstrated. They observed problems of dispersing equal amounts of solutions to each reaction channel, most probably due to imperfections in fabrication of the chip.

In this Chapter carbon dioxide absorption in sodium hydroxide solution was performed in the metallic mesh scale out microreactor. 4 meshes were integrated in the metallic meh microreactor of chapter 4. CFD simulations were carried out in the scale out microreactor in order to ensure equal flow distribution in each plate of the scale out 9amicoreactor.

9.2 Reactor design and experimental conditions

In this Chapter, ‘scale-out’ of the metallic micromesh reactor shown in Chapter 4 (see figure 4.1c and 4.2a for the mesh used) for CO_2 absorption in NaOH solution was investigated. A

‘scale-out’ micromesh was made in which four meshes (see figure 4.2a for the mesh used) were integrated. The plates of the single metallic mesh reactor were designed based on the CFDs simulations (see Chapter 3) by varying geometrical parameters such as: width of inlet and outlet flow distribution regions, different shapes of inlet and outlet flow distribution regions, shifting the channels in parallel, effect of the channels in order to achieve uniformity of the fluid flow over the plates of the reactor. The scaled out reactor was designed based on the results of the CFDs (see section 9.4.1) which showed even flow distribution in each plate of the scale out metallic mesh reactor.

Figure 9.1 shows the flow configuration which was implemented for the ‘scale-out’ metallic mesh and a picture of the components of the scale out reactor with three meshes for simplifications. In order to use four meshes in the scale out microreactor and have the flow configuration of Figure 9.1 three acrylic plates were machined in both sides (one side gas chamber and the other side liquid chamber) and placed in parallel between the top and the bottom plates of the metallic mesh reactor. All the dimensions of these three plates (for the gas and liquid chambers) are the same with the dimensions of the top and the bottom plates (see chapter 4) apart from the thickness of the plates which are 18 mm for the top and bottom plates and 8 mm for the three middle plates. The experimental set-up used for the scale out metallic mesh reactor is the same with the one used in Chapter 4 (figure 4.3). Gas flowrate varied from 920-1416 ml/min and liquid flowrate varied from 6.64-10.24 ml/min based on 4 times larger flowrate of the metallic mesh reactor (see Chapter 4). The pressure difference between gas and liquid phase was kept at P_G-P_L≈15-20 cm H_2O. Figure 9.1 shows the assemble device of the scale out metallic mesh reactor used in our experiments.

(a)

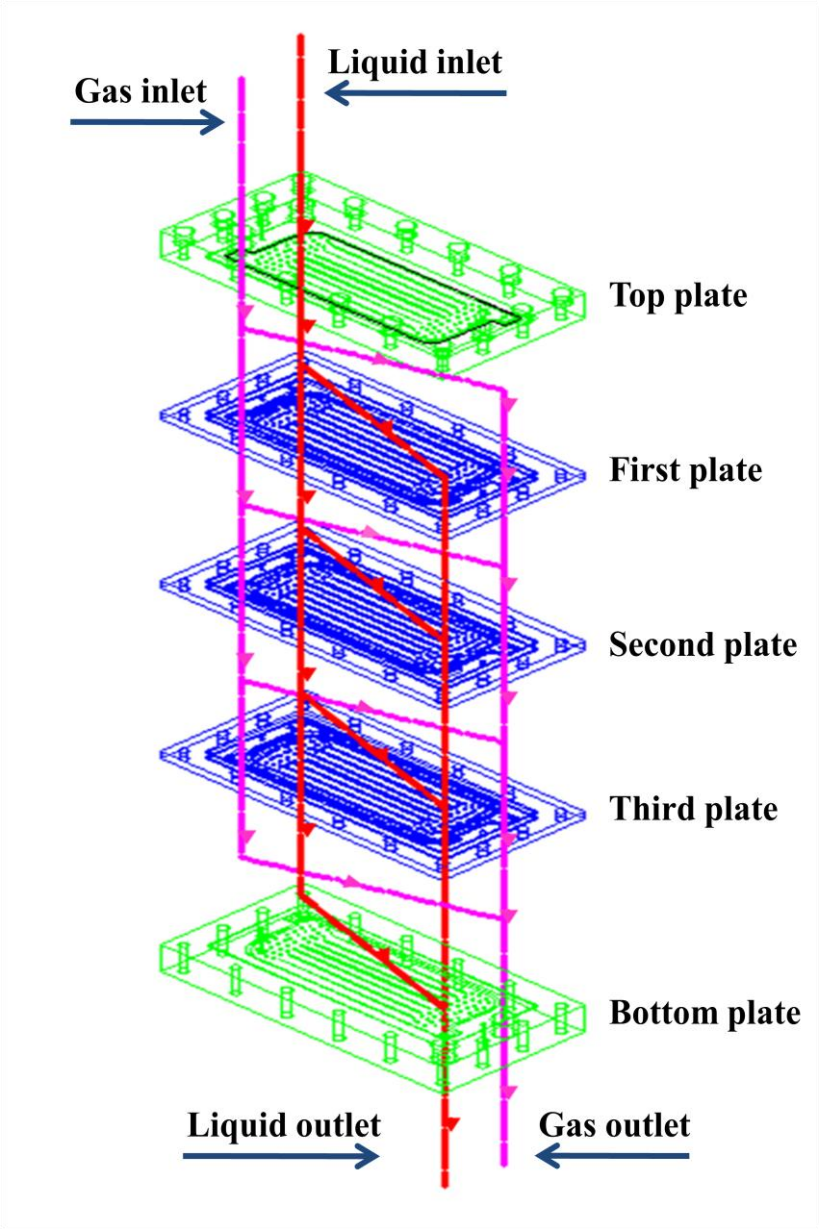
Gas inlet
Liquid inlet
Top plate
First plate
Second plate
Third plate
Bottom plate
Liquid outlet
Gas outlet

(b)

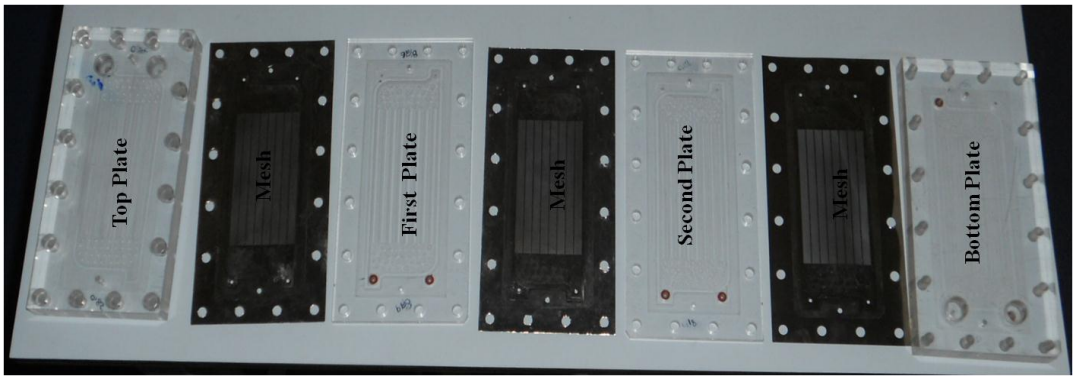
Top Plate
Mesh
First Plate
Mesh
Second Plate
Mesh
Bottom Plate

(c)

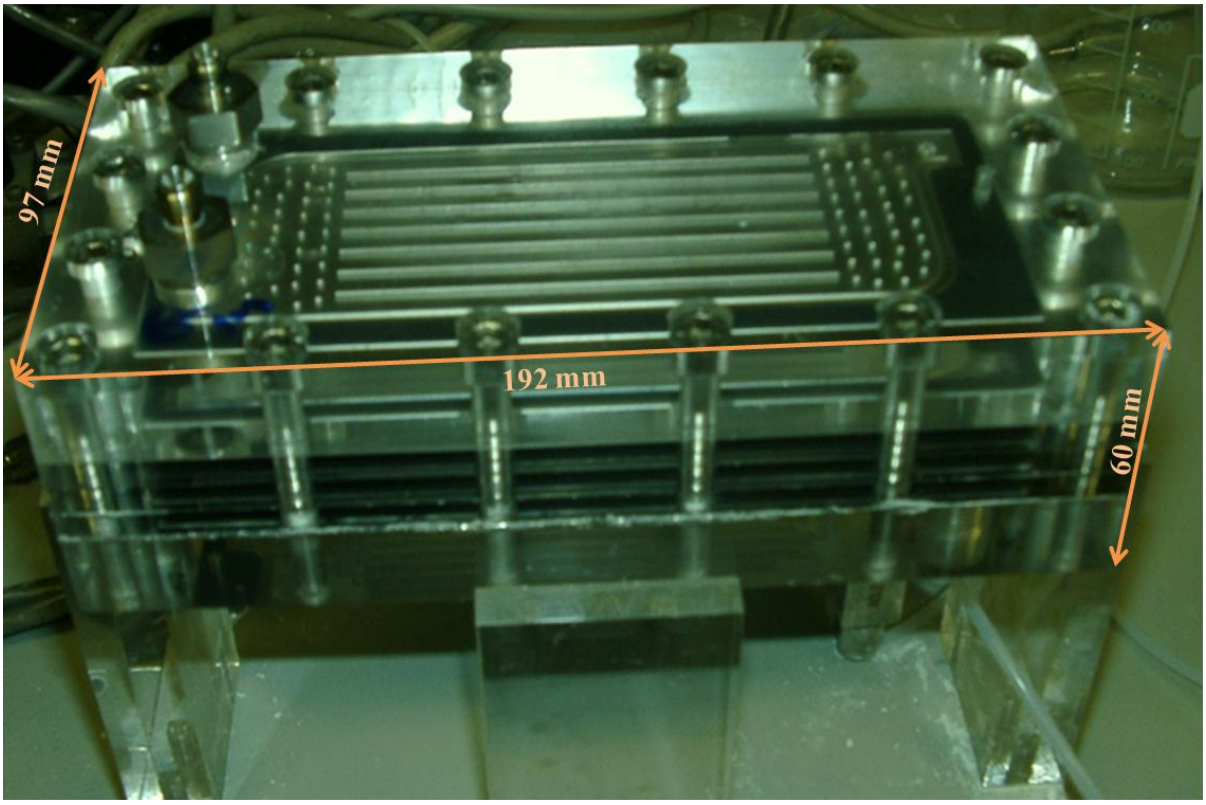

Figure 9. 1 (a) Flow configuration of the scale out microreactor (b) Picture of the components of the scale out microreactor (c) Picture of assembled scale out micromesh reactor.

9.3 Flow distribution in the scale out metallic mesh reactor

In order to ensure equal flow distribution in each layer of the scale out microreactor CFD simulations carried out. For the CFD simulations the incompressible Navier-Stokes equations:

$$\vec{u} \cdot \nabla \vec{u} = -\nabla p + \mu_i \nabla^2 \vec{u} \qquad (9.1)$$

combined with the equation of continuity,

$$\nabla \cdot \vec{u} = 0 \qquad (9.2)$$

where $\vec{u}$ is the fluid velocity vector, and p is the pressure, are solved with COMSOL 3.5a. A three-dimensional model was employed with, no-slip boundary conditions at all walls, and a fixed pressure at the outlet ($p=0N\ m^{-2}$). A mesh consisting of 317001 number of elements and 1633752 degrees of freedom is used to execute the simulations in Windows XP with Pentium IV 2.93GHz CPU and 24GB of RAM. At this number of elements the solution was found to be mesh independent Figure 9.2 shows the three- dimensional computational domain of the scale out microreactor.

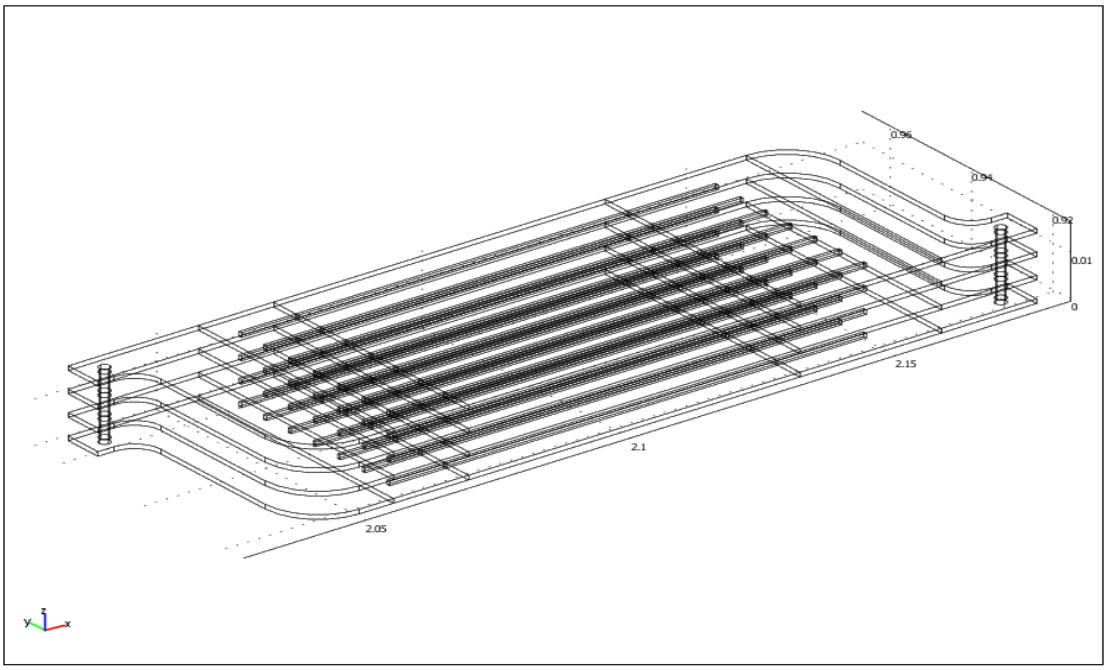

Figure 9. 2 Three-dimensional computational domain of the scale out microreactor.

9.4 Results and Discussion

9.4.1 Flow distribution in the scale-out mesh reactor

As already mentioned, it is important to ensure equal flow distribution in each plate of the scale out microreactor. In order to compare the quality of flow distribution within the channels of each plate, average velocities u(i) within each channel are calculated by integration of the velocity profiles in the y and z planes. In Figure 9.3, normalized average

velocities within channels (each plate consists of 8 channels) $u(i)/u_{mean}$ are shown where the mean velocity is given by:

$$u_{mean} = \frac{1}{n}\sum_{i=1}^{n} u(i) \tag{9.3}$$

The maximum difference between average velocities was found to be $[u(i)_{max}-u(i)_{min}] / u_{mean}<0.1\%$. For each one of the four plates (gas side) of the scale out microreactor the normalized average velocities were found the same and are shown below, confirming equal flow distribution in each plate of the scale out microreactor. In addition, simulations were performed for the plates (liquid side) of the scale out microreactor. Maximum difference between average velocities within channels was found to be <0.1% for each plate (liquid side) as well (results are not shown), confirming equal flow distribution in each plate (liquid side) of the scale out metallic mesh reactor.

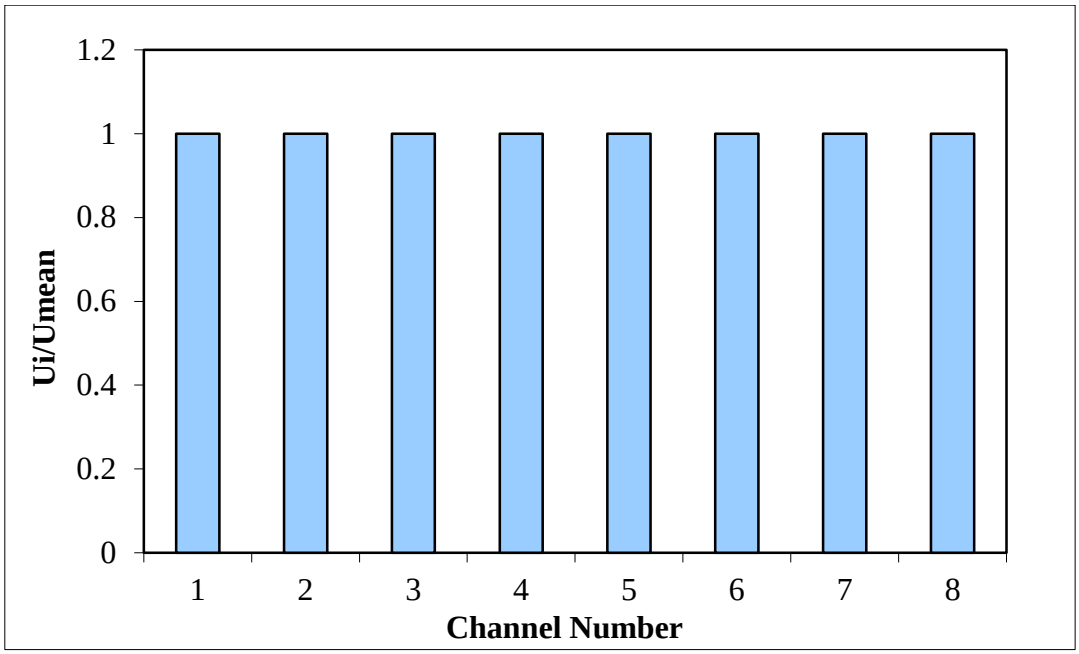

Figure 9. 3 Normalized velocity distribution within microchannels for the plate (gas side) of the scale out microreactor at inlet gas flow rate Y_G=1416 ml/min.

9.4.2 Comparison between the metallic mesh reactor with the scale-out metallic mesh reactor

Figure 9.4 shows the comparison between the scale out metallic mesh reactor (4 meshes were integrated) with the metallic mesh reactor (1 mesh see Chapter 4) for CO_2 absorption in NaOH solution as a function of plate gas flowrates. As it can be seen CO_2 removal efficiency for the scale out reactor is significantly lower than the metallic mesh reactor. Such a poor performance might be caused by uneven distribution to each plate. Despite the fact that CFD simulations indicate even flow distribution to every plate, maldistribution can be the reason for such a poor performance. Yue *et al.* [166] in their studies of flow distribution and mass transfer in a parallel microchannel contactor, observed significant flow maldistribution across parallel channels, despite the fact that the CFD simulations showed even distribution. To ensure equal distribution to each plate in a scale out reactor, each plate must be accurate made. Imperfections in fabrication of any of the plates can cause uneven flow distribution. In addition to that in our case after measuring the gas and liquid chambers heights, imperfections on the fabrication of the plates were observed (chamber heights from the inlet to the outlet of each plate varied by about 10%) , which can lead to uneven distribution to each plate of the reactor. Furthermore, a possible explanation for the different behaviour of the scale out metallic mesh reactor might be the fact that breakthrough of liquid in the gas phase occurs in the second or in the third plate where visualisation is not possible. Such a breakthrough most likely would cause the formation of stagnant liquid in the gas side of the plates which might affect the gas residence times and hence lower CO_2 removal efficiency.

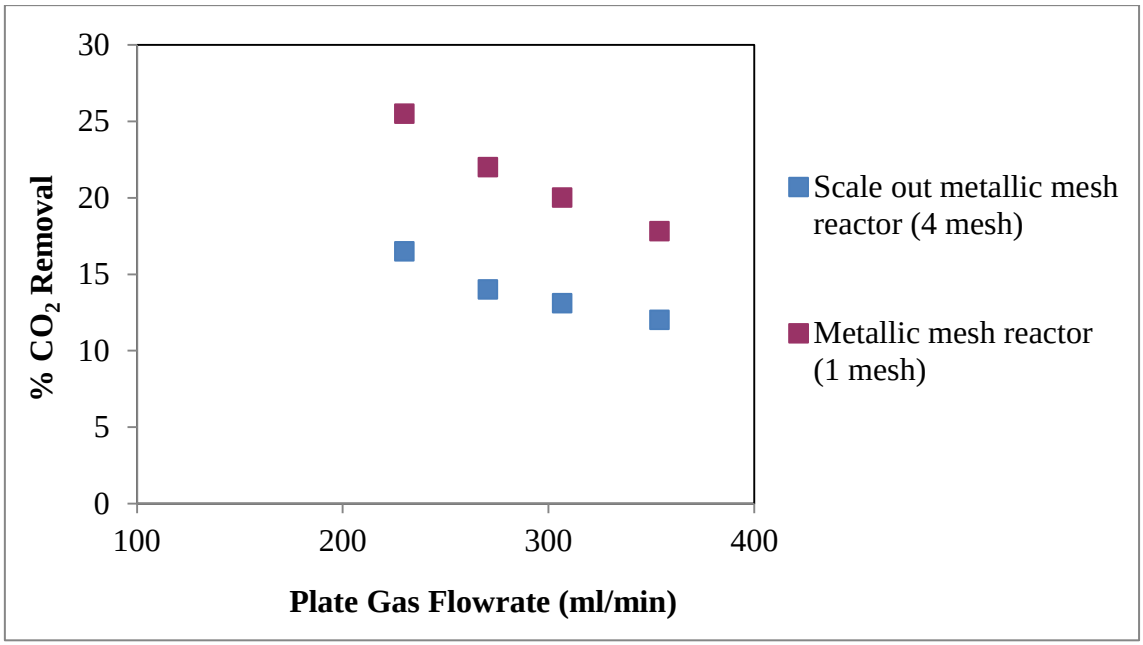

Figure 9. 4 Experimental comparison between the metallic mesh reactor (1-mesh) with the scale out metallic mesh reactor (4-mesh) for CO_2 absorption in 2M NaOH solution. δ_G=850 μm, δ_L=200 μm, Y_{CO_2}/Y_{NaOH}=139.5, mesh porosity 15%.

In order to improve the flow distribution in each plate of the scale out reactor, which might have caused the problem of lower performance for the scale out metallic mesh reactor, experiments were performed by installing inserts with different channel widths (0.2, 0.5, 0.75, 1 mm) in every inlet of each plate (gas and liquid side) of the scale out reactor (see figure 9.5), in order to control better the pressure drop along each plate of the scale out reactor and keep it the same in each plate. This should lead the same volumetric flowrates in each plate. Despite the new modification by installing different inserts at all the inlets of each plate of the scale out metallic mesh reactor the performance of the 'scale-out' reactor was less efficient compared with the metallic mesh reactor and the experimental results were identical to the original as shown in Figure 9.4 before the modifications were made. In order to improve the performance of the scale out reactor a good idea which might help, is the installation of one metering valve in each plate (at each liquid outlet), hence each plate can be controlled better (better control of pressure drop along each plate) and not just by one metering valve at the liquid outlet of the bottom plate of the scale out reactor and hence, breakthrough and maldistribution in each plate can be avoided.

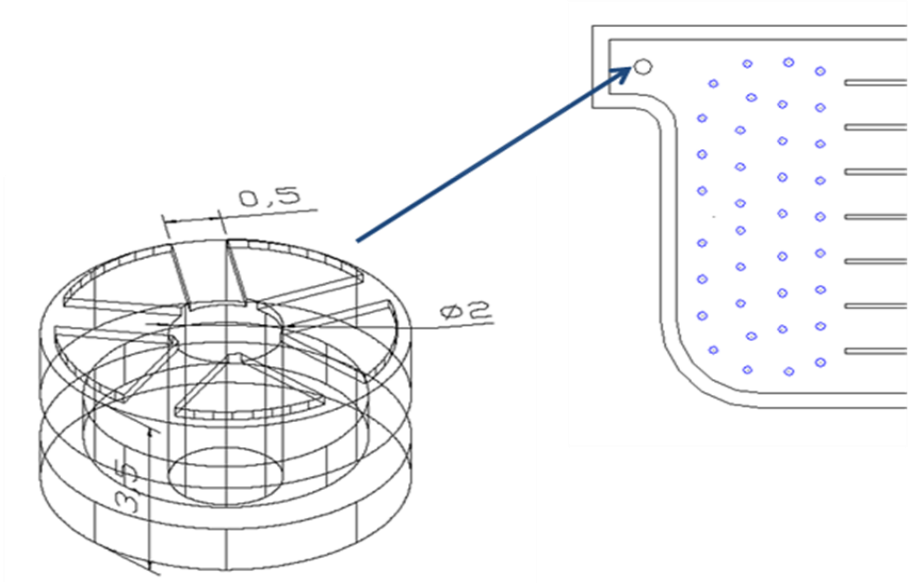

Figure 9. 5 Schematic of acrylic insert of 0.5 mm channel width, and a part of acrylic plate of the scale out metallic mesh reactor showing the inlet of the plate where the insert was installed.

9.6 Conclusions

Carbon dioxide absorption in sodium hydroxide solution was performed in metallic mesh scale out microreactor (4-mesh) in order to compare its performance with the metallic mesh microreactor (1-mesh). CO_2 removal efficiency for the scale out reactor was significantly lower than the metallic mesh reactor. Despite the fact that CFD simulations indicates even flow distribution to every plate, such a poor performance might be caused by uneven distribution to each plate. Breakthrough of liquid in the gas phase (stagnant liquid) in the second or in the third plate where visualisation is not possible might be a possible reason for such a poor performance as well. Furthermore, in order to improve the flow distribution in each one of the plates of the scale out reactor inserts with different channel widths (0.2, 0.5, 0.75, 1 mm) were installed in every inlet of each plate (gas and liquid side) of the scale out reactor in order to control better the pressure drop along each plate of the scale out reactor and keep it the same in each plate. Despite the new modification by installing different inserts at all the inlets of each plate of the scale out reactor the performance of the scale out metallic mesh reactor did not improve.

CHAPTER 10

CO_2 ABSORPTION IN SILICON NITRIDE MESH CONTACTOR

10.1 Introduction

Silicon nitride microsieves [167, 168, 169, 170, 171, 172, 173, 174, 175, 176] are mesh manufactured with photolithographic techniques developed in the semi-conductor industry. Microsieves are mostly used for analytical purposes and also, are under investigation for the clarification of beer and filtration of milk [177, 178] for large scale applications. Due to their thin silicon nitride layer, their relatively large porosity, and their open support structure the fluxes can be two or three orders of magnitude larger than for conventional membranes, even when using very low transmembrane pressures.

The study of this chapter concerns the use of a new type of silicon nitride mesh contactor, developed by Bayer Technology Services and FluXXion's microstructure technology to improve the mass transfer efficiency. The use of this new technology could provide modular micro-structured contactor devices enabling mass and heat transfer efficiency to increase compared to conventional techniques for mass transfer. As a result the following advantages can be pointed out [179]:

- Less energy intensive than conventional processes
- Less initial investment in infrastructure, lower overall investment

- Small size, weight; high surface area to contactor volume, low hold-up volume
- Large turndown ratio; high flexibility with flowrates
- Highly modular and scalable
- Supports “green chemistry” and “process intensifications” initiatives
- Independent pressure control of gas and liquid streams
- Independent flow control of gas and liquid streams (may obviate typical column problems: flooding, weeping, priming, dumping, entrainment, and channelling)
- No physical mixing of phases (bubble-less gasification controls froth and foam)

In this chapter, CO_2 absorption in sodium hydroxide and amine solutions was conducted in the silicon nitride mesh contactor. Breakthrough was investigated first in the silicon nitride mesh contactor in order to establish the operation pressure difference between gas and liquid phase. Various conditions such as gas and liquid flowrates, different types of solutions (NaOH, Amines), type of the flow, were investigated, in order to evaluate, understand and improve its performance of the silicon nitride mesh contactor.

10.2 Reactor design and experimental conditions

The silicon nitride mesh contactor comprised of a silicon microstructured plate with a one-micron thick mesh layer of silicon nitride, placed between two polycarbonate plates 12 mm thick, containing inlet and outlet ports for the fluids· The 1 μm thick silicon nitride layer forms the mesh which after it was etched through using advanced semiconductor processes, contains a very high density of very uniform 0.5 μm pores (see figure 10.1a) with porosity of 20.3%. A top foil made of stainless steel defined the liquid channel of 25 μm height, while the gas channel height approximately is 500 μm, (note that the gas channel is largely within the wafer and is more complicated than the 500 μm that suggested). In addition to this 500μm there is an extra height from the gas channel of 340 μm and another 2.37 mm height from a nickel support which makes the total gas channel height at 3210 μm , see figure 10.2).The gas chamber volume is 1.39 cm^3 based on the total height of 3210 μm, and the liquid chamber

volume is 0.01 cm^3. The reactor measures 80 mm x 64 mm (see figure 10.1b). Two viton gaskets 1 mm thick are placed in 0.75 mm deep grooves in the polycarbonate plates to provide the sealing. The silicon microstructured plate consists of 4 blocks (see figure 10.1c) and the directions of the fluid streams are perpendicular to the distribution channels. The porous area of the mesh is 42.68 x 9 mm and defines the contact area between the two fluids. Two pin holes were employed in both polycarbonate plates for alignment, while 6 screws were used for clamping all components together. A schematic of all components of the reactor is shown in Figure 10.1d. A picture and a schematic of the experimental set up for CO_2 absorption is shown in Figure 10.3. An HPLC pump (Waters 5100) was used to drive the liquid 2M NaOH solution or the 2M diethanolamine solution on the top chamber of the reactor, while the gas 20vol% CO_2/N_2 was controlled by a mass flow controller (Brooks 5850) and flowed below the mesh. The differential pressure between the two phases was controlled by two metering valve (Swagelok) at the outlet of the gas and the liquid phases. The gas phase pressure and liquid phase pressures were measured by pressure sensors (Honeywell; pressure range 0-15 psi, power supply; Traco 5V, use of the Labview program running by computer for pressure readings) located at the inlets/outlets of the gas and liquid channels. During typical operation the pressure difference between gas and liquid phase was kept at P_G-P_L≈130-170cm H_2O. The outlet of the gas phase passed through a liquid trap to avoid any liquid getting into the gas chromatograph (GC) in case of breakthrough of the liquid in the gas phase, and then connected to a GC (Shimadzu GC-14B) for carbon dioxide concentration determination· Experimental data were obtained varying the liquid flow rate in the range 1.28-2.56 ml/min and gas flowrate in the range 160-246.7 ml/min. These flowrates resulted to residence times, based on the gas/liquid volumes in contact with the mesh area, 0.3-0.5 s for the gas and 0.23-0.36 s for the liquid respectively. All the experiments were carried out at room temperature (approximately 20^oC). The CO_2 removal efficiency was calculated from:

$$X_{CO_2} = 1\text{-}\frac{F_{CO_2 out}}{F_{CO_2 in}} \qquad (10.1)$$

where F is the molar flowrate of CO_2. The experimental error in CO_2 removal was assessed to be ± 5%. Two to three chromatographs were taken for each measurement and the deviation between them was about ± 5%.

(a)

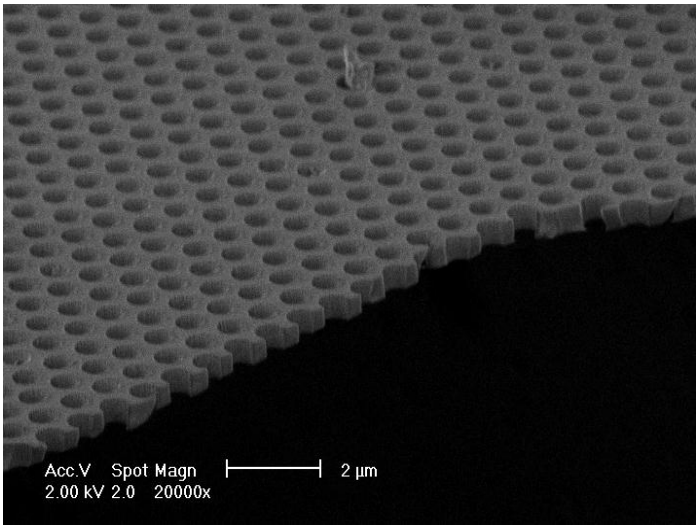
Acc.V Spot Magn
2.00 kV 2.0 20000x
2 µm

(b)

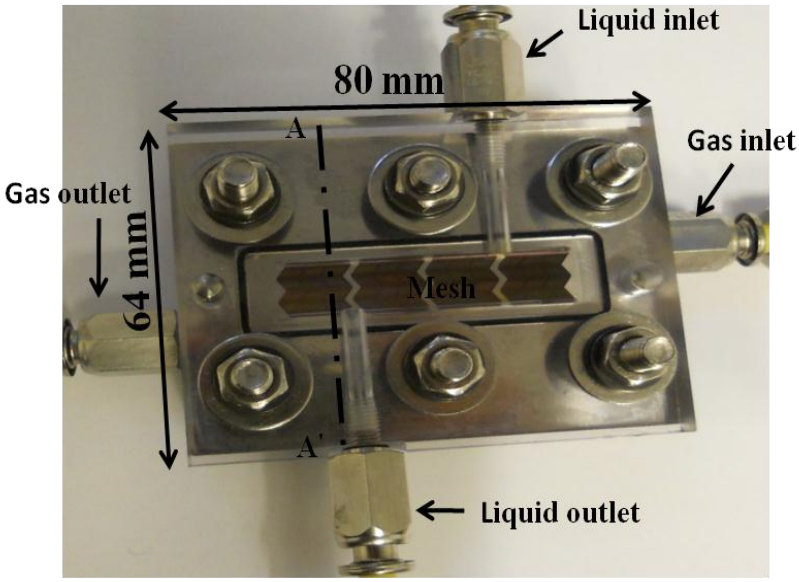
Liquid inlet
80 mm
A
Gas inlet
Gas outlet
64 mm
Mesh
A'
Liquid outlet

(c)

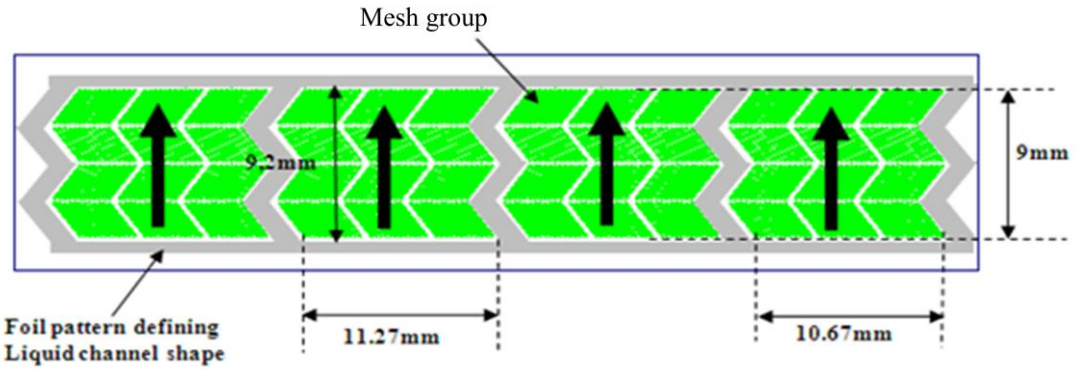
Mesh group
9.2mm
9mm
Foil pattern defining
Liquid channel shape
11.27mm
10.67mm

(d)

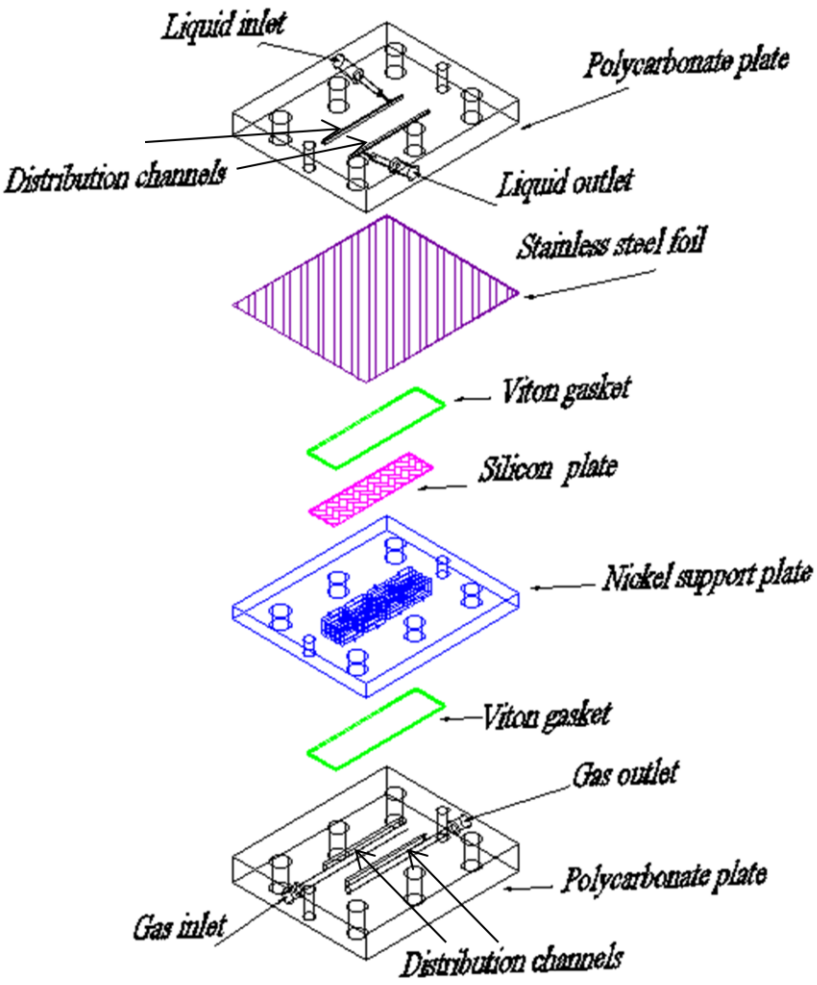

Figure 10. 1 (a) SEM picture of the silicon nitride mesh (b) Picture of the mesh reactor (the reactor measures 80 mm x 64 mm) (c) Schematic of the mesh plate for the silicon nitride mesh contactor with liquid flow direction (see arrows) (dimensions are in mm) (d) Exploded schematic view of the silicon nitride mesh reactor.

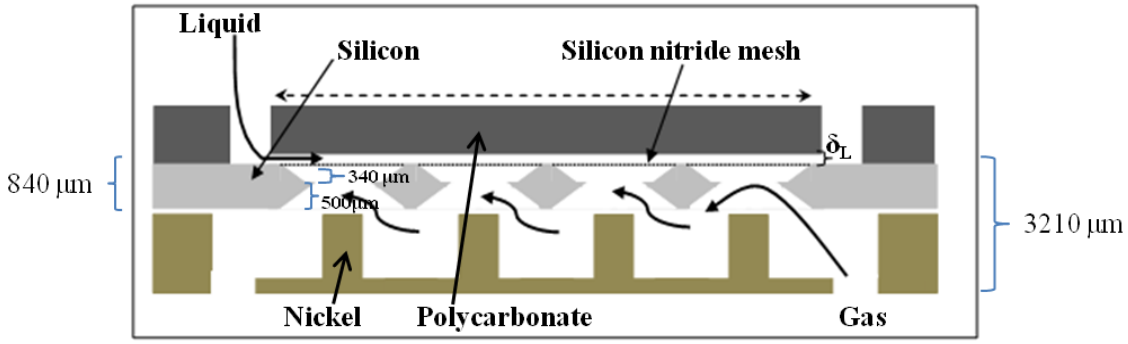

Figure 10. 2 Module cross-section between A-A' see figure 10.1b.

(a)

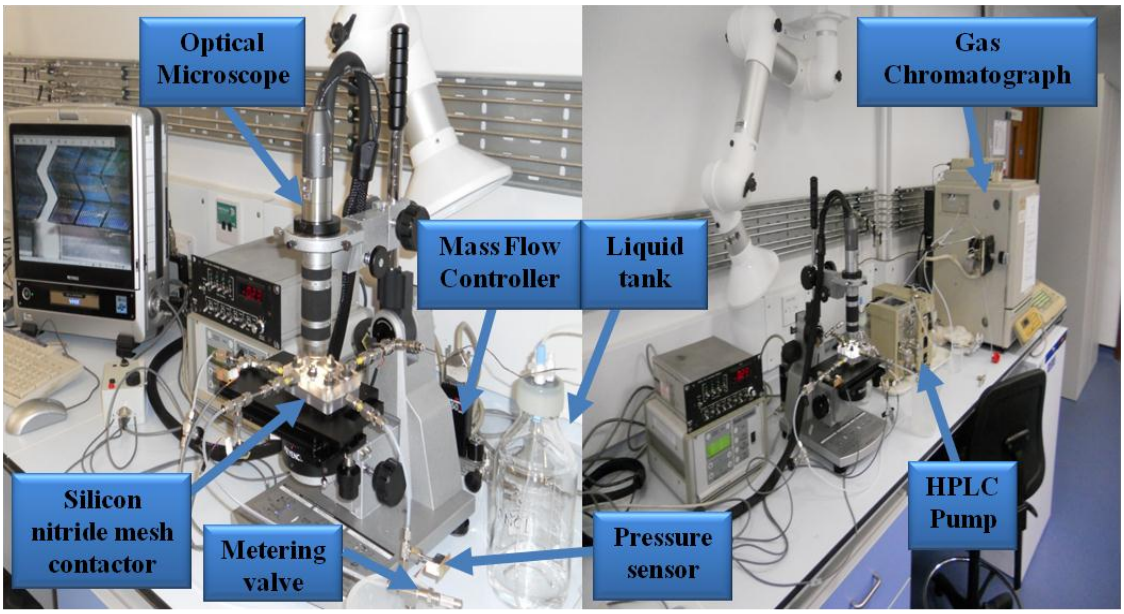

(b)

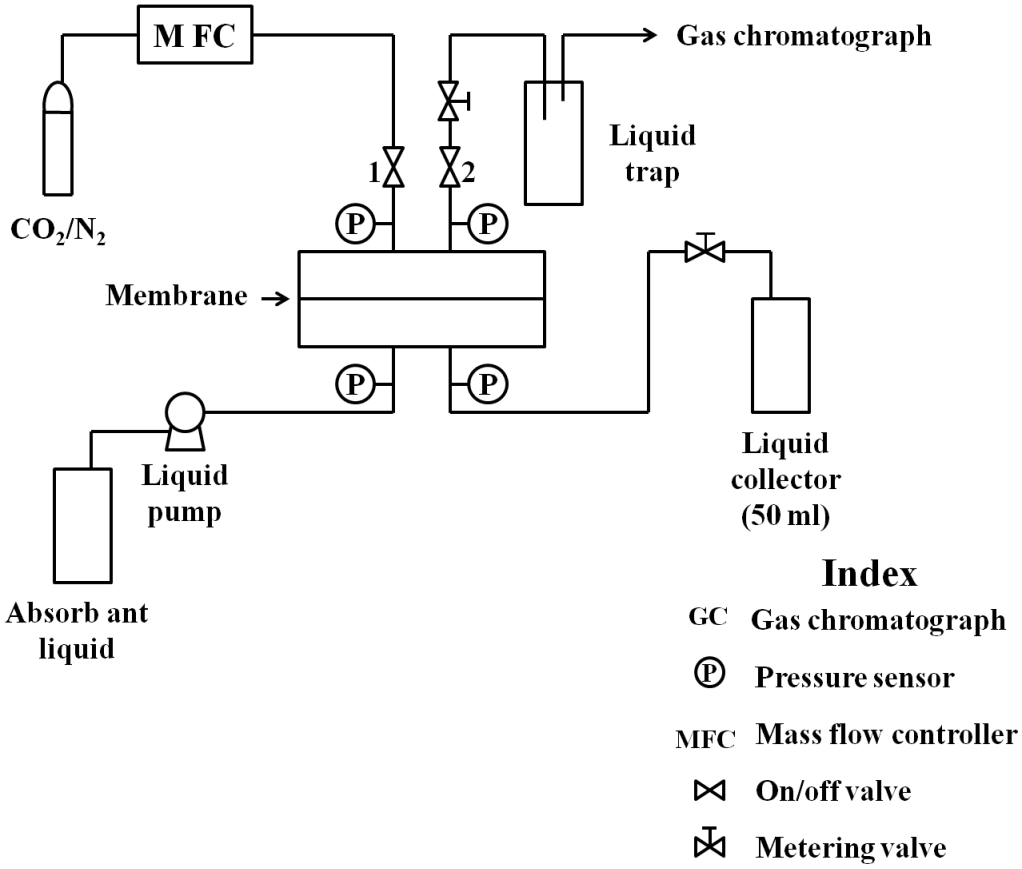

Figure 10. 3 (a) Picture of the experimental set-up used in this work (b) Schematic of the experimental set-up.

10.3 Mathematical model development

In order to compare the experimental results with theory a two-dimensional model of the microstructured mesh reactor was formulated. The model called "pseudo-homogeneous model", where the mesh is considered as a homogeneous medium with $D_{iL}^{M} = \varepsilon D_{L}^{L}$. Since as the gas chamber height was not 500 μm but more complicated as it is shown in Figure 10.2, two extreme cases were taken into account for the "pseudo-homogeneous model". The first one uses as a total gas height of 840 μm (see figure 10.2), and the second one takes account also the extra 2.37 mm of the nickel support which makes the total gas channel height at 3210 μm. The reason of choosing the two different heights for the gas channel is to observe the

contribution of this extra height of 2.37 mm, which is created from the nickel support on the performance of the reactor. The differential mass balances to describe the concentration profiles of components in the three domains gas, mesh, and liquid with the assumptions made are shown in Chapter 5. All the parameters used for the calculations are shown in table 10.1 while the reaction systems of NaOH and DEA with CO_2 are shown in Chapter 5 and 6 respectively. COMSOL Myltiphysics 3.5.a was used to solve the differential mass balances. A mesh consisting of 84000 number of elements and 442303 degrees of freedom was used to execute the simulations in Windows XP with Pentium IV 2.93GHz CPU and 24GB of RAM. At this number of elements the solution was found to be mesh independent.

Table 10. 1 Values of parameters used in the simulations. All the parameters were taken for T= 20^{o}C.

Parameter	Value	Reference
$D^{G}_{CO_2}$ (m^2/s)	$1.64x10^{-5}$	Cussler [95]
$D^{L}_{CO_2}$ (m^2/s)	$2.35x10^{-6}\exp(-2119/T)$	Versteeg and Van Swaaij [96]
D^{L}_{NaOH} (m^2/s)	$1.67 \times D^{L}_{CO_2}$	Nijsing *et al.* [97]
$m_{CO_2/NaOH}$ (-)	0.8314	Zanfir *et al.* [10]
$k_{CO_2/}$ (m^3/mol s)	$10^{(11.916-2382/T)}$	Pohorecki and Moniuk [94]
$D^{L}_{CO_2}$ (m^2/s)	$1.05x10^{-9}$	Zhang *et al.* [50]
D^{L}_{DEA} (m^2/s)	$4.97x10^{-10}$	Zhang *et al.* [50]
$m_{CO_2/DEA}$ (-)	0.8	Paul *et al.* [109]
k_{DEA} (m^3/mol s)	2.3	Zhang *et al.* [50]

10.4 Results and Discussion

10.4.1 Phase Breakthrough

Breakthrough was investigated in order to establish the acceptable operational pressure difference between gas and liquid which keeps the two phases separated. Figure 10.4 shows an experiment with indication of breakthrough, where gas from the bottom chamber has entered the liquid-phase (top channel) when the mesh cracked after the first use of the module. The theoretical breakthrough pressure of NaOH can be calculated by the Young-Laplace equation (4.24) and it was found to be 0cm H_2O, while the theoretical breakthrough pressure of CO_2 /N_2 was calculated by equation (4.25) and it was found 6756 cm H_2O. Due to limitation of the sealing material (acceptable operational pressure without leakage is 1000 cm H_2O) it was not feasible to test the module in its maximum operational pressure difference which keeps the two phases separated. During typical operation, pressure difference between gas and liquid phase was kept at $(P_G\text{-}P_L)_{inlet}\approx$130-170 cm H_2O (Figure 10.5 shows the indications of the pressure sensors at the gas and liquid phase).

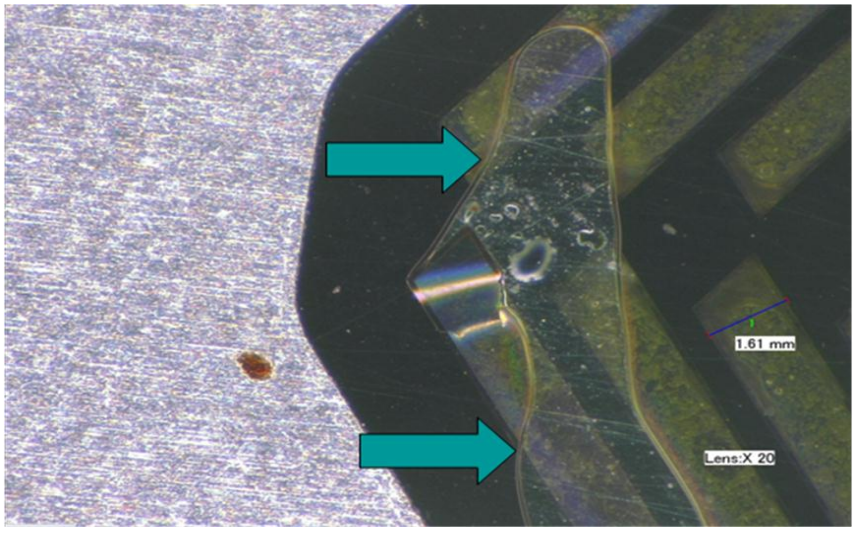

Figure 10. 4 Picture of the top (liquid) side of the reactor, during breakthrough of gas in the liquid side. The arrows indicate air bubbles in the liquid chamber.

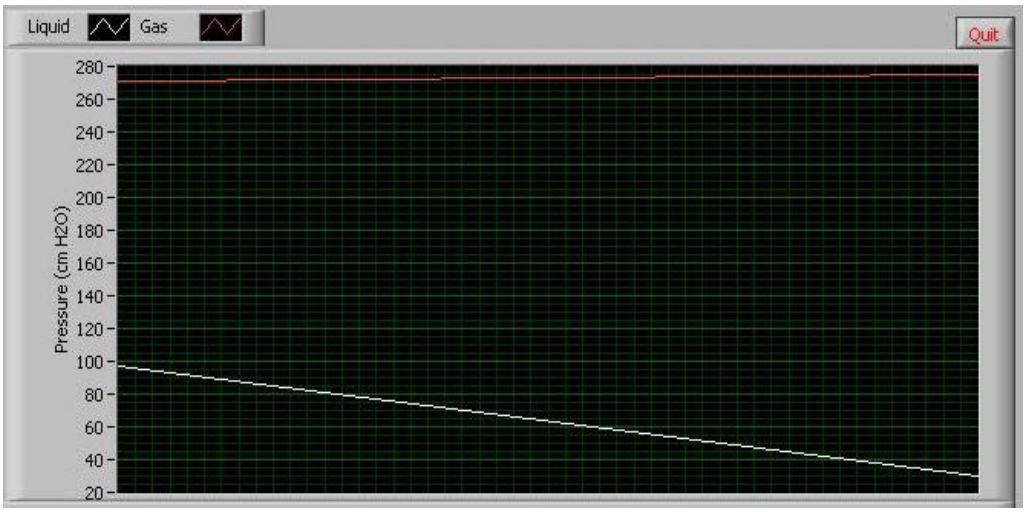

Figure 10. 5 Pressure profile in gas liquid phases in a co-current operation.

10.4.2 Model Prediction for CO_2 Absorption in NaOH Solution

As it was mentioned before, in order to observe the influence of the two different heights of the gas chamber (see figure 10.2) in the performance of the silicon nitride mesh reactor, two extreme cases were taken into account. The predictions of the two extremes of the pseudo-homogeneous model are compared with experimental results, obtained from carbon dioxide absorption in sodium hydroxide solution and are shown in Figure 10.6. The model shows better agreement with the experimental results when the gas channel height is considered to be 3210 μm instead of 840 μm. 19.7-23.1% of the carbon dioxide contained in the inlet stream was removed within 0.3-0.5 s experimental gas residence time (see figure 10.7). It can be seen from Figure 10.6 that the percentage of CO_2 removal decreases by increasing the gas flowrate. This is due to the fact that the increase of the gas flowrate reduces the residence time in the module, hence it results to lower removal of carbon dioxide.

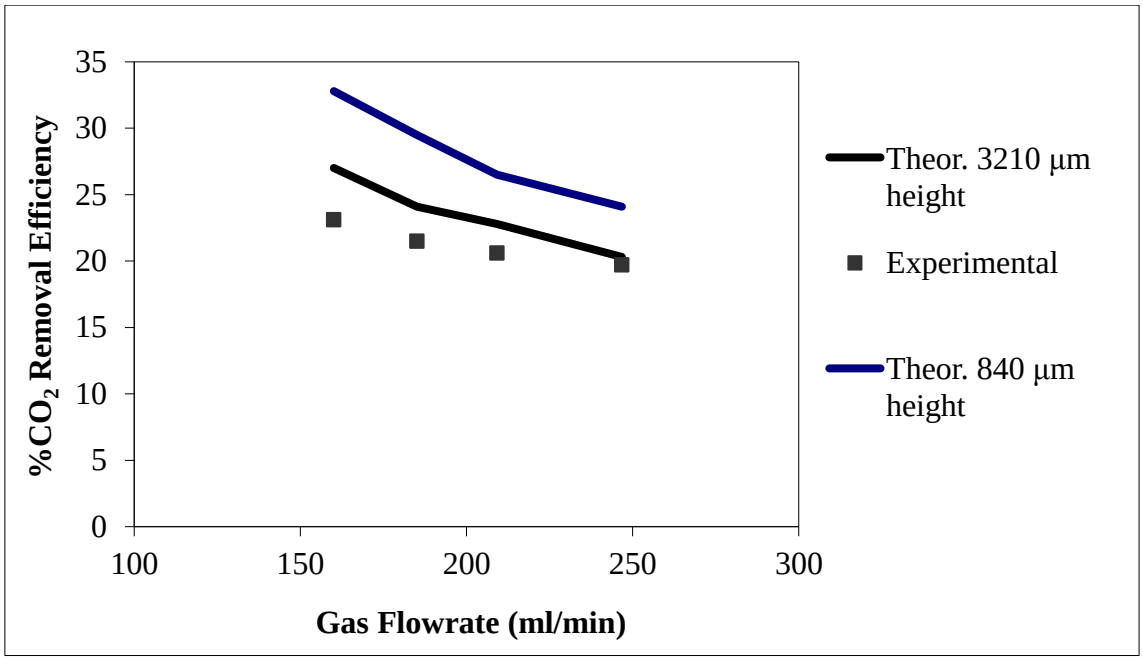

Figure 10. 6 Amount of CO_2 removed from the gas phase as a function of gas flowrate, obtained experimentally and by the pseudo-homogeneous model for the two extreme cases. Mesh porosity=20.3%, Y_{CO_2}/Y_{NaOH}=96.4, δ_L=25 µm, NaOH=2M.

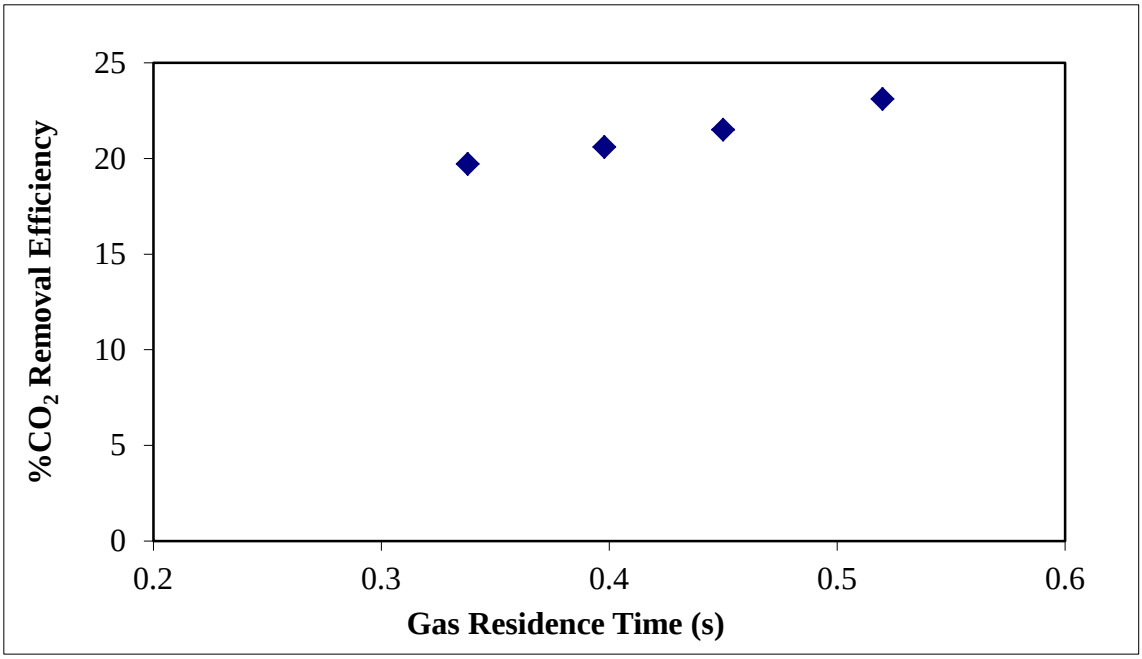

Figure 10. 7 Amount of CO_2 removed from the gas phase as a function of gas residence time based on the total height of 3210 µm , obtained experimentally. Mesh porosity=20.3%, Y_{CO_2}/Y_{NaOH}=96.4, δ_L=25 µm, NaOH=2M.

10.4.3 Influence of liquid flowrates

Figure 10.8 shows the comparison of the model with the experimental results for CO_2 removal as a function of liquid flowrates when the gas flowrate was kept constant. The percentage of CO_2 removal increases by increasing the liquid flowrate. As the liquid flowrate increases, the concentration of NaOH is kept higher since more fresh liquid is replacing the consumed NaOH and hence, increasing the driving force for CO_2 removal. The increase of CO_2 absorption is however relatively small, in agreement with similar trends observed. Rongwong *et al.* [46] in their experimental studies on membrane wetting in gas-liquid membrane contacting process for CO_2 absorption by single and mixed absorbents they observed that the CO_2 absorption flux increased with increasing liquid phase velocity. For 1M MEA solution and for liquid velocity between 0.5-1.4 m/s their fluxes were around 0.00033-0.00038 mol/m^{2}s while in our case for 2M NaOH and for a liquid velocity between 0.023-0.035 m/s our fluxes were found to be 0.013-0.016 mol/m^{2}s. Yan *et al.* [180] studied experimentally the separation of CO_2 from flue gas using hollow fiber membrane contactors with aqueous MEA, MDEA and potassium glycinate as absorbent liquids. They observed that the mass transfer rate of CO_2 increases slightly with liquid flow rate.

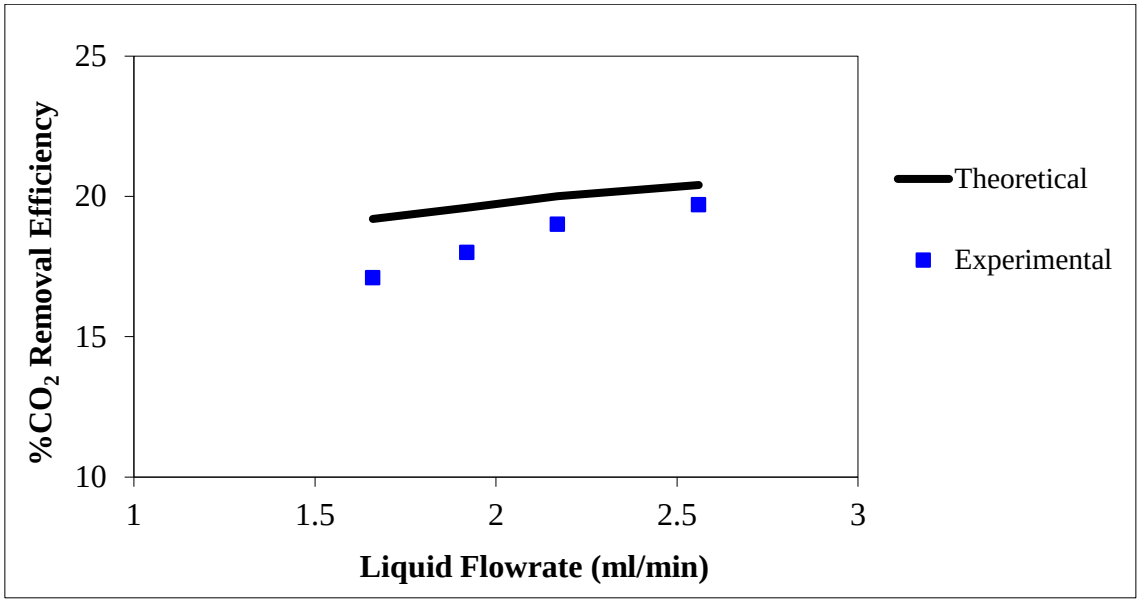

Figure 10.8 Amount of CO_2 removed from the gas phase as a function of liquid flowrate obtained experimentally and theoretically by the pseudo-homogeneous model, for constant gas flowrate. Mesh porosity=20.3%, δ_G=3210 μm, δ_L=25 μm, Y_G=246.7 ml/min, NaOH 2M.

10.4.4 Influence of liquid phase height

In order to observe the influence of the liquid channel height on CO_2 removal efficiency simulations were performed for two different liquid channel heights, one with 25 μm and one with 50 μm. Figure 10.9 shows the theoretical comparison of the two different heights for CO_2 removal as a function of gas flowrates when the liquid velocities were kept the same in order to have the same residence times for the two different heights. As it can be seen from the graph by increasing the liquid side height from 25 to 50 μm the CO_2 removal efficiency remains the same. An explanation for that might be the fact that the reaction is too fast and hence, the CO_2 consumed within 2-3 μm from the mesh/liquid interface so an extra increase of liquid side height will not create more resistance to mass transfer and as a result, no effect on CO_2 removal efficiency.

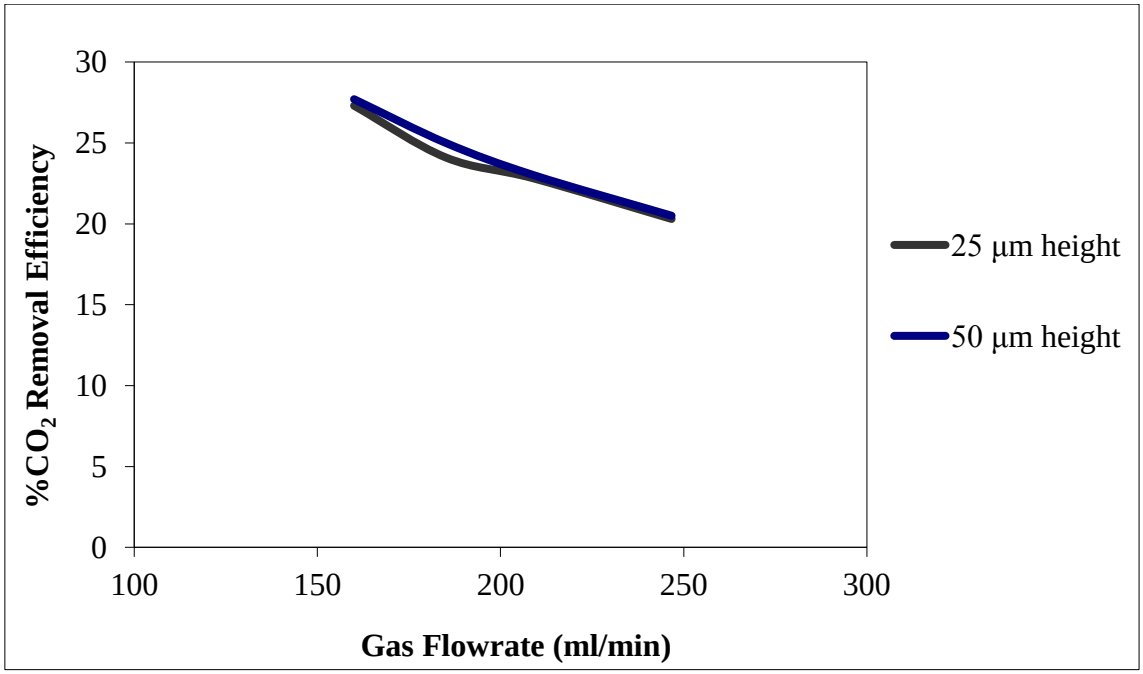

Figure 10. 9 Amount of CO_2 removed from the gas phase as a function of gas flowrate obtained theoretically by the pseudo-homogeneous model. Mesh porosity=20.3%, δ_G=3210 μm, NaOH 2M, $\mathbf{Y_{CO_2}/}Y_{NaOH}$=96.4 for the 25 μm height and $\mathbf{Y_{CO_2}/}Y_{NaOH}$=50.4 for the 50 μm height .

10.4.5 Model Prediction for CO_2 Absorption in DEA Solution

Two extreme cases were taken into account (see figure 10.2) in order to simulate the silicon nitride mesh reactor. The predictions of the two extremes of the pseudo-homogeneous model are compared with experimental results, obtained from carbon dioxide absorption in 2M diethanolamine (DEA) solution and are shown in Figure 10.10. The model shows better agreement with the experimental results when the gas channel height is considered to be 840 μm instead of 3210 μm. 16.8-20.4% of the carbon dioxide contained in the inlet stream was removed within 0.3-0.5 s experimental gas residence time. In addition it can be seen from the graph below that the percentage of CO_2 removal decreases by increasing the gas flowrate.

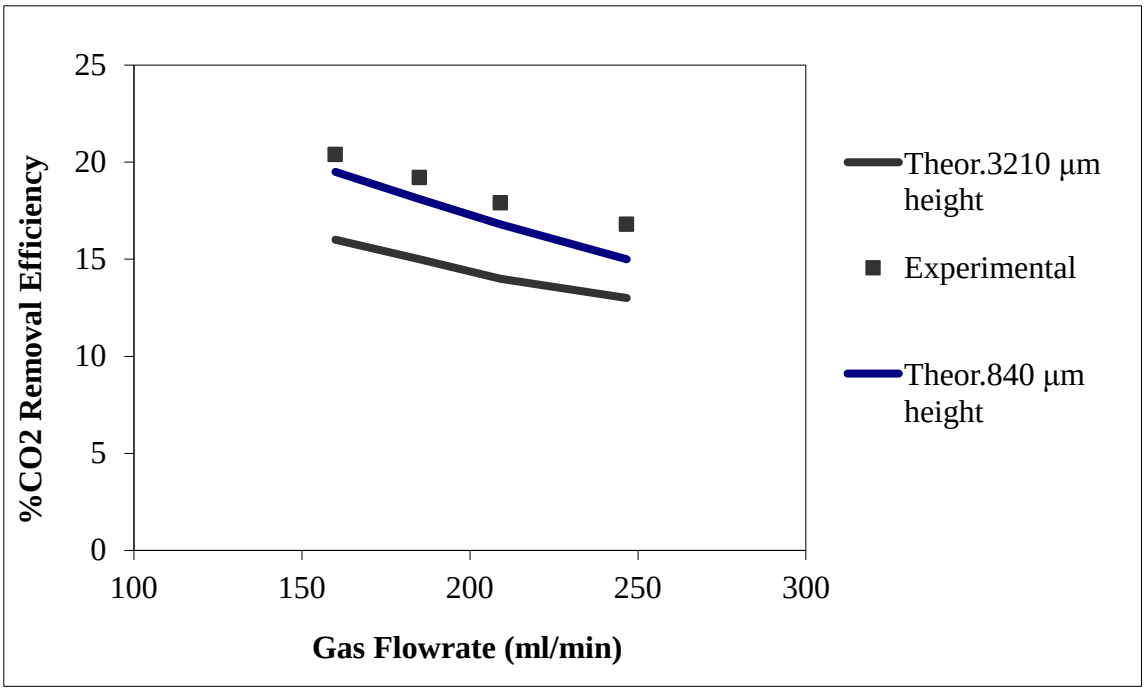

Figure 10. 10 Amount of CO_2 removed from the gas phase as a function of gas flowrate, obtained experimentally and by the pseudo-homogeneous model for the two extreme cases. Mesh porosity=20.3%, Y_{CO_2}/Y_{NaOH}=96.4, δ_L=25 μm, DEA 2M.

10.4.6 Influence of the type of the flow

Experiments were performed with two different flow patterns co-current and counter current in order to observe the influence of the type of the flow on CO_2 removal when 2M diethanolamine solution (DEA) was used. Figure 10.11 shows the performance of the mesh microreactor when the gas flow is counter or co-current to the liquid flow. As it can be seen from Figure 10.11 the operating flow pattern does not have an effect as both co-current and counter current flow patterns show the same results for CO_2 removal under the conditions were investigated. This is due to the fact that the diethanolamine is in excess (25%), which maximise the CO_2 driving force and this, in turn, minimises the effect of flow patterns on the CO_2 removal efficiency. Hoff *et al.* [181] performed experiments and modelling of carbon dioxide absorption in aqueous alkaloamine solutions using membrane contactors and they pointed out that the concentrations changes in a single module are modest, thus making the difference between counter and co-current flow very small.

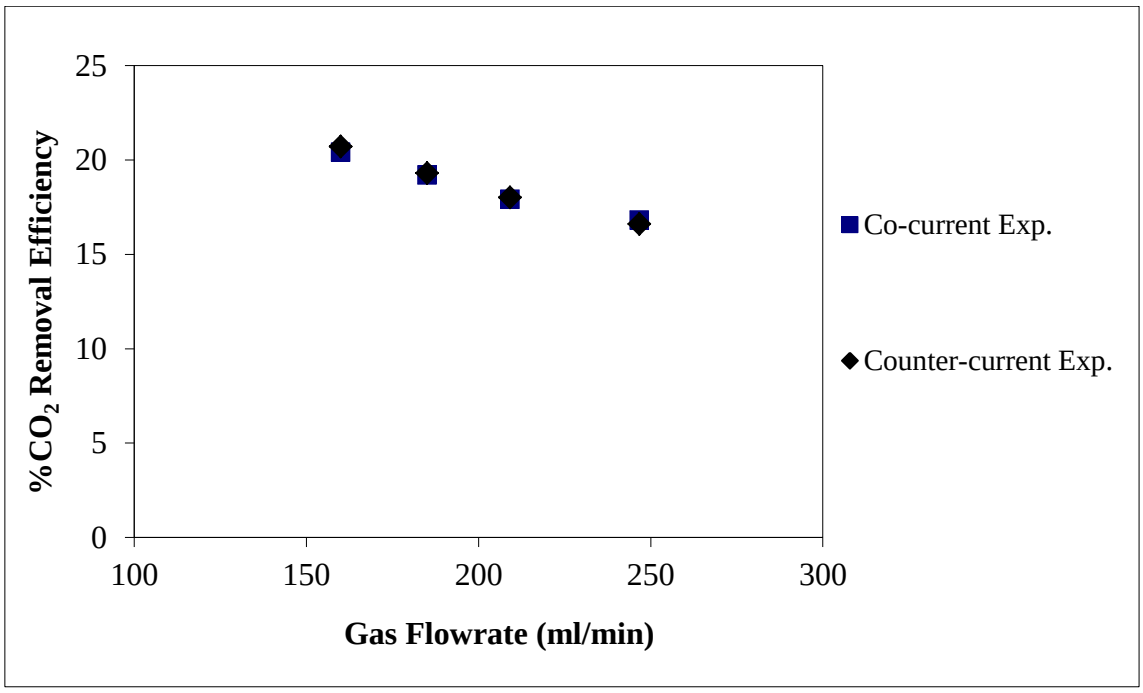

Figure 10. 11 Amount of CO_2 removed from the gas phase as a function of gas flowrate, obtained experimentally for two different flow patterns co-current and counter current. Mesh porosity=20.3%, Y_{CO_2}/Y_{DEA}=96.4, δ_G=3210 μm, δ_L=25 μm, DEA 2M.

10.4.7 Influence of the type of the absorbent solution

Experiments were performed with two different absorbent solutions 2M NaOH and 2M DEA in order to examine the effect on CO_2 removal. Figure 10.12 shows the experimental prediction of CO_2 removal using aqueous solutions of NaOH and DEA as a function of gas flowrate. As it can be seen from the graph below the CO_2 removal efficiency is higher when NaOH is used for absorbent liquid. The reaction rate constant of CO_2 and OH^- is higher than that of CO_2 and DEA, as a result higher CO_2 removal efficiency. Atchariyawut *et al.* [114] showed that in the case of chemical reaction, a higher CO_2 flux was achieved using NaOH than MEA for CO_2 absorption in hollow fiber membrane contactor for the reason mentioned above.

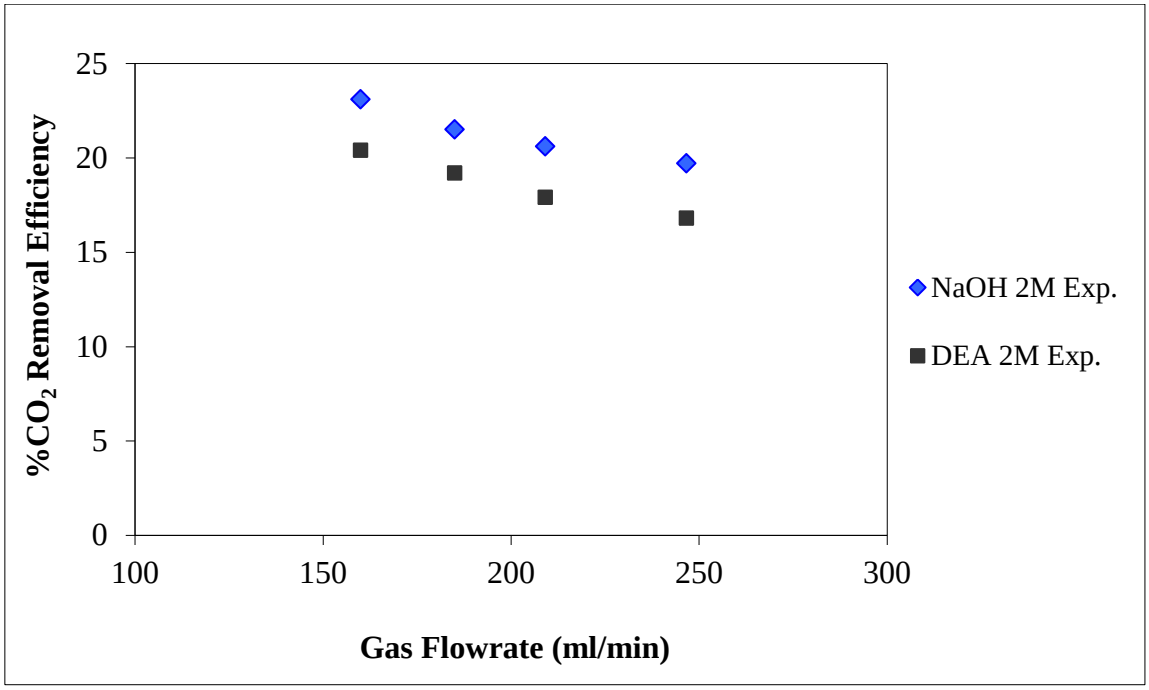

Figure 10. 12 Amount of CO_2 removed from the gas phase as a function of gas flowrate, obtained experimentally for two different types of solutions. Mesh porosity=20.3%, Y_{CO_2}/Y_{NaOH}=96.4, Y_{CO_2}/Y_{DEA}=96.4 δ_G=3210 μm, δ_L=25 μm, DEA 2M, NaOH 2M.

10.4.8 Comparison between the fluxxion module with other contactors

Figure 10.14 shows the comparison of the silicon nitride mesh reactor with the PTFE membrane single channel reactor (see chapter 5), the metallic mesh reactor (see chapter 4) and the CRL mesh reactor (see chapter 4) for CO_2 absorption using aqueous solution of NaOH 2M. Since the gas chamber height is not only the height inside the silicon wafer but also is defined from an extra height form the nickel support (see figure 10.2), is more precise to compare with other module based on the modified residence times. Modified gas residence time is defined as the surface area of the mesh over inlet volumetric flowrate. Figure 10.13 shows the shapes of the gas/liquid contact areas of the four modules used for the comparison. Table 10.2 shows the conditions used to calculate the modified residence times for the four different modules. As it can be seen from the Figure below silicon nitride mesh reactor has the best performance among the modules. CO_2 removal efficiency is higher than the single channel PTFE membrane reactor for smaller modified residence times and it is around the same with the metallic mesh reactor for much lower modified residence times. Finally CRL mesh reactor has higher removal efficiency than the metallic mesh but it seems that, by extrapolating the data from Figure 10.14 for the silicon nitride mesh reactor, for the same modified residence time, CO_2 removal efficiency of the CRL will be close to the silicon nitride mesh reactor. Silicon nitride mesh reactor has the best performance due to the very thin mesh (just 1μm thick), which makes the resistance to mass transfer very small compared to the other reactors.

(a)

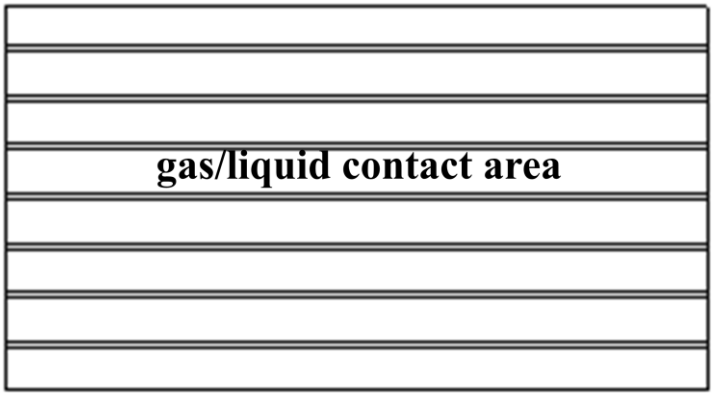

(b)

(c)

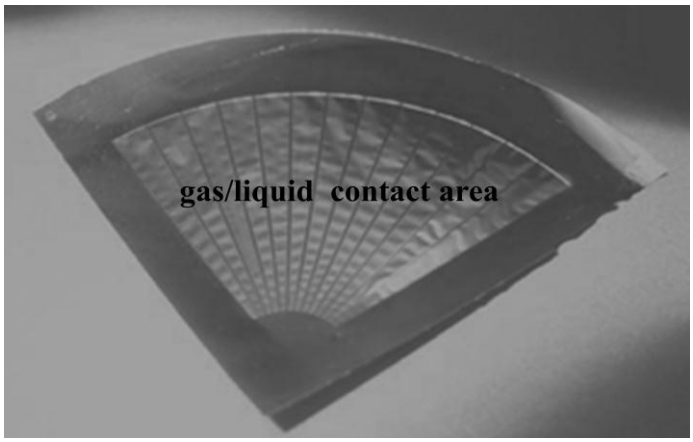

(d)

Figure 10. 13 Schematics of the gas/liquid contact areas for (a) metallic mesh microreactor (b) PTFE membrane microreactor (c) CRL microreactor (d) silicon nitride mesh microreacror.

Table 10. 2 Conditions used for calculations of the modified residence times for four different modules.

Silicon nitride mesh	**Metallic mesh**	**PTFE membrane**	**CRL mesh**
Gas flow rate [cm^3/s]	**Gas flow rate [cm^3/s]**	**Gas flow rate [cm^3/s]**	**Gas flow rate [cm^3/s]**
4.11	5.90	4.11	0.75
3.49	5.12	3.49	0.66
3.08	4.45	3.08	0.59
2.67	3.75	2.67	0.51
Surface area [cm^2]	**Surface area [cm^2]**	**Surface area [cm^2]**	**Surface area [cm^2]**
4.34	39.42	4.93	5.23
Modified gas residence time [s/cm]	**Modified gas residence time [s/cm]**	**Modified gas residence time [s/cm]**	**Modified gas residence time [s/cm]**
1.06	6.68	1.20	6.95
1.25	7.70	1.41	7.89
1.41	8.86	1.60	8.86
1.63	10.51	1.85	10.25

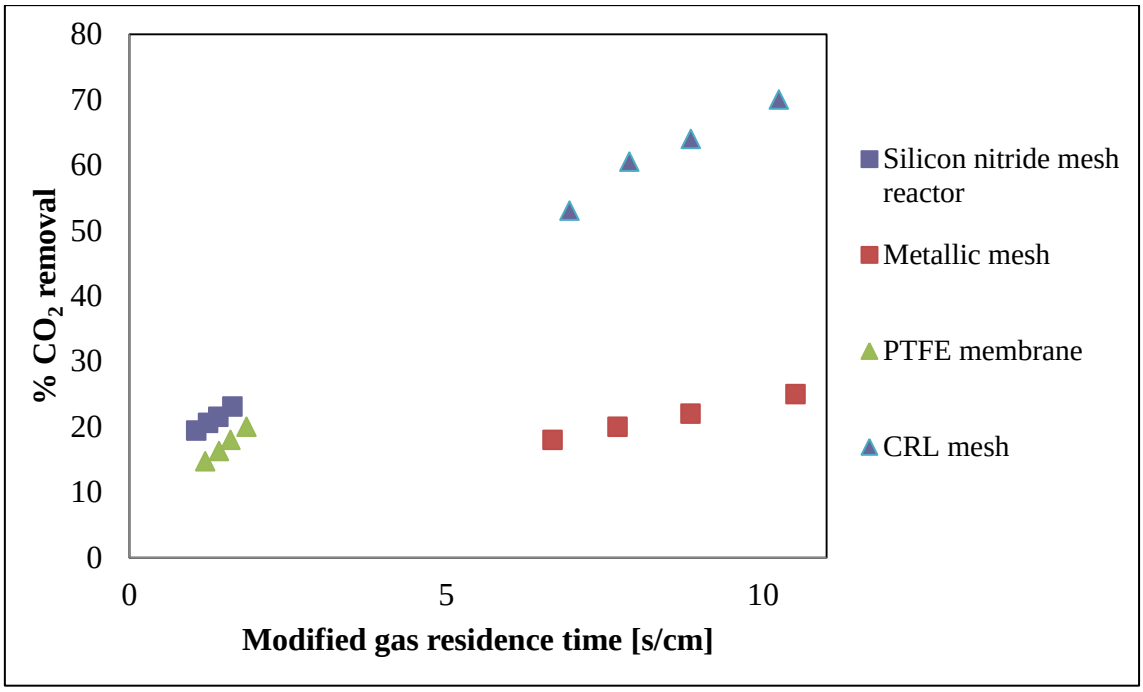

Figure 10. 14 Amount of CO_2 removed from the gas phase as a function of modified residence times, obtained experimentally for four different modules: silicon nitride mesh, PTFE membrane, metallic mesh and CRL mesh, NaOH 2M.

10.4.9 Comparison between silicon nitride mesh reactor and conventional packed contactors from literature based on height of transfer unit (HTU)

Figure 10.15 shows the comparison between the silicon nitride mesh reactor with a conventional packed contactor from literature [182] for CO_2 absorption in monoethanolamine solution (MEA). The HTU (height of transfer unit) was calculated from equation 10.2 [183] (for details see Appendix D):

$$HTU = \frac{u}{K * \alpha} \tag{10.2}$$

where u is the velocity (m/s), K is the overall mass transfer (m/s) and

$$\alpha = \frac{\text{gas/liquid contact area}}{\text{contactor volume}} (m^2/m^3)$$

The overall mass transfer coefficient can be calculated from equation 10.3 based on the liquid driving force as followed:

$$\frac{1}{K} = \frac{H}{k_g} + \frac{1}{k_m} + \frac{1}{k_l} \tag{10.3}$$

where k_l , k_m, k_g are the liquid, mesh , gas mass transfer coefficients, and H the henry's constant.

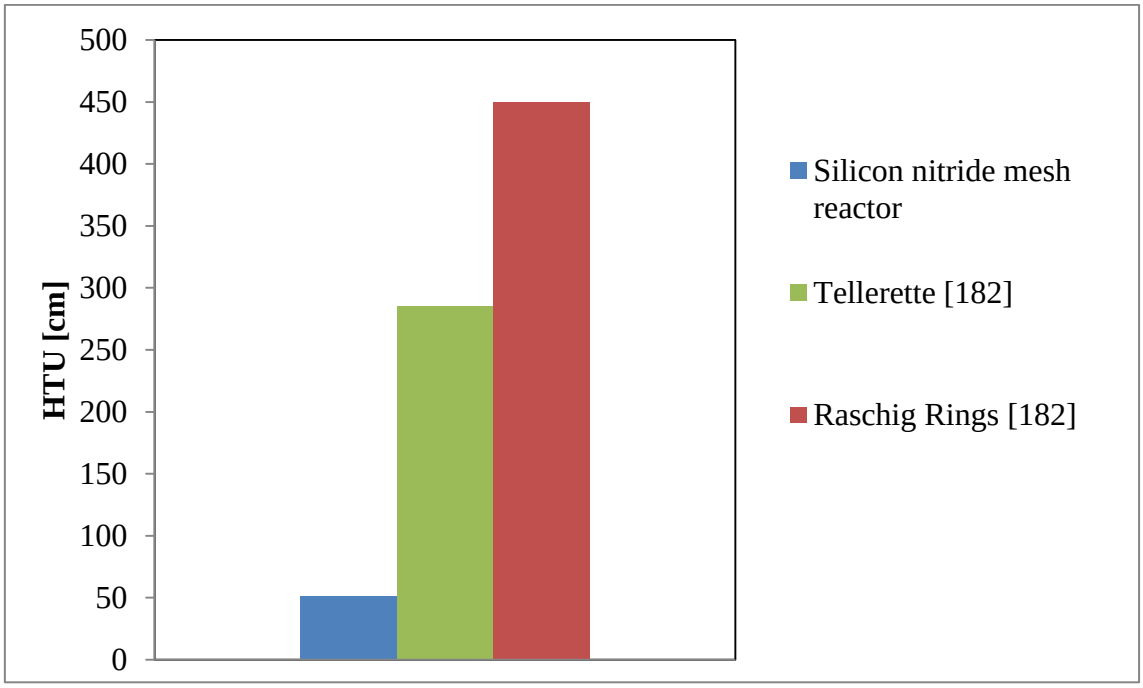

Figure 10. 15 Comparison of the height of transfer unit (HTU) between silicon nitride mesh reactor and conventional packed columns from literature for CO_2 absorption using MEA solution.

Figure 10.15 shows the comparison of the silicon nitride mesh reactor with a packed column from literature [182] when two different packing materials were used. The internal diameter of the column is 20.32 cm and height is 173cm. When Tellerettes packing (1.9 x 5.1 x 2 cm polyethylene) was used gas and liquid velocities were 0.73cm/s and 1.271 cm/s respectively with temperature between 38-48^{o}C using of 3.2M MEA as absorbent solution, with 2-10%vol of CO_2 inlet concentration, while when Rasching packing (2.54 x 2.54 x 0.16cm carbon steel) was used gas and liquid velocities were 0.11cm/s and 0.19cm/s respectively with temperature between 38-48°C, with 3.2 MEA solution and 2-10%vol of CO_2 inlet concentration. In our case gas and liquid velocities were 1.73 cm/s and 2.3 cm/s respectively for T=20^{o}C, with 2M

MEA solution and CO_2 inlet concentration of 20%vol. As it can be seen from the Figure 10.15 the HTU values for the silicon nitride mesh reactor are significantly lower (≈6-9 times) than those of a conventional packed contactor for CO_2 absorption in MEA solution. This leads to lower specific area requirements and, hence, to a reduction in absorber investment costs compared to packed towers.

10.5 Conclusions

Carbon dioxide absorption was studied in aqueous solutions of NaOH and diethanolamines (DEA) in the silicon nitride mesh reactor. Significant absorption was observed with gas residence time around 0.5 s. In order to compare the experimental results with theory, and examine the influence of the two different heights of the gas chamber (see figure 10.2) on the reactor performance two extreme cases were implemented. For the NaOH simulations the model shows better agreement with the experimental results when the gas channel height considered to be 3210 μm instead of 840 μm. Furthermore, model predictions and experimental results showed that, the percentage of CO_2 removal increases by increasing the liquid flowrate, due to the fact that the concentration of NaOH is kept higher as a result, the driving force for CO_2 removal is increased. Simulations showed that the height of the liquid channel does not affect the CO_2 removal efficiency. In addition the predictions of the two extremes of the pseudo-homogeneous model are compared with experimental results, when 2M diethanolamine (DEA) solution was used as absorbent. The model showed better agreement with the experimental results when the gas channel height is considered to be 840 μm instead of 3210 μm. Experiments showed that the operating flow pattern does not have an effect as both co-current and counter current flow patterns showed the same results for CO_2 removal under the conditions were investigated for CO_2 absorption in DEA solution. This can be explained by the fact that the diethanolamine is in excess, which maximises the CO_2 driving force and this, in turn, minimises the effect of flow patterns on the CO_2 removal efficiency. CO_2 removal efficiency was higher when NaOH was used for absorbent liquid than DEA since the reaction rate constant of CO_2 and OH^- is higher than that of CO_2 and DEA. Comparison between the silicon nitride mesh reactor with the PTFE single channel reactor, the metallic mesh reactor, and the CRL reactor using NaOH as absorbent based on the modified residence times, showed that the silicon nitride mesh reactor had the best

performance among the four modules due to the very thin mesh of 1μm thick, which makes the resistance to mass transfer very small. Finally the HTU analysis showed that the HTU values for the silicon nitride mesh reactor are significantly lower (≈6-9 times) than those of a conventional packed contactor, which leads to a reduction in absorber investment costs compared to packed towers.

CHAPTER 11

CONCLUSIONS & FUTURE WORK

The objective of this work was to study experimentally and theoretically novel reactors, particularly ones manufactured through microtechnology, for carbon dioxide absorption in sodium hydroxide and amine solutions in order to evaluate, understand and improve their performance. For these reasons CO_2 absorption in sodium hydroxide and amine solutions has been performed in a microstructured metallic mesh reactor, PTFE single channel membrane reactor and the High Efficiency Contactor with silicon nitride membrane. Various parameters such as gas and liquid flowrates, gas and liquid film thickness, membrane open area, type of the flow, type of absorbent liquid, concentration of the absorbent liquids, gas residence time, influence of ultrasound, influence of staggered herringbones and numbering up were investigated.

In Chapter 3 3D CFD models were performed by varying in turn geometrical parameters such as: width of inlet and outlet flow distribution regions, different shapes of inlet and outlet flow distribution regions, shifting the channels in parallel, effect of the channels, in order to approach a design which allows the flow distribution to be as uniform as possible over the plate. Simulations performed on a plate without channels and the results have revealed that fluid bypass exists, leading to the formation of two stagnation regions with very low fluid velocities compared to the central part of the plate. As a result the use of channels over the microplate appears to be crucial when the fluid must be distributed over the plate with uniform velocity. Furthermore, it has been shown by decreasing the width of the inlet and outlet chamber the fluid tends to cover the top and the bottom channels with a higher velocity compared to the middle area of the plate. Finally the results showed that the shape of the inlet

and outlet manifolds is an important factor to take into consideration as it can significantly affect the quality of the flow distribution within the microchannels.

In Chapter 4 CO_2 absorption in sodium hydroxide solution was conducted in a metal microstructured mesh reactor. A two-dimensional model was formulated to simulate the reactor. Two variations of the model were implemented in order to compare the experimental results with theory. The first one, called "segregated model", where the solid part of the perforated area is neglected and the open area of the mesh is utilised to modify the effective length of the reactor, and the second called "pseudo-homogeneous model", where the mesh is considered as a homogeneous medium. Results showed that in less than 1.2 s gas residence time approximately 30% of the carbon dioxide was removed. The segregated model showed much better agreement with experimental data. Parametric studies showed that CO_2 removal efficiency increases by increasing the liquid flowrate and decreasing the gas flowrate. The model indicated that the carbon dioxide is consumed within few microns from the gas-liquid interface, and the dominant resistance for mass transfer is located in the mesh because it is wetted by the liquid reactant. As a consequence, increasing the open area of the mesh from 15% to 25% increased the CO_2 removal efficiency significantly. Finally, experiments performed in the CRL mesh reactor. CO_2 removal was increased using CRL reactor. This is due to the fact that in the CRL reactor the thickness of the mesh was 5 times thinner from the mesh used in the acrylic reactor, hence it has less resistance to mass transfer.

In Chapter 5 in order to overcome the limitation of the extra resistance to the mass transfer in the metallic mesh, since the pores of the metallic mesh are liquid filled, PTFE membranes were used, which are considered as hydrophobic to aqueous solutions of amines. CO_2 absorption in amine solutions of monoethanolamine (MEA) and diethanolamine (DEA), which are widely used for industrial absorption processes, was performed in a membrane PTFE single channel microreactor. A two dimensional model was formulated to simulate the reactor, and experimental results were compared to model predictions in terms of CO_2 removal efficiency. The model showed very good agreement with experimental data. Both model and experimental results showed that, MEA solution absorbed more CO_2 than DEA. Experimental and model results showed less CO_2 removal efficiency with lower MEA concentration. Experiments were performed with larger contact area between gas and liquid. CO_2 removal efficiency increased by increasing the contact area between gas and liquid.

In Chapter 6 CO_2 absorption in NaOH solution was contacted in a membrane PTFE single channel microreactor. A two dimensional model with using wetted and non-wetted operation conditions was formulated to simulate the reactor, and experimental results were compared to model predictions in terms of CO_2 removal efficiency. Experimental results showed better agreement with the wetted-mode operation conditions than the non-wetted conditions. An explanation to that might be the fact that the pores of the PTFE membrane are partially wetted (some pores are completely liquid filled and some pores are completely gas filled) and not 100% gas filled. Experiments showed that the CO_2 removal efficiency reduces with decreasing concentration of NaOH. Furthermore, experiments were performed with larger contact area between gas and liquid. CO_2 removal efficiency increases by increasing the contact area between gas and liquid. Using NaOH as an absorbent liquid showed higher CO_2 removal efficiency than when DEA was used as an absorbent liquid. Comparison between the 8 channel (PTFE) microreactor and mesh (metallic) microreactor showed much higher CO_2 removal efficiency for the PTFE membrane reactor than the mesh microreactor, due to less restriction to mass transfer when the PTFE membrane was used. In order to understand the effect of the pore-to pore distances on the PTFE membrane, on the performance of the microreactor, a single pore was simulated in order to examine the concentration profiles of CO_2 and NaOH in the liquid side of the microreactor. Results showed that CO_2 concentration exists in a distance of approximately 2-3 μm (x direction) adjacent to the pore walls, which indicates that the micropores in the membrane can be close together in a distance of more than 2-3 μm without causing overlap of diffusion fields which might affect the performance of the reactor. Future investigations should focus on further understanding of partial wetting in the hydrophobic membranes which is not fully established by researchers so far, and particularly to examine the behaviour of the fluid meniscus into the non-wetting pores, since the structure of the pores inside the PTFE membrane is more complex than the pores in the metallic mesh which are straight.

In Chapter 7, carbon dioxide absorption in sodium hydroxide was studied in the single channel PTFE membrane reactor with the use of staggered herringbones on the floor of the liquid channel of the reactor, in order to enhance mass transfer. Experiments were performed with the staggered herringbones engraved on the floor of the liquid channel of the acrylic reactor and by using silicon inserts with the staggered herringbones on them placed in the liquid side of the acrylic reactor. Results showed no improvement of CO_2 removal efficiency compared with the flat channel when the acrylic or the silicon inserts herringbones were used.

A three-dimensional model with and without the use of staggered herringbones was employed which agreed with the experimental results that the staggered herringbones do not have any improvement on CO_2 removal efficiency compared to a flat channel without the staggered herringbones. Based on Hatta number analysis a possible reason for that behaviour is due to the fact that enhancement factor is practically constant. For a fast second order reaction in liquid film with high concentration of NaOH the apparent rate equation is independent from k_l and hence, any change of mass transfer k_l achieved by staggered herringbones will not increase the apparent reaction rate and consequently will not increase the CO_2 removal efficiency. Furthermore, an analytical model for the stripping of acetone from water was formulated. Non improvement of the ratio $\frac{C_{Ac,out}}{C_{Ac,in}}$ was observed with the use of staggered herringbones compared with the flat channel. Based on Candu Perez [147] work which showed that the highest stirring intensity therefore, higher convecting mass transfer was found close to the channel floor, it will be a good idea for future work to execute 3D simulations with the staggered herringbones as closer as possible to the liquid/membrane interface or even incorporate them in the membrane in order to examine the efficiency of stirring on mass transfer when we are close to the reaction zone between CO_2 and NaOH.

In Chapter 8 preliminary investigation of the effect of ultrasound on carbon dioxide absorption in sodium hydroxide solution is presented when the single channel PTFE membrane reactor was used. The experimental results obtained from the use of ultrasound did not have any effect on mass transfer compared to the experimental results without the use of ultrasound. Furthermore, experiments were performed with different orientations of the membrane reactor inside the ultrasonic bath, in order to achieve streaming in the liquid side of the membrane reactor. No improvement was observed when experiments were performed with different orientations of the reactor. Further investigation and understanding of the acoustic field inside the ultrasonic cleaner is worth carrying out in order to achieve acoustic streaming in the liquid side of the membrane reactor. Micro PIV (particle image velocimetry) could be used to observe the velocity profile inside the liquid side of the reactor in order to understand if the ultrasound creates the appropriate streaming which will increase the mass transfer.

In Chapter 9 in order to increase throughput carbon dioxide absorption in sodium hydroxide solution was performed in the metallic mesh scale out microreactor (4 mesh), and its performance was compared with the metallic mesh microreactor (1 mesh). CO_2 removal

efficiency for the metallic mesh scale out reactor was significantly lower than the metallic mesh reactor. This might be caused by uneven flow distribution to each plate, despite the fact that CFD simulations showed even flow distribution to every plate of the scale out reactor or by breakthrough of liquid in the gas phase (stagnant liquid) in the second or in the third plate where visualisation was not possible. In order to control better the pressure drop along each plate of the scale out reactor and keep it the same inserts with different channel widths were installed in every inlet of each plate (gas and liquid side) of the scale out reactor. Despite the new modification on the metallic mesh scale out reactor, CO_2 removal was significantly less than the metallic mesh reactor. For better control of each plate a good idea, is the installation of one metering valve in each plate (at each liquid outlet) hence, breakthrough and maldistribution in each plate can be avoided.

In Chapter 10 the silicon nitride mesh contactor developed by Bayer Technology Services and FluXXion was used for CO_2 absorption in aqueous solutions of NaOH and DEA. Two extreme cases were implemented for the "pseudo-homogeneous model", since the gas channel height was more complicated than the suggested height. Model predictions and experimental results when NaOH was used as absorbent showed that the percentage of CO_2 removal increases by increasing the liquid flowrate. Experiments showed that the operating flow patterns become unimportant as both co-current and counter current flow patterns showed the same results for CO_2 removal under the conditions investigated for CO_2 absorption in DEA solution. When NaOH was used as absorbent liquid, CO_2 removal efficiency was higher since the reaction rate constant of CO_2 and OH^- is higher than that of CO_2 and DEA. The silicon nitride mesh contactor showed better performance (regarding CO_2 removal efficiency) than the PTFE single channel reactor, the metallic mesh reactor reactor and the CRL reactor, due to the very thin mesh (1 μm thick), which makes the resistance to mass transfer very small. Finally the calculated HTU values for the silicon nitride mesh contactor are significantly lower (≈6-9 times) than those of a conventional packed contactor, resulting to lower investment costs compared to packed towers. Future investigations should focus on a more detailed model which can describe more precisely the gas height of the module, and particularly to examine what is the influence of the gas channels (located between the support structure of the silicon sieve and the membrane) in the performance of the module.

Physical and chemical characteristics of small micro scale spaces, namely short diffusion length, large specific surface area can be effective for improvement of mass and heat transfer

processes. As a result, precise control of reaction conditions becomes possible in microreactors and potentially leads to higher yields. In general these advantages have been clearly demonstrated. Miniaturized continuous flow reactors are expected to replace some large batch-type reactors commonly used in conventional chemical plants. Scale-up issues have not received as much development attention so far. The transition from lab-scale to industrial scale chemical processing will probably gain more attention in the coming years.

REFERENCES

[1] Li, J.L., Chen, B.H. 2005. Review of CO_2 Absorption Using Chemical Solvents in Hollow Fiber Membrane Contactors. *Separation and Purification Technology*, 41(2), pp. 109-122.

[2] Hessel, V., Angeli, P., Gavriilidis, A., Loewe, H. 2005. Gas-liquid and Gas-Liquid-Solid Microstructured Reactors: Contacting Principles and Applications. *Industrial & Engineering Chemistry Research*, 44(25), pp. 9750-9769.

[3] Kuiper, S., Van Rijn, C.J.M., Nijdam, W., Elwenspoek, M.C. 1998. Development and Applications of Very High Flux Microfiltration Membranes. *Journal of Membrane Science*, 150(1-8), pp. 1.

[4] Wenn, D.A., Shaw, J.E.A., Mackenzie, B. 2003. A Mesh Microreactor for 2-Phase Reactions. *Royal Society of Chemistry*, 3, pp. 180-186.

[5] Gavriilidis, A., Sun, X. 2008. Scalable Reactor Design for Pharmaceuticals and Fine Chemicals Production. Part 3: A Novel Gas-Liquid Reactor for Catalytic Asymmetric Transfer Hydrogenation with Simultaneous Acetone Stripping. *Organic Process Research & Development*, 12(6), pp. 1218-1222.

[6] Manz, A., Graber, N., Widmer, H. 1990. Miniaturized total chemical analysis systems: a novel concept for chemical sensing. *Sensors and Actuators B*, 1(1-6), pp. 244-248.

[7] Roberge, D., Ducry, L., Bieler, N., Cretton, P., Zimmermann, B. 2005. Microreactor technology: A revolution for the fine chemical and pharmaceutical industries? *Chemical Engineering & Technology*, 28(3), pp. 318-323.

[8] Shaw, J., Gavriilidis, A. Unit Operations-Separation Units, pp. 9-11.

[9] Jahnisch, K., Barens, M., Hessel, V., Ehrfeld, W., Harekamp, V., Lowe, H., Wille, Ch., Guber A. 2000. Direct Fluorination of Toluene Using Elemental Fluorine in Gas/Liquid Microreactors. *Journal of Fluorine Chemistry*, 105, pp. 117-128.

[10] Zanfir, M., Gavriilidis, A. 2005. Carbon Dioxide Absorption in a Falling Film Microstructured Reactor. *Industrial & Engineering Chemistry Research*, 44(6), pp. 1742-1751.

[11] Trambouze, P., Landeghem, V., Wauquier, H.J.P. 1998. Chemical Reactors: Design/Engineering/Operation, Gulf Publishing: Paris.

[12] Ehrfeld, W., Hessel, V., Holger, L. 2000. Microreactors, New Technology for Modern Chemistry, Wiley-VCH: Weinheim.

[13] Sun, X. 2007. Studies of catalytic asymmetric transfer hydrogenation in batch and continuous reactors. Thesis (Ph.D), University College London.

[14] Brans G., Kromkamp J., Pek, N., Gielen J., Heck J.,van Rijn C.J.M, van der Sman R.G.M., Schroen C.G.P.H., Boom R.M. 2006. Evaluation of microsieve membrane design, *Journal of Membrane Science*, 278(1-2), pp. 344–348.

[15] Kralj, G.J., Sahoo, R.H., Jensen, F.K. 2007. Integrated Continuous Microfluidic Liquid-Liquid Extraction, *Lab on a Chip*, 7(2), pp. 256-263.

[16] Hartman, L.R., Sahoo, R.H., Yen, C.B., Jensen, F.K. 2009. Distillation in microchemical systems using capillary forces and segmented flow. *Lab on a Chip*, 9, pp. 1843-1849.

[17] Adiche C., Sundmacher K. 2010. Experimental investigation on a membrane distillation based micro-separator. *Chemical Engineering and Processing*, 49(4), pp. 425-434.

[18] Aota, A., Mawatari, K., Takahashi, S., Matsumoto, T., Kanda, K., Anraku, R., Hibara, A., Tokeshi, M., Kitamori, T. 2009. Phase Separation of Gas-Liquid and Liquid-Liquid Microflows in Microchips. *Microchim Acta*, 164(3-4), pp. 249-255.

[19] Timmer, B.H., Delft, K.M van Delft, Olthuis, W., Bergveld, P., Van den Berg, A. 2003. Micro-evaporation electrolyte concentrator. *Sensors and Actuators B*, 91(1-3), pp. 342-346.

[20] Castell, K.O., Allender, J.Ch., Barrow, A.D. 2009. Liquid-liquid phase separation: characterisation of a novel device capable of separating particle carrying multiphase flows. *Lab on a Chip*, 9(3), pp. 388-396.

[21] TeGrotenhuis Ward E. and Stenkamp Victoria S. Normal Gravity Testing of a microchannel Phase Separator for Insitu Resource Utilization, NASA/CR—2001-210955 [online] Available: http://gltrs.grc.nasa.gov/GLTRS [accessed: 2 February 2011].

[22] TeGrotenhuisa W. E., Cameron. R. J.,Butcher M. G., Martin P. M., Wegeng R. S, 1999. Microchannel devices for efficient contacting of liquids in solvent extraction, 34 (6-7), pp. 951-974.

[23] Chan T.Y., Priestman, G.H. , MacInnes J.M., Allen R.W.K. 2008. Development of a micro-channel contactor-separator for immiscible liquids, *Chemical engineering Research and Design*, 86(A1), pp. 65-74.

[24] Gabelman A., Hwang, S.T. 1999. Hollow Fiber Membrane Contactors. *Journal of Membrane Science*, 159(1), pp. 61-106.

[25] Cussler E.L. ed. 1994. Hollow Fiber Contactors in Membrane Processes in Separation and Purification, Kluwer Academic Publishers. NATO ASI Series E. Dordrecht.

[26] Feron, P.H.M.; Jansen, A.E. 1995. Capture of Carbon Dioxide Using Membrane Gas Absorption and Reuse in The Horticultural Industry. *Energy Conversion & Management*, 36(6-9), pp. 441-414.

[27] Torove, Leiknes, 2001. Gas transfer and degassing using hollow fiber membranes. Thesis (Ph.D), Norwegian University of Science and Technology.

[28] Mulder M. 1996. Basic Principles of Membrane Technology. Kluwer Academic Publishers, Dordecht, The Netherlands, Chapter VIII, pp. 465-472.

[29] Esato, K., Eiseman, B. 1975. Experimental Evaluation of Gore-Tex Membrane Oxygenator. Journal of Thoracic and Cardiovascular Surgery, 69(5), pp. 690-697.

[30] Tsuji, T., Suma, K., Tanishita, K., Fukazawa H., Kanno, M., Hasegawa, H., Takahashi, A. 1981. Development and Clinical Evaluation of Hollow Fiber Membrane Oxygenator. Transactios- American Society for Artificial Internal Organs, 27(1-6), pp. 280-284.

[31] Qi, Z., Clussler, E.L. 1985. Microporous Hollow Fibers for Gas Absorption. I. Mass Transfer in the Liquid, Journal of Membrane Science, 23(3), pp. 321-332.

[32] Semmens, M. J., Qin, R., Zander, A. 1989. Using a Microporous Hollow Fiber Membrane to Separate VOC_s from Water. Journal AWWA, 81(4), pp. 162-167.

[33] Qi, Z., Clussler, E.L. 1985. Microporous hollow fibers for gas absorption: II. Mass transfer across the membrane, *Journal of Membrane Science***,** 23(3), pp. 331-345.

[34] Cypes, H.St., Engstrom, J.R. 2004. Analysis of a toluene stripping process: a comparison between a microfibricated striping column and a conventional packed tower. *Chemical Engineering Journal*, 101(1-3), pp. 49-56.

[35] Karoor, S., Sirkar, K.K. 1993. Gas absorption studies in microporous hollow fiber membrane modules, *Industrial & Engineering Chemistry Research*, 32(4), pp**.** 674-684.

[36] Kreulen, H., Smolders, C.A., Versteeg, G.F., Swaaij, W.P.M. Van. 1993. Microporous Hollow Fibre Membrane Modules as Gas-Liquid Contactors: Part 1. Physical Mass Transfer Processes. A Specific Application: Mass Transfer in Highly Viscous Liquids, *Journal of Membrane Science*, 78(3), pp. 197-216.

[37] Kreulen, H., Smolders, C.A., Versteeg, G.F., Swaaij, W.P.M. Van. 1993. Microporous Hollow Fibre Membrane Modules as Gas-Liquid Contactors. Part 2: Mass Transfer with Chemical Reaction, *Journal of Membrane Science*, 78(3), pp. 217-238.

[38] Rangwala, H.A. 1996. Absorption of Carbon Dioxide into Aqueous Solutions Using Hollow Fiber Membrane Contactors, *Journal of Membrane Science*, 112(2), pp. 229–240.

[39] Kim, Y.S., Yang S.M. 2000. Absorption of Carbon Dioxide Through Hollow Fiber Membranes Using Various Aqueous Absorbents. *Separation and Purification Technology*, 21(1-2), pp. 101-109.

[40] Bhaumik, D., Majumdar, S., Sirkar, K.K. 1998. Absorption of CO_2 in a Transverse Flow Hollow Fiber Membrane Module Having a Few Wraps of the Fiber Material. *Journal of Membrane Science*, 138(1), pp. 77-82.

[41] Wang, R., Li, D.F., Liang, D.T. 2004. Modelling of CO_2 Capture by Three Typical Amine Solutions in Hollow Fiber Membrane Contactors, *Chemical Engineering and Processing*, 43(7), pp. 849-856.

[42] Feron, P.H.M., Jansen, A.E. 2002. CO_2 Separation with Polyolefin Membrane Contactors and Dedicated Absorption Liquids: Performances and Prospects. *Separation and Purification Technology*, 27(3), pp. 231-242.

[43] Dindore, V.Y., Brilman, D.W.F., Feron, G.F.H., Versteeg, G.F. 2004. CO_2 Absorption at Elevated Pressures Using a Hollow Fiber Membrane Contactor, *Journal of Membrane Science*, 235(1-2), pp. 99-109.

[44] Atchariyawut, S., Feng C., Wang, R., Jiraratananon R., Liang, D.T. 2006. Effect of Membrane Structure on Mass-Transfer in the Membrane Gas-Liquid Contacting Process Using Microporous PVDF Hollow Fibers. *Journal of Membrane Science*, 285(1-2), pp. 272-281.

[45] Paul, S., Ghoshal, A.K., Mandal, B. 2008. Theoretical Studies on Separation of CO_2 by Single and Blended Aqueous Alkanolamine Solvents in Flat Sheet Membrane Contactor (FSMC), *Chemical Engineering Journal*, 144(3), pp. 352-360.

[46] Rongwong, W., Jiraratananon, R., Atchariyawut, S. 2009. Experimental Study on Membrane Wetting in Gas-Liquid Membrane Contacting Process for CO_2 Absorption by Single and Mixed Absorbents. *Separation and Purification Technology*, 69(1), pp. 118-125.

[47] Rajabzadeh, S., Yoshimoto, S., Teramoto, M., Marzouqi, M.Al., Matzuyama, H. 2009. CO_2 Absorption by using PVDF Hollow Fiber Membrane Contactors with Various Membrane Structures. *Separation and Purification Technology*, 69(2), pp. 210-220

[48] Delgado, A.J., Uguina, M.A., Sotelo, J.L., Agueda, V.I., Sanz, A. 2009. Simulation of CO_2 Absorption into Aqueous DEA using a Hollow Fiber Membrane Contactor: Evaluation of Contactor Performance. *Chemical Engineering Journal*, 152(2-3), pp. 396-405.

[49] Ksaisri, S., de Montigny, D., Tontiwachwuthikul, P., Jiraratananon, R. 2009. A Mathematical model for Gas Absorption Membrane Contactors that Studies the Effect of Partially Wetted Membranes, *Journal of Membrane Science*, 347(1-2), pp. 228-239.

[50] Zhang, H.Y., Wang, R., Liang, D.T., Tay, J.H. 2008. Theoretical and Experimental Studies of Membrane Wetting in the Membrane Gas-Liquid Contacting Process for CO_2 Absorption. *Journal of Membrane Science*, 308(1-2), pp. 162-170.

[51] Aronu, U.E., Svendsen, H.F., Hoff, K.A. 2010. Investigation of Amine Amino Acid Salt for Carbon Dioxide Absorption. *International Journal of Greenhouse Gas Control*, 4(4), pp. 771-775.

[52] Boucif, N., Favre, Eric., Roizard, D. 2008. CO_2 capture in HFMM Contactor with Typical Amine Solutions; A numerical analysis. *Chemical Engineering Science*, 63(22), pp. 5375-5385.

[53] Godino P., Pena, L., Mengual J.I. 1996. Membrane distillation: Theory and Experiments. *Journal of the membrane Science*, 1996, 121(1), pp. 83-93.

[54] Findley, M.E. 1967. Vaporization trough porous membranes. *Industrial & Engineering Chemistry Process Design and Development*, 6(2), pp. 226-230.

[55] Sarti, G.C. Gostoli C. 1990. Vacuum membrane distillation through capillary polypropylene membranes. *In Proceedings International Congress of Membranes*, 1, pp. 65-67.

[56] Schofeild, R. W., Fane, A. G., Fell, C.J.D. 1987. Heat and Mass Transfer in Membrane Distillation. *Journal of Membrane Science,* 33(3), pp. 299-313.

[57] Lefebvre, M.S., Johnson R.A., Yip, V. 1987. Theoretical and Practical Aspects of Osmotic Distillation. *International Congress of Membranes*, Tokyo (Japan).

[58] Lawson K. W., Lloyd D. R. 1997. Membrane Distillation. *Journal of Membrane Science*, 124(1), pp. 1-25.

[59] Ho, W.S., Sirkar, K.K. 1992. Membrane Handbook, Van Nostrand Reinhold, NEW YORK.

[60] Baker, Richard. W. 2004. Membrane Technology and Applications, *John Wiley and Sons*, England.

[61] Binning, R. C., Stuckey J.M.S, 1962. Method of separating hydrocarbons using ethyl cellulose selective membrane, U.S. Patent 2958657.

[62] Binning, R. C., Jennings, J.F., Martin, E.C. 1962. Process for Removing Water from Organic Chemicals, U.S. Patent 3035060.

[63] Ballweg, A.H., Bruschke, H.E.A., Schneider, W.H. 1982. Pervaporation Membranes, Fifth International Alcohol Fuel Technology Symposium.

[64] Blume, I.; Wijmans, J.G.; Baker, R.W. 1990. The Separation of Dissolved Organics from Water by Pervaporation, *Journal of Membrane Science*, 49(3), pp. 253-286.

[65] Chen, M.S.K., Glazer, J.L., Wensley, C.G. 1988. Pervaporation Process for Separating Alcohols from Ethers, U.S. Patent 4774365.

[66] Schucker, R.C. 1995. Separation of Organic Liquids by Pervaporation, Proceedings of Seventh International Conference on Pervaporation Process in the Chemical Industry, pp. 321-332.

[67] Cai, Z., Fang, Q., Chen, H., Fang, Z. 2006. A Microfluidic Chip Based Liquid-Liquid Extraction System With Microporous Membrane. *Analytica Chimica Acta*, 556(1), pp. 151-156.

[68] Jonsson, J.A., Mathiasson, L. 1999. Membrane Extraction For Sample Preparation, *Trends in Analytical Chemistry*, 18(5), pp. 318-320.

[69] Mason, E.A., Malinauskas, A.P. 1983. Gas Transport in Porous Media: The Dusty Gas Model, *Elsevier*: Amsterdam.

[70] Amador, C. 2006. Principles of Two-Phase Flow Microreactors and their Scale-Out. Thesis (Ph.D), University College London.

[71] Adamson A.W., Gast A.P. 1997. Physical Chemistry of Surfaces, *John Wiley & Sons*.

[72] Dindore, V.Y., Brilman, D.W.F., Geuzebroek, F.H., Versteeg, G.F. 2004. Membrane-Solvent Selection for CO_2 Removal Using Membrane Gas-Liquid Contactors, *Separation and Purification Technology*, 40(2), pp. 133-145.

[73] Byoung-sik K., Harriot P. 1984. Critical Entry Pressure for Liquids in Hydrophobic Membrane. *Journal of Colloid and Interface Science*, 115(1), pp. 1-8.

[74] Prasad R., Khare S., Sengupta A., Sirkar K.K., 1990. Novel Liquid in Pore Configuration in Membrane Solvent Extraction, *AIChE*, 36(10), pp. 1592-1596.

[75] Vaidya A.M., Bell G., Halling P.J. 1994. Aqueous-organic Membrane Bioreactors. Part II: Breakthrough Pressure Measurement, *Journal of Membrane Science*, 97, pp. 13-26.

[76] Adam N.K. 1948. Principles of Penetration of Liquids into Solids, Discuss. *Faraday Society*, 3, pp. 5-11.

[77] Volpe C.D., Maniglio D., Morra M. and Siboni S. 2002. The Determination of a 'Stable Equilibrium' Contact Angle on Heterogeneous and Rough Surfaces, *Colloids and Surfaces A (Physicochemical and Engineering aspects)*, 206(1-3), pp. 47-67.

[78] Wang, R., Zhang, H.Y., Feron, P.H.M., Liang, D.T. 2005. Influence of Membrane Wetting on CO_2 Capture in Microporous Hollow Fiber Membrane Contactors, *Separation and Purification Technology*, 46(1-2), pp. 33-40.

[79] Wang, R., Li, D.F., Zhou, C., Liu, M., Liang, D.T. 2004. Impact of DEA Solutions with and without CO_2 Loading on Porous Polypropylene Membranes Intended for Use as Contactors, *Journal of Membrane Science*, 229(1-2), pp. 147-157.

[80] Nishikawa, N., Ishibashi, M., Ohta, H., Akutsu, N. 1995. CO_2 Removal by Hollow-Fiber Gas-Liquid Contactor, Energy Convers.Mgmt, 36(6-9), 415-418.

[81] Matsumoto, H., Kitamura, H., Kamata, T., Ishibashi, M., H. Ota and N. Akutsu, 1995. *Chemical Engineering Journal*, 28**,** pp. 125.

[82] Fiqueroa, J.D., Fout, T., Plasynski, S., Mcllvried, H. 2008. Advances in CO_2 Capture Technology- The U.S. Department of Energy's Carbon Sequestration Program, *International Journal of Greenhouse Gas Control*, 2(1), pp. 9-20.

[83] IEA Clean Coal Centre. 2005. The World Coal-fired Power Plants Database, Gemini House, Putney, London, UK.

[84] Yang, H., Xu, Z.; Fan, M.; Bland, A.E, 2008. Progress in Carbon Dioxide Separation and Capture: A Review. *Journal of Environment Science*, 20(1), pp. 14-27.

[85] IPCC Special Report on Carbon dioxide Capture and Storage.

[86] Wilson, M.A., Wrubleski, R.M., Yarborough, L. 1992. Recovery of CO_2 From Power Plant Flue Gases Using Amines. *Energy Conservation Management*, 33(5-8), pp. 325-331.

[87] Nsakala, N. Liljedahl, G.N. 2003. Greenhouse Gas Emissions Control by Oxygen Firing in Circulating Fluidized Bed Boilers: Phase 1 – A Preliminary Systems Evaluations. Final report, U.S Department of Energy, DE-FC26-01NT41146.

[88] Griffini, G. 2005. Thermo-fluid Dynamic Issues in Microstructured Devices By Means of Finite-Element Calculations, Thesis (Undergraduate), University of Milano.

[89] Commenge J.M., Falk, L., Corriou, J.P., Matlosz, M. 2002. Optimal Design for Flow Uniformity in Microchannel Reactors. *AIChE Journal*, 48(2), pp. 345-351.

[90] Tonomura, O., Tanaka, S., Noda, M., Kano, M., Hasebe, S., Hashimoto, I. 2004. CFD-Based Optimal Design of Manifold in Plate-Fin Microdevices. *Chemical Engineering Journal*, 10(1-3), 397-402.

[91] Griffini, G., Gavriilis, A. 2007. Effect of Microchannel Plate Design on Fluid Flow Uniformity at Low Flow Rates, *Chemical Engineering Technology*, 30(3), pp. 395-406.

[92] Jensen, K. F. 2001. Microreaction engineering - Is Small Better? *Chemical Engineering Science*, 56(2), pp. 293-303.

[93] Gavriilidis, A., Angeli, P., Cao, E., Yeong, K.K., Wan, Y.S.S. 2002. Technology and Applications of Microengineered Reactors. *Chemical Engineering Research & Design*, 80(A1), pp. 3-30.

[94] Pohorecki, R., Moniuk, W., 1988. Kinetics of Reaction Between Carbon Dioxide and Hydroxyl Ions in Aqueous Electrolyte Solutions. *Chemical Engineering Science*, 43(7),1677.

[95] Cussler, E.L. 1984. Diffusion Mass Transfer in Fluid Systems, *Cambridge University Press*, Cambridge.

[96] Versteeg, G.F., Van Swaaij, W.P.M. 1988. On the kinetics Between CO_2 and Alkanolamines Both in Aqueous and Non-Aqueous Solutions. I. Primary and Secondary Amines, *Chemical Engineering Science*, 43(3), pp. 573-585.

[97] Nijsing, R.A.T.O., Hendriksz, R.H., Kramers, H. 1959. Absorption of CO_2 in Jets and Falling Films of Electrolyte Solutions, with and without Chemical Reaction. *Chemical Engineering Science*, 10(1-2), pp. 88-104.

[98] Barbe, A.M., Hogan, P.A., Johnson, R.A. 2000. Surface morphology changes during initial usage of hydrophobic, micro-porous polypropylene membranes, *Journal of Membrane Science*, 172(1-2), pp. 149-156.

[99] Schlichting H., 1958. boundary-Layer theory, *McGraw Hill*, London.

[100] Al-Marzouqi, M., El-Naas, M., Marzouki, S. 2008. Modeling of Chemical Absorption of CO_2 in Membrane Contactors. *Separation Purification Technology*, 62(3), pp. 499-506.

[101] Keshavarz, P., Fathikalajahi, J., Ayatollahi, S. 2008. Analysis of CO_2 Separation and Simulation of Partially Wetted Hollow Fiber Membrane Contactor, *Journal of Hazardous Materials*, 152(3), pp. 1237-1247.

[102] TeGrotenhuis, W.E., Cameron, R.J., Viswanathan, V.V., Wegeng, R.S. 2000. Solvent Extraction and Gas Absorption Using Microchannel Contactors: 3rd Int. Conf. on Microreaction Technology, Proc. of IMRET 3, *Springer-Verlag*, Berlin, pp. 541-549.

[103] Zhang, H.Y., Wang, R., Liang, D.T., Tay, H.J. 2006. Modeling and Experimental Study of CO_2 Absorption in a Hollow Fiber Membrane Contactor, Journal of Membrane Science, 2006, 279(1-2), pp. 301-310.

[104] Li, K., Teo, W.K. 1998. Use of Permeation and Absorption Methods for CO_2 Removal in Hollow Fibre Membrane Modules, *Separation and Purification Technology*, 13(1), pp. 79-88.

[105] Bougie, F., Iliuta, M.C. 2009. Kinetics of Absorbtion of Carbon Dioxide Into Aqueous Solutions of 2-Amino-2-Hydroxymethyl-1,3-Propanediol, *Chemical Engineering Science*, 64(1), pp. 153-162.

[106] Astarita, G. 1967. Mass Transfer with Chemical Reaction, *Elsevier Publishing Company*, Amsterdam/London/New York.

[107] Danckwerts, P.V. 1970. Gas-Liquid Reactions, *McGraw-Hill*, United States.

[108] Versteeg, G.G., Little, R.J., Swaalj, W.P.M. 1991. Kinetics of CO_2 with Primary and Secondary Amines in Aqueous Solutions. Influence of Temperature on Zwitterion Formation and Deprotonation Rates, *Chemical Engineering Science*, 47(8), pp. 2037-2045. [online] Available at: http://doc.utwente.nl/11172/1/Littel92kinetics2.pdf [accessed 14 March 2011].

[109] Paul, S., Ghoshal, A.K., Mandal, B. 2007. Removal of CO_2 by Single and Blended Aqueous Alkanolamine Solvents in Hollow-Fiber Membrane Contactor: Modeling and Simulation. *Industrial & Engineering Chemistry Research*, 46 (8), pp. 2576-2588.

[110] Rivera-Tinoco, R., Bouallou, C. 2010. Comparison of absorption rates and absorption capacity of ammonia solvents with MEA and MDEA aqueous blends for CO_2 capture. *Journal of Cleaner Production*, 18(9), pp. 875-880.

[111] Hey J .M., Kingston, G. J. 2007. The apparent contact angle for a nearly spherical drop on heterogeneous surface, *Chemical Physics Letters*, 447(1-3), pp. 44-48.

[112] Marzouqi, Al.M., Faiz R. 2009. Mathematical modeling for the simultaneous absorption of CO_2 and H_2S using MEA in hollow fiber membrane contactors. *Journal of Membrane Science*, 342(1-2), pp. 269-278.

[113] Shirazian, S., and Ashrafizadeh, S.N. 2010. Mass transfer simulation of carbon dioxide absorption in a hollow fiber membrane contactor, *Separation Science and Technology*, 45(4), pp. 515-524.

[114] Atchariyawut, S., Jiraratananon, R., Wang, R. 2007. Separation of CO_2 from CH4 by using gas-liquid membrane contacting process, *Journal of Membrane Science*, 304(1-2), pp. 163-172.

[115] Aroonwilas, Adisorn., V., A., Tontiwachwuthikul, P. 1999. Behaviour of the mass transfer coefficient of structured packings in CO_2 absorbers with chemical reactions. *Industrial & Engineering Chemistry Research*, 38(5), pp. 2044-2050.

[116] Stroock, A., Dertinger, S., Ajdari, A., Mezic, I., Stone, H., Whitesides, G. 2002. Chaotic mixer for microchannels, Science, 295(5555), pp. 647-651.

[117] Ansari, M., Kim, K. 2007. Shape optimization of a micromixer with staggered herringbone groove. Chemical Engineering Science, 62(23), pp. 6687-6695.

[118] Aubin, J., Fletcher, D., Bertrand, J., Xuereb, C. 2003. Characterization of the mixing quality in micromixers. *Chemical Engineering & Technology*, 26(12), pp. 1262-1270.

[119] Aubin, J., Fletcher, D., Xuereb, C. 2005. Design of micromixers using CFD modelling. *Chemical Engineering Science,* 60(8-9), pp. 2503-2516.

[120] Camesasca, M., Kaufman, M., Manas-Zloczower, I. 2006. Staggered passive micromixers with fractal surface patterning. *Journal of Micromechanics and Microengineering*, 16(11), pp. 2298-2311.

[121] Hassell, D., Zimmerman, W. (2006). Investigation of the convective motion through a staggered herringbone micromixer at low Reynolds number ow. *Chemical Engineering Science,* 61(9), pp. 2977-2985.

[122] Kang, T., Kwon, T. 2004. Colored particle tracking method for mixing analysis of chaotic micromixers. *Journal of Micromechanics and Microengineering*, 14(7), pp. 891-899.

[123] Kee, S., Gavriilidis, A. 2008. Design and characterisation of the staggered herringbone mixer. *Chemical Engineering Journal*, 142(1), pp. 109-121.

[124] Liu, Y., Kim, B., Sung, H. 2004. Two-aid mixing in a microchannel. *International Journal of Heat and Fluid Flow*, 25(6), pp. 986-995.

[125] Williams, M., Longmuir, K., Yager, P. 2008. A practical guide to the staggered herringbone mixer. *Lab on a Chip*, 8(7), pp. 1121-1129.

[126] Yang, J., Huang, K., Lin, Y. 2005. Geometric e_ects on uid mixing in passive grooved micromixers. *Lab on a Chip*, 5(10), pp. 1140-1147.

[127] Kirtland, J. D., McGraw, G. J., Stroock, A. D. 2006. Mass transfer to reactive boundaries from steady three-dimensional flows in microchannels. *Physics of Fluids*, 18(7), pp. 073602-073615.

[128] Yoon, S., Fichtl, G., Kenis, P. 2006. Active control of the depletion boundary layers in microuidic electrochemical reactors. *Lab on a Chip*, 6(12), pp. 1516-1524.

[129] Golden, J., Floyd-Smith, T., Mott, D., Ligler, F. 2007. Target delivery in a microuidic immunosensor. *Biosensors and Bioelectronics*, 22(11):2763-2767.

[130] Lopez, M. and Graham, M. 2008. Enhancement of mixing and adsorption in microuidic devices by shear-induced diffusion and topography-induced secondary law. *Physics of Fluids*, 20(5), pp. 053304-053316.

[131] Ghiotto. F. 2011. Gas Absorption and Stripping in membrane contactors. Thesis (Undergraduate), University College London.

[132] William B.J. Zimmerman. 2006. Multiphysics modeeling with finite element methods, World Scientific.

[133] Skelland A.H.P. 1974. Diffusional mass transfer , *John Wiley & Sons*, Hoboken.

[134] Shah R.K., London A.L. 1978. Laminar flow forced convection in ducts. A source book for compact heat exchanger Analytical Data, *Academic Press*, New York.

[135] Lu Gang-Jian, Zheng Fei-You, Cheng Dong-Min. 2008. Wetting mechanism in mass transfer process of hydrophobic membrane gas absorption, *Journal of Membrane Science*, 308(1-2), pp. 180-190.

[136] Ziegenbalg, D., Lob, P., Al-Rawashdeh, M., Kralisch, D., Hessel, V., Schonfeld, F. 2010. Use of smart interfaces to improve the liquid-sided mass transport in a falling film microreactor, *Chemical Engineering Science*, 65, pp. 3557-3566.

[137] Cantu, Perez. 2010. Modelling and Experiments of Microchannels Incorporating Microengineered Structures, Thesis (Ph.D), University College London.

[138] Levenspiel, O. 1999. Chemical Reaction Engineering, *John Wiley & Sons*, New York.

[139] Mason, J.T. 1997. Ultrasound in synthetic organic chemistry. *Chemical society reviews*, 26(6), pp. 443-451.

[140] Lepoint, Tand Mullie, F. 1994. What exactly is cavitation chemistry? *Ultrasonic Sonochemistry*, 1(1), pp. S13-S22.

[141] Suslic, K.S., Casadonte, D.J., Green, M.L.H., Thomson, M.E. 1987. Effects of High intensity ultrasound on inorganic solids, *Ultrasonics*, 25(1), pp. 56-59.

[142] Fogler, H.S and Lund K. 1973. Acoustically augmented diffusional transport, *Journal of Acoustic Society of America*, 53(1), pp. 59-64.

[143] Chisti, Y. 2003. Sonobioreactors: using ultrasound for enhanced microbial productivity, *Trends in biotechnology*, 21(2), pp. 89-93.

[144] Zabaneh, Munder and Bar R. 1991. Ultrasound-Enhanced Bioprocess.II: Dehydrogenation of hydrocortisone by arthrobacter simplex, *Biotechnology and bioengineering*, 37(11), pp. 998-103.

[145] Bar, R. 1988. Ultrasound-Enhanced Bioprocess: Cholesterol Oxidation by Rhodococcus erythropolis, *Biotechnology and bioengineering*, 32(5), pp. 655-663.

[146] Moholkar, S.V and Warmoeskerken, M.M.C.G, 2004. Mechanism of mass transfer enhancement in textiles by ultrasound, *AIChE Journal*, 50(1), pp. 58-64.

[147] Moholkar, V.S., and Warmoeskerken, M.M.C.G. 2004. Investigations in mass transfer enhancement in textiles with ultrasound, *Chemical Engineering Science*, 59(2), pp. 299-311.

[148] Sohbi, B.,Emtir, M.,Elgarni. 2007. The effect of vibration on the absorption of CO_2 with chemical reaction in aqueous solution of calcium hydroxide. *World Academy of Science, Engineering and Technology*, 29, pp. 311-313.

[149] Schueller, S.B.; Yang, R.T. 2001. Ultrasound Enhanced Adsorption and Desorption of Phenol on Activated Carbon and Polymeric Resign, *Industry & Engineering Chemistry Research*, 40(22), pp. 4912-4918.

[150] Yamashita, C.Akihiro.,Akagi, Akitsuna.,Tojo, J.Kakuji.,Sakai, Tadasu., Popovich, Robert.P., Moncrief, W.Jack. 2000. Enhanced mass transfer in peritoneal dialysis with application of ultrasound, *Memoirs of Shonan institute of technology*, 34(1), pp.123-128

[151] Riera, E., Golas, Y.,Blanco, A.,Gallego, J.A.,Blasco, M.,Mulet, A. 2004. Mass transfer enhancement in supercritical fluids extraction by means of power ultrasound. *Ultrasonics sonochemistry*, 11(3-2), pp. 241-244.

[152] BenYi, L and YiGang L. 2008. The ultrasonic-enhanced factor of mass transfer coefficient in the supercritical carbon dioxide extraction, *Science in china press*, 51(10), pp. 1496-1504.

[153] Pugin. B. 1987. Qualitative characterization of ultrasound reactors for heterogeneous sonochemistry, *Ultrasonics*, 25(1), pp.49-55

[154] Schenk, R., Hessel, V., Hofmann, C., Kiss, J. 2004. Lowe Holger.,Ziogas Athanasios, Numbering- up of micro devices: a first liquid-flow splitting unit, Chemical Engineering Journal, 101(1-3), pp. 421-429.

[155] Appleyard, D. 2005. Micro-players edge microreactors into the mainstream, The Chemical Engineer, 765(2), pp. 42-43.

[156] Spicer, Dean., Mcmullin, N.James.,Rourke, Holly. 2006. A multi-layer biochip with integrated hollow fiber waveguides, J.micromech.microeng, 16(8), pp. 1674-1680.

[157] Mendorf, Matthias., Nachtrodt, Henrik.,Agar, David, 2010. Externes numbering up fur flussig/flussig-systeme in kapillarreaktoren, chemie.ingenieur.technik, 82(3), pp. 259-264.

[158] Vankayala, Kiran,B.,Lob, P., Hessel, V.,Menges, G.,Hofmann, C., Metzke, D.,Krtschil,U.,Kost, H-J. 2007. Scale up of process intesifying falling film microreactors to pilot production scale. *International Journal of Chemical Reactor Engineering*, 5(A91).

[159] Saber, M., Commenge, J.M., Falk, L. 2010. Microreactor numbering up in multi scale networks for industrial scale applications: Impact of flow maldistribution on the reactor performances. *Chemical engineering science*, 65(1), pp. 372-379.

[160] Mas, de Nuria, Gunther, A., Kraus, T., Schmidt, M.A., Jensen, K.F. 2005. Scaled out multilayer gas-liquid microreactor with integrated velocimetry sensors. *Industrial & Engineering Chemical Research*, 44(24), pp. 8997-9013.

[161] Kashid, M.N., Gupta, A., Renken, A.,Kiwi-Minsker, L. 2010. Numbering up and mass transfer studies of liquid-liquid two phase microstructured reactors. *Chemical engineering journal*, 158(2), pp. 233-240.

[162] Perry, R.H and Green, D.W. 1997. Perry's Chemical Engineer's Handbook (7th Edition), McGraw-Hill.

[163] Kikutani, Y., Hibara, A., Uchiyama, K., Hisamoto, H., Tokeshi, M., Kitamori, T. 2002. Pile-up glass microreactor. *Lab on a Chip*, 2(4), pp. 193-196.

[164] Tonkovich, A., Kuhlmann, D., Rogers, A., Mcdaniel, J., Fitzgerald, S., Arora, R.,Yuschak, T. 2005. Microchannel technology scale up to commercial capacity, 7th World Congress of Chemical Engineering. *Chemical Engineering Research and Design*, 83(6), pp. 634-639.

[165] Kikutani, Y., Horiuchi, T., Uchiyama, K., Hisamoto, H., Tokeshi, M., Kitamori, T. 2002. Glass microchip with three-dimensional microchannel network for 2x2 parallel system, *Lab on a Chip*, 2(4), pp. 188-192.

[166] Yue, J., Boichot, R.,Luo, L., Gonthier, Y.,Chen, G.,Yuan, Q. 2010. Flow distribution and mass transfer in a parallel microchannel contactor integrated with constructal distributors. *AIChE journal*, 56(2), pp. 298-317.

[167] Tong, H.D., Jansen, H.V., Gadgil, V.J., Bostan, C.G., Berenschot, E., Van Rijn, Cees. J.M., Elwenspoek, M. 2004. Silicon nitride nanosieve membrane, *Nano Leterst*, 4(2) pp.283-287. [online] Available: http://www.utwente.nl/ewi/ioms/publications/2014-Scientific-Output-2004/Files-Scientific-Output-2004/Tong-H.D-Bostan-C.G.-Nanoletters-Vol-4-no-2-2004-pp%20283-287.pdf [accessed 5 January 2011].

[168] Brans, G., Kromkamp, J., Pek. N.J., Gielen, J., Heck, J., Van Rijn, C.J.M., Van der Sman, R.G.M., Schroen, C.G.P.H., Boom, R.M. 2006. Evaluation of microsieve membrane design. *Journal of Membrane Science*, 278(1-2), pp. 344-348.

[169] McGeoch, J.E.M., McGeoch, M.W., Carter, D.J.D., Shuman, R.F., Guidotti, G. 2000. Biological-to-electronic interface with pores of ATP synthase subunit C in silicon nitride barrier. *Medical and biological engineering and computing*, 38(1), pp. 113-119.

[170] Schenkel, T., Radmilovic, V., Stach, E.A., Park, S.J., Persaud, A. 2003. Formation of a few nanometer wide holes in membranes with a dual beam focused ion system. *Journal of Vacuum Science & Technology B (Microelectronics and Nanometer Structures)*, 21, pp. 2720-2723 [online] Available: http://www-ebit.lbl.gov/publications/JoVSaTB-2003-21:2720-schenkel.pdf [accessed 5 January 2011].

[171] Deshmukh, M.M., Ralph, D.C., Thomas, M., Silcox, J. 1999. Nanofibrication using a stencil mask, *Applied Physics Letters*, 75(11), pp. 1631-1633.

[172] Schmidt, Ch., Mayer, M., Vogel, H. 2009. A chip based biosensor for the functional analysis of single ion channels, International Edition. *Angewandte Chemie*, p. 39.

[173] Striemer, C.C., Gaborski, Th.R., McGrath, J.L., Fauchet, M.Ph. 2007. Charge and size based separation of macromolecules using ultrathin silicon membranes, *Letters to Nature*, 445, pp. 749-753.

[174] Li, J., Stein, D., McMullan, C.B, Aziz D., Golovchenko M.J., Jene. A. 2001. Ion beam sculpting at nanometre length scales, *Letters to Nature*, 412(6843), pp. 166-169.

[175] Kuiper, S., Van Rijn, C.J.M., Nijdam, W., Krijnen, G.J.M.,Elwenspoek, M.C, 2000. Determination of particle-release conditions in microfiltration: a simple single-particle model tested on a model membrane, *Journal of Membrane Science*, 180(1), pp. 15-28.

[176] Kurt, E.P. 1982. Silicon as a Mechanical Material, *Proceedings of the IEEE*, pp. 70.

[177] Van Rijn, C.J.M., Nijdam, W., Van der Stappen L.A.V.G., Rapse, O.J.A. Broens L., Hoof, S. 1997. Innovation in yeast cell filtration: cost saving technology with high flux membranes. *Proceedings of the European Brewery Conference*, Maastrick, The Netherlands, pp. 501.

[178] Van Rijn C.J.M., Kromkamp, J. 2001. Method for filtering milk, WO Patent 0209527.

[179] Fluxxion: Separation by precision. The High Efficiency Contactor (HEC) Solution. [online]. Available from: http://www.fluxxion.com/index.php?option=com_content&view=article&id=79&Itemid=75 [accessed 15 December 2010].

[180] Yan, S.P., Fang, M.X., Zhang, W.F., Wang, S.Y., Xu, Z.K., Luo, Z.Y., Cen, K.F, 2007. Experimental study on the separation of CO_2 from flue gas using hollow fiber membrane contactors without wetting. *Fuel Processing Technology*, 88(5), pp. 501-511.

[181] Hoff, K.A., Juliussen, O., Svendsen, H.F, 2004. Modeling and experimental study of carbon dioxide absorption in aqueous alkanolamine solutions using a membrane contactor, *Industrial & Engineering Chemistry Research*, 43(16), pp. 4908-4921.

[182] Teller, A.J., Ford H.E. 1958. Packed Column Performance of Carbon Dioxide-Monoethanolamine System. Division of Industrial &Engineering Chemistry: 131st meeting, ACS, Miami.

[183] Gabelman, A., Hwang S.T. 1999. Hollow Fiber membrane contactors. *Journal of Membrane Science*, 159(1-2), pp. 61-106.

APPENDIX A

STANDARD OPERATING PROCEDURES

Operation of CO_2 Absorption with Microstructure Membrane Reactor Set-up

1.0 Introduction

1.1 For information regarding the operations of the instruments refer to the appropriate manuals

Mass Flow Controllers: BROOKS 5850.

Gas Chromatograph: SHIMADZU GC-14B.

4 Channel Readout: 0154.

HPLC Pump: Waters 510.

1.2 Refer to figure of the set-up (Figure A.1).

2.0 Pre-operation Checks

2.1 Check electrical power of GC, extract fan, CO_2 alarm, and mass flow controllers (MFCs).

2.2 The extract fan of fume cupboard and CO_2 alarm must be on before opening the gas cylinders.

2.3 Calibration of the MFCs at least once a month.

2.4 Calibration of the GC every month.

2.5 Calibration of the HPLC pump (Waters 510) every month.

3.0 Start-up and Normal Operation

3.1 Make sure GC is ready for analysis.

3.2 Set MFCs at desired flow rates.

3.3 Set HPLC pump (Waters 510) at desired flow rates.

3.4 Make sure GC and integrator are ready for the analysis.

3.5 Open CO_2/N_2 gas cylinder (Set the outlet pressure at 0.5 bar).

3.6 Switch the MFCs on.

3.7 Switch the HPLC pump (Waters 510) on.

3.8 Check for leaks around the connections of the reactor and around the gas cylinder.

3.9 Check the concentration of CO_2 with the GC.

3.10 Clean the reactor with D.I water.

3.11 Fill the reactor with ethanol (70%wt) and keep the ethanol inside the reactor until the next experiment.

3.12 The MFCs and the HPLC pump are connected with filters to avoid any particles to get in the reactor and block the membrane's pores.

3.13 Priming of the reactor

3.14 Close the on-off valves 1&2 at the gas inlet/outlet.

3.15 Set HPLC pump (Waters 510) at desired flow rates

3.16 Fill the liquid and the gas phase with ethanol.

3.17 Set MFCs at desired flow rates.

3.18 Begin to turn on the on-off valves 1&2 slowly.

3.19 Wait until you have the desire pressure deference between the gas and the liquid phase (PGin=220, PGout ≈220, PLin =160, PLout=110), and you have complete separation of the two phases.

3.20 3.1.8 After a successful separation with ethanol you repeat the priming procedure twice, once using D.I water (to clean the reactor from ethanol) and the second time with NaOH (for CO2 absorption).

4.0 Shut Down

4.1. Switch off TCD current.

4.2. Set GC oven to 30^{o}C.

4.3. Wait for temperature to cool down.

4.4. Switch off GC.

4.5. Turn off the cylinders (CO_2/N_2, He).

4.6. Turn the MFC of N_2 off.

4.7. Turn the HPLC pump (Waters 510) off.

4.8. Open the purge valve from the cylinder (CO_2/N_2).

4.9. Close the purge valve when the regulator is zero.

4.10. Turn regulator knob fully anticlockwise.

5.0 Emergency Shut Down

5.1 Close all gas cylinders.

5.2 Switch all electric power off at the wall.

5.3 Inform people in the lab, supervisor and / or safety officer about the emergency.

6.0 Safety Measures

6.1 People enter the lab must wear protective equipment such as: labcoat, goggles and gloves.

6.2 In case of contact with the chemicals (NaOH, Amines solutions) (MSDS are kept in 303B Combustion lab).

6.3 Eye contact- Irrigate with eye wash for at least 10 minutes, seek medical attention.

6.4 Skin contact- Drench skin with water. Seek medical attention unless contact has been slight.

6.5 Ingestion- Wash mouth thoroughly, and drink plenty of water, seek medical advice.

6.6 Eyes can be protected by wearing protective goggles during the experiment.

7.0 Additional Information

7.1 Schematic of the CO_2 Absorption with Fluxxion Membrane Reactor Set-up.

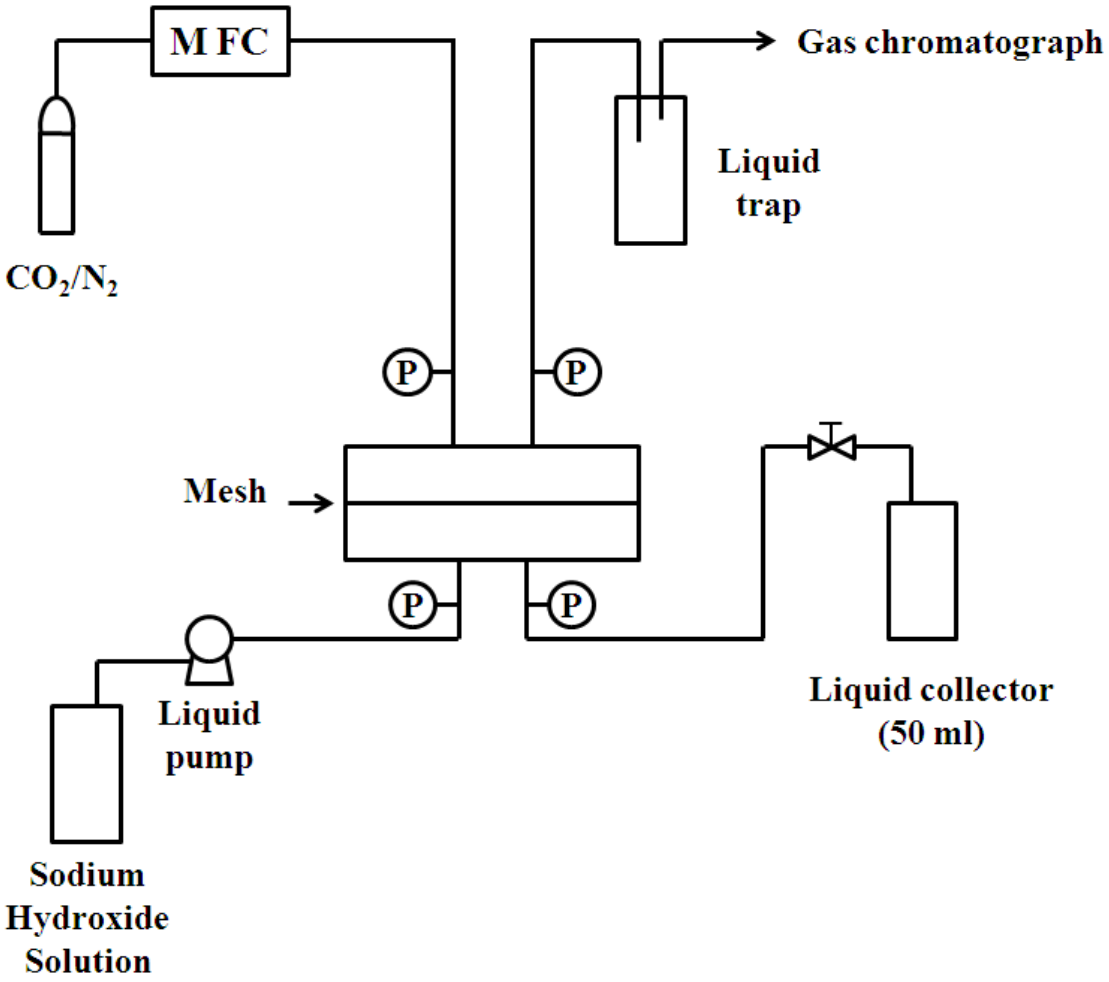

Figure A. 1 Schematic of the CO_2 Absorption with the Fluxxion Membrane Reactor Set-up.

Operation of Gas Chromatograph: SHIMADZU GC-14B

1.0 Pre-operation Checks

1.1 Calibration of the GC every month.

2.0 Start-up and Normal Operation

2.1 Open CO_2/N_2 gas cylinder (Set the outlet pressure at 0.5 bar).

2.2 Open Helium gas cylinder (Set the outlet pressure at 6 bar).

2.3 Turn power on for the GC.

2.4 Turn power on for the integrator.

2.5 Set GC (P) pressure at 600 KPa.

2.6 Set GC (M) pressure at 280 KPa.

2.7 Turn the heater on.

2.8 Set GC column temperature at 190 ^{o}C.

2.9 Set GC gas sampling valve temperature (AUX2) at 50 ^{o}C.

2.10 Set GC detector temperature at 200 ^{o}C .

2.11 Switch on TCD current.

2.12 Set GC injector temperature at 200 ^{o}C.

2.13 Set GC detector current at 35 mA.

2.14 Leave the GC and the detector signal on the integrator to stabilize for 1 hr.

2.15 Check the gas sampling valve to be anticlockwise.

2.16 Press the start1 button from the GC integrator and turn the sampling valve clockwise and wait for ten seconds.

2.17 Turn the sampling valve anticlockwise.

2.18 Check the concentration of CO_2 with the GC and press stop1 on the integrator to finish.

3.0 Shut Down

3.1 Switch off TCD current.

3.2 Set GC oven to 30^{o}C.

3.3 Wait for temperature to cool down.

3.4 Switch off heater.

3.5 Switch off GC.

3.6 Turn off the cylinders (CO_2/N_2, He).

5.0 Emergency Shut Down

4.1 Close all gas cylinders.

4.2 Switch all electric power off at the wall.

Inform people in the lab, supervisor and / or safety officer about the emergency.

Calibration of the GC

Two different concentrations of 20:80 CO_2:N_2 (vol%) and 100 (vol%) CO_2 were analyzed in the GC. Three measurements for each concentration of (20:80, 100%) were taken and after averaging them a graph (Figure A.1) was plotted. A linear relation between the peak area and the concentration of CO_2 is shown in Figure A.1. The calibration curve will be used to calculate the (vol%) concentration of CO_2 in the outlet of the reactor based on the peak areas.

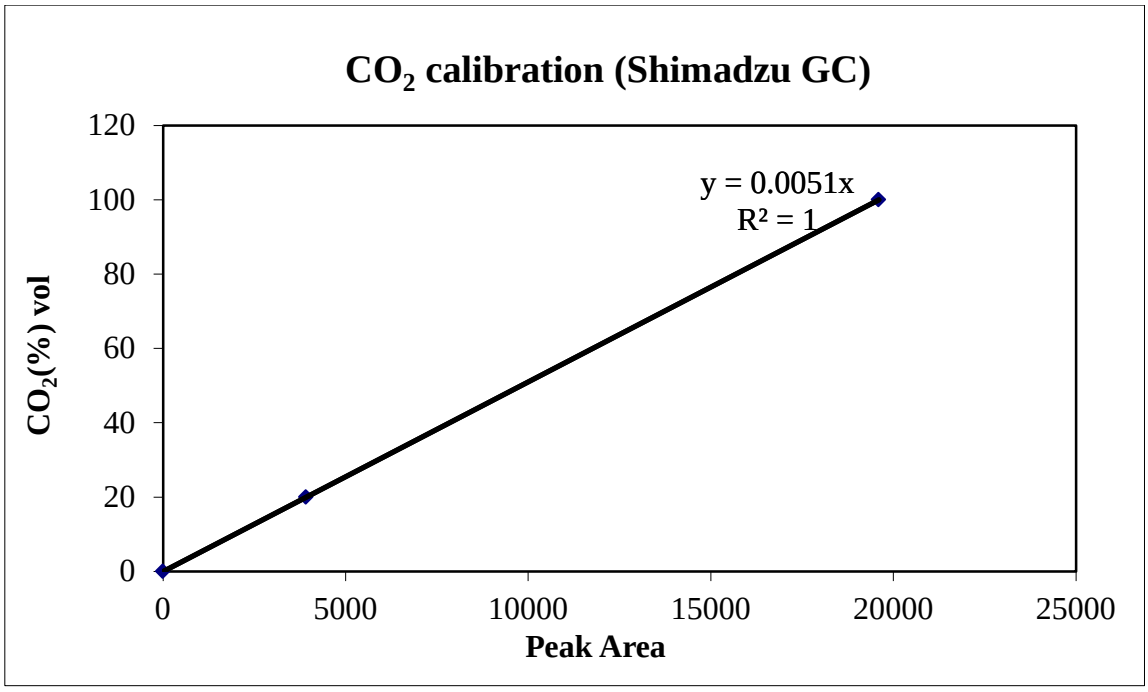

Figure A. 2 Calibration curve of CO_2

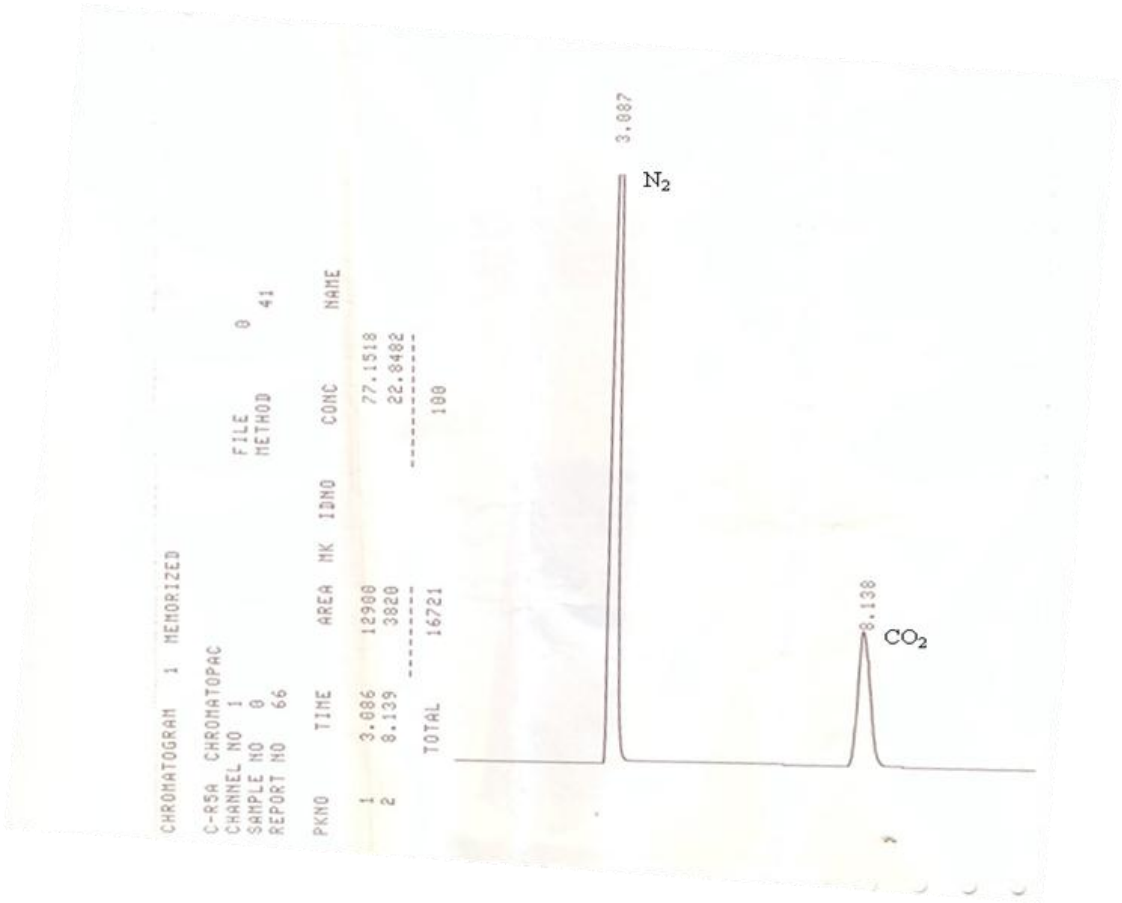

Figure A. 3 A typical GC chromatograph for 20:80 CO_2:N_2

APPENDIX B
FABRICATION METHOD FOR STAGGERED HERRINGBONES (WORK BY LOUIS LAM)

Fabrication

Silicon inserts with the staggered herringbones on them used in chapter four were fabricated using conventional semi-conductor processing techniques. In brief, purchased silicon wafers (n-type, <100>, 525um thick) were pre-cleaned by Piranha solution (50vol% H_2SO_4 and 50vol% H_2O_2) at 100^oC for 15 minutes. After rinsing by de-ionised water and drying at 200^oC for 10 minutes, a thick photoresist layer (Rohm and Haas, SPR-220-7) was spin-coated on the wafer at 4000rpm, followed by soft-baking at 110^oC for 90 seconds. The designed herringbones structures on a photomask were transferred to the photoresist layer using a contact aligner (Quintel Q4000-6). The exposure energy for the photoresist was 470mJ/cm^2, which was approximately equivalent to exposure of 300nm UV light for 36 seconds. The photoresist was then aged for 45 minutes at room conditions to reinforce the adhesion of photoresist on the silicon surface. The patterns were developed by immersing the wafers into a standard photoresist developer (Shipley Microposit MF-26A), for 90 seconds. After thorough rinsing, a final post-baking process at 110^oC for 90 seconds was carried out.

The patterned wafers were etched by deep reactive ion etching (STS ASE®). The etched depth of the micro-channels was measured by surface profiler (Veeco Dektak 8).

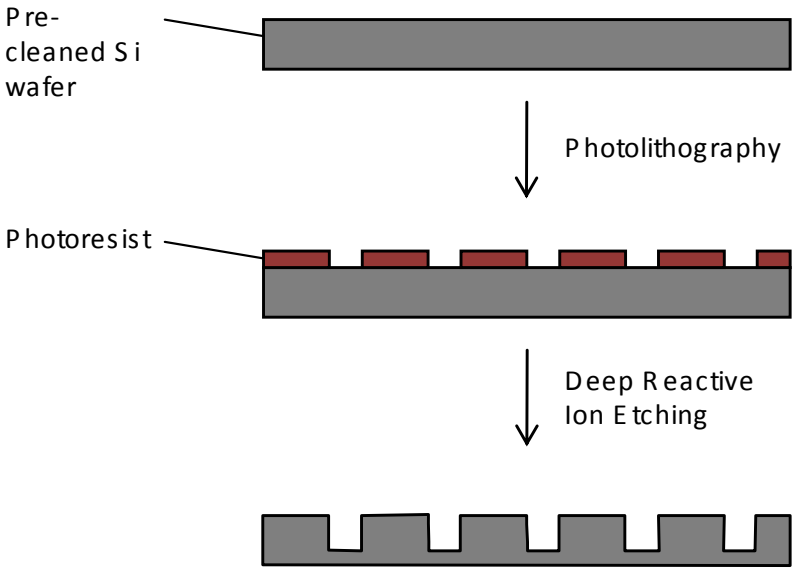

Figure B. 1 Microfabrication procedure of silicon inserts

APPENDIX C
DESIGN EQUATIONS FOR CO-CURRENT FLOW MESH CONTACTOR

A detailed derivation of eq. (1) is shown below:

The analysis below was made for the system represented in figure 1-B and is based on the assumptions:

- Isothermal and isobaric conditions.
- Gas flowrate and liquid flowrate are constant.
- The mixtures are considered to be dilute.
- Mass transfer coefficients are constant.

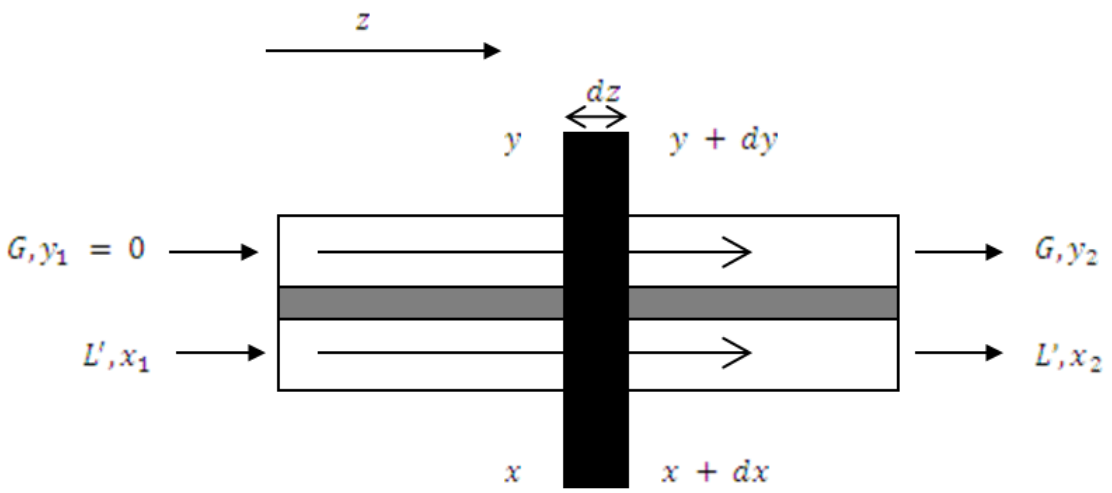

Figure C. 1 Schematic of a membrane gas-liquid contactor with co-current flow.

First the following parameters are defined:

$$G = \frac{\text{moles of gas}}{(\text{unit time})\cdot(\text{unit cross section of the contactor})}$$

$$L' = \frac{\text{moles of liquid}}{(\text{unit time})\cdot(\text{unit cross section of the contactor})}$$

y = molar fraction of acetone in the gas phase

x = molar fraction of acetone in the liquid phase

K_y = overall gas transfer coefficient in terms of moles fraction $\left[\frac{\text{Kmol}}{\text{m}^2 \cdot \text{s}}\right]$

K_x = overall liquid transfer coefficient in terms of moles fraction $\left[\frac{\text{Kmol}}{\text{m}^2 \cdot \text{s}}\right]$

$$L' = \frac{F_l \cdot \rho}{M \cdot A}$$

$$G = \frac{F_g \cdot P}{R \cdot T \cdot A}$$

$$A = w \cdot H$$

$$C_{total} = \frac{\rho}{M}$$

$$a = \frac{\text{interface area}}{\text{unit volume of the reactor}} = \frac{A_m}{V}$$

interfacial area for transfer $= a \cdot dV = a \cdot A \cdot dz$

The flux is

$$N_A = \frac{\text{kmol of acetone stripped}}{\text{s·unit interfacial area}}$$

In general, the equation for the mass transfer is expressed as:

$$N_A \cdot a \cdot A \cdot dz = K \cdot (\text{driving force}) \cdot a \cdot A \cdot dz \quad (1)$$

Defining a fictitious mole fraction in the gas phase that is in equilibrium with the liquid phase:

$$y^* = m \cdot x \quad (2)$$

where m is the solubility of acetone

$$N_A \cdot a \cdot A \cdot dz = K_y \cdot (y * - y) \cdot a \cdot A \cdot dz \quad (3)$$

$$N_A = K_y \cdot (y * - y) = K_x \cdot (x - x *) \quad (4)$$

Considering that the moles of acetone leaving the liquid phase is the same as those taken up by the gas phase:

$$A \cdot G \cdot dy = A \cdot L' \cdot dx \quad (5)$$

- **For the gas phase**

This amount is also the same as the flux of acetone through the membrane in the corresponding volume.

$$G \cdot A \cdot dy = N_A \cdot a \cdot dV \quad (6)$$

$$G \cdot A \cdot dy = N_A \cdot a \cdot A \cdot dz \quad (7)$$

$$G \cdot dy = N_A \cdot a \cdot dz \quad (8)$$

Using eq. (2) and (4)

$$N_A = K_y \cdot (m \cdot x - y)$$

$$G \cdot dy = K_y \cdot (m \cdot x - y) \cdot a \cdot dz \quad (9)$$

$$dz = \frac{G}{K_y \cdot a} \cdot \frac{dy}{(m \cdot x - y)} \quad (10)$$

Now this relationship can be integrated:

$$\int_0^L dz = \frac{G}{K_y \cdot a} \cdot \int_{y_1=0}^{y_2} \frac{dy}{(m \cdot x - y)} \quad (11)$$

$y_1 = 0$ because at the inlet in the gas phase there is no acetone

$$\int_0^L dz = L = \frac{G}{K_y \cdot a} \cdot \int_{y_1=0}^{y_2} \frac{dy}{(m \cdot x - y)} \quad (12)$$

- **The same relationship can be developed for the liquid**

$$L' \cdot A \cdot dx = N_A \cdot a \cdot dV \quad (13)$$

$$L' \cdot A \cdot dx = N_A \cdot a \cdot A \cdot dz \quad (14)$$

$$L' \cdot dx = N_A \cdot a \cdot dz \quad (15)$$

Substituting in eq. (4) $N_A = K_x \cdot (x - x*)$

where $x* = \frac{y}{m}$ (16)

$$L \cdot dx = K_x \cdot \left(\frac{y}{m} - x\right) \cdot a \cdot dz \quad (17)$$

$$dz = \frac{L'}{K_x \cdot a} \cdot \frac{dx}{\left(\frac{y}{m} - x\right)} \quad (18)$$

Now this relationship can be integrated:

$$\int_0^L dz = \frac{L'}{K_x \cdot a} \cdot \int_{x_1}^{x_2} \frac{dx}{\left(\frac{y}{m} - x\right)}$$

(19)

Where x_1 is the liquid phase inlet mole fraction and x_2 is the outlet liquid phase mole fraction

$$\int_0^L dz = L = \frac{L'}{K_x * a} * \int_{x_1}^{x_2} \frac{dx}{\left(\frac{y}{m} - x\right)} \quad (20)$$

Now we can analyze eq. (11): $\int_0^L dz = L = \frac{G}{K_y \cdot a} \cdot \int_{y_1=0}^{y_2} \frac{dy}{(m \cdot x - y)}$

From the mole balance between z=0 and z:

$$G \cdot (y - y_1) = L' \cdot (x_1 - x) \quad (21)$$

Since $y_1 = 0$

$$x = x_1 - \frac{G}{L'} \cdot y$$

$$\int_0^{y_2} \frac{dy}{(m \cdot x - y)} = \int_0^{y_2} \frac{dy}{m \cdot \left(x_1 - \frac{G}{L'} y\right) - y} = \int_0^{y_2} \frac{dy}{m \cdot x_1 - \left(1 + \frac{m \cdot G}{L'}\right) \cdot y} \quad (22)$$

Defining $\frac{m \cdot G}{L'} = A'$

$$\int_0^{y_2} \frac{dy}{m \cdot x_1 - (1+A') \cdot y} \tag{23}$$

Next we calculate the integral

$$-\frac{1}{1+A'} \cdot \int_0^{y_2} \frac{d[(1+A') \cdot y]}{(1+A') \cdot y - m \cdot x_1} \tag{24}$$

$$-\frac{1}{1+A'} \cdot \ln \frac{(1+A') \cdot y_2 - m \cdot x_1}{0 - m \cdot x_1} = -\frac{1}{1+A'} \cdot \ln \frac{m \cdot x_1 - (1+A') \cdot y_2}{m \cdot x_1} \tag{25}$$

Substituting $\frac{m \cdot G}{L'} = A'$

$$-\frac{1}{1+A'} \cdot \ln \frac{m \cdot x_1 - \left(1+\frac{m \cdot G}{L'}\right) \cdot y_2}{m \cdot x_1} = -\frac{1}{1+A'} \cdot \ln \frac{m \cdot x_1 - y_2 - m \cdot \left(\frac{G}{L'} y_2\right)}{m \cdot x_1}$$

(26)

From the molar balance eq. (20) $x = x_1 - \frac{G}{L'} \cdot y \;\rightarrow\; -\frac{G}{L'} \cdot y_2 = x_2 - x_1$

$$-\frac{1}{1+A'} \cdot \ln \frac{m \cdot x_1 - y_2 - m \cdot (x_1 - x_2)}{m \cdot x_1} = -\frac{1}{1+A'} \cdot \ln \frac{m \cdot x_2 - y_2}{m \cdot x_1} \tag{27}$$

The same can be done for the liquid starting from eq. (19): $\int_0^L dz = L = \frac{L'}{K_x \cdot a} \cdot \int_{x_1}^{x_2} \frac{dx}{\left(\frac{y}{m} - x\right)}$

From the molar balance eq. (20):

$$y = \frac{L'}{G} \cdot x_1 - \frac{L'}{G} \cdot x$$

Substituting it into the starting equation:

$$\int_{x_1}^{x_2} \frac{dx}{\left(\frac{y}{m} - x\right)} = \int_{x_1}^{x_2} \frac{dx}{\frac{L'}{m \cdot G} \cdot (x_1 - x) - x} = \int_{x_1}^{x_2} \frac{dx}{\frac{L'}{m \cdot G} \cdot x_1 - (1 + \frac{L'}{m \cdot G}) x} \tag{28}$$

Defining $\frac{L'}{m \cdot G} = B$

$$\int_{x_1}^{x_2} \frac{dx}{B \cdot x_1 - (1+B) x} \tag{29}$$

$$-\frac{1}{1+B} \cdot \int_{x_1}^{x_2} \frac{d[(1+B) \cdot x]}{(1+B) x - B \cdot x_1} \tag{30}$$

The integral is

$$\ln[(1+B) \cdot x - B \cdot x_1] \tag{31}$$

This has to be calculated between x_2 and x_1:

$$\ln[(1+B) \cdot x_2 - B \cdot x_1] - \ln[(1+B) \cdot x_1 - B \cdot x_1] \tag{32}$$

So the result is:

$$-\frac{1}{1+B}\cdot\ln\frac{(1+B)\cdot x_2-B\cdot x_1}{(1+B)\cdot x_1-B\cdot x_1}=-\frac{1}{1+B}\cdot\ln\frac{(1+B)vx_2-B\cdot x_1}{x_1} \quad (33)$$

Substituting $\frac{L'}{m\cdot G}=B$

$$-\frac{1}{1+\frac{L'}{m\cdot G}}\cdot\ln\frac{x_2+\frac{L'}{m\cdot G}\cdot x_2-\frac{L'}{m\cdot G}\cdot x_1}{x_1} \quad (34)$$

From the molar balance eq.(20) $y=\frac{L'}{G}\cdot x_1-\frac{L'}{G}\cdot x$

$$-\frac{1}{1+\frac{L'}{m\cdot G}}\cdot\ln\frac{x_2-\frac{y_2}{m}}{x_1}=\boxed{-\frac{1}{1+\frac{1}{A'}}\cdot\ln\left(\frac{m\cdot x_2-y_2}{m\cdot x_1}\right)} \quad (35)$$

So now we can come back to the expression of the contactor length in eq. (11) we substitute eq. (26):

$$L=\frac{G}{K_y\cdot a}\cdot\left[-\frac{1}{1+A'}\cdot\ln\frac{m\cdot x_2-y_2}{m\cdot x_1}\right]=\frac{L'}{K_x\cdot a}\cdot\left[-\frac{1}{1+\frac{1}{A'}}\cdot\ln\left(\frac{m\cdot x_2-y_2}{m\cdot x_1}\right)\right]$$

(36)

To find the exit concentration we can substitute eq. (32) in eq. (19):

$$L=\frac{L'}{K_x\cdot a}\cdot\left[-\frac{1}{1+B}\cdot\ln\frac{(1+B)\cdot x_2-B\cdot x_1}{x_1}\right]=\frac{L'}{K_x\cdot a}\cdot\left\{-\frac{1}{1+B}\cdot\ln\left[\frac{x_2}{x_1}\cdot(1+B)-B\right]\right\} \quad (37)$$

Rearranging this equation:

$$-\frac{L\cdot K_x\cdot a\cdot(1+B)}{L'}=\ln\left[\frac{x_2}{x_1}\cdot(1+B)-B\right] \quad (38)$$

Taking the exponential of both terms:

$$\exp\left[-\frac{L\cdot K_x\cdot a\cdot(1+B)}{L'}\right]=\frac{x_2}{x_1}\cdot(1+B)-B \quad (39)$$

Solving for $\frac{x_2}{x_1}$ and substituting B:

$$\frac{x_2}{x_1}=\left\{\exp\left[-\frac{L\cdot K_x\cdot a}{L'}\cdot\left(1+\frac{L'}{m\cdot G}\right)\right]+\frac{L'}{m\cdot G}\right\}\cdot\frac{1}{\left(1+\frac{L'}{m\cdot G}\right)} \quad (40)$$

Now multiplying top and bottom of the last fraction with $\frac{m\cdot G}{L'}$:

$$\frac{x_2}{x_1}=\frac{1}{\left(\frac{m\cdot G}{L'}+1\right)}\cdot\left\{\frac{m\cdot G}{L'}\cdot\exp\left[-\frac{L\cdot K_x\cdot a}{L'}\cdot\left(1+\frac{L'}{m\cdot G}\right)\right]+1\right\} \quad (41)$$

Using:

$$L'=\frac{F_l\cdot\rho}{M\cdot A}$$

$$G = \frac{F_g \cdot P}{R \cdot T \cdot A}$$

$$A = w \cdot H$$

$$C_{total} = \frac{\rho}{M}$$

$$H_e = \frac{C^L_{acetone}}{C^G_{acetone}} = \frac{x \cdot C_{total} \cdot R \cdot T}{y \cdot P_{total}} = \frac{1}{m} \cdot \frac{C_{total} \cdot R \cdot T}{P_{total}}$$

$$m = C_{total} \cdot \frac{R \cdot T}{H_e \cdot P_{total}}$$

we calculate $\frac{m \cdot G}{L'}$

$$\frac{m \cdot G}{L'} = \frac{\frac{C_{total} \cdot R \cdot T}{H_e \cdot P_{total}} \cdot \frac{F_g \cdot P_{total}}{R \cdot T \cdot A}}{\frac{F_l \cdot \rho}{M \cdot w \cdot H}} = \frac{F_g}{F_l} \cdot \frac{1}{H_e} = \Omega$$

Introducing the total mass transfer coefficient in terms of concentration: $K_T = \frac{K_x}{C_{total}}$

Now remember that $= \frac{A_m}{V}$, where $A_m = L \cdot w$, the term $\frac{K_x \cdot a}{L'}$ can be calculated:

$$\frac{K_x \cdot a}{L'} = \frac{C_{total} \cdot K_T \cdot \frac{L \cdot w}{L \cdot w \cdot H}}{\frac{F_L \cdot \rho}{M \cdot w \cdot H}} = \frac{1}{F_l} \cdot w \cdot K_T = \frac{K_T}{\delta_l \cdot u_l} = \frac{K_T \cdot \tau_l}{\delta_l \cdot L} = \beta$$

Then equation (40) becomes

$$\frac{x_2}{x_1} = \frac{C_{out}}{C_{in}} = \frac{1}{(\Omega + 1)} \cdot \left\{ \Omega \cdot \exp\left[-\beta \cdot \left(1 + \frac{1}{\Omega} \right) \cdot L \right] + 1 \right\}$$

where:

$$\Omega = \frac{F_g}{F_l} \cdot \frac{1}{H_e}$$

$$\beta = \frac{K_T \cdot \tau_l}{\delta_l \cdot L}$$

and δ_l is the height of the liquid channel, τ_l the liquid residence time and L the contactor length.

Notation

F_g	gas flow rate (ml/min)
F_l	liquid flow rate (ml/min)
$H_e = \frac{C^L_{acetone}}{C^G_{acetone}}$	Henry constant (-)
δ_l	height of the liquid channel (m)
$\tau_l = \frac{V_l}{F_l}$	liquid residence time (s)
A	cross sectional area of the contactor (m^2)
a	surface of the interface per unit volume of the reactor (1/m)
H	height of the contactor (m)
K_T	total mass transfer coefficient (m/s)
L	Length of contactor (m)
M	molar mass (g/mol)
R	ideal gas constant (l·Pa/K·mol)
T	temperature (K)
w	width of contactor (m)
ρ	density of solution (Kg/m^3)
x	gas phase mole fraction
y	liquid phase mole fraction

Subscript

1 inlet

2 outlet

g gas

l liquid

i interface

APPENDIX D

HTU CALCULATIONS

Parameters and equations used for HTU determination in silicon nitride mesh contactor

Membrane surface= 4.34cm^2

δ_g= 0.321 cm

$\delta_l = 25 * 10^{-4}$cm

$\delta_m = 1 * 10^{-4}$cm

$\varepsilon = 0.203$

$\tau = 1$

L=0.9cm

W= 4.8cm

H= 0.8314 (-)

$Sh_l = 4.8 = \frac{K_l * 2 * \delta_l}{D^L_{MEA}}$

$Sh_g = 4.8 = \frac{K_g * 2 * \delta_g}{D^G_{CO_2}}$

HTU Calculations

$$\frac{1}{K_m} = \frac{\tau * \delta_m}{D^L_{MEA} * \varepsilon}$$

$$D^G_{CO_2} = 1.63 * 10^{-5}\ \frac{m^2}{s}$$

$$D^L_{CO_2} = 1.4 * 10^{-9}\ \frac{m^2}{s}$$

$$D^L_{MEA} = 7.7 * 10^{-10}\ \frac{m^2}{s}$$

$$HTU = \frac{\upsilon}{K_t * a}$$

$$\upsilon = \frac{F_l\ [\frac{cm^3}{s}]}{(\text{Cross sectional area})[cm^2]}$$

$$\text{Cross sectional area} = \text{width} * \delta_g$$

$$a = \frac{\text{gas/liquid contact area}}{\text{contactor volume}}\ m^2/m^3$$

$$\frac{1}{K} = \frac{H}{K_g} + \frac{1}{K_m} + \frac{1}{k_l}$$